A measurement of the branching ratio of the $K_L^0 \rightarrow p^0 v\bar{v}$ decay

Mikhail Yur'evich DOROSHENKO

March 2005

Department of Particle and Nuclear Physics,
School of High Energy Accelerator Science,
The Graduate University for Advanced Science (SOKENDAI),
Tsukuba, Ibaraki, Japan

Acknowledgments

My first thanks go to Prof. Takao Inagaki, my advisor at the Graduate University for Advance Science (Sokendai), who spent much of his time to teach me and to help me accommodate myself in Japan. I am also grateful to his wife, Mrs. Fukoko Inagaki, who has always been very kind to me.

I would like to thank my Russian adviser, Dr. Alexander Kurilin, who strongly supported me during this period, and made great efforts together with Prof. Inagaki to make this visit to Japan possible.

My big thanks go to Prof. Hideki Okuno, who involved me to join the production and testing of the detectors. Without his organization talent my work for the E391a experiment would have been much harder. Dr. Yoshio Yoshimura helped me in mechanical work and gave me good advice. I would like to thank Prof. Takahiro Sato, who participated in my teaching and Dr. Gei-Youb Lim who always shared his time for discussions and explaining physics to me. Great thanks go to the Dr. Takeshi Komatsubara for organizing useful seminars about theory and experimental techniques. Special thanks go to Prof. Taku Yamanaka for his fruitful criticisms in discussions of new ideas.

I would like to thank Dr. Mitsuhiro Yamaga and Dr. Hiroaki Watanabe who were always ready to explain to me hard-to-understand points, and discussed with me new ideas. Dr. Watanabe greatly helped me in writing this thesis. Also, my big thanks go to Ph.D students Mr. Ken Sakashita and Mr. Toshi Sumida for fruitful discussions and team-work. I am also grateful to master students from Saga and Osaka Universities, especially, Mr. Shojiro Ishibashi, who participated in many work and nice evening-parties.

I am grateful to Dr. Evgenii Kuzmin from Joint Institute for Nuclear research (JINR), who guided me in constructing of the detectors, and taught me necessary software techniques. He showed me the way how to reach the goal. I would like to thank the JINR team for fruitful team-work.

My special thanks go to Elene Podolskoi, who greatly supported me during my stay in Japan, and especially during writing the thesis. I could complete the thesis during a tight period thanks to her.

This work was supported by a grant of the Japanese government.

Abstract

The $K_L^0 \to \pi^0 \nu\bar{\nu}$ decay is a golden channel to study the origin of CP violation. The branching ratio is proportional to the parameter η, which measures the magnitude of the CP violation in the CKM matrix; the theoretical uncertainties are so small that the measurement allows us to make a precise test of the Standard Model of CP violation.

Experiment E391a was designed to measure $K_L^0 \to \pi^0 \nu\bar{\nu}$ decay with a goal of $3 \cdot 10^{-10}$ single-event sensitivity. A $K_L^0 \to \pi^0 \nu\bar{\nu}$ decay is searched for by a signal of $K_L^0 \to \pi^0\ (\pi^0 \to \gamma\gamma)$ + *nothing*. The energies and positions of the gammas were measured with a CsI calorimeter. The "*nothing*" was confirmed by no additional signals in the veto system, which covered the whole decay region. Several unique techniques were developed for E391a, such as a well-collimated "pencil" beam, differential pumping, a double-decay chamber and highly sensitive veto detectors to cover almost the whole 4π geometry.

During the beam time in February-June 2004, we collected about 6Tb of data, equivalent to a full 60 days of operation. As the first step, we performed an analysis of one day of data, which is a main topic of the present thesis. Good quality and stability of the data were confirmed by this analysis. All detectors were calibrated by using punch-through and/or cosmic muons. In addition, the CsI calorimeter was calibrated more precisely by using γ's from the π^0's produced with an aluminum target. The reconstruction of neutral decays ($K_L^0 \to 3\pi^0, 2\pi^0, \gamma\gamma$) showed good agreement with MC simulations and in the number of the K_L^0 yield. The pure signal and background samples of $K_L^0 \to 3\pi^0, 2\pi^0, \gamma\gamma$ were used for a veto study, and showed good agreement of the acceptance loss due to the veto cuts.

In the 2γ sample, which contains candidates for $K_L^0 \to \pi^0 \nu\bar{\nu}$ decays, we observed various sources of background events surrounding the signal box. They were from the other K_L^0 decays and from halo neutron interactions; in addition, we found a clear effect due to the interactions of the beam-core neutrons with the membrane separating the two vacuum chambers, which fell down into the beam axis, accidentally.

Finally, we opened the signal box and observed no event inside. The single-event sensitivity for $K_L^0 \to \pi^0 \nu\bar{\nu}$ decay was estimated to be 8.3×10^{-7}. This led to an upper limit of the branching ratio of $1.9 \cdot 10^{-6}$ at the 90% confidence level.

We conclude that the analysis of the one-day data was very valuable to understand the performance of the experiment and to develop new software techniques for the analysis. The results of this study were reflected in an upgrade of the experimental setup for the next run, RUN II, which started in the middle of January, 2005.

Contents

Chapter 1

Motivation of the experiment

1.1 Theoretical background

The asymmetry between a particle and its anti-particle, which is called CP violation, was discovered in the neutral K-meson system in 1964 [1]. On the macroscopic scale, CP violation is necessary to explain matter domination in the universe. On the microscopic scale, it has been an important guide to understand elementary-particle interactions. The origin of CP violation, however, is still not clear. Notably, the Koboyashi-Maskawa model, the Standard Model (SM) of elementary particles, does not give strong enough CP violation effects to explain matter domination in the universe. In order to uncover the origin of CP violation, it is important to test predictions of the Kobayashi-Maskawa model. Measurements of direct CP violation processes are especially important, since they offer power to discriminate various theoretical models.

Experiments for studying of CP violation using K-mesons have been actively pursued, because K-mesons are easy to generate, and their CP sensitivity is high [1]. Similar to the K-meson system, the B-meson system also has a high sensitivity for CP violation. Recently, Bfactory experiments, such as KEK-BELLE and SLAC-BABAR, have confirmed large CP violation in the B-meson system [2], where the validity of the KM model has been established by observing the predicted indirect CP violation in the B-meson system due to mixing phenomena. On the other hand, it is not yet clear if direct CP violation in B-meson decays is consistent with the KM-model predictions.

We believe that the E391 experiment, which is searching for the $K_L^0 \to p^0 v\bar{v}$ decay [3], will shed light on the validity of the KM model and in the search for a new source of CP violation in Nature. According to the Standard Model, the branching ratio of the $K_L^0 \to p^0 v\bar{v}$ decay is predicted to be $3\text{x}10^{-11}$ [4]. The $K_L^0 \to p^0 v\bar{v}$ decay measurement can unambiguously determine the height, h, of the unitarity triangle of the fundamental CKM (Cabibbo-Kobayashi-Maskawa) parameters, because this process is theoretically very clean. On the other hand, the experiment of B-meson decays can measure the angle, $f_1(b)$, of the unitarity triangle. Therefore, it is possible to test the KM Model and to search for a new source of CP violation by combining all of the experimental results from K-meson and B-meson decays.

CP violation arises naturally in the three-generation Standard Model [5]. CP violation in the Standard Model appears only in the charged-current interactions of quarks, and is described by only one complex phase, the Kobayashi-Maskawa phase. First, a brief summary of CP violation in the KM model is described. Then, the physics of the $K_L^0 \to p^0 v\bar{v}$ decay is discussed.

1.1.1 General

The Lagrangian of the weak charged-current interactions of quarks is written as follows:

$$L_{CC} = \frac{g_2}{\sqrt{2}}\left(\overline{u_L} g^m V_{CKM}\, d_L \cdot W_m^+ + \overline{d_L} g^m \left(V_{CKM}\right)^+ u_L \cdot W_m^-\right), \tag{1.1}$$

where

$$\bar{u} = \left(\bar{u}, \bar{c}, \bar{t}\right),\ d = \begin{pmatrix} d \\ s \\ b \end{pmatrix}.$$

V_{CKM} is the Cabibo-Koboyashi-Maskawa unitary matrix, g_2 is the weak-coupling constant and g^m are the Dirac matrices. The subscript L denotes “left-handed” spinors; $q_L \equiv \frac{1}{2}(1-g_5)q$. The symbols u, d, s, c, b and t denote the quark mass eigenstates of each flavor.

The Lagrangian changes under the CP transformation as follows:

$$CP(L_{CC}) = \frac{g_2}{\sqrt{2}}\left(\overline{d_L} g^{m} (V_{CKM})^T u_L \cdot W_m^- + \overline{u_L} g^{m} (V_{CKM})^* d_L \cdot W_m^+\right). \quad (1.2)$$

Therefore, if $V_{CKM} \neq (V_{CKM})^*$, that is, if the CKM matrix contains an imaginary parameter, which cannot be absorbed by re-phasing of the quark fields, CP symmetry is violated in the weak charged-current interactions of quarks.

A unitary $n \times n$ matrix for n quark generations is characterized by $n_q = n(n-1)/2$ rotation angles and $n_d = (n-1)(n-2)/2$ physical phases. For $n = 2$, only the Cabibbo angle remains, since we have $n_q = 1$ and $n_d = 0$. For three generations, we have $n_q = 3$ and $n_d = 1$. Therefore, one CP phase in V_{CKM} appears.

From the Lagrangian, the weak eigenstate of quarks is described by a mixed state of the mass eigenstates of quarks with the 3×3 matrix, V_{CKM}. Since V_{CKM} is not diagonal, the $W^{\pm}$ boson can couple to quarks of different generations.

Wolfenstein parameterization of the CKM matrix in terms of four parameters $(l, A, r$ and $h)$ is convenient, because it help us to estimate the hierarchy of the magnitudes of the matrix elements[6]:

$$V_{CKM} = \begin{pmatrix} V_{ud} & V_{us} & V_{ub} \\ V_{cd} & V_{cs} & V_{cb} \\ V_{td} & V_{ts} & V_{tb} \end{pmatrix}$$

$$\approx \begin{pmatrix} 1 - l^2/2 & l & Al^3(r - ih) \\ -l & 1 - l^2/2 & Al^2 \\ Al^3(1 - r - ih) & -Al^2 & 1 \end{pmatrix} + O\left(l^4\right), \quad (1.3)$$

where $l \equiv \sin(q_c)$, q_c is the Cabibo angle. The parameter h represents the imaginary component of V_{CKM} in the Wolfenstein parameterization.

Our present knowledge of the CKM matrix elements comes from the following sources:

- $|V_{ud}|$ =0.9738 $\pm$ 0.0005 [7]. The value was derived from two distinct sources: the nuclear beta decays [8] and the decay of free neutrons [9]
- $|V_{us}|$ =0.2200 $\pm$ 0.0026 [10]. It was obtained from K_{e3} decays [11] with various corrections [12,13]
- $|V_{cd}|$ =0.224 $\pm$ 0.012 [10]. It was deduced from neutrino and antineutrino production of charm quark off valence d quarks [14-16]

- $|V_{cs}|=0.996 \pm 0.013$ [13]. It was obtained from direct measurements of the charm-tagged W decays [12]. However, the most precise value was derived from measurements of the branching fraction of the leptonic decays of the W boson [13].
- $|V_{cb}| = (41.3 \pm 1.5) \cdot 10^{-3}$ [17]. It was extracted from exclusive measurements of $B \to D^{*} l\nu$ decays and the inclusive one using the semileptonic width of $B \to X l\bar{\nu}$ decays.
- $|V_{ub}| = (3.67 \pm 0.47) \cdot 10^{-3}$ [18]. The world average was calculated as the weighted mean from inclusive and exclusive measurements of $b \to u l \nu$ decays of B mesons.
- $\dfrac{|V_{tb}|^2}{|V_{td}|^2 + |V_{ts}|^2 + |V_{tb}|^2} = 0.94(+0.31, -0.24)$ [19]. This constraint was obtained from a study of the branching fraction of $t \to b l^{+} \nu$ decays.

The remaining CKM matrix elements were calculated using the unitarity condition,

$$V_{CKM} \cdot V_{CKM}{}^{+} = 1 \cdot \qquad (1.4)$$

In the Wolfenstein parameterization, the parameters were determined as follows [14] (in brackets the relative errors are shown):

$$\lambda = 0.2200 \pm 0.0026 \;\; (1.1\%),$$
$$A = 0.853 \pm 0.037 \;\; (4.3\%),$$
$$\bar{\rho} = 0.20 \pm 0.09 \;\; (4.5\%),$$
$$\bar{\eta} = 0.33 \pm 0.05 \;\; (15\%),$$

where $\bar{\rho} = \rho(1 - \lambda^2/2)$ and $\bar{\eta} = \eta(1 - \lambda^2/2)$. Thus the most ambiguous parameter is $\bar{\eta}$, which has a 15% relative error.

The unitarity of V_{CKM} can be visually expressed as a triangle, "Unitarity Triangle". Fig. 1.1 shows one of the typical Unitarity Triangles. If all CP violation phenomena can be explained by the Standard Model, the Unitarity Triangle is strictly closed. On the other hand, if the Unitarity Triangle is not closed, there is new physics beyond the Standard Model. Since the relative importance of the new physics effects may be different for each process, precise measurements of various CKM parameters should be the keys to identify any new source of CP violation.

The current $(\bar{r},\bar{h})$ values are constrained by the following three data:

- $\dfrac{|V_{ub}|}{|V_{cb}|}$ gives a radius in the $(\bar{r},\bar{h})$ plane

$$\frac{1}{l}\frac{|V_{ub}|}{|V_{cb}|}=\frac{\sqrt{\bar{r}^2+\bar{h}^2}}{1-l^2/2}. \tag{1.5}$$

$\dfrac{|V_{ub}|}{|V_{cb}|}=0.089\pm 0.011$ [18]

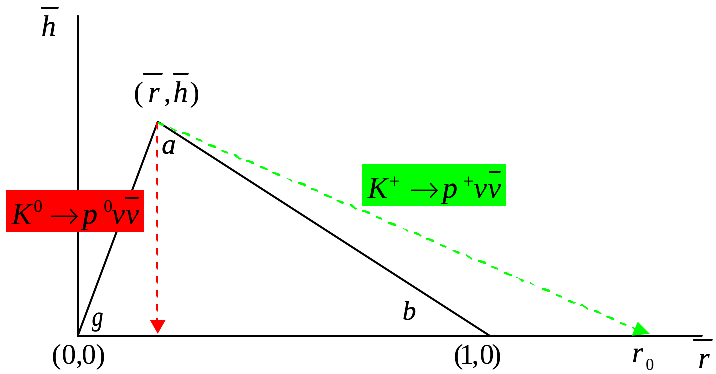

Fig. 1.1 Typical Unitarity Triangle. $(a,b,g)=(f_2,f_1,f_3)$

- $|V_{tb}{}^*V_{td}|$ is connected to $(\bar{r},\bar{h})$ through the following relation:

$$\frac{1}{Al^3}|V_{tb}{}^*V_{td}|=\frac{\sqrt{(1-\bar{r})^2+\bar{h}^2}}{1-l^2/2}, \tag{1.6}$$

where $|V_{tb}{}^*V_{td}|=(8.3\pm 1.6)\cdot 10^{-3}$ [15] from a measurement of ΔM_d in the $B_d^0-\overline{B_d^0}$ oscillation. The main uncertainty comes from an estimation of the hadronic matrix element.

- The e parameter of the $K^0-\overline{K^0}$ mixing matrix is connected to $(\bar{r},\bar{h})$ through the following relation [4]:

$$e=\bar{h}\left[1.248(1-\bar{r})A^2\left(\frac{m_t}{170GeV}\right)^{1.52}+0.31\right]A^2B_K, \tag{1.7}$$

where $B_K=0.86\pm 0.06\pm 0.14$, to gap parameter, [16], which is the ratio between the matrix element of the four-quark operator and its value in the vacuum insertion approximation. B_K is the main source of uncertainty for the constraint. This equation specifies a hyperbola in the $(\bar{r},\bar{h})$ plane, where the experimental va lue of e is given by [20]

$$e=(2.284\pm 0.014)\cdot 10^{-3}.$$

- $\sin 2b = \sin 2f_1 = 0.736 \pm 0.049$ [15], which comes from the asymmetry of the $B_d \to yK_S$ and other B_d decay modes.

In Fig. 1.2, these constraints and the possible Unitarity Triangle with an apex in the preferable area are shown.

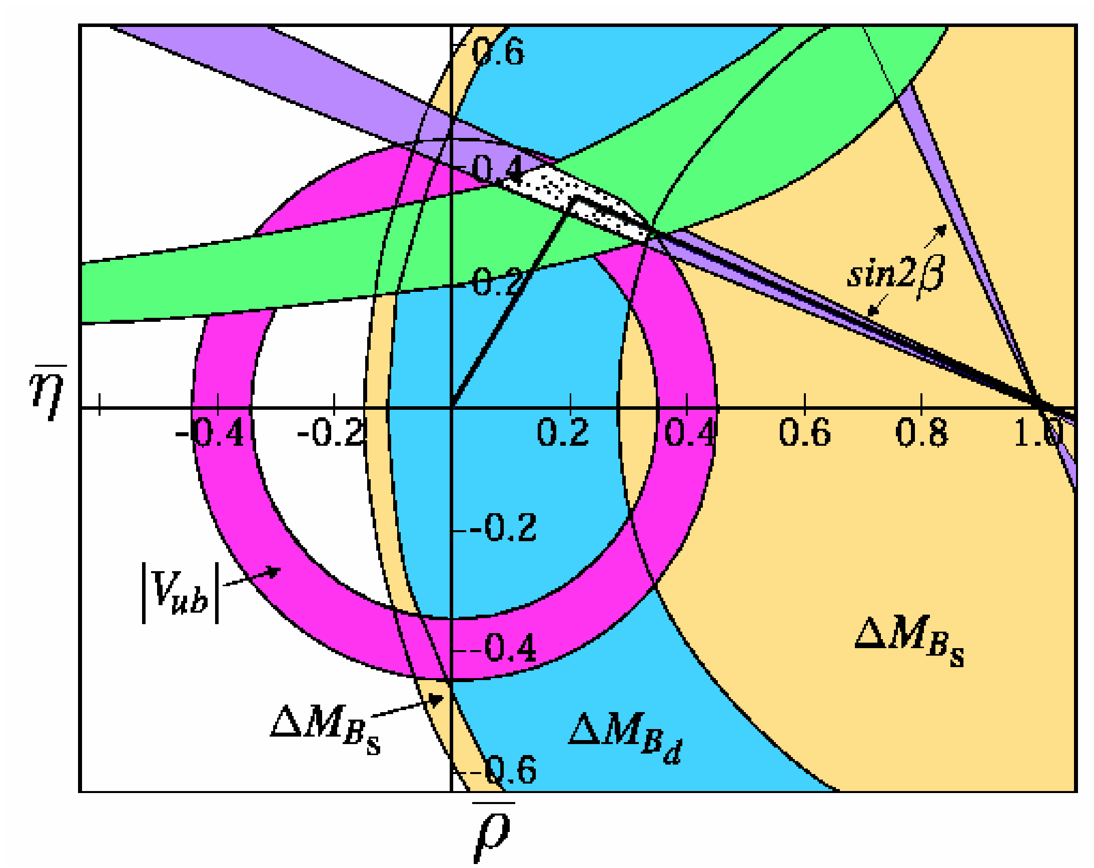

Fig. 1.2 Constraints on the Unitarity Triangle ($\pm 1s$). The possible Unitarity Triangle with an apex in the preferable area is shown($b = f_1$).

A further constraint can be obtained from a rare kaon decay, $K_L^0 \to p^0 v\bar{v}$, which provides information about the height of the Unitarity Triangle with small theoretical uncertainties. The theoretical uncertainties in estimating the branching ratio of the decays $K_L^0 \to p^0 v\bar{v}$ and $K^+ \to p^+ v\bar{v}$ are about 2% and 7%, respectively. The combination of the B-decay experiment and the rare kaon decay experiment is expected to provide valuable information to determine the origin of CP violation.

Finally, we note two CP violation processes of a neutral K-meson system, that is, a direct CP violation process and an indirect one. The direct one is a direct transition between different CP-states. The parameter h appears in the decay process through a box or penguin diagrams. On the other hand, the indirect one appears in decays into the same CP-state, which is produced by $K^0 - \overline{K^0}$ oscillation. In the case of indirect CP violation, the h parameter appears in the oscillation process.

1.1.2 $K_L^0 \to p^0 \nu\bar{\nu}$ decay in the Standard Model

In this section, the theoretical bases of the $K_L^0 \to p^0 \nu\bar{\nu}$ decay within the Standard Model, namely the branching ratio prediction and its relation to the parameter h, are described.

The $K_L^0 \to p^0 \nu\bar{\nu}$ decay offers one of the most transparent probes concerning the origin of CP violation. It proceeds through the diagrams shown in Fig. 1.3.

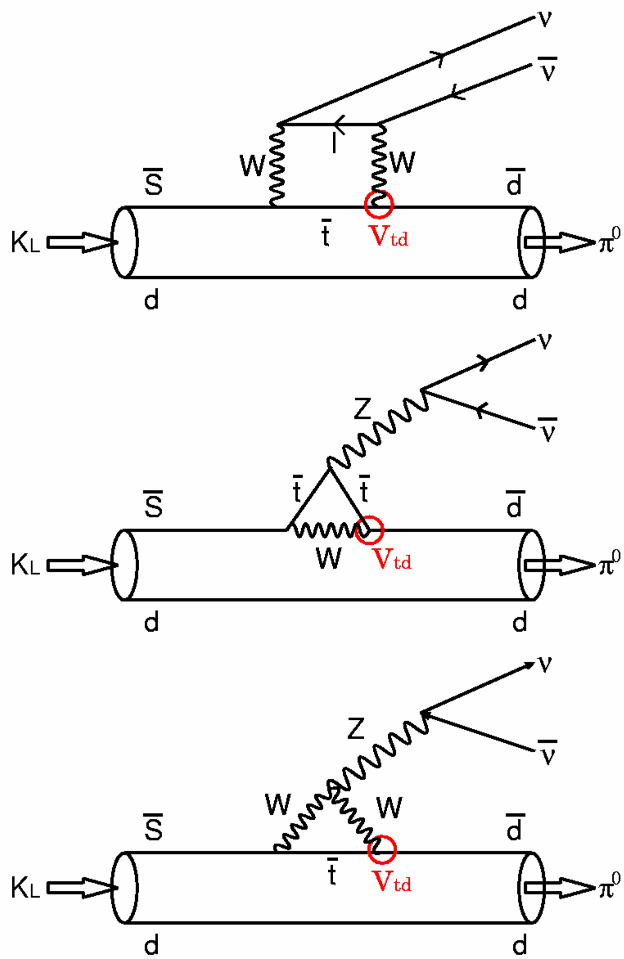

Fig. 1.3. Diagrams of the $K_L^0 \to p^0 \nu\bar{\nu}$ decay

From these diagrams, we can easily see that this process is sensitive to the CP violating parameter, h, as follows[4]:

$$A(K_L^0 \to p^0 v\bar{v}) \approx A(K^0 \to p^0 v\bar{v}) - A(\overline{K^0} \to p^0 v\bar{v})$$

$$\propto V_{td} - V_{td}^* = 2 \cdot \mathrm{Im}(V_{td}) \propto h\ , \qquad (1.8)$$

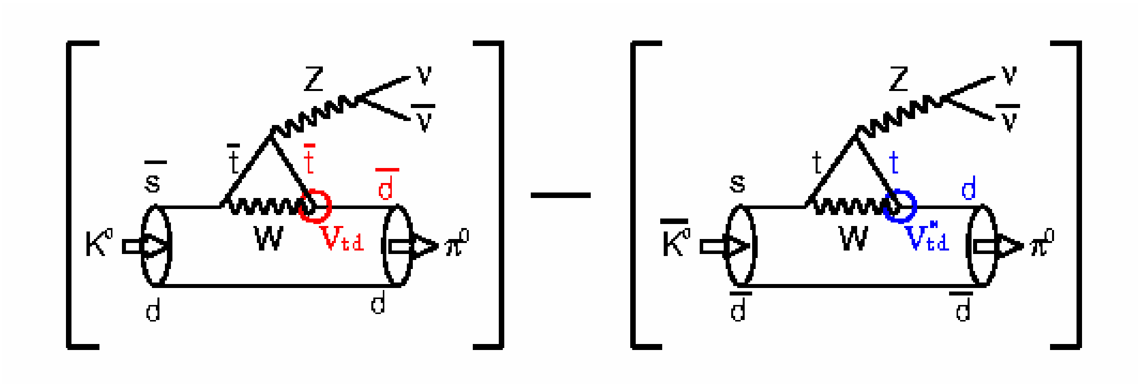

Fig. 1.4. Typical diagrams for the $K_L^0 \to p^0 v\bar{v}$ decay.

This decay is entirely the second-order weak processes determined by the Z-penguin and W-box diagrams. It is completely dominated by "short-distance" loop diagrams with a top-quark exchange. Since photons do not couple to neutrinos, there is no electromagnetic contribution in the leading order. The $K \to pv\bar{v}$ decay is theoretically clean because the hadronic transition amplitudes are described by the matrix elements of quark currents between mesonic states, which can be extracted from the semileptonic decays using the isospin symmetry.

The amplitude of the $K \to pv\bar{v}$ decay through the box diagram can be written by a simple calculation [22]:

$$A_{box}(K \to pv\bar{v}) = C_K \sum_{i=c,t} V_{id} V_{is}^{\ *} X_{box}(x_i) \langle p \,|(\bar{s}d)_{V-A}|\, K\rangle [\bar{v}g_a(1-g_5)v], \quad (1.9)$$

where $C_K \equiv \frac{-G_F}{\sqrt{2}} \frac{a}{2p \sin^2 q_w}$, $X_{box} = \frac{x_i(x_i - \ln x_i - 1)}{(x_i - 1)^2}$, $x_i \equiv \left(\frac{m_i}{m_w}\right)^2$ (1.10)

and q_w is the Weinberg angle. Here, $\langle p\,|\bar{s}g^a(1-g_5)d|\,K\rangle$ is written as $\langle p\,|(\bar{s}d)_{V-A}|\,K\rangle$. Because of the isospin symmetry, the relation $\langle p^+|(\bar{s}d)_{V-A}|K^+\rangle = \sqrt{2}\langle p^0|(\bar{s}u)_{V-A}|K^0\rangle$ is a very good approximation. The matrix element of the weak current $(\bar{s}d)$ between K^+ and p^+ is related by the isospin symmetry to the well-known matrix element of the operator $(\bar{s}u)_{V-A}$ between K^+ and p^0:

$$\langle p^+|(\bar{s}d)_{V-A}|K^+\rangle = \sqrt{2}\langle p^0|(\bar{s}u)_{V-A}|K^+\rangle. \qquad (1.11)$$

The matrix element of the operator $(\bar{s}u)_{V-A}$ is measured in $K^+ \to p^0 e^+ v$ decays. The amplitude for this transition is given by

$$A(K^+ \to p^0 e^+ v_e) = \frac{G_F}{\sqrt{2}} V_{us} \left\langle p^0 \left| (\bar{s}d)_{V-A} \right| K^+ \right\rangle \left[\bar{v} g_a (1 - g_5) e \right]. \qquad (1.12)$$

By using the $K^+ \to p^0 e^+ v$ data, the branching ratio of $K^+ \to p^+ v\bar{v}$ is expressed as

$$B(K^+ \to p^+ v\bar{v}) = B(K^+ \to p^0 e^+ v_e) \frac{a^2}{2p^2 \sin^4 q_w} \left(\frac{|D|}{l} \right)^2, \qquad (1.13)$$

where $D = \sum_{i=c,t} V_{id} V_{is}^* X(x_i)$.

We can express the amplitude of $K_L^0 \to p^0 v\bar{v}$ decay as

$$A(K_L^0 \to p^0 v\bar{v}) = eA(K_1^0 \to p^0 v\bar{v}) + A(K_2^0 \to p^0 v\bar{v}), \qquad (1.14)$$

where K_1 and K_2 are CP even and odd states, respectively. The an amplitudes of K_1 and K_2 decays are written as follows:

$$A(K_1^0 \to p^0 v\bar{v}) = \frac{1}{\sqrt{2}} \left[A(K^0 \to p^0 v\bar{v}) + A(\overline{K^0} \to p^0 v\bar{v}) \right] = \mathrm{Re}\, A(K^+ \to p^+ v\bar{v}), (1.15)$$

$$A(K_2^0 \to p^0 v\bar{v}) = \frac{1}{\sqrt{2}} \left[A(K^0 \to p^0 v\bar{v}) - A(\overline{K^0} \to p^0 v\bar{v}) \right] = i\, \mathrm{Im}\, A(K^+ \to p^+ v\bar{v}), (1.16)$$

Since the CP parity of K_1^0 is even, which is the same as that of the $p^0 v\bar{v}$ system, the amplitude of $K_1^0 \to p^0 v\bar{v}$ contributes to the process through indirect CP violation in the $K^0 - \overline{K^0}$ oscillation proportional to the parameter e.

From the above equations, the branching ratio can be approximated as a sum over the contribution from indirect and direct CP-violation process,

$$Br(K_1 \to p^0 v\bar{v})_{indirect} \approx 2.73 \cdot 10^{-5} |e|^2 \left[X(x_c) + A^2 l^4 (1 - r) X(x_t) \right], \qquad (1.17)$$

$$Br(K_2 \to p^0 v\bar{v})_{direct} \approx 2.73 \cdot 10^{-5} \left[A^2 l^4 h X(x_t) \right]. \qquad (1.18)$$

Since $|e|$ is small, ~10^{-3}, the indirect contribution is negligibly small. The charm contribution, which gives rise to some theoretical ambiguity, is small because the charm term is significant only in the indirect contribution. This is the reason why the theoretical ambiguity is small for $K_L^0 \to p^0 v\bar{v}$ decay, as compared to $K^+ \to p^+ v\bar{v}$ decay.

By adding the Z-penguin diagrams, the $X(x_i)$ function given by Inami and Lim[23] is

$$X(x_i) = \frac{x_i}{8} \left[\frac{3x_i - 6}{(x_i - 2)^2} + \frac{2 + x_i}{x_i - 1} \right]. \qquad (1.19)$$

The SM prediction is hence

$$Br(K_L^0 \rightarrow p^0 v\bar{v}) \approx Br(K_1^0 \rightarrow p^0 v\bar{v})_{direct} = 4.08 \cdot 10^{-10} A^4 h^2 = (2.8 \pm 1.1) \cdot 10^{-11}, \quad (1.20)$$

Isospin-symmetry-violating quark mass effects and the electroweak radiative corrections reduce this branching ratio by 5.6%.[24]. Next-to-leading order QCD effects are known with an accuracy of $\pm$ 1.1%[25]. The overall theoretical uncertainty is estimated to be below 2%.

Finally, the theoretical features of $K_L^0 \rightarrow p^0 v\bar{v}$ decay in the Standard Model are summarized as follows:

- The branching ratio is predicted to be (2.8 $\pm$ 1.1)10^{-11}, which is quadratically proportional to the CP violation parameter, h.
- The direct CP violating processes are dominating. The contribution of the indirect CP violating processes is about 10^{-4} of the contribution of the direct processes.
- The ambiguity in the theoretical prediction is very small, ~1 %, which is much smaller than that of the $K^+ \rightarrow p^+ v\bar{v}$ decay due to the small charm contribution.

1.1.3 $K_L^0 \rightarrow p^0 v\bar{v}$ decay beyond the Standard Model

There are many models beyond the Standard Model (BSM). The predictions for the $K_L^0 \rightarrow p^0 v\bar{v}$ branching ratio by various BSM models of CP violation process are listed in Table 1.1. These models are classified into three classes: SUSY (supersymmetry) models, extended Higgs models and models with new fermions.

One feature of these BSM models is that the number of CP phases is increased. These new phases generally contribute to additional diagrams. Therefore, whether the BSM models has 4th generation, extra "vector-like" quarks, L-R (left-right) symmetry or many Higgs bosons, the branching-ratio prediction tends to be larger than that of the Standard Model. For SUSY models, the scale of e_K gives a strong constraint among additional CP phases, such that they tend to predict a branching ratio that is almost the same as that predicted by the Standard Model. On the other hand, a larger effect from the SUSY CP phases is expected for the $B_d \rightarrow J/yK_S$ decay. Therefore, the Unitarity Triangle can become inconsistent between the $B_d \rightarrow J/yK_S$ and $K_L^0 \rightarrow p^0 v\bar{v}$ decays. From the pattern of inconsistency, there is a possibility to identify the specific BSM model.

Table 1.1 Summary of the branching ratio predictions by BSMs

Who	What	BR($K_L^0 \to p^0 v\bar{v}$), x10^{-11}
Buchalla[26]	Standard Model CKM fit	2.8 ± 1.1
Plaszczynski [27]	Conservative SM fit	1-5
Buras [28]	Generic SUSY with minimum particles	0-40
Buras [29]	MSN without new CP phase	(0.41-1.03)xSM
Brhik [30]	All CP-violation due to SUSY	~0.23
Chanowitz [31]	Multi Higgs Models	2.8-10.6
Hattori [32]	4-th generation	0.5-220
Xiao [33]	Top-color assisted Technicolor	0.1-29.5
Xiao [34]	Multi-scale walking Technicolor	1.23-233
Kiyo [35]	Seesaw L-R model	(1-1.3)xSM
Buras [36]	Fit with new CP violating phase	31 ± 10

Resent results concerning measurement of the branching ratios of $B \to pp, pK$ by Belle [37] and BaBar [38] collaborations shows some inconsistency with the SM predictions. It can be explained by assuming the existence of a new CP-violating term [36] in the electroweak penguin sector. This requires an additional large CP-violation phase. As a result, the branching ratio of the $K_L^0 \to p^0 v\bar{v}$ decay can increase up to $(3.1 \pm 1.0) \cdot 10^{-10}$, which is achievable for the E391a experiment.

1.2 Current status of experimental studies

Up to now, the experimental upper limit of the $K_L^0 \to p^0 v\bar{v}$ branching ratio is 5.9x10^{-7} at the 90% confidence level, which is given by the KTeV experiment [39]. The experiment has been carried out by using two p^0-decay modes, $p^0 \to gg$ [40] and $p^0 \to e^+e^-g$ [39].

An advantage of the $p^0 \to e^+e^-g$ mode is in the possibility to directly measure a decay vertex point using e^+e^- and to reconstruct the invariant mass of p^0. Therefore, the kinematical constraint is tighter than that of the $p^0 \to gg$ mode (acceptance is about 24-times less). The current upper limit of 5.9x10^{-7} was obtained by the $p^0 \to e^+e^-g$ mode. However, this method may not be applicable beyond the 10^{-9} sensitivity because [39]:

- the branching ratio of the $p^0 \to e^+e^-g$ decay is small, ~1%.
- the final state in the radiative $K_L^0 \to p^{\pm}e^{\mp}gv$ decay looks like $p^0 \to e^+e^-g$ + *nothing* if $p^{\pm}$ is misidentified as $e^{\pm}$. Since the branching ratio of $K_L^0 \to p^{\pm}e^{\mp}gv$ decay is as large as 3.62x10^{-3}, the miss-identification probability for $p^{\pm}$ must be below 10^{-10}, which seems to be difficult to achieve.

Therefore, further progress beyond the 10^{-9} sensitivity will be obtained by the $p^0 \to gg$ mode [40]. Fig 1.5 shows a scatter plot of P_T versus the decay vertex, *Z*, obtained for the $p^0 \to gg$ mode. In this plot two photons are required to accompany no additional particles in the final state. The box shows the signal region. Three components can be clearly seen. The events around *Z*=160 m are p^0 events due to neutron interactions in the vacuum window. The band near P_T = 100 MeV/c is due to $\Lambda \to np^0$. The events around P_T = 0 are due to $K_L^0 \to gg$.

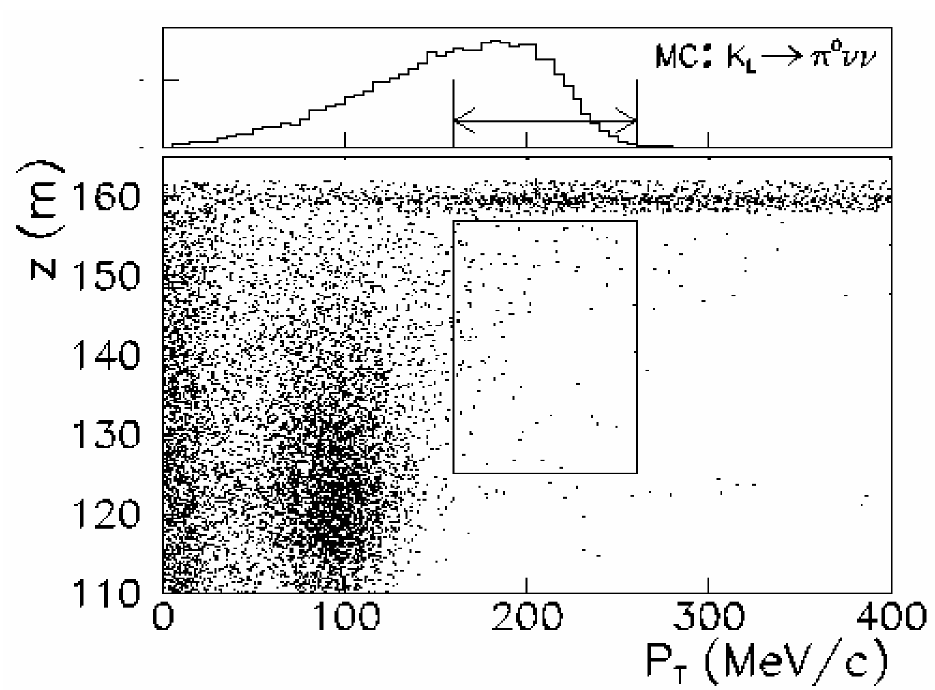

Fig. 1.5 Scatter plot of P_T vs. decay obtained from the $p^0 \to gg$ mode [40].

Fig 1.6 shows the P_T distribution after all cuts were applied The arrow indicates the signal region. As shown in the figure, there are many Λ events around P_T=100MeV/c due to the high beam momenta of 800 GeV primary protons. In addition, since the veto efficiency for additional gammas from the other K_L^0 decay modes is not high enough, the events from the $K_L^0 \to p^0p^0$ decay appear in the signal region, even for the 10^{-6} sensitivity. The remaining events in the signal box are consistent with those events due to neutron interactions with the vacuum window at the end of the decay region. As a result, they obtained an upper limit of $1.6\text{x}10^{-6}$ at the 90% confidence level [40].

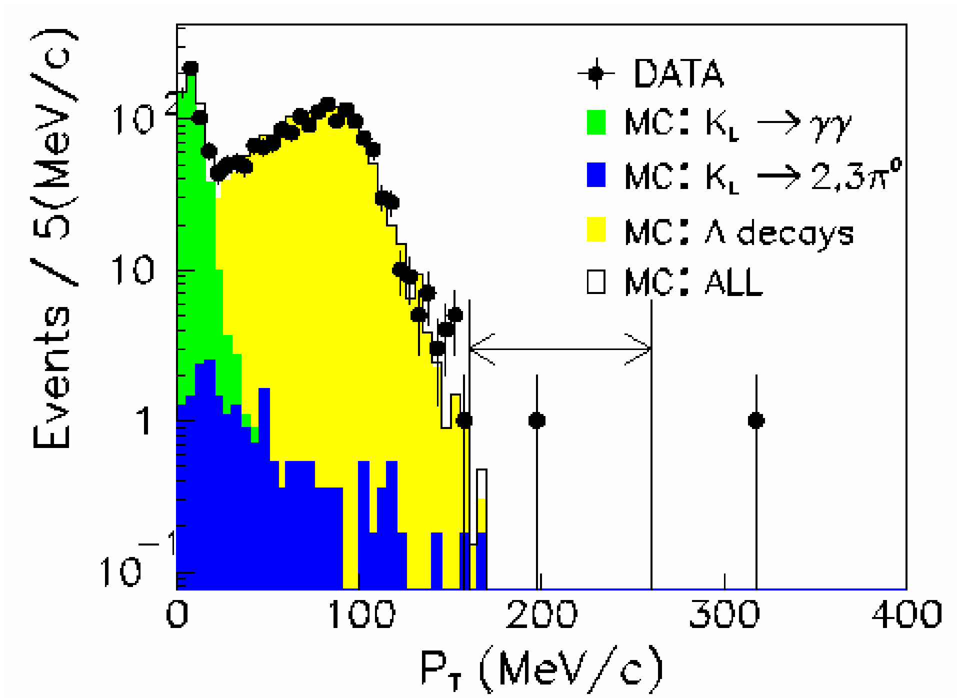

Fig. 1.6. P_T distribution after all cuts, except for the P_T-cut. One event in the signal region is consistent with the neutron background [40].

1.3 Next step: E391 experiment

As mentioned in section 1.2, in the KTeV experiment using the $p^0 \rightarrow gg$ mode they found one event in the signal region, and claimed that it came from two p^0's produced by a neutron interaction with a vacuum window at the end of the decay region, which was outside of the signal region. In this case, the two p^0's would have decayed into four gammas and two gammas would have escaped from the veto system; two remaining gammas from different p^0's, odd combination, were detected. Since they were considered to be from one p^0, the decay vertex was wrongly reconstructed, and it accidentally entered into the signal box region. In order to avoid such a process, it results in two requirements: a high-sensitive veto system should fully cover the decay region in order to prevent the escape of particles after decay, and material should be minimized along beam line to reduce interactions. Material means not only detector/structure material, but also air in the decay region. Therefore, a tighter veto system and no material, including air, are the keys to measure $K_L^0 \rightarrow p^0 \nu\bar{\nu}$ decays using the $p^0 \rightarrow gg$ mode.

One more important point is a narrow beam ('pencil beam'). Because the decay vertex is reconstructed on the beam axis, the reconstructed transverse momentum of p^0 is smeared due to the size of the beam. Better P_T resolution is crucial to discriminate the background, because many sources, such as multi-body decay, odd combination and hyperon decay, produce background in the lower P_T region. Although a narrow beam is better for background rejection, but there is a competing process that restricts the size of the beam. If we collimate the beam into a small size, the K^0_L flux is reduced. An optimum point should be chosen.

In the KTeV experiment an average K^0_L momentum was about 70 *GeV/c*. Even after a long flight of 90 m from target, the beam contained hyperons. They could easily produce p^0 in the decay region. It is serious background because the neutron, which is the other decayed participle, is hard to be detected. Since hyperons have a short lifetime compared with K^0_L, their flux surviving at the detector region decreases with a decrease of the beam momentum. A smaller momentum of K^0_L can reduce such backgrounds.

The E391 experiment was proposed in 1996 to search of the $K_L^0 \to p^0 \nu\bar{\nu}$ decay at a single-event sensitivity of 3×10^{-10}. All hints from the KTeV experiment mentioned above are realized in E391 setup. The veto system fully covers the decays region. The background decays at the entrance of the decay region is suppressed by a long additional decay chamber installed before the main decay chamber. A high vacuum is reached by separating of the decay region and the detector region by a thin membrane, and separated evacuation systems for two vacuum regions are used. Vacuum windows are located far from the decay region. The beam is collimated within 2 mrad by the system of 6 collimators. The average K^0_L momentum is about 2 *GeV/c*. A detailed description of the apparatus is presented in chapter 2.

1.4 Motivation of the one day analysis

We had runs for about 100 days, and took physics data for about 60 days. We then performed a detail analysis of a one-day data sample, which is reported in this thesis. A careful analysis of a small fraction of the data is very valuable for understanding the quality of the data, and for setting up a working strategy for further analysis. Since the sensitivity obtained from the one-day sample is expected to be comparable with that of the previous KTeV experiment, the result will be a good starting point. Any problems that we encounter in the one-day analysis will guide us to more a effective strategy for processing a large data sample in the future. The MC tools and the reconstruction routines can be checked critically in this analysis. The data skimming process is one of the crucial tools to be developed and tested. Moreover, we can examine the consistency between our expectations and reality. Unexpected phenomena may appear beyond our expectations.

In summary, an analysis of the one-day sample is very valuable for the first overall check of the E391a experiment at a comparable sensitivity with that of KTeV. Since the data size is not very big and can be processed within a reasonable time, it is convenient for developing and testing reconstruction routines. Further analysis of large samples, as well as modifications of the experimental setup in successive runs, will be done based on knowledge obtained from this one-day analysis.

Chapter 2

Experimental method

2.1 Detection method

The $K_L^0 \to p^0 v\bar{v}$ decay is planned to be observed by a signal of $K_L^0 \to p^0(p^0 \to gg)$ + *nothing*. The energies and positions of two photons are measured with a CsI calorimeter. The "*nothing*" is confirmed by no additional signals in a veto system that covers the whole K^0_L decay region.

All background K^0_L decays have additional photons or charged particles, which can be detected by the veto system. Although the $K_L^0 \to gg$ decay has no additional particles, it can be discriminated from the $K_L^0 \to p^0 v\bar{v}$ decay using transverse momentum and acoplanarity angle cuts.

Since the CsI calorimeter measures two g's positively, precise energy and position determinations of g are important to identify the $K_L^0 \to p^0 v\bar{v}$ decay. In addition, a precise hit-timing measurement is mandatory to reject accidental hits in the CsI calorimeter. An undoped-

CsI crystal, which has a moderate light output and a fast time response, is one of the best materials to meet these requirements.

2.1.1. Setup

The experimental setup is shown in Fig. 2.1. Two g's decaying from p^{0} are detected by the CsI crystal calorimeter. Surrounding the CsI calorimeter, photon and charged-particle veto detectors are arranged in a cylindrical shape in order to reject backgrounds from other K^{0}_{L} decays, like $K_L^0 \rightarrow 3p^0$ and $K_L^0 \rightarrow 2p^0$. High detection efficiencies of these detectors are crucial for background rejection. These are arranged so as to tightly cover the fiducial K^{0}_{L} decay region, and placed in a vacuum to minimize any dead material in front of them.

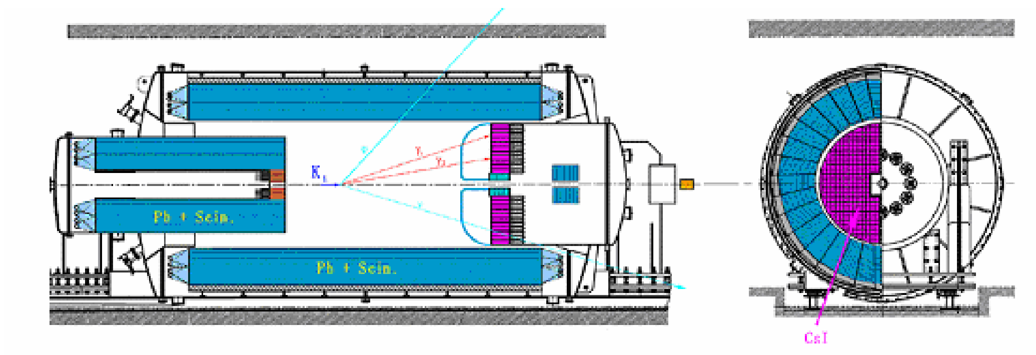

Fig. 2.1. E391a detector.

The length of the setup is about 10 m, and the diameter is about 3.5 m. Almost all detectors are located inside a steel vacuum tank. The signal and HV cables from the PMT's are led out through special electric vacuum connectors.

The vacuum tank is placed on rails, which allows one to adjust the position of the setup relative to the beam line, and also to move the whole system during assembling.

The E391 setup is located inside a cave surrounded by 1m thick concrete blocks. In order to reduce the variation of the temperature, we used an air conditioner, which maintained the stable temperature during data-taking.

As was mentioned above, the $K_L^0 \rightarrow p^0 \nu\bar{\nu}$ decay was observed by $2g$ clusters in the CsI calorimeter and the absence of any signal in the veto system. In order to reach the proposed single-event sensitivity of $3\text{x}10^{-10}$, we adopted special principles in designing of the detector, which were realized in the E391 setup as follows.

2.1.2. *Pencil beam*

In the $K_L^0 \to \pi^0 \nu\bar{\nu}$ decay, only two γ's as a product of the π^0 decay are detectable. A measurement of the direction of γ is not so easy, and only the energy and the hit position can be measured with good accuracy. Without direction measurements of γ's, the decay vertex can be obtained with an assumption that two γ's come from π^0. In this case, there still remains an ambiguity of the vertex position in the transverse direction. It is thus required to assume that the decay vertex is on the beam axis. This results in a requirement concerning the very small size of the beam cross section.

In the E391 experiment, we used a so-called 'pencil beam'. A system of collimators selects only a 2 mrad angle from the target, so that at the exit of the last collimator, C6, the radius of the core beam is about 2 cm. At the calorimeter position (~18 m from the target), the radius of the core beam is less than 4 cm. A halo of the beam is suppressed by more than 5 orders of magnitude relative to the beam core intensity, as described in 2.2.2.

2.1.3. *High vacuum in a decay volume*

From a MC study of the interaction of neutrons with air, it was found that the background contribution is less than 0.1 events at a vacuum pressure of 10^{-5} Pa for a sensitivity of $3x10^{-11}$ for the $K_L^0 \to \pi^0 \nu\bar{\nu}$ decay. Since the E391a experiment proposes to reach a sensitivity of $3x10^{-10}$, a vacuum higher than 10^{-4} Pa is required in order to reduce the background down to a negligible level (< 0.1 events).

In the E391 setup, almost all detectors are located inside of the vacuum region. This makes it hard to reach the required vacuum level of ~ 10^{-4} Pa, or better, because of out-gassing from large a lead-scintillator sandwich detectors. We adopted the solution of differential pumping, in which a low vacuum region containing detectors and a high vacuum decay volume are separated with a thin membrane of 20 mg/cm^2 thickness. Each vacuum level is maintained by a different evacuation system, namely by the mechanical booster pumps for the low-vacuum region and by the turbo-molecular pumps for the high-vacuum region.

2.1.4. *Double decay chamber*

The background events from the other decays may appear in a signal box of the $K_L^0 \to \pi^0 \nu\bar{\nu}$ decay due to additional particles escaping from the veto system. We tightly cover almost all of the decay volume with a 4π geometry by veto detectors. However, if the K^0_L decay occurs at the entrance of the decay volume, the particles can escape back from the veto system. In order to avoid this situation we developed an additional decay chamber before the main decay volume. Decays occurring in the first decay volume are rejected by a front barrel veto detector surrounding the beam axis and the CC02 counter located at the end of the first decay volume. The γ's going forward are suppressed by a small beam hole of CC02. If a decay occurs at the border between the first and the main decay volumes, the possibility for γ's to escape in the backward direction along the beam line is suppressed by a long (2.75 m) front barrel veto detector.

2.1.5. *Highly-sensitive veto system*

The K^0_L decay, which may become a main background source, is $K_L^0 \to 2\pi^0$ decay, where two γ's from the π^0 decay hit the CsI calorimeter and remaining γ's are not detected by the veto system. The branching ratio of this decay is 9.27×10^{-4}, which is about 8 orders higher than that of the $K_L^0 \to \pi^0 \nu\bar{\nu}$ decay. This results in a requirement of the inefficiency of the veto system to be level of about 10^{-4} for an individual γ. We carefully developed, constructed and assembled the veto detectors while aspiring to reach this inefficiency level.

2.2. Apparatus

2.2.1. Overview

The E391 setup consists of the CsI calorimeter and veto detectors that cover almost the full 4π geometry of the K^0_L decay volume. In Fig. 2.2, a schematic view is presented.

The front barrel and CC02 form a first decay chamber for collimating of the decays before the main decay volume. The main barrel surrounds the decay volume, and covers some part of the front barrel and the CsI calorimeter. In order to suppress charge decay modes, a main charge veto before the calorimeter and a barrel charge veto on the inner surface of the main barrel are installed. The main charge veto detector also covers the beam path between the charge veto and CC03.

A large gap between the front barrel and the main barrel (~10cm) is used for a channel for evacuating of the K^0_L decay region. A small gap between the main barrel and the CsI calorimeter (~2cm) is used for readout of the charge veto counters.

Collar counters CC02-07 are located along the beam line around the beam. CC02 covers the exit of the first decay chamber at the end of the front barrel (Fig. 2.2). CC03 is installed inside of the CsI calorimeter. CC04, CC05, CC06 and CC07 cover the edge effect of the CC03 and each other. They are also located so as to defend the CsI calorimeter from particle backsplash from the 'beam-anti' detector (BA), which is installed at the end of the beam line. Just before them, a beam hole charge veto (BHCHV) is installed.

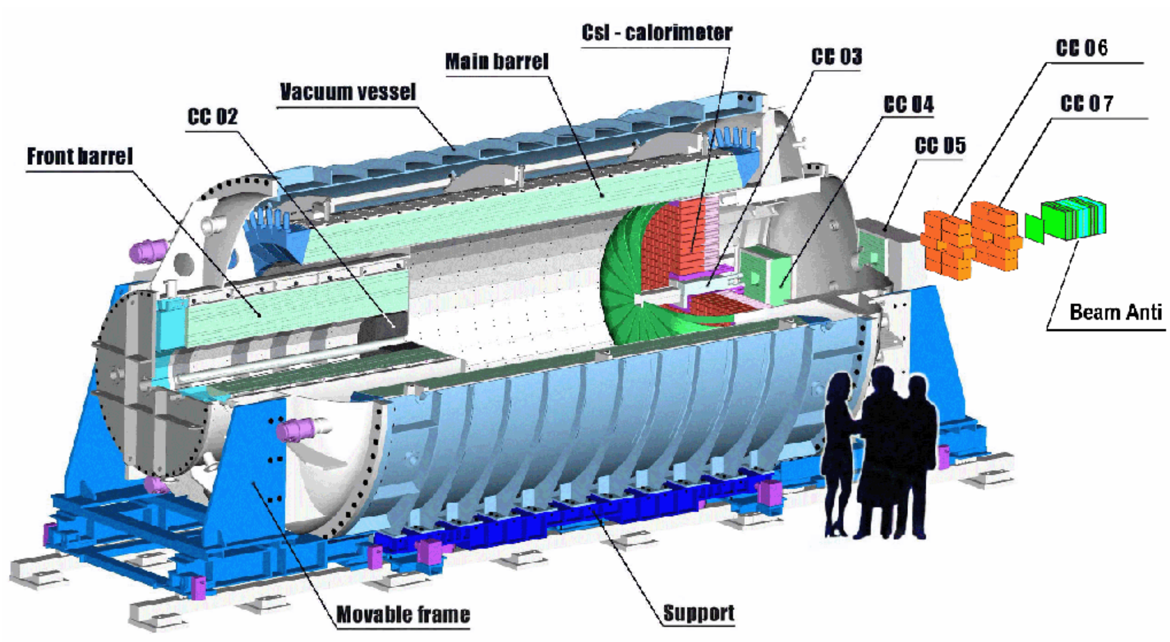

Fig. 2.2 Schematic view of the E391 setup.

2.2.2. Beam line

In order to identify the $K_L^0 \rightarrow p^0 v\bar{v}$ decay using a transverse momentum and an acoplanarity angle of two photons, the most essential requirement is a well-collimated 'pencil' beam with a minimum halo.

A primary proton beam with a momentum of 13 GeV/c hits the K^0_L production target made of platinum with 60 mm thickness and 8 mm diameter. The target is inclined by 4^o horizontally relative to the primary beam axis.

In Fig. 2.3(a), the beam collimator scheme is shown [41]. It consists of 6 collimators, a pair of sweeping magnets, as well as Be and lead absorbers. The first three collimators (C1,C2,C3) are used to define the beam profile with an aperture of 2 mrad in a half-cone angle. The last two collimators (C5 and C6) are used to trim the beam halo. The lead and Be absorber is used to reduce the g and neutron fluxes relative to the K^0_L flux. Two dipole magnets are used for sweeping out charged particles. The last collimator (C6) also acts as a sensitive detector to veto the background events produced by a beam halo at that place. Because the length of the beam line is about 10 m, hyperons in the neutral beam are reduced to a negligible level.

In Fig. 2.3 (b), the beam collimation scheme is presented by various lines:

- A-line is drawn as a line of the 2 mrad cone from the target center. The inner surfaces of collimators C2 and C3 are placed along this line and define the core profile of the beam.
- B-line is a line connecting T^* and P3. C5 and the upstream-half of C6 are arranged along this line. This line shows penumbra due to the finite size of the target. The aperture of C5 and the upstream-half of C6 have a clearance of 0.2 mm with respect to the B-line. Then, the particles produced at the target do not hit C5 and C6 directly.
- C-line connects $P2^*$ and P6. A lead absorber of 5 cm thick is placed between C1 and C2. Since its lateral size is small (1cm in diameter) and it is within the C-line (extrapolated to the upstream direction), the free run-through of the secondaries produced at the absorber is limited in the cone defined by this C-line.
- D-line is a line connecting PV^* and P6. Since the upstream defining collimators are enveloped in the D-line, it is a boundary for secondaries produced at the defining collimators. It is also a boundary for the secondaries scattered by air before the vacuum region and the window. The tertiaries originating from the secondaries at C1 are also within this envelope, because the acceptance of the secondaries from C1 is limited by the E-line. The latter half of C6 is arranged along the D-line in order to prevent edge scattering of the particles from the tertiaries mentioned above.
- E-line connects $P2^*$ and P3. The inner surface of C1 is arranged along this line. Secondaries, which are produced at C1, should have a larger angle than the E-line.

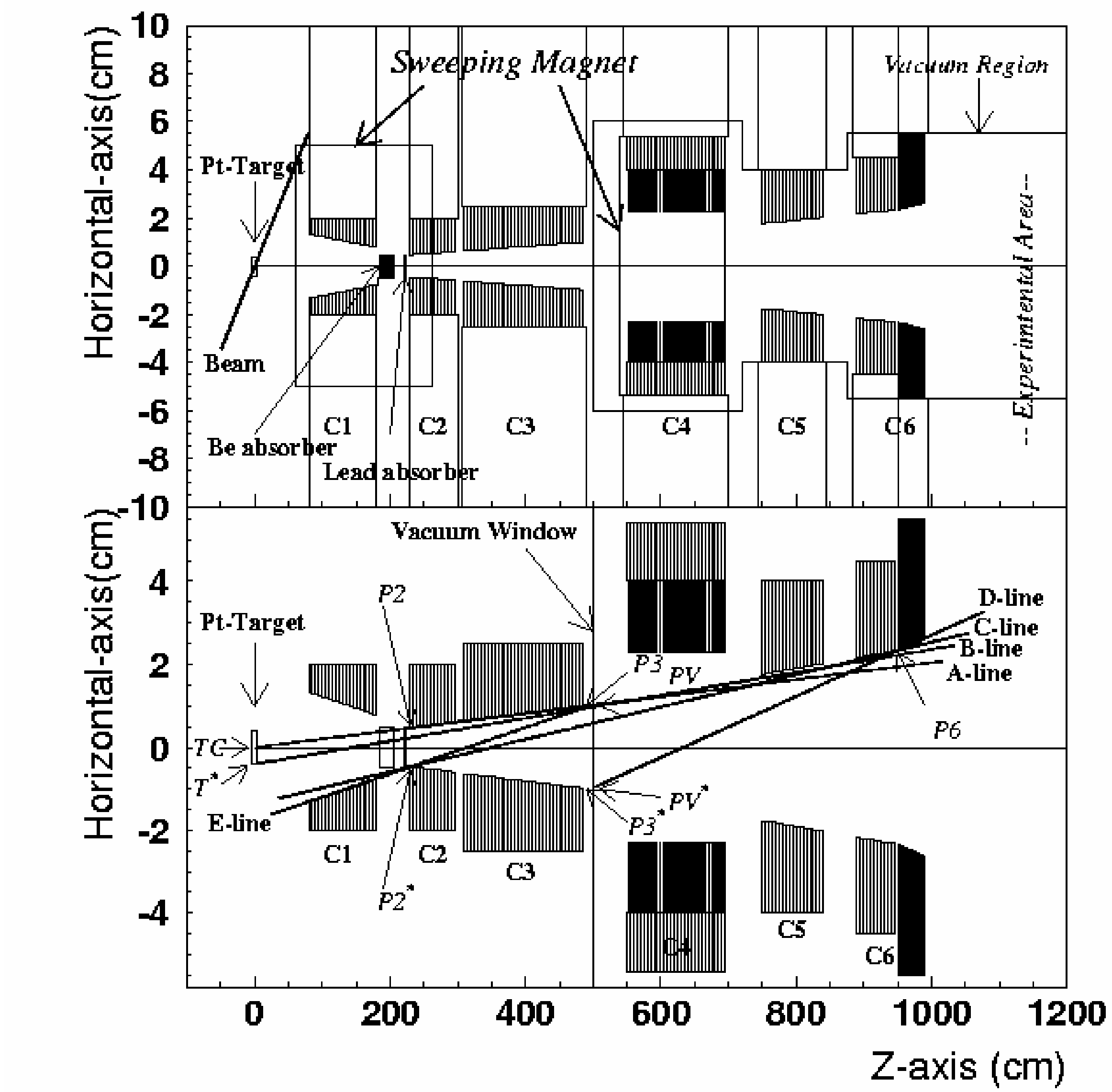

Fig. 2.3. Schematic view of the collimator system (a) and schematic view of the principles of the arrangement of the collimators (b).

In summary, the D-line is a boundary of the beam halo from all secondary beam sources (defining collimators, absorber, air and the vacuum window) and a tertiary beam source from the hottest collimator C1. More steps of interactions and penetrations through the material might be sources of the wider beam halo.

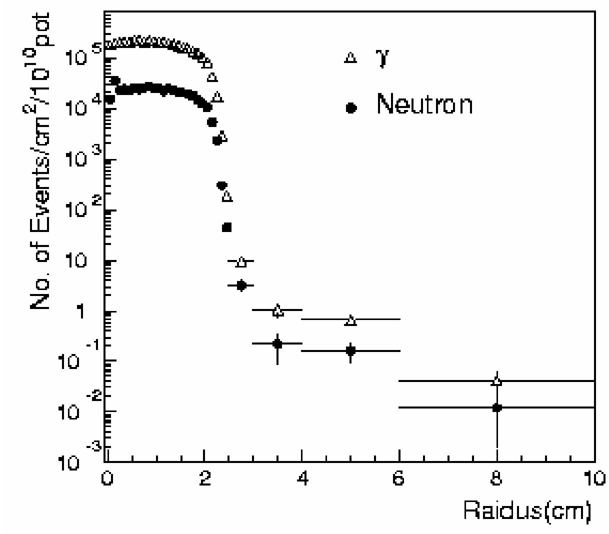

Fig 2.4 Beam profiles at the exit of the C6 collimator obtained by the MC simulation (no absorber case).

An MC simulation of the beam line was performed [41] using GEANT-3 with a G-FLUKA package for the hadron interaction. The MC result was in a good agreement with that of the beam survey experiment. In Fig. 2.4, the distributions of *g*'s and neutrons in a beam line at the exit of the C6 collimator are shown. The halo is suppressed by 5-6 orders of magnitude relative to the core flux of the beam. The n/ K^0_L ratio above 100 MeV is ~ 60 (no absorber case).

2.2.3. CsI calorimeter

2.2.3.1. Overview

The CsI calorimeter consists of 576 crystals stacked in a round shaped wall with a diameter of 2 m. The arrangement of the CsI crystals in a support cylinder is shown in Fig.2.5. In the center surrounding the square beam hole of 6 cm, the collar counter CC03, which is made of tungsten and scintillator plates, is placed. Around them, 24 CsI crystals of 5x5x50 cm^3 are arranged (KTeV crystals). After these, 496 CsI crystals of the size, 7 x 7 x 30 cm^3 (main CsI), are stacked. The gaps on a periphery of the cylinder are filled by 56 CsI modules of a trapezoidal shape and 24 modules of a lead-scintillator sandwich. The gaps between crystals are less than 100 µm, which were controlled by applying pressure during stacking [43].

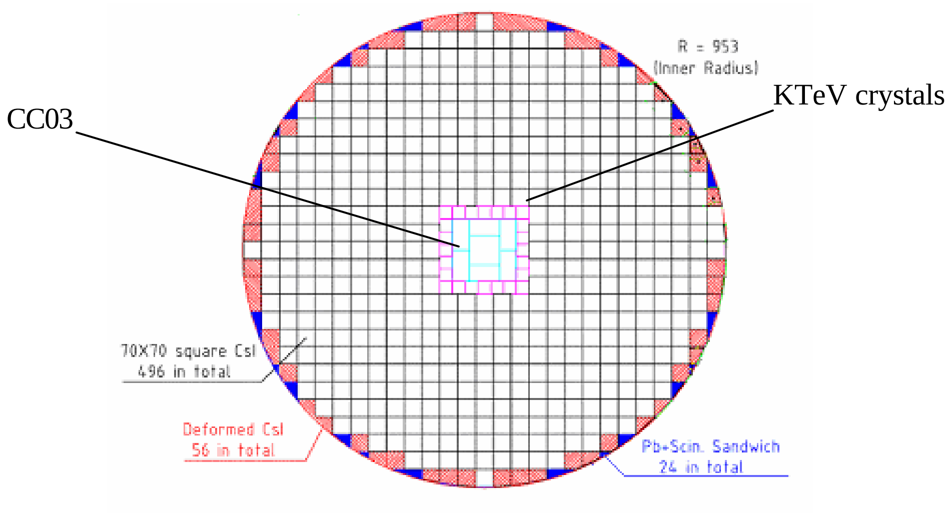

Fig.2.5. Arrangement of CsI crystals.

2.2.3.2. CsI modules

For our electromagnetic calorimeter, we used undoped-CsI crystals. Its main property is the exhibition of fast scintillating light. Due to the high density and high atomic number, Z, CsI has a relatively short radiation length for electromagnetic showers. The attenuation length for its own radiation is more than 1 m, which enables single-end readout for a 30 cm crystal. They are very easy to machine and easy to handle, although they are slightly hygroscopic. The scintillation properties for undoped-CsI are summarized in Table 2.1.

Table 2.1 Undoped-CsI properties.

density (g/cm^3)	4.53
hygroscopic	slightly
Wave length at peak yield,(nm) Refractive index	315 1.80
Photons /MeV	2300
Decay time, (ns)	10, 36
Radiation length, (cm)	1.85
Molieré radius, (cm)	3.8
dE/dx for MIP, (MeV/cm)	5.6
Nuclear interaction length, (cm)	36.5

Schematic drawings of two types of CsI modules, the main CsI and the KTeV CsI, are shown in Fig.2.6. The crystals were wrapped by a Teflon sheet of 100 μm thickness for reducing light leakage to outside of the crystal, and then by the aluminum foil of 20 μm thickness. A supporting structure for the PMT at the end was glued to the crystal, and further tightly pressed by stainless-steel belts of 100 μm thickness. A silicon cookie was used for removing the air gap between the crystal and the PMT. The light transmittance for the cookie was measured to be 93% at a wavelength longer than 305 nm. Then, a UV-filter was used to pass selectively the fast component with a wavelength of 300-400 nm. It cut off most of the slow components. Also, a 20mm light guide (quartz) with a light transmittance above 80% at the wavelength of 300 nm was glued to the PMT window.

Since these modules are operated in a vacuum, we modified the HV divider so as to reduce any heat dissipation by decreasing the divider current and to reduce heat conduction from the divider to the PMT and CsI crystal by increasing the space between the divider and PMT tube. The divider of PMT was filled up with heat-conductive glue (METACAST 5448), and was thermally connected to the cooling system. Also, in a vacuum test it was found that under a vacuum pressure of less than 1 Pa, the working HV setting for the PMT at 1.2-1.5 kV is safe against electric discharge.

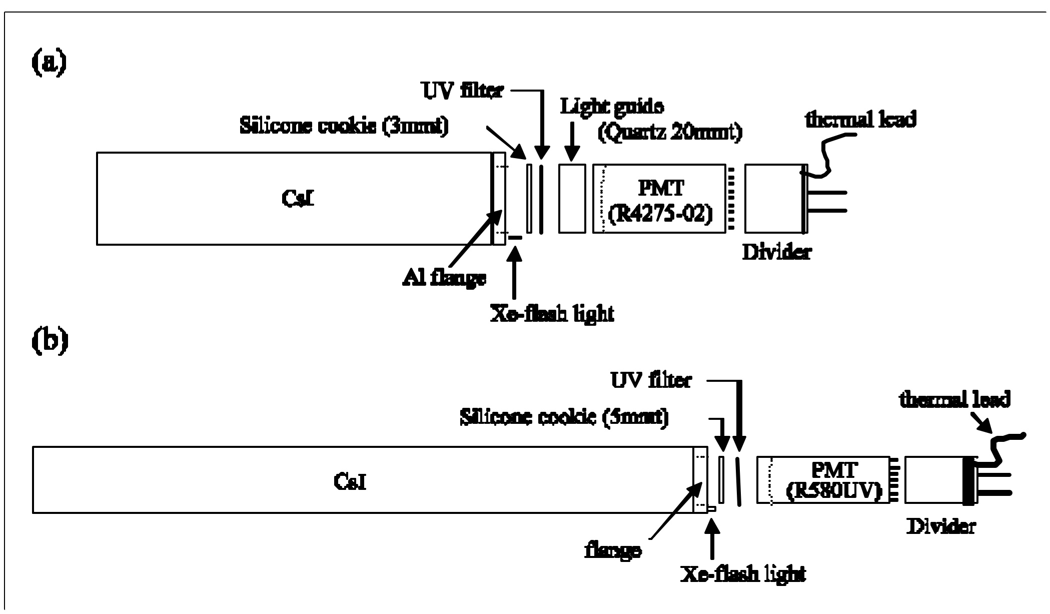

Fig.2.6. Schematic drawings of the CsI modules. (a) The Main CsI (70x70x300mm^3) and (b) The KTeV CsI (50x50x500mm^3).

2.2.3.3. Cooling system

Most heat is generated at the PMT voltage divider. It is only 0.6W for each PMT, but reaches 300W in total. In a vacuum, the heat is transferred to the vacuum vessel, mostly through the PMT and crystals by conduction, if there is no special cooling system. This results in increasing the temperature of the divider and the PMT, especially for PMT's near the beam hole, which may lead to unstable operation of the PMT due to a local increase of out-gassing. The other problem is an inhomogeneity of the temperature within a single crystal. Since the light output from an undoped-CsI crystal depends largely on the temperature, such a local variation of the temperature might cause several problems in the linearity and resolution.

In order to avoid these problems, we used the water-cooling configuration shown in Fig.2.7. Temperature-controlled water is circulated through copper pipes of 8mm diameter. Eight parallel lines are placed just behind the PMT divider, and each line covers about 70 PMT's. A copper-braided flat cable, which is usually used for the ground line in electronics, connects the PMT divider and the copper pipe. The cable surrounding the aluminum cylinder containing the PMT divider.

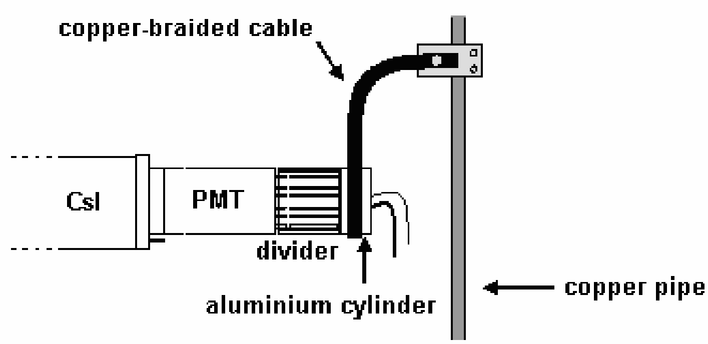

Fig.2.7. Cooling scheme of the PMT divider. Thermal connection between the PMT divider and the cooling pipe is made by a copper-braided cable.

By watching the temperatures at the front and rear faces of several crystals, we optimized the water temperature to be set as 10^{o}C lower than the room temperature. We could keep the fluctuation of the PMT and crystal temperatures within 0.2^{o}C during whole running time for 5 months, from February to June, by setting the room and water temperatures to be 20 ^{o}C and 10 ^{o}C, respectively. Such extremely good stability is a benefit of the setup where large detectors are placed in a vacuum.

2.2.4. Main and front barrels

2.2.4.1. Main barrel

The main barrel modules of about 550cm length are lead/scintillator sandwiches with wavelength shifter fiber readout form both ends. The readout layers are separated into two parts: the inner part with 16 lead plates with 1mm thickness, and the outer part with 29 lead plates with 2mm thickness. The thickness of the scintillator is 5 mm. The scintillation light is collected by wavelength shifter fibers (KURARAY-Y11-M). For reducing the light loss, reflector sheets of TiO_2PET with a thickness of 188 μm were inserted between the lead and scintillator layers. All fibers from each layer were collected to one PMT, so that each module had 4 PMT's. In total, we had 128 readout channels.

For mechanical strength of the module, a thick stainless-steel plate was used as a backbone structure. The scintillators and lead sheets were tightened to the backbone plate by 50 bolts of 5 mm diameter passing through holes in the scintillator and lead plates over the 550 cm length. A 3 mm-thick steel plate was placed at the opposite side of the backbone plate to fix the nuts, as shown in Fig.2.9.

2.2.4.2. Barrel charge veto

A barrel charge veto detector was installed on the inner surface of MBR, as shown in Fig 2.9. Two scintillator sheets of 5mm each were glued to each other with a small shift to cover the gap between the modules. The ends of the bolts of the main barrel modules were used for fixing the scintillators on the inner surface of the main barrel. A reflector sheet of TiO_2PET was glued over the scintillator to reduce any light leakage. Fibers at each side were connected to a 1-inch PMT. The total number of readout channels is 64.

2.2.4.3. Front barrel

The front barrel (FBR) is a veto detector consisting of 16 lead/scintillator modules with a length of 275cm. They are stacked around the beam axis in the region before the decay volume. The outer diameter is about 150 cm, so that it can be inserted inside the main barrel.

As in the case of the MBR, the readout channels of the module was separated into an inner part with 27 scintillator layers and an outer part with 32 scintillator layers. The thickness of the lead plate is 2mm. Because one end of the front barrel is located inside the decay volume, light collection was made by BCF-91A Bicron fibers only from other end. All fibers from the inner and outer parts were collected on each PMT. The total number of readout channels is 32.

For mechanical strength, a similar scheme as in the main barrel case with belts and bolts was used. (Fig.2.8)

Table.2.2 Parameters of the barrel photon detectors.

	Front barrel	Main barrel
Length [m]	2.75	5.5
Outer diameter [m]	1.6	2.8
Inner diameter [m]	0.6	2.0
No. of modules	16	32
No. of scinti. layers	59 (5-mm thick)	45 (5-mm thick)
No. of lead layers	59(1.5-mm thick)	15 (1-mm thick) + 30 (2-mm thick)
Thickness [X_0]	16.5	14.0
Module weight [kg]	850	1,500
Readout units/Module	Two (front:27 + rear: 32) Single end	Two (front:15 + rear: 30) Both ends
No. of PMT's	32(16 x 2)	128 (32 x 4)

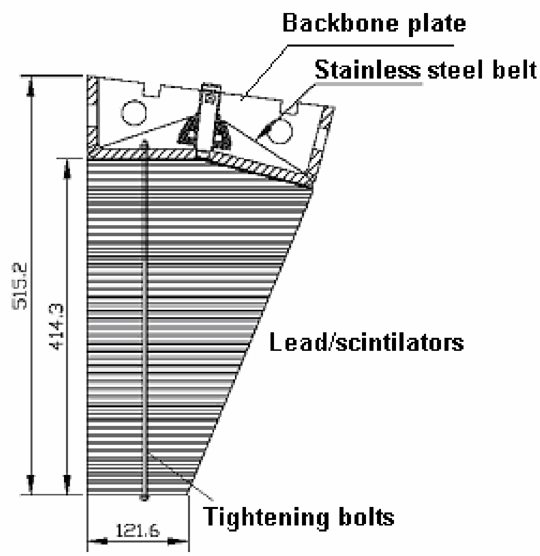

Fig.2.8 Cross section of the front barrel module.

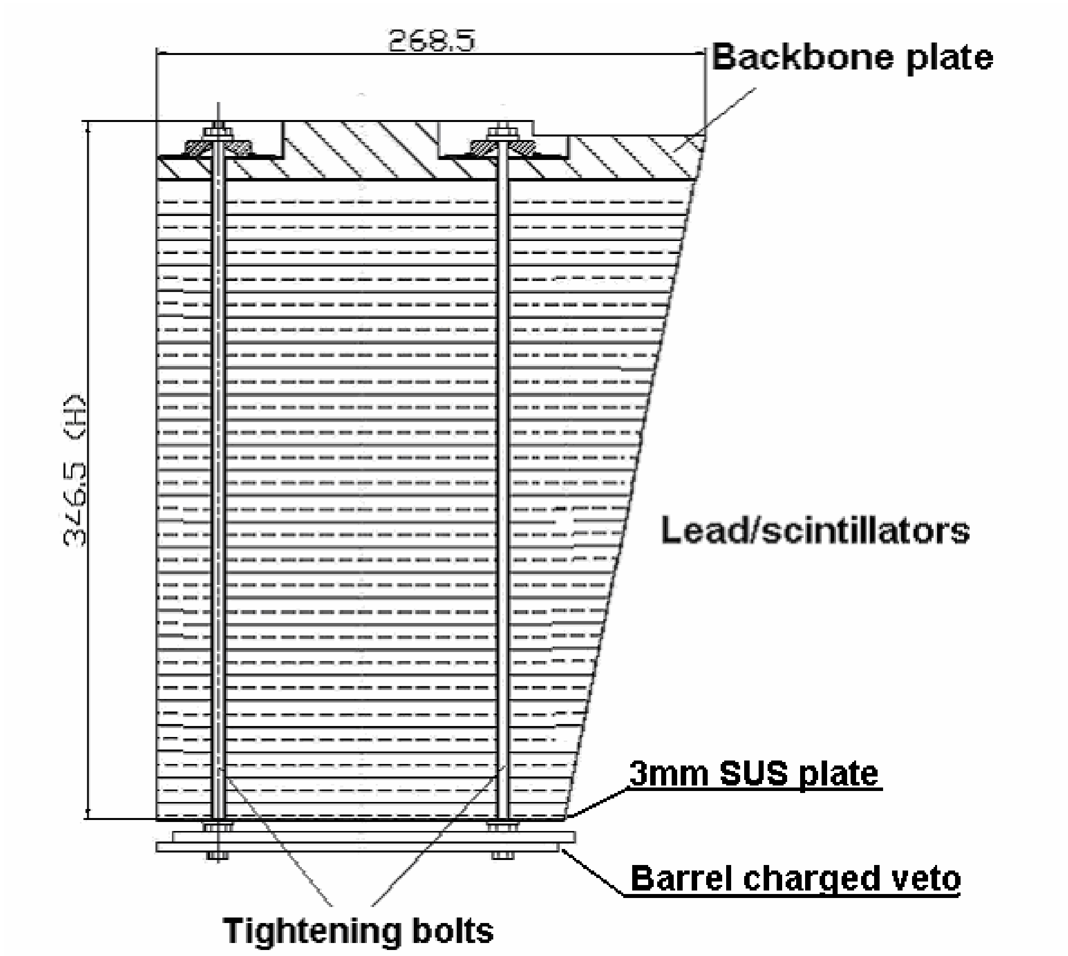

Fig. 2.9. Cross section of the main barrel module with the installed barrel-charged veto scintillators.

2.2.4.4. Assembling of modules

First, multiple grooves were processed on scintillator plates. Holes for the tightening bolts were also drilled. In order to keep accurate dimensions, this machining was done at a room temperature of $20^{o}\pm1^{o}$.

For gluing fibers, we used special acryl glue (NOP61), which can be cured by UV light. Two sets of UV-light exposure tables were prepared. The fiber grooves were filled by glue, and then fibers were placed; during UV-light exposition, tension was applied to both ends of the fibers.

By this method, we could fabricate 15 plates of the MB per day. Since the total number of plates is 1,500, it took about 8 months, including the R&D period.

For stacking the scintillator and lead plates, we prepared an inclined table (inclination angle of 20^{o}). For position adjustments of the scintillator plate and the lead sheet, we used the bolts passing through the module. Since the length of the lead sheet is limited to be less than 1.5 m for easy handling, we used four separate sheets for the MBR and two for the FBR. Between the scintillator plate and the lead sheet, we inserted a reflector sheet of TiO_2PET. After stacking a half layer of the laminate, we applied a pressure of 3 tons/m from the backside by a press. By doing this press, lead sheets were flattened and the thickness of the module could be checked during the stacking process. Inaccuracies of the thickness resulted from thickness variations of the lead sheets.

After stacking all lead and scintillator plates, we attached the backbone plate and applied a pressure of about 3 tons/m for at least 12 hours. Under the pressed condition, we attached five steel belts and six stud bolts for the FBR, and 50 stud bolts for the MBR. After adjusting the torque for each nut, we released the pressure that had been applied by the press.

Light readout was made from a single end in the case of the FBR and from both ends in the case of the MBR. These fibers were bundled at the end, and fixed to a plastic holder with glue. We then cut the fiber bundle together with the plastic holder with a diamond cutter to make a flat contact surface. For a good optical transmission of light, we polished the cut surface with polishing powders. PMT's were attached to the flat surface through silicone rubber of 3 mm-thick.

2.2.5. Collar counters and beam anti(BA)

The CC02 is a lead/scintillator sandwich counter of the 'shashlik' type, in which lead and scintillator plates are placed perpendicular to the beam axis. It consists of 8 modules, as shown in Fig. 2.10. Each module has 43 lead/scintillator layers; 7 layers at the front and 7 layers at the rear have a combination of 1mm lead and 5mm scintillator plates, and intermediate 29 layers have a combination of 2mm lead and 5 mm scintillator plates. This structure is designed so as to increase the detection efficiency for low-energy photons coming from the upstream and downstream decay volumes. The total thickness is 13.4 X_0. Light readout was made with 2.8 m long wavelength shifter fibers that passed through the first decay volume.

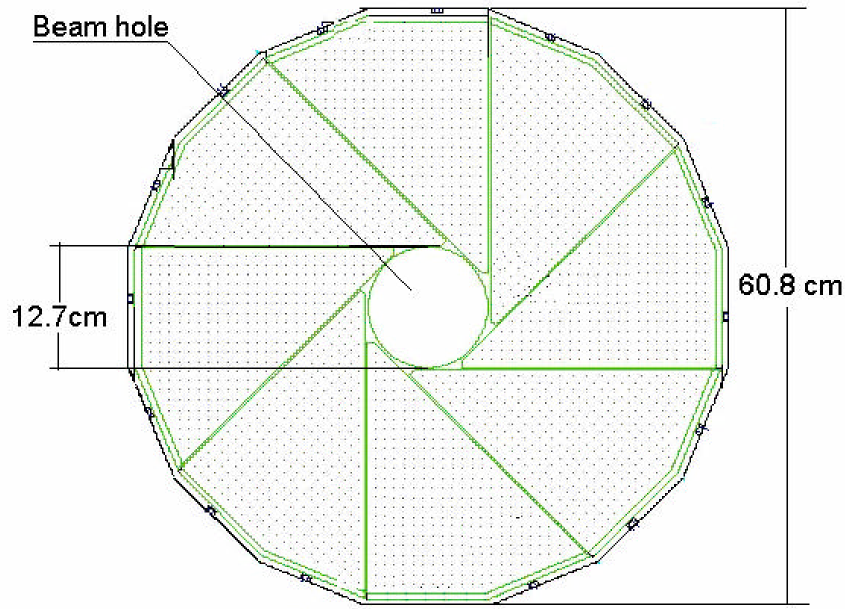

Fig. 2.10 CC02 schematic view. The CC02 counter is installed inside the front barrel.

The CC03 consists of 6 tungsten/scintillator sandwich modules, which are located around the beam, as shown in Fig. 2.11. The CC03 has the role to detect photos emitted from K^0_L decays in the region close to or inside the CsI calorimeter. Therefore, the sandwich structure is parallel to the beam axis. The thickness of CC03 is 5.2 X_0

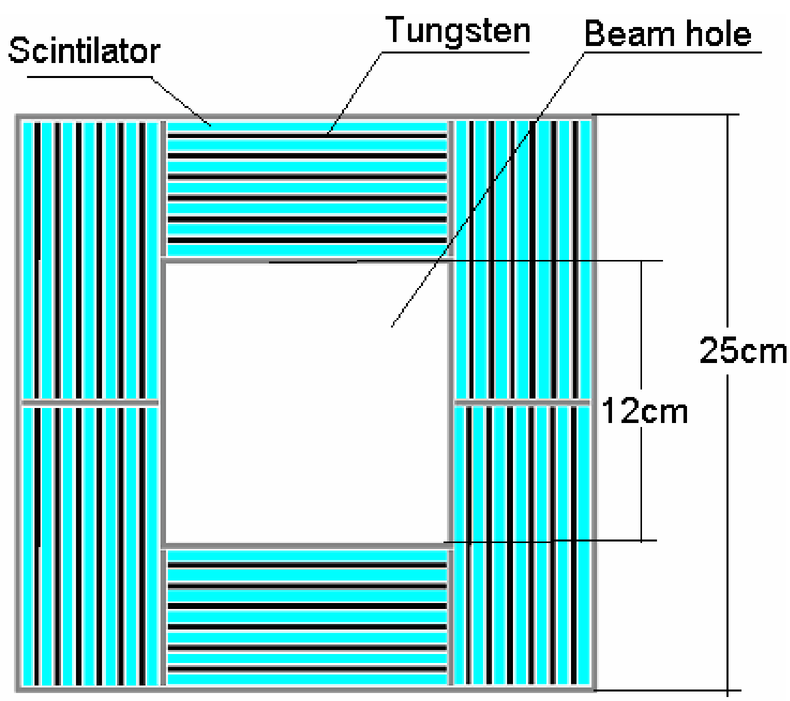

Fig. 2.11. CC03 schematic view. The CC03 counter is installed in the beam hole of the CsI calorimeter. The laminate structure is parallel to the beam axis.

The CC04 (Fig.2.12) is installed inside the vacuum region. The calorimeter part consists of 32 scintillator sheets of 5mm thick and 32 lead sheets of 2mm thick with a total thickness of 11.8 X_0. Two scintillator layers are placed in front of calorimeter for charged particle registration. Each scintillator layer with a size of 40x40 cm and an inner hole of 6.2x6.2 cm is made of 4 sheets, as shown in Fig. 2.12.(c). In order to avoid a gap between the scintillator sheets in one layer, the orientation was changed layer by layer. The grooves for WLS fibers in scintillator were placed in such a way that the fibers were collected at the lateral sides, left and right, where they were connected to PMT's. Two PMT's were used for the calorimeter part, and an additional two for the charged-particle detection layers. The light output collected on one PMT for passing through particle depends on the hit position, because the number of scintillator layers is different, as shown in Fig 2.12.(c). This dependency is called as the 'structure function' of CC04. The sum of the left and right PMT signals eliminates it.

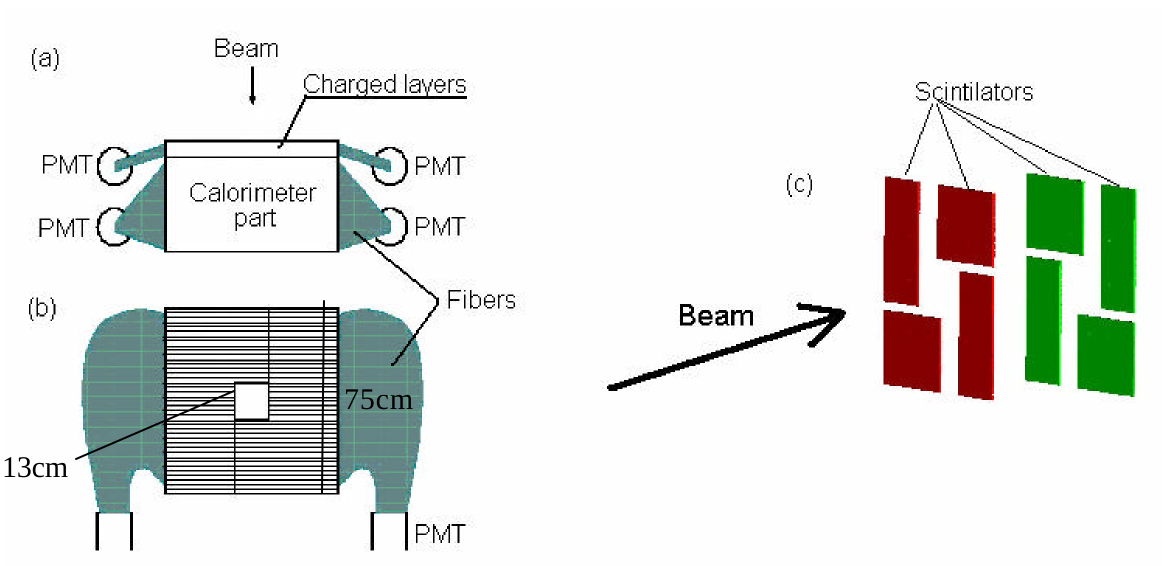

Fig. 2.12. CC04 schematic views from the top (a) and from the front (b). The scintillator layer structure is shown in (c)

The CC05 is the same detector as CC04, but for the calorimeter part only 30 scintillator layers are used. The last two layers form the charged particle detection layers for the backsplash from further downstream collar counters. In total, it has 6 PMT's.

Ten lead-glass rectangular blocks with a size of 15x15x30 cm^3 and a thickness of 11 X_0 were used for the CC06 counter. The blocks were staked and formed a wall with a beam hole, as shown in Fig. 2.13. CC07 is the same detector as CC06, and is installed after CC06, just before BA. The PMT's were glued to a butt-end of each block.

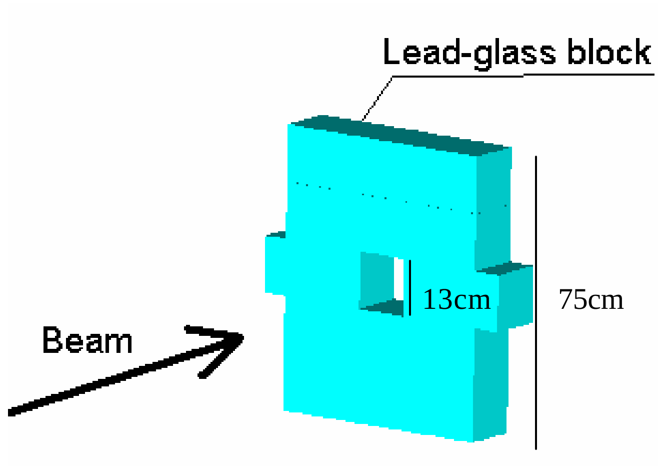

Fig. 2.13. CC06 schematic view. It consists of 10 lead-glass blocks stacked on each other.

The BA counter is placed at the end of the E391 detector for covering the forward hole in 4π geometry of the veto system. The beam core neutrons hit the BA together with gammas from K_L^0 decays, so the highly efficient method of neutron/gamma separation is required. This can be done by measuring of the longitudinal profiles of the shower. We divided the BA into 6 lead/scintillator blocks and 6 quartz blocks in the beam direction, as shown in Fig. 2.14. Quartz layers were made of 3x3.5x24.5cm^3 crystals stacked perpendicular to the beam in order to decrease the single counting rate. PMT's were glued to the butt-end of each crystal. The lead/scintillator block consists of 6 scintillator (5mm) layers and 6 lead (2mm) sheets and has a thickness of 9.49 X_0. WLS fibers were glued so that both ends were on one side with bending on the other side (7cm radius). All fibers on one scintillator sheet were collected on one PMT. In total, there are 78 channels; 36 PMT's are attached to scintillator layers and 42PMT's – to quartz crystals.

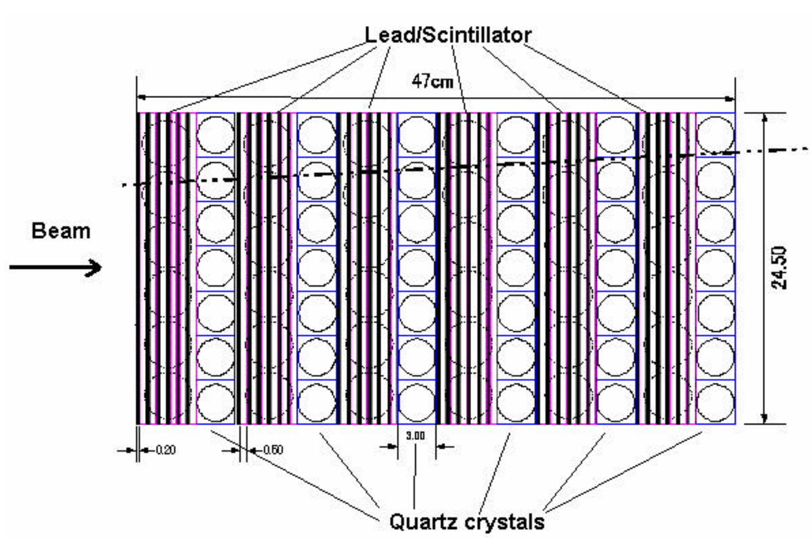

Fig. 2.14. BA schematic view.

2.2.6. Vacuum system

2.2.6.1. Overview

For the $K_L^0 \to p^0 \nu\bar{\nu}$ decay, a very high vacuum along the beam path is required to reduce the background due to interactions of the beam with residual gas. For our experimental setup, an estimation of the background has already been done [41]. Background events of 0.08 (G-FLUKA), 0.01 (G-CALOR) and 0.006 (GHEISHA) are predicted at a vacuum pressure of 10^{-5} Pa for a sensitivity of $3\text{x}10^{-11}$ for the $K_L^0 \to p^0 \nu\bar{\nu}$ decay. Therefore, in the case of E391a, whose sensitivity is $3\text{x}10^{-10}$, a vacuum of higher than 10^{-4} Pa is required in order to reduce the background down to a negligible level (< 0.1 events), even for the worst case predicted by G-FLUKA. On the other hand, an experiment for $K_L^0 \to p^0 \nu\bar{\nu}$ decay requires highly sensitive detection for particles in order to reduce the backgrounds from other decay modes and from interactions of the halo neutrons.

In the E391 experiment, we separate the decay volume (high vacuum region) and the detector volume (low vacuum region) by a thin membrane. Such a separation of the vacuum volume and the differential pumping system allows us to reduce the evacuation time and to reach a good vacuum level in the decay volume. Almost all detectors, except for CC05,CC06,CC07 and BA, are installed in the low-vacuum region, as shown in Fig 2.15.

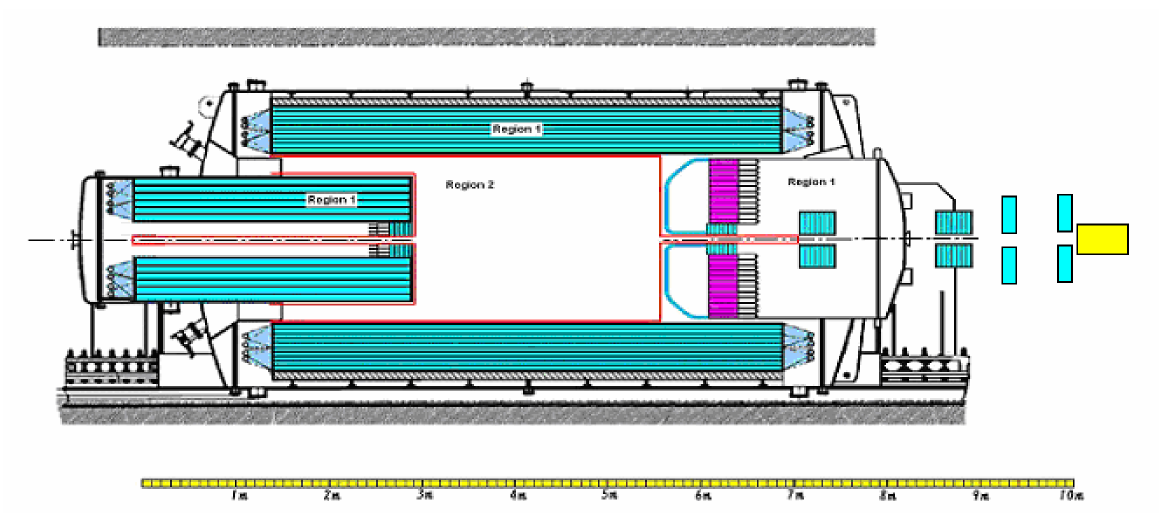

Fig. 2.15 Schematic view of the E391 detector and the separation of the vacuum volume into two regions by a thin membrane (red line): region 1, the detector volume, and region 2, the K^0_L decay volume.

2.2.6.2. *Scheme of pumping*

A block diagram of the E391a vacuum system is shown in Fig.2.16. The low-vacuum region, “Region 1”, is evacuated by two high-speed rough-pumping sets consisting of a rotary pump (RP) of 1,500 l/min and a pair of Roots pumps (Mechanical Booster, MB) of 250m^3/h and 1,000 m^3/h (300 l/sec). They are connected in parallel. The high-vacuum region, “Region 2”, is evacuated by four turbo-molecular pumps (TMP) that have a pumping speed of 800 l/s each and 3200 l/s in total.

At an initial stage of evacuation, valve GV1 is opened in order to balance the pressures of both regions. Evacuation operation begins from a small pump. This is because there are always strong concerns about the possibility that a strong force would be loaded to the membrane, due to a non-uniformity of the pressure at the initial stage when the pressure is still high. Then a set of Root pumps (mechanical booster, MB) join for evacuation. After reaching a vacuum level of several Pa, the valve, GV1 is closed and TMP’s start to evacuate the air only from the high-vacuum region (region 2).

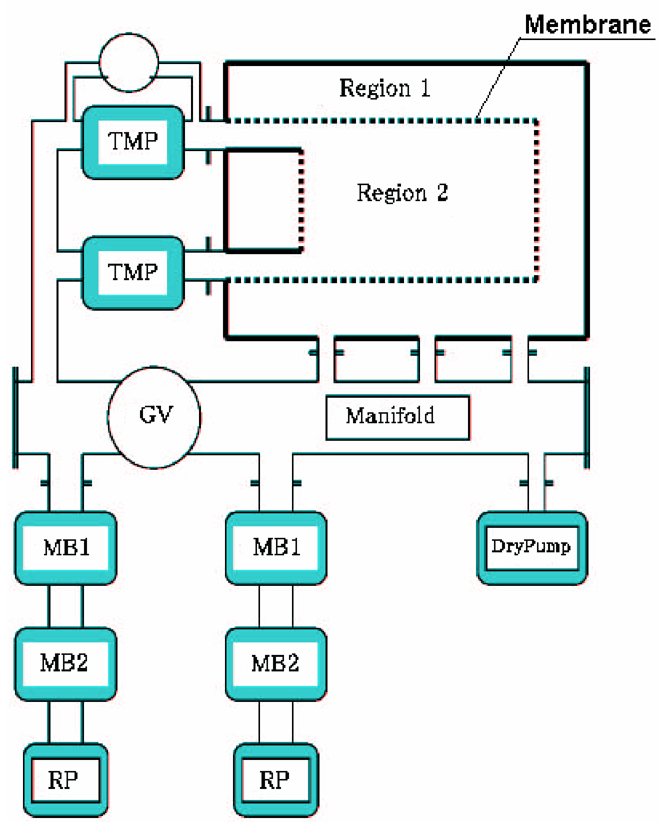

Fig. 2.16 Block diagram of the pumping system of the E391 detector. Regions 1 and 2 are low and high-vacuum regions, respectively. RP – rotary pump, MB – mechanical booster pump, TMP – turbo molecular pump, GV – gate valve.

2.2.6.3. Bench tests of the membrane

To separate the low and high-vacuum regions, a plastic sheet, called EVON, was chosen. It is a lamination of 80 μm low-density polyethylene, 15 μm aluminized EVAL film, 15 μm nylon and 80 μm low-density polyethylene. It is ordinarily used for an airship, which is required to be mechanically very strong. The total thickness of the sheet is 20 mg/cm^2.

Through a bench test, it was found that the outgassing rate is 9×10^{-6} Pa m^3 / (sec m^2) at room temperature after 167.7 hours of evacuation. It was also observed that a kind of baking effect decreased the outgassing rate to 4.2×10^{-8} Pa m^3 / (sec m^2) after a heat-up to 50 degrees. The main component of the out-gas, which was analyzed by a mass separator, was water vapor. According to their catalogue, transmission of gas through EVON is 1, 0.030, <0.1 and <0.01 cc/m^2 /24 hours for He, O_2, CO_2 and N_2 gas, respectively. These values are far below the required level for the E391 vacuum.

Another merit of this material is that sheets can be easily jointed with each other by applying heat to the low-density polyethylene layers on both sides.

Chapter 3

Data taking in a physics run

3.1 DAQ system

3.1.1 Overview

A distributed and parallel processing DAQ system has been developed for the E391a experiment. Data from front-end FASTBUS-ADC's and TKO-TDC's are read out by VME board computers, and sent to the server computer via a network.

The E391 detector consists of electromagnetic calorimeter and veto counters covering full 4π geometry. All of these detectors use photomultipliers (PMT) for light readout. Table 4.1 lists the number of channels of each detector subsystem. Both the charge and the timing of each PMT signal are measured by the DAQ system. These signals are also used for online triggering. The total number of readout channels is about 1000.

Table 4.1 Number of readout channels for all detectors.

Detector subsystem	No. of readout channel
CsI calorimeter	576
Front barrel	32
Main barrel	192
Beam collar counter	44
Charged veto scintillation counter	36
Beam anti Sandwich counter	72 24
Total	976

The signals from PMT's are sent to a special Amp/Disc module (see below), which produces 3 signals simultaneously: an analog signal for ADC, alogic signal for TDC and an analog sum of 8 input channels for triggers. The individual analog signal is transferred to ADC through a 90 m-long coaxial cable. The analog sum output used for the trigger logic is transferred by a 30 m-long coaxial cable. The Trigger signal opens the gate of ADC's and starts the counting of TDC's, which are stopped by a logical signal produced by Amp/Disc module for each channel. The level of the signal discrimination for TDC can be adjusted manually. A 30m twisted pair cable and an additional 100ns logic delay are used to delay a stop signal to TDC (Fig.4.1).

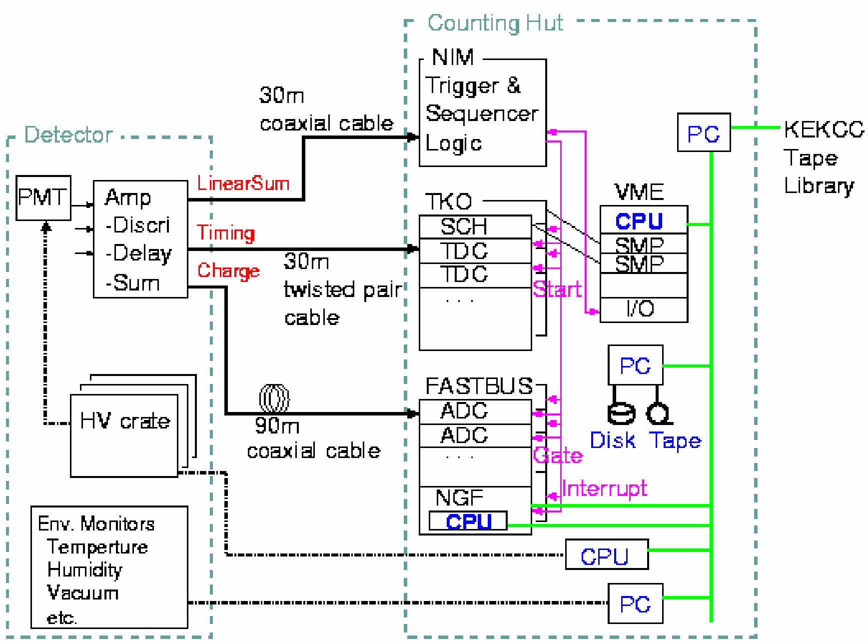

Fig. 4.1. DAQ system overview.

The HV power supplies are installed in the beam area near to the detectors. We used 7 CAEN SY527 crates which have a remote control system, and allow us to board up 10 modules. Modules (A737N) having 16 channels with an output HV of up to 3kV were used.

Various environmental parameters, the temperature, the vacuum level and so on are monitored. Information from them is saved to the disk for the further analysis.

Information from FASTBUS and TKO is collected by a CPU (UltraSPARCII 500MHz) built in the VME board, and then sent to DAQ using the TCP/IP protocol through a Gigabit Ethernet. VME CPU works under Solaris 8 OS. In order to increase the speed of the DAQ, data are collected and kept on the VME board during an on-spill period, and are transferred to the server during an off-spill period (Fig. 4.2)

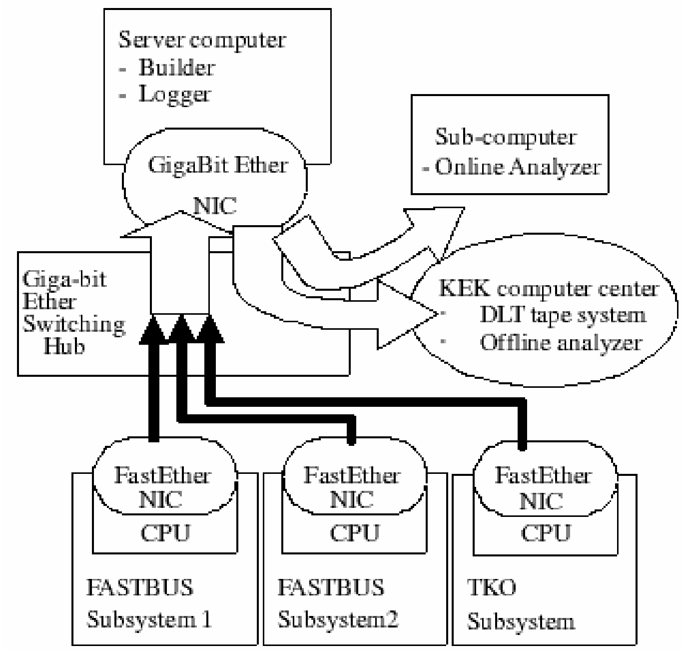

Fig. 4.2 Conceptual scheme of the DAQ system. The data flow is shown by arrows.

The DAQ software is prepared based on MIDAS [10], which is a free open-source data-acquisition system. MIDAS can run on both Solaris OS and Linux OS. MIDAS provides functions of a front-end framework, buffer management, data logging, data distribution via a network, event build, run control and so on.

3.1.2 Electronics

In order to measure the 1 MeV energy deposit precisely, an ADC resolution of 10 channels per 1 MeV will be preferable. Also, it is needed to measure the energy up to 3 GeV for the CsI calorimeter. We used the LeCroy 1885N, 96ch FASTBUS ADC, which has a 50 fC resolution per channel. The charge conversion time is 750 μsec, which restricts the speed of data acquisition up to 1000 Hz, at most.

In order to reduce accidental background events, 1 nsec of the event-timing resolution is required. In some cases, we also have to distinguish the incident angle of γ to the CsI calorimeter for a further reduction of the background. For that purpose, less than 0.1 nsec of the timing resolution is necessary. We decided to use 64ch TKO-TDC as a TDC module. The resolution is 0.05 nsec. The TDC is operated in the common-start and individual-stop mode.

Multihit TDC is useful in some cases. BA suffers from a huge counting rate due to the neutral beam. We need to separate the γ's from K^0 decays and γ's and neutrons in the beam. We have chosen the LeCroy 1877S FASTBUS TDC. It has 96 channels in a module, and each channel has a 16 bit depth of the buffer. Because dynamic range is 32 μsec, the resolution is 0.5 nsec The data-conversion time is less than 80 μsec.

3.1.3 Trigger logic

The global trigger logic accepts multiple trigger signals simultaneously from multiple subsystems: a random trigger from the clock generator, a cosmic event trigger from MBR, a Xenon/LED flush, number-of-CsI-cluster ($N_{cluster}$) trigger from the cluster counting logic, accidental triggers and so on. A trigger decision is made within 200 nsec after a trigger request. During the data collection time, the next trigger requests and a flash of the xenon lamp are suppressed.

The main trigger is the N-cluster trigger. All 576 CsI crystals were divided into groups with 8 channels. The channels in each group were connected to one Amp/Disc module, and the sum signal was transferred to the trigger logic. In total, the CsI calorimeter was divided onto 72 clusters, as shown in Fig. 4.3.

In the trigger logic, the analog cluster signals were discriminated at the level of 60 MeV and then 72 logic output signals were summed up. Discriminators with different thresholds were used to generate signals corresponding to an event with the number of hit-clusters equal or grate than N ($\geq N$). A special trigger as $N = 2$ was obtained by a simple logic $(N \geq 2) \cdot \overline{(N \geq 3)}$.

The sum signals of CC02, CC03, CC04, CC05; the sum of the downstream MBR, the sum signal of each cluster of FBR and CV detectors were used for online vetoing. The threshold levels were optimized to reduce the trigger rate down to an acceptable rate. Also, the veto signal from each detector was taken into account only when it was inside the time window that was set depending on the detector.

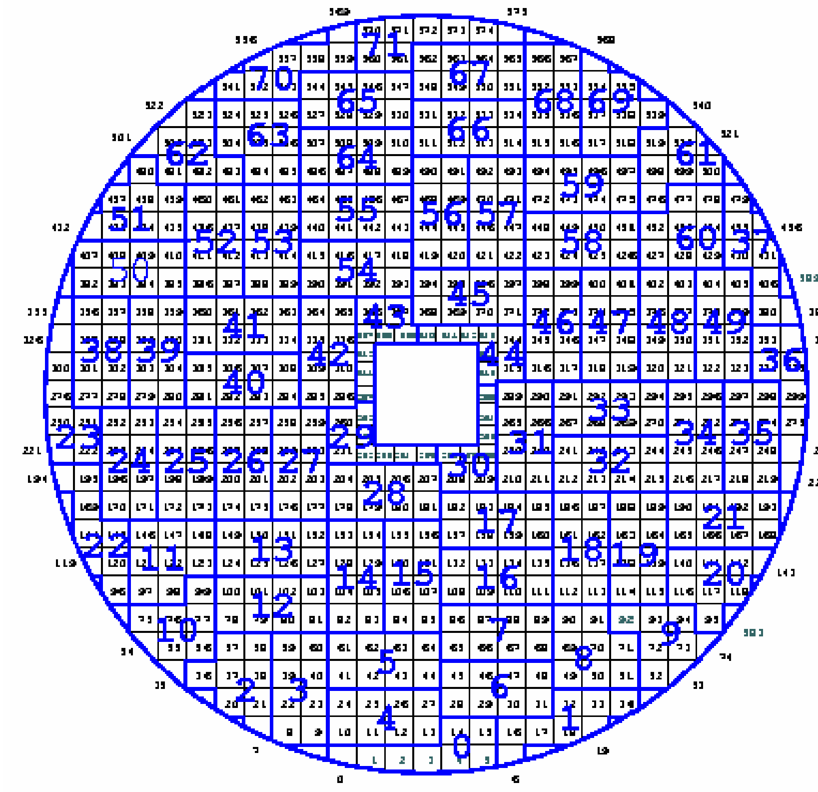

Fig. 4.3 Scheme of the CsI cluster layout.

3.1.4 Server computer and network

The server computer is a PC with a Linux OS. Data from each detector are collected on the server and built by using MIDAS builder software, and are saved on the hard disk of the server (Fig. 4.2). Online analysis is performed by a sub-computer using a part of the built data sent via the network. The stored data are sent to a tape library in the KEK central computer-system in order to perform an offline analysis. The VME computer has a network interface (NIC) for the Fast Ethernet.

Although the network speed is sufficient to send data from each subsystem, the total traffic with sending data to the tape library is huge. Therefore we adopted a NIC of Giga-Bit Ethernet on the server computer. The server computer and subsystems are connected with a switching hub, which is used for both the Fast and Giga-bit Ethernet.

3.1.5 DAQ performance

The beam from KEK-PS comes in a 4-second cycle and the beam duration is about 2 seconds. The subsystem stores data during a beam spill, and sends the stored data when the beam is off. The dead time for one-event data taking is 1800 m sec for FASTBUS and 420 m sec for TKO

The DAQ was tested in an Engineering run in Oct.-Dec. in 2002. At that time, not all of the detectors were ready. However, our main detector, the CsI calorimeter that has the largest number of channels, had been prepared for the engineering run. The proton-beam intensity was about 10^{12} per spill and the trigger rate was less than 200 Hz. In a physics run in 2004, the FASTBUS ADC's were upgraded in terms of reducing the dead time. We reached a dead time of 1000 m sec which allowed us to increase the trigger rate up to about 500 Hz during the physics run.

3.2 Data taking in 2004 physics runs

In February 15, we started physics data taking. The beam run continued until June 30. The first two weeks were used for beam tuning, DAQ tuning and detector calibration by the muon beam. At the end of the data taking, 15 shifts were used for calibration of the CsI calorimeter by π^0's produced on a target. In total, we had 175 shifts of physics data taking. The duration of the shift is 8 hours.

3.2.1 Triggers during physics data taking

- *Physics trigger*

During physics data taking, we collected data with various triggers simultaneously. The main trigger was $N_{cluster} \geq 2$ + veto. Our goal was to collect as many 2γ events as possible. Furthermore, data from other decay modes, such as $K_L^0 \to 3p^0$ and $K_L^0 \to 2p^0$, were needed to monitor the number of K_L^0's coming to the E391 setup. Thus, this trigger mode allowed us to collect data for all K_L^0 decays with the number of γ's more than or equal to 2.

The online veto thresholds were optimized so as reduce background events, and not to lose real events. In order to reduce the acceptance loss due to accidental hits, the time windows of the veto signals were set in the trigger logic.

- *Monitor triggers*

In order to monitor accidental events, three special triggers were prepared. They were the signal of TMON, a counter telescope near the K^0 production target used to monitor the targeting efficiency; the signal of C6, located at the exit of the beam line; and the signal from BA.

The pedestal events triggered by a clock and the Xenon/LED events triggered by a signal to the flash Xenon lamp and LED were used to monitor the drift of the system during data taking. These triggers were fired in both the beam-on and off periods in order to check the beam-loading effects.

- *Minimum bias triggers*

To study the veto inefficiency, a minimum bias trigger was also prepared. It was $N_{cluster} \geq 1$ without any veto. An additional one was $N_{cluster} \geq 2$ without any veto, which was useful to study the veto inefficiency with the same trigger condition as the main physics trigger.

- *Triggers for calibration*

Additional triggers were a cosmic trigger, a coincidence of the opposite main barrel clusters; and a muon trigger, a coincidence of the CC04 and CC05 beam collar counters. The comic trigger was fired only in the beam-off time. The muon trigger was used to calibrate the beam counter, and during physics data taking, for monitoring their gain constants.

3.2.2 *Data taking*

- *Physics data*

We collected about 6Tb data by the physics trigger $N_{cluster} \geq 2$ + veto. The main trigger allowed us to collect data of various K^0 decay modes. The $K_L^0 \to 3\pi^0$ decay is very clean in terms of the background, and can be used for a detailed comparison of the data and the MC simulation results. The $K_L^0 \to 2\pi^0$ and $K_L^0 \to \gamma\gamma$ decays can be used to monitor the number of K^0's coming to the E391 setup.

- *Special runs for the detector calibration*

For detector calibration, we performed special runs using the muon beam by closing the C3 collimator. For CsI calibration, the trigger was $N_{cluster} = 1$ without any veto. The collar counters were calibrated using the coincidence of the CC04 and CC05 as a trigger. The data for the BA calibration was taken by a self-trigger. Special runs using cosmic rays were performed to calibrate the CsI calorimeter during a beam break.

- *CsI calibrations with* p^0.

For the CsI calorimeter, a special run to use γ's from p^0 was performed by inserting an aluminum target in the decay volume. p^0 mesons were produced at the target and decayed into 2γ. It was an overall and absolute calibration of the CsI calorimeter because of the well-defined decay point, as described in the next section. The data sizes for the different triggers are listed in Table 4.2.; 80% of the collected data are physics data.

Table 4.2 Data size for different triggers and data type.

Physics trigger	~6Tb (57 days)
Cosmic trigger	All time in off spill + special runs
Muon beam trigger	~ 300 Gb
p^0 calibration	~500 Gb

Chapter 4

Calibration of the detectors

4.1 Pedestals

In order to monitor the stability of the electronics system, we measured the ADC pedestals with a 1Hz frequency in the physics run. Our ADC's work in two modes: a high-gain mode (0.05 pC/ch) and a low-gain mode (0.4 pC/ch). The pedestals in both modes were periodically measured during the beam-off and the beam-on periods.

In Fig. 4.1, typical distributions of the pedestals for all detectors (high-gain mode) in the beam-on period are presented. All of the detectors, except for the sandwich counters (see below), have small pedestal fluctuations (s) of about 1.5 channels (high-gain mode) and about 1 channel (low-gain mode). The pedestals of some detectors suffer from accidental hits, but there is no meaningful difference between the peak position of the pedestals in on-spill data and that in off-spill data. In Fig. 4.2, the distributions of the pedestal width (s) for the high and low-gain modes for all CsI crystals are shown. All other detectors, except the sandwich counters, have the same width of pedestals.

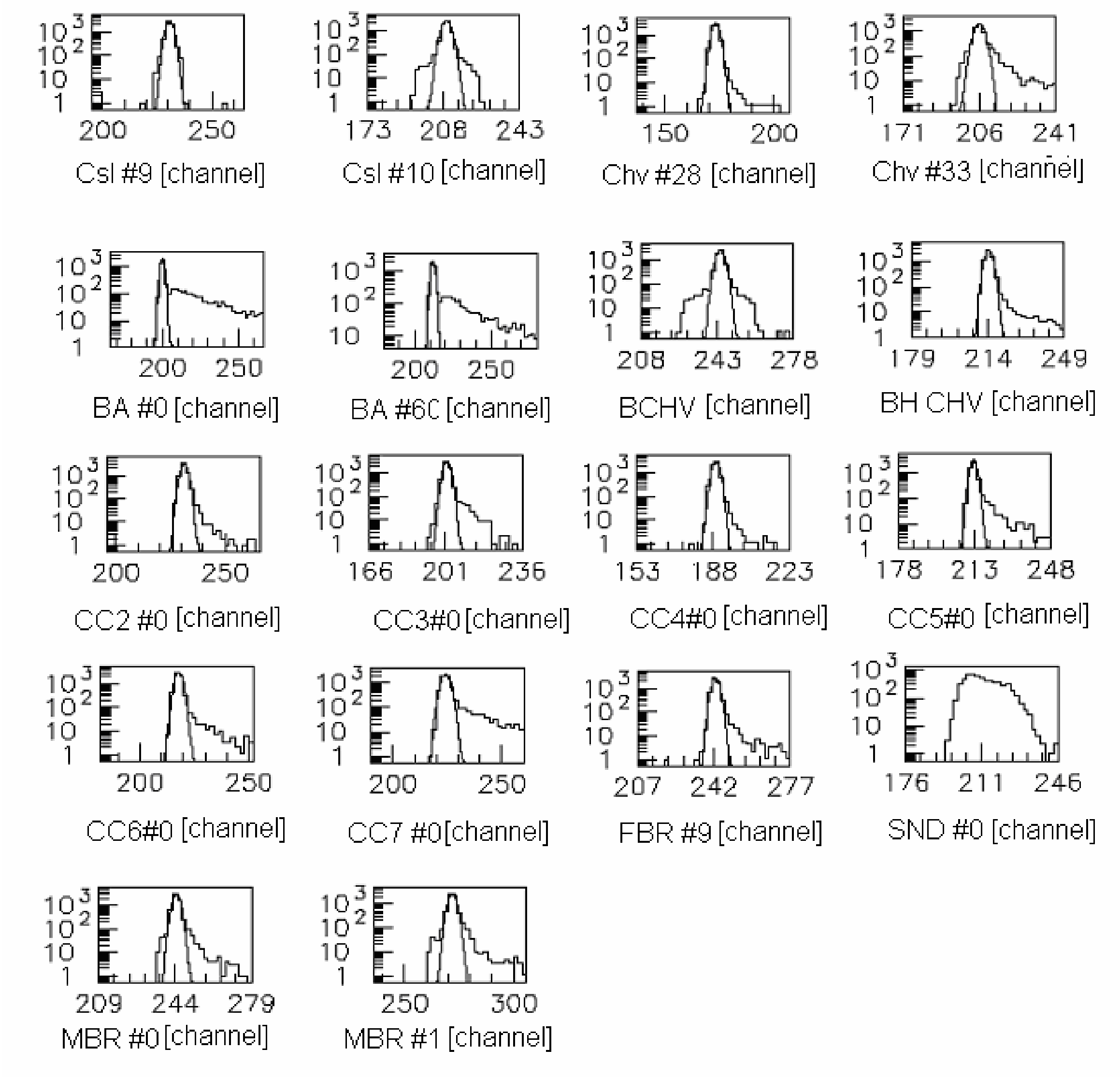

Fig.4.1. Typical distributions of pedestals for various detectors in a high-gain mode.

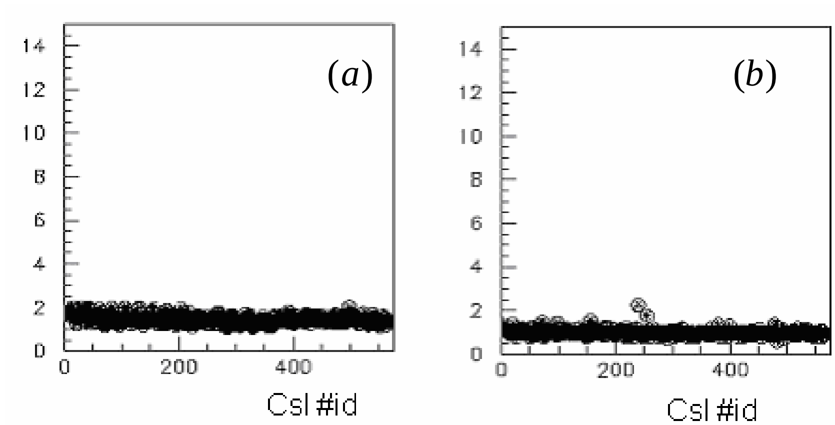

Fig.4.2 Distributions of the pedestal width (s) of the CsI calorimeters for the high-gain (a) and the low-gain (b) modes.

Sandwich counters have a relatively large noise in the electronics, which leads to a wide distribution of the pedestals, about 8 channels in the high-gain mode (Fig. 4.1). Since all channels have common-mode noises, they are correlated. It was found that the correlations appear in 3 groups: channels #1-#6, #7-#18 and #19-#24. These groups of channels belong to the same Amp/Disc module.

For each run these correlations were fitted with $Ped_i = a_j^i * Ped_j + b_j^i$, where a_j^i, b_j^i - coefficients for correlation between the i-th and j-th modules. The table of coefficients allows us to calculate the pedestals for all other channels in a group using only one reference channel. For physics data, we corrected the pedestals of sandwich counters event by event. The reference channels in each group were also changed event by event; actually, it was easily found as a channel without the TDC signal (1MeV threshold). The result of the correction is shown in Fig. 4.3. The pedestal width (s), about 2-3 channels, became almost the same as those of the other detectors. However channel #17 with a s of about 5 channels had additional noise.

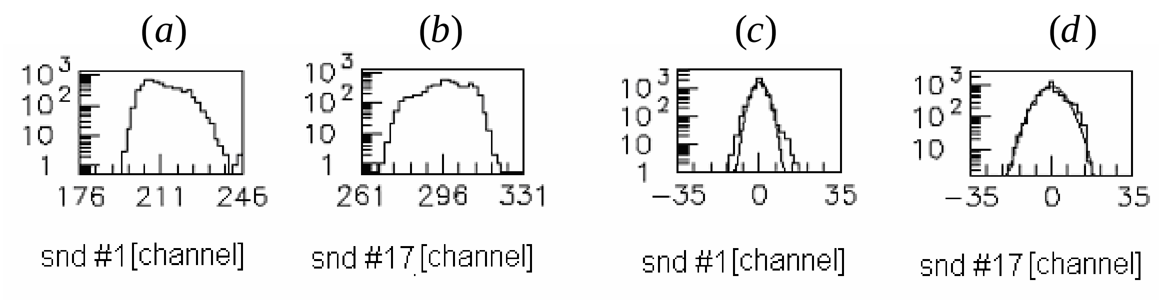

Fig. 4.3. Pedestal distributions of the sandwich counters before (a,b) and after (c,d) corrections.

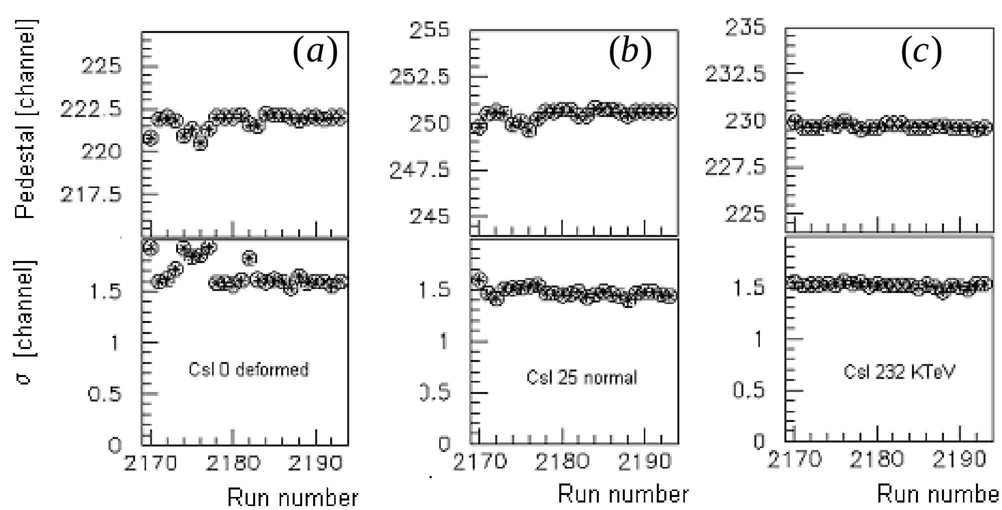

Fig. 4.4. Typical behavior of the pedestal stability of the CsI crystals for a "one-day run". The data are for the peripheral (a), main KEK (b) and KTeV crystals (c).

During a long period of data taking, we need good stability of the electronics. Here in Fig. 4.4 is presented the behavior of the CsI pedestals during the 2170-2193 run (this is a so-called ‘one-day run’). The pedestal drift is about 1-2 channels, which is comparable to the pedestal width. Other detectors also show good stability.

4.2 Gain monitoring system (Xenon/LED)

We have to keep a good gain stability of the detector over a long period of data taking. The most important item is the gain drift of PMT’s. In order to eliminate uncertainty due to a change of the PMT gain, a monitoring system was prepared. We used two sources of light from a xenon lamp and an LED. The xenon system (Xe) is used for the CsI and the CC03-4-5 detectors. The LED system is used for the barrel detectors, CC02, CC06-7 and BA. The Charge Veto and Sandwich counters don’t have a gain monitoring system.

A xenon flash lamp was used to generate of the light pulses. Using an optical divider, light is distributed to the detectors. The stability of the lamp is monitored by a special PMT placed in a box with a constant temperature. The width of the light pulse is about 400 μsec, and during a flash a veto is applied to the DAQ trigger. The trigger rate is about 0.01 Hz.

In Fig 4.5, typical ADC spectra of Xe/LED signals for each detector are shown. The peak positions and widths of the distributions vary with the detector. These data were taken during an on-spill time. Off-spill data have the same distributions, but the histograms are cleaner without accidental events.

Fig 4.6 shows the typical behavior of Xe/LED signals. The gain factors show good stability for a single run (1000 spills ~ 1 hour). Such a long-term stability over the runs is very important for physics data taking.

The low-frequency noise in the electronics, the instability of the PMT, itself, and the gain drift of the PMT due to overloading by the beam may cause an instability of the system. The fluctuation of the Xenon lamp, itself, which is used for gain monitoring, can also simulate the gain drift of the detectors.

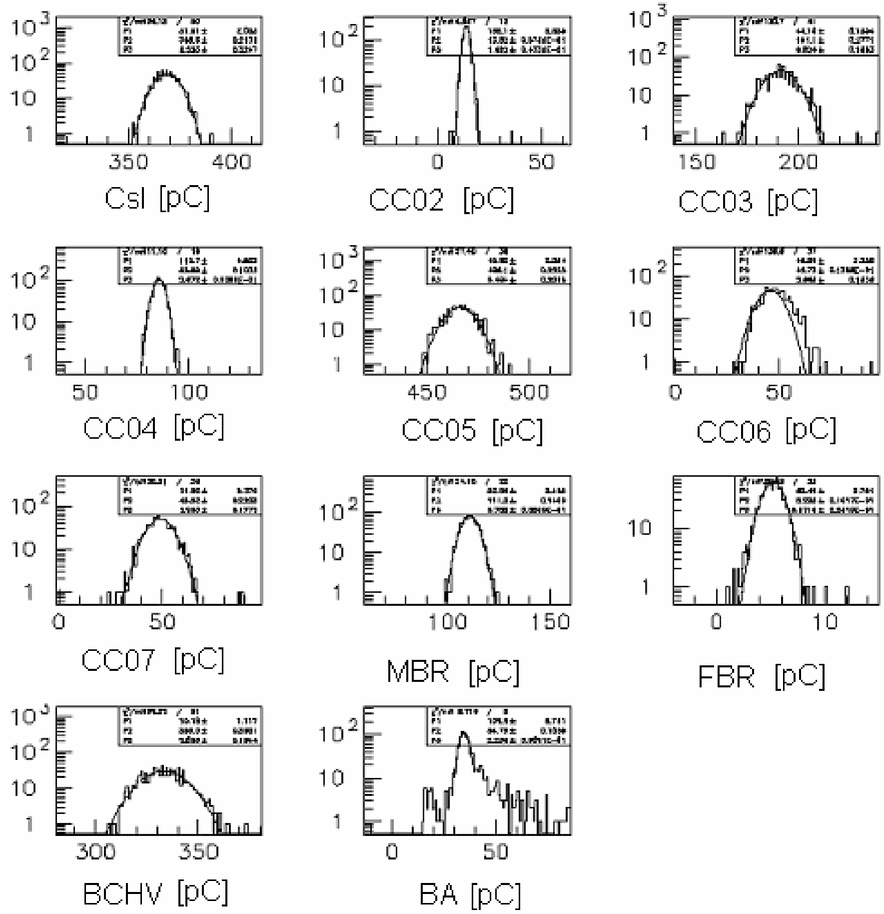

Fig. 4.5. Typical charge spectra of the Xenon/LED signal for all detectors in the on-spill period.

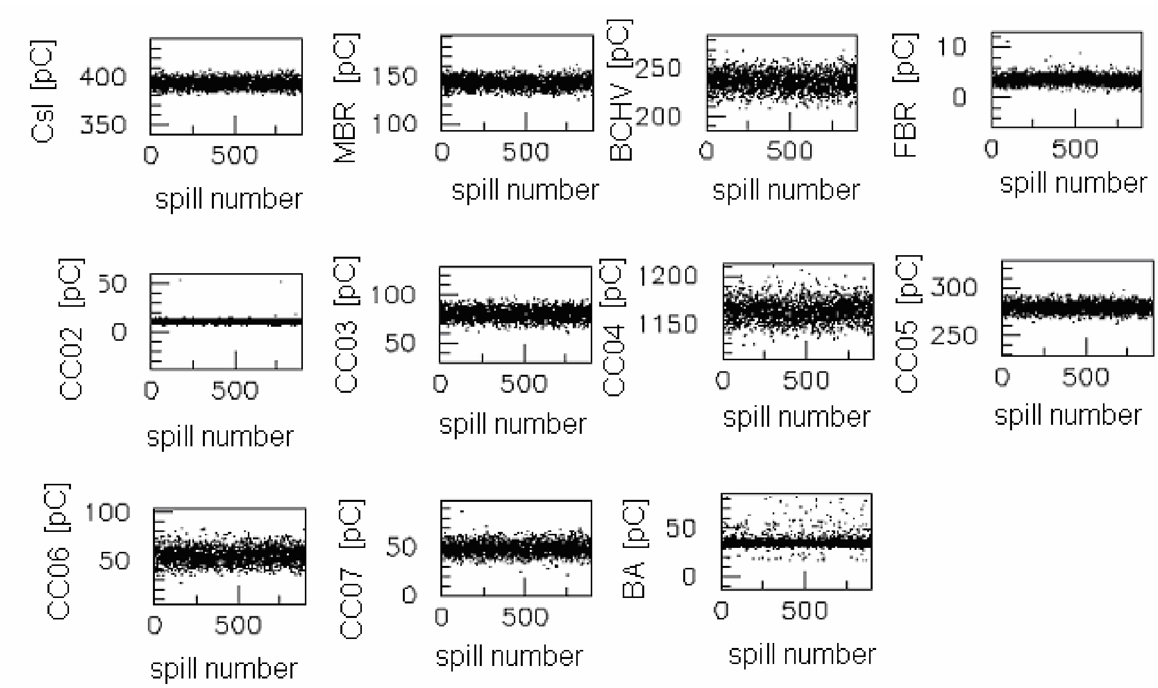

Fig. 4.6. Typical behaviors of the Xe/LED peak over the spill number. Here, ~1 hour of data are presented.

Low-frequency noise generally has an outside origin – the noise in a ground connection, the influence of an external apparatus and the instability of a power supply. This leads to a change of the charge coming from the PMT in a systematic way. We paid big attention to reduce such electronic noise: the ground connection was independent from those of other power supplies, power stabilizers were introduced, and the electronics were disconnected from the external networks. We also made an effort to separate the grounds of all detectors in order not to disturb the whole system by one bad channel.

The instability of the PMT, itself, is also a problem. We observed that one CsI channel (#91) shows such a behavior. In Fig. 4.7, the stability of the xenon signal of this channel is shown. The gain drifts in time. For a gain correction we sliced the xenon data by 50 spills and took a mean value in each slice (dots in Fig. 4.7.a). The correction factor for events in each slice was calculated as the ratio of the mean-value point to a fixed value for this channel. We obtained a similar stability with others after a correction (Fig. 4.1.b).

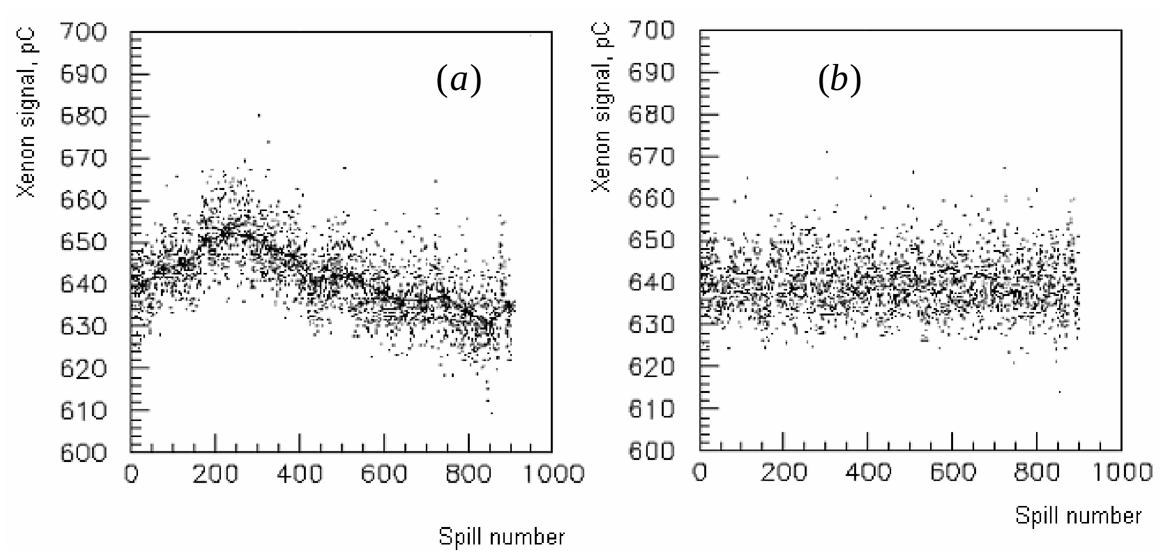

Fig. 4.7. Behavior of the unstable CsI #91 PMT (a) and after correction by slicing (b). The correction factor for events in each slice was calculated as the ratio of the mean-value point in this slice to a fixed value for the given channel.

Another instability is connected with a beam intensity. Some PMT's don't work properly under a high-rate environment, and their gains shift. When the beam load disappears, the gain returns to the normal level. We checked this gain drift by comparing the Xe/LED peak position of the on-spill data with that of off-spill data. In Fig 4.8.a-b, the relative difference of the peak values of on and off spills is shown for all detectors. The CsI calorimeter is stable within a 1% level. Only a few crystals showed a light dependency on the beam loading. The main veto detector, the main barrel, is also very stable within a 2% level. Other veto detectors are stable within 5 – 10%. Since the LED light for FBR is very weak (~3 pC), it fluctuates with photon statistics. In any case, all veto detectors, except for BA, show a tolerable level of stability of 10%.

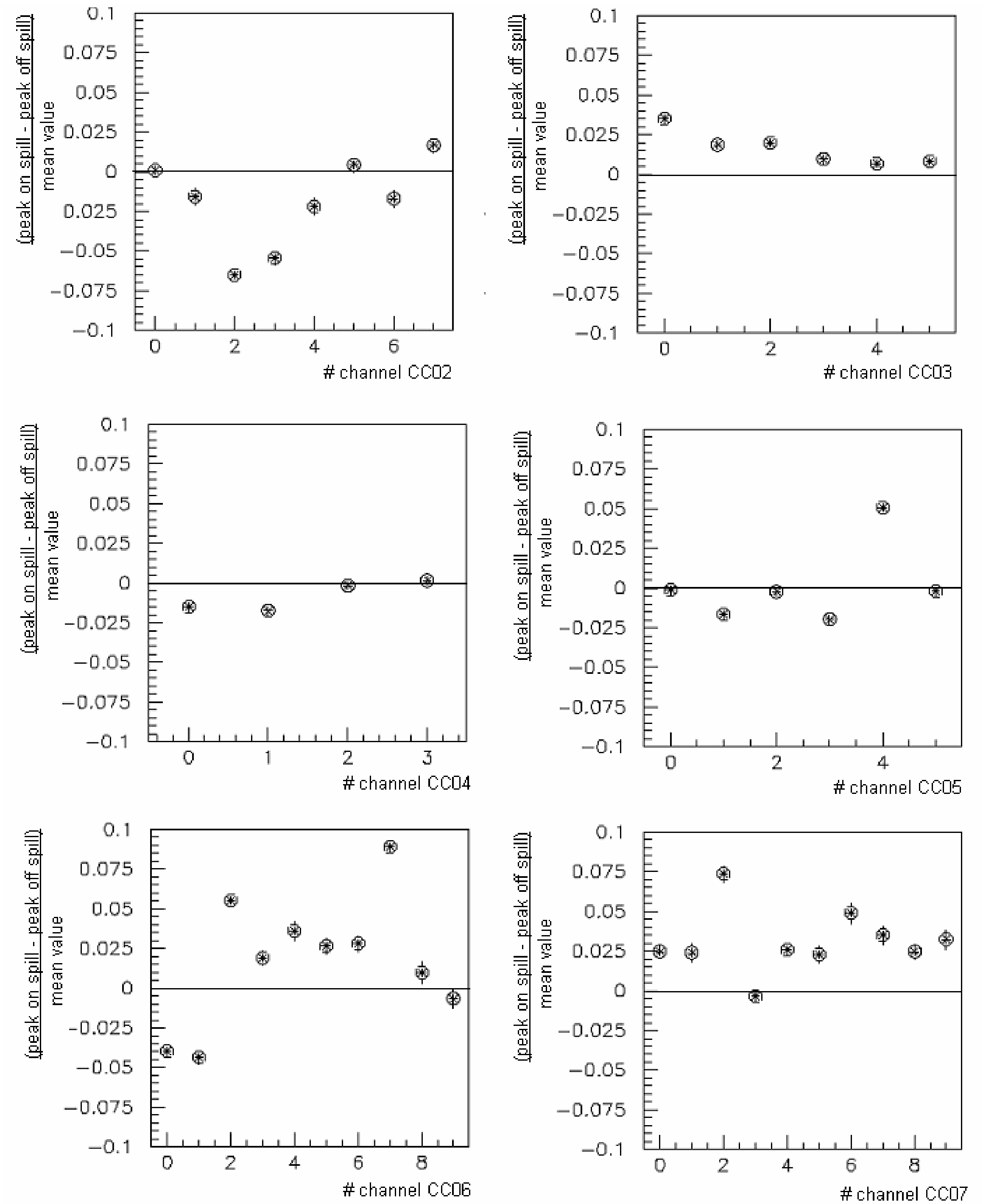

Fig. 4.8.a. Relative gain drifts due to beam loading for the detector channels.

The BA needs a special consideration because the beam directly hits it. The scintillator part shows a 15% effect, as shown in Fig. 4.8.b. In Fig. 4.9 the behavior of the BA scintillator channel inside the beam spill is shown. We can observe a distinguished spill structure. However, by applying a gain correction by slicing 50 events each, it is possible to correct the gain drift (Fig. 4.9.b).

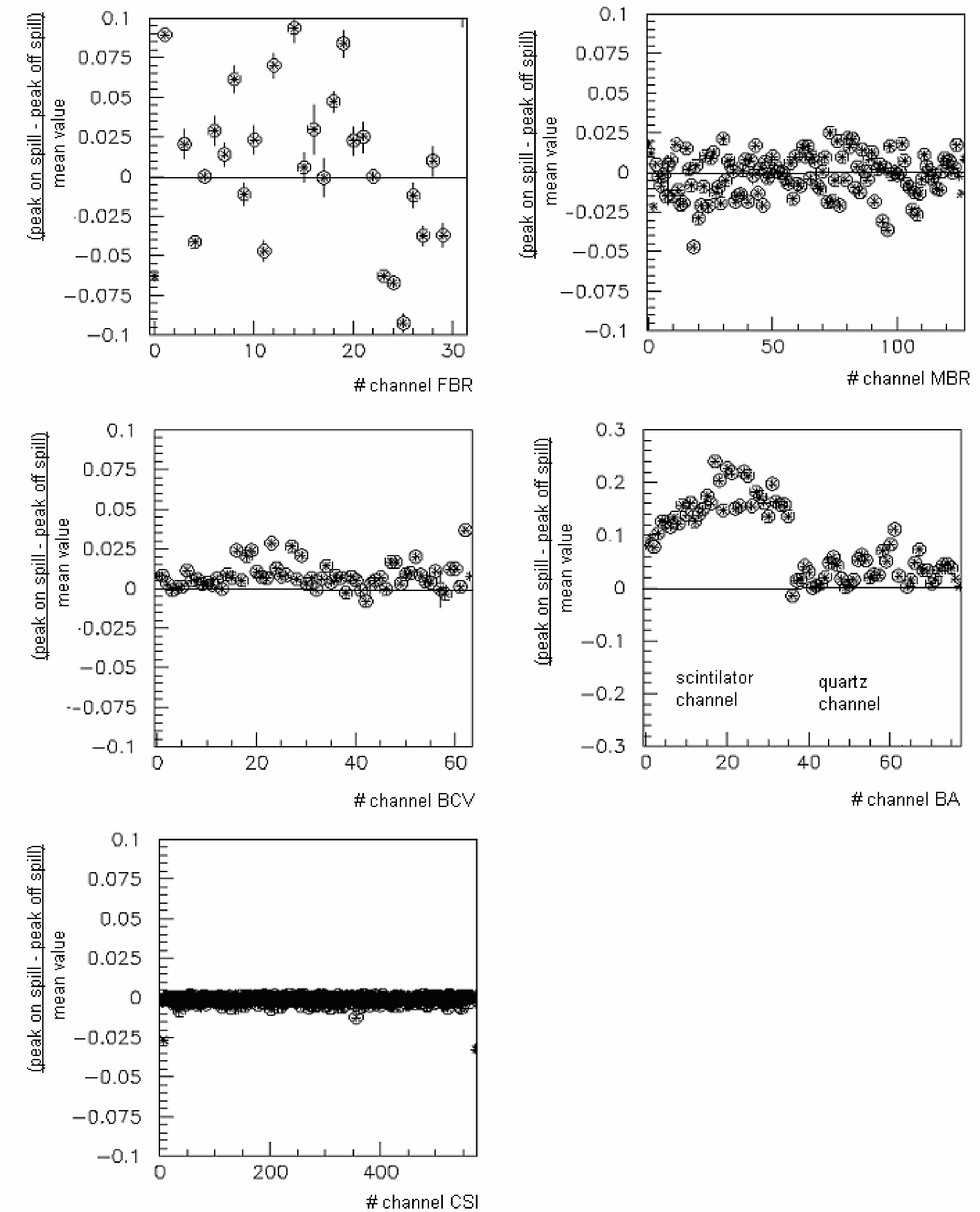

Fig. 4.8.b. Relative gain drifts due to beam loading for the detector channels. The CsI calorimeter channels are stable within 1%, except for a few channels.

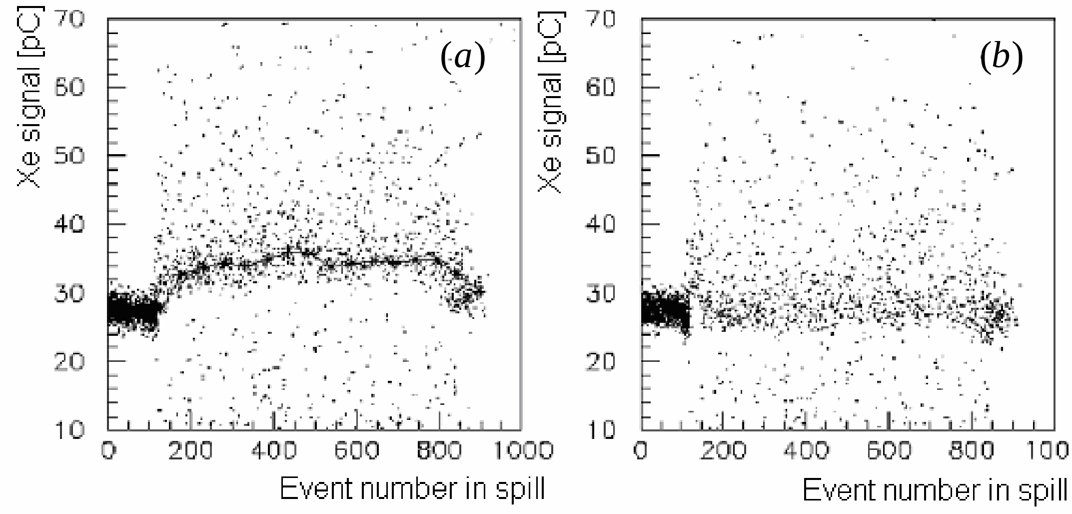

Fig. 4.9. Spill structure for BA scintillator channel 17 without correction (a) and with (b) ones.

The stability of the xenon lamp, itself, was monitored by 8 PMT's. Fig. 4.10.a shows the time variation of the Xe peak of one CsI channel. All other channels have similar variations. and the Xe monitor PMT's also show the same variation (Fig. 4.10.b). By normalizing to a Xenon monitor signal, the drift was eliminated (Fig. 4.10.c). However, actually, a such variation was found only in one run. At all other times, the Xenon lamp was very stable and didn't need such correction.

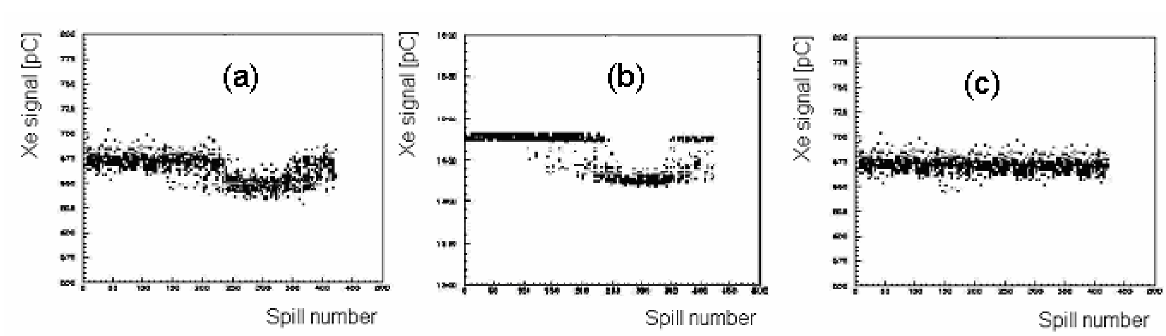

Fig. 4.10 Xenon signal behavior over the spill number for the CsI channel (a). The Xenon monitor (b) shows the same behavior. By normalizing (c) the Xe signal of CsI with the Xe monitor signal, we can eliminate the effect of the Xe lamp instability.

In Fig. 4.11, the long-term variation of the xenon peak, run by run, is shown. Almost all channels are stable within a few %. The Xe and LED were used to recalculate the gain factor to bridge over the extensive calibrations.

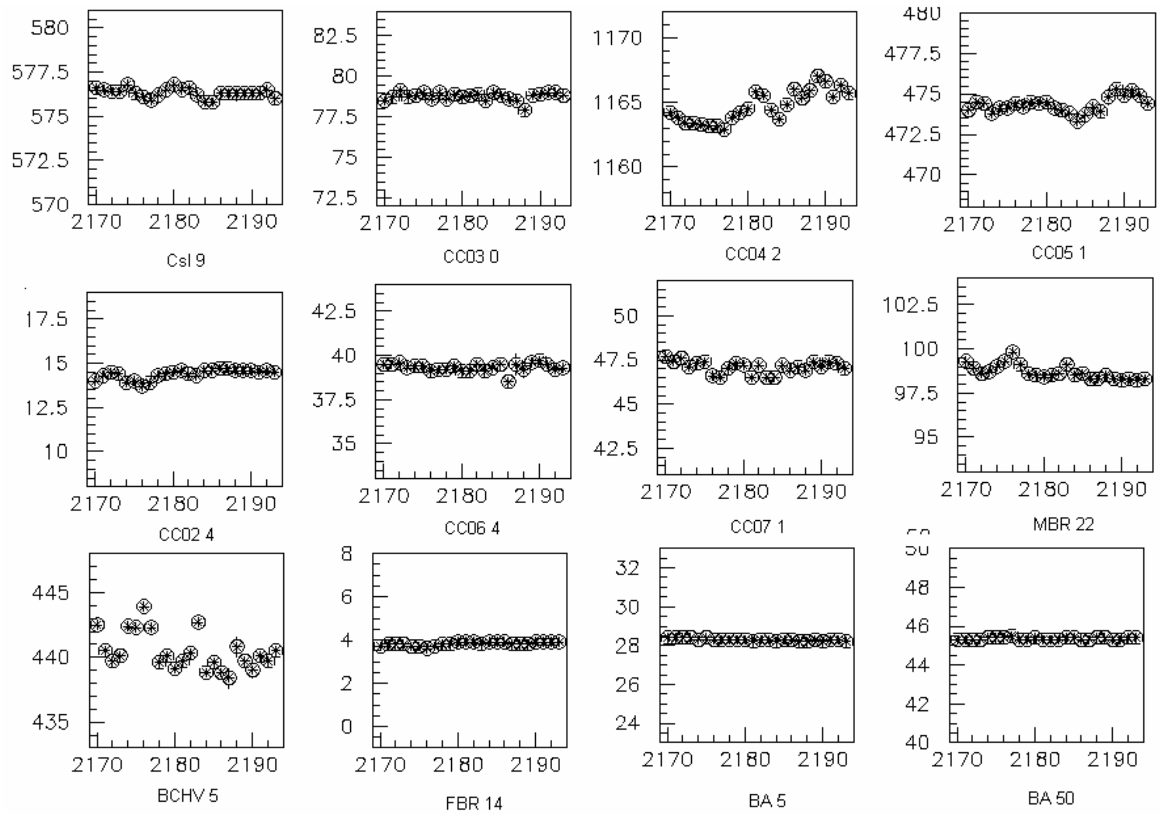

Fig. 4.11. Long-term behaviors of the xenon peak position for typical detector channels. The X axis is a run number. The Y axis is a xenon peak charge [pC].

4.3 Energy calibration of the CsI calorimeter

4.3.1 Calibration by cosmic muons

We took data of cosmic muons for calibration [43]. The trigger was generated by $N_{cluster} \geq 4$ in the CsI calorimeter. In the off-line analysis of each event, all nieghborhood crystals with an energy deposition more than 1MeV were connected together in one cluster. We drew a line through all crystals in a cluster using the least-squared method by minimizing

$$S = \sum \frac{(x_i - a \cdot y_i - b)^2}{1 + a^2},$$

where a and b are parameters of the track $x_i = a \cdot y_i + b$,. x_i, y_i- coordinates of the center of the i-th crystals in the cluster.

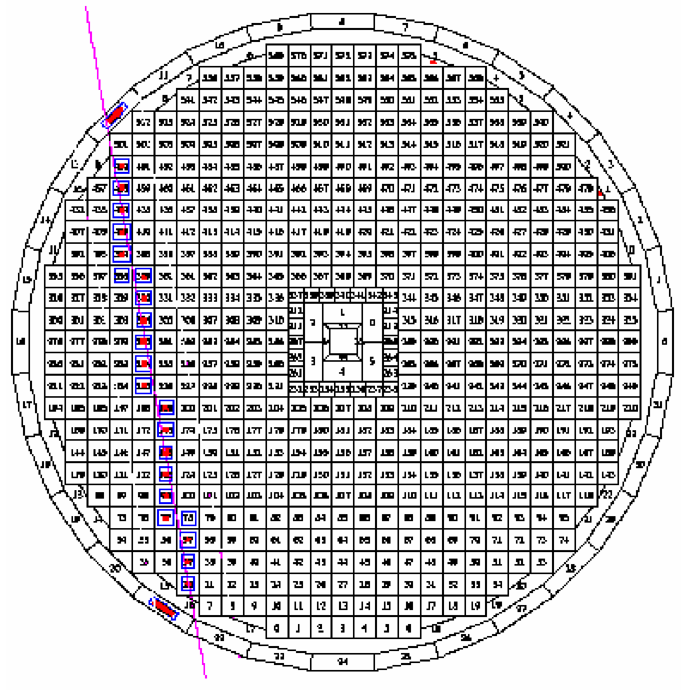

Fig 4.12 The front view of the CsI calorimeter and an example of the cosmic muon track. The size of red box is proportional to charge deposit.

In Fig. 4.12, an example of a cosmic-ray track is shown. The size of the red box is proportional to the charge deposited in a crystal. The line shows a reconstructed track. For a good fitting we rejected events with a track length less than 70 cm or with deviations of more than 12 (Fig.4.13). The big number of events with S=0 corresponds to vertical tracks.

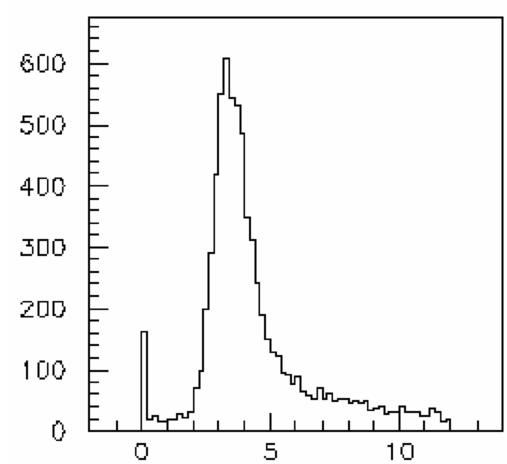

Fig. 4.13. Distribution of the calculated deviation, S.

Using track information, we calculated the path length of a cosmic muon through each crystal in a track. Then, the charge deposited in a crystal was normalized by the path length. In Fig. 4.14, the distributions of the raw charge spectra (upper figures), the calculated path length (middle) and normalized spectra (down) for three types of crystals are shown: normal 7x7 cm (left figures), small 5x5 cm (middle) and deformed crystal (right). Tracking allowed us to calculate the normalized charge deposit, even for deformed crystals.

The charge distribution was fitted by a Landau approximation function

$$F(x) = A \cdot \exp(-l - e^{-l}),$$

where $l = \frac{x-m}{s}$; m is the most probable value of the energy loss per centimeter. The mean energy loss by MIP (minimum ionizing particle) of 5.63 MeV/cm was used for calibration.

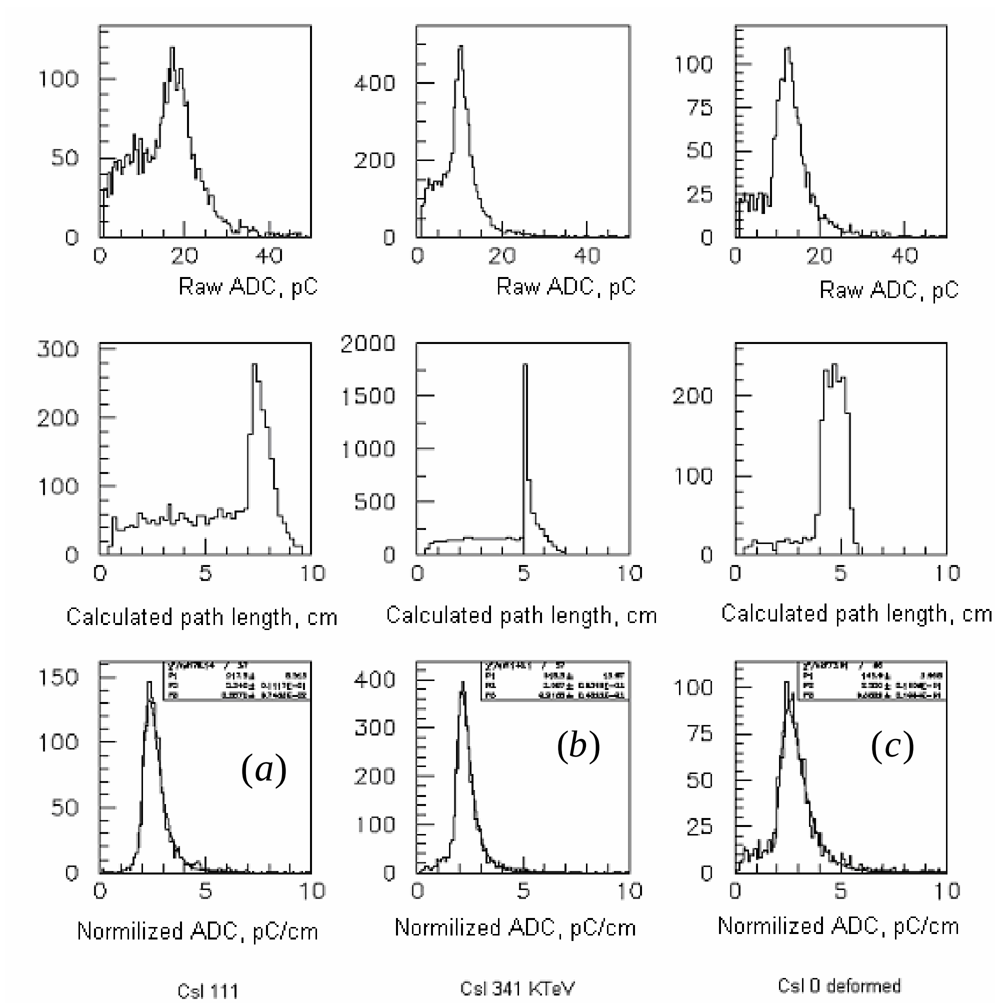

Fig. 4.14 Distribution of the raw charge (upper figures), calcula ted path length (middle) and normalized value (down) for each type of CsI crystal: main 7x7 cm (a), KTeV - 5x5 cm (b) and peripheral crystals (c).

Fig.4. 15 (a) shows the distribution of the gain factors obtained by cosmic muons. The ratio of s over the mean is presented in Fig.415 (b). In this way, we considered the cosmic track as a 2-dimensinal track that inserted some ambiguity in the path-length calculations.

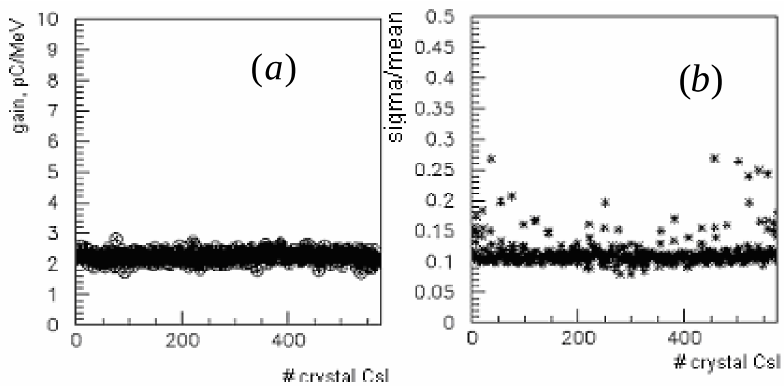

Fig. 4.15 Gain distribution (a) and s -over-mean (b) for all CsI crystals.

4.3.2 Calibration by punch-through muons

Another method to calibrate the CsI calorimeter is to use punch-through muons [43]. When the beam shutter is closed in the neutral beam line, widely distributed muons come to the K0 experimental area and hit the CsI calorimeter uniformly. The trigger $N_{cluster}$ =1 was used for this data taking. We selected an event where only one crystal had an energy deposit, as shown Fig. 4.16. For inner KTeV crystals, we also required the absence of an energy deposit in CC03. The muon deposits an energy of 169 MeV in the KEK crystals (30 cm long) and 281 MeV in the KTeV crystals (50 cm long).

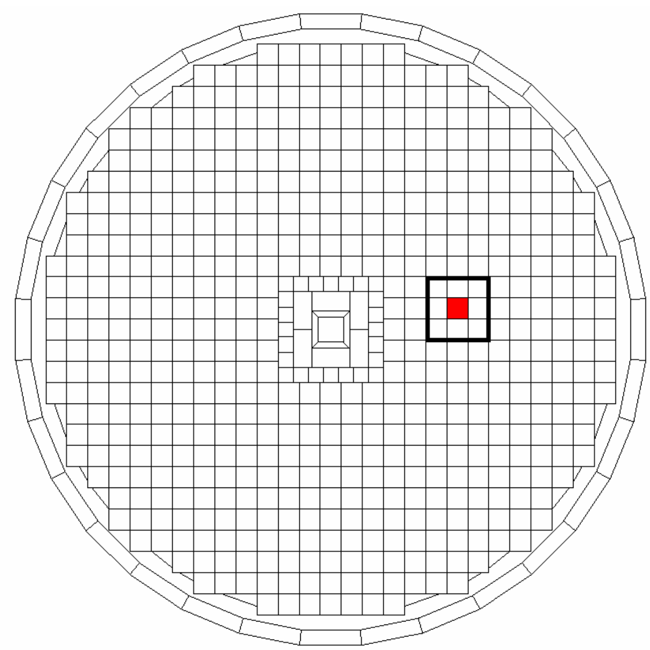

Fig 4.16 Example of a muon event in the CsI calorimeter.

Fig. 4.17 shows the charge spectrum for the main KEK, peripheral and KTeV crystals. Even for the edge (KTeV and peripheral) crystals, the MIP peak can be distinguished. The tails below the MIP peak (Fig. 4.17 b,c) come from muons that pass through only a part of the crystal, and escape through the lateral side. It is still possible to bit the muon peak for the edge crystals. The gain factors were calculated by normalizing the peak position to the MIP energy deposit.

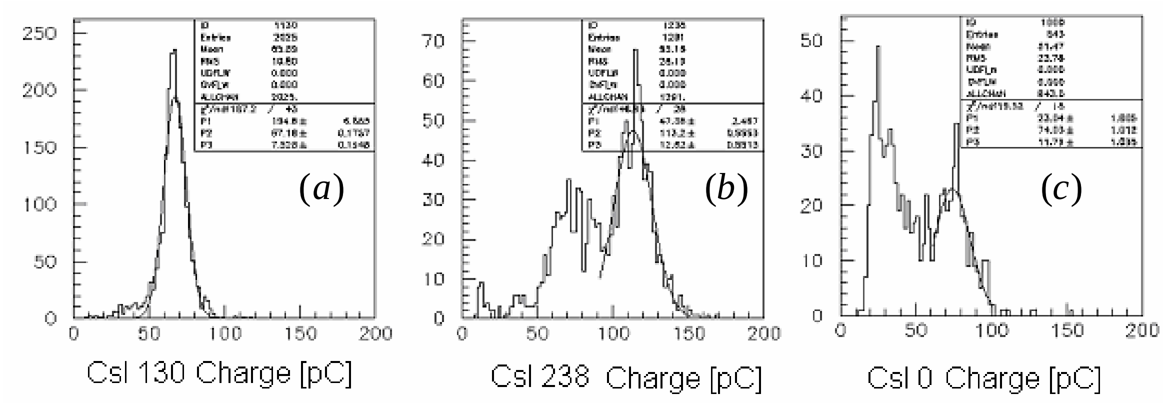

Fig. 4.17 Charge spectrum of the muon beam for the main KEK (a), KTeV (b), and peripheral (c) crystals.

Fig. 4.18 shows the distribution of the gain factors and the relative width of the muon peaks (ratio of s -over mean).

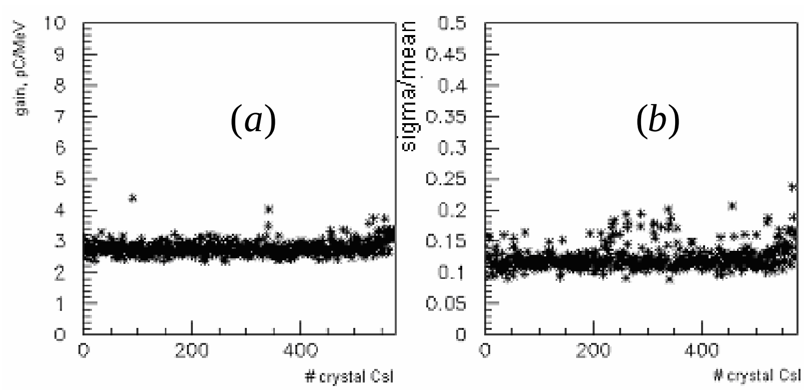

Fig. 4.18 Gain distribution (a) and s -over-mean (b) for CsI crystals.

4.3.3 Comparison of the gain factors obtained by cosmic muons and punch-trough muons

We used cosmic and punch-through muons for CsI calibration. Both of them are muons, and we assumed the MIP energy deposit. Since two sources were different in the path length and the incident direction, it was important to compare the results.

Fig. 4.19 shows the correlation between two gain constants. It shows a good agreement between them within a few% level [43].

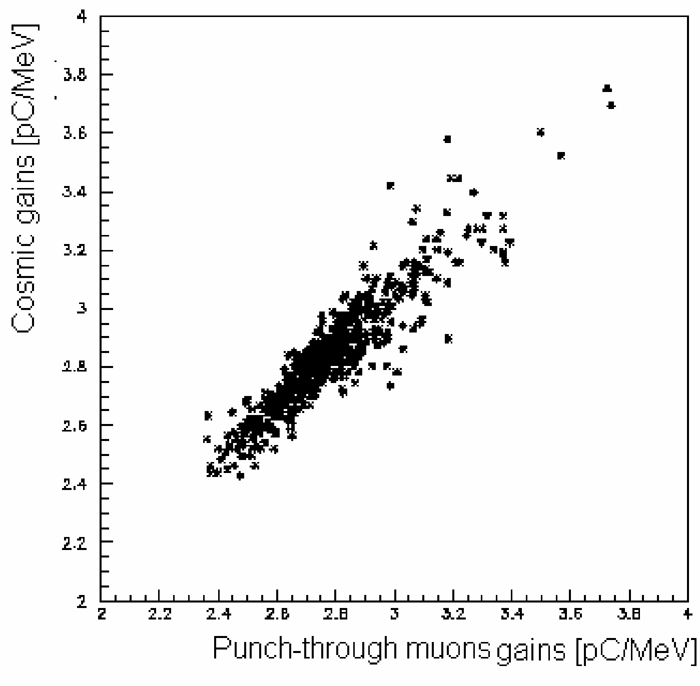

Fig. 4.19. Correlation between the gain factors obtained by cosmic and punch-through muons.

4.3.4 Calibration by p^0's produced on an aluminum target

The CsI calorimeter is an electromagnetic calorimeter that has a role to measure the energy and hit position of a g. In calibration using muons we assumed the mean energy deposit in CsI as that of MIP. Since the momentum distributions of cosmic and punch-through muons are not well known, a systematic error might exist in the absolute gain factors. Although we confirmed an agreement between the results with the muon and the electron beam within 5% in the test experiment, T510, it was done only for several crystals. In order to make an absolute calibration for g, we carried out special runs by inserting a 5 mm-thick aluminum target in the detector [43], as shown in Fig. 4. 20.

In this setup we know the exact vertex point of $p^0 \to gg$, which allows us to reconstruct the $g\,g$ invariant mass.

In Fig 4.21, the spectrum of the reconstructed invariant mass of $2g$ is shown. In this reconstruction we used the gain parameter obtained by the cosmic-muon calibration. The peaks of p^0 and h are clearly seen. However, the positions of the peaks are shifted: p^0 mass is 126MeV/c^2 instead of 135 MeV/c^2 and h mass is 508 MeV/c^2 instead of 547 MeV/c^2.

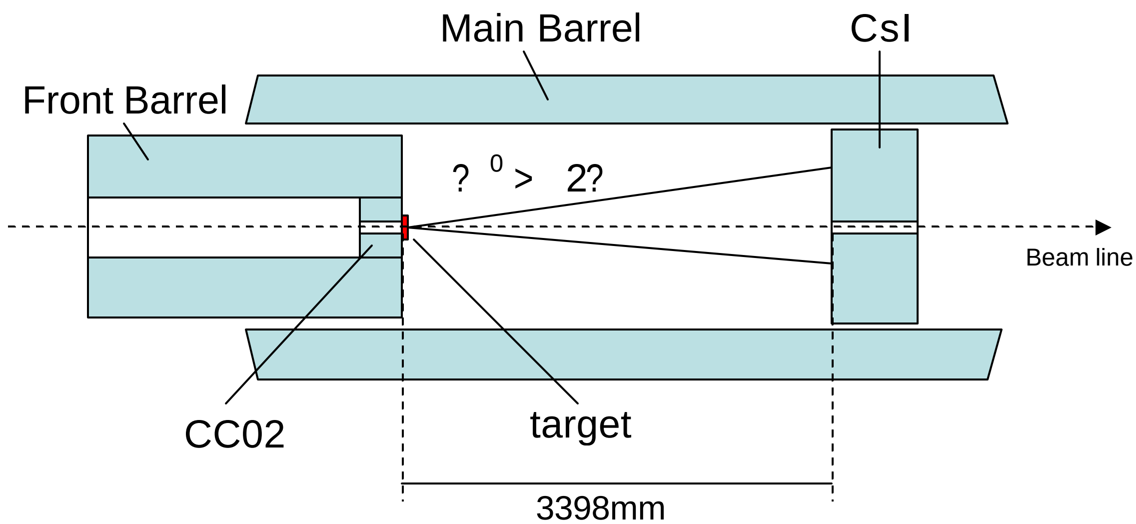

Fig. 4.20. Layout of the CsI calibration by p^{0}'s produced on the aluminum target hit by a neutron. The target is inserted at the beginning of the K_L^0 decay volume.

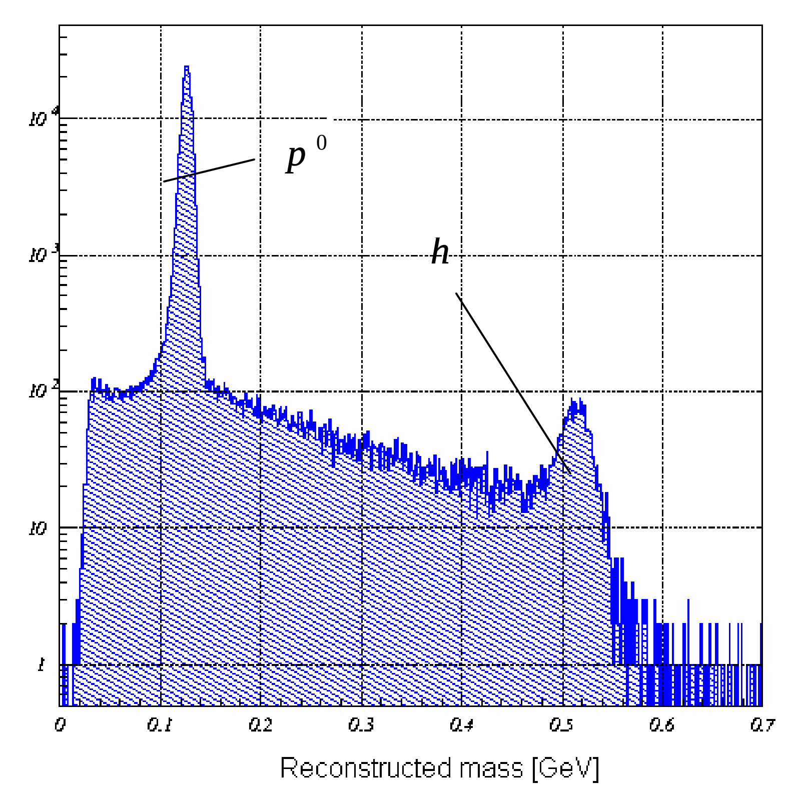

Fig. 4.21. Distribution of the reconstructed mass of *gg* from the aluminum target hit by the neutrons.

At first, we tried to reduce the background and to improve the signal-to-noise ratio.

- If the distance between g's is small, then the clusters start to overlap with each other, which leads to an overestimation of the g energy and an incorrect estimation of the hit position. As shown in Fig. 4.22, there is a correlation between the reconstructed mass and distance between g's. A cut of events with the distance less than 30 cm helps to reduce the background.
- As sown in Fig 4.23, there is also a correlation between the reconstructed mass and the energy ratio of the two g's (E_1/E_2, where $E_1 > E_2$). The low-mass background mostly comes from events with unbalanced energies. We applied a cut of $E_1/E_2 < 5$.
- One more source of the background is other decay modes, such as $2g$ hitting the CsI calorimeter and other g's escaping to the veto system. In order to reduce this background, the main barrel was applied as a veto. In Fig 4.24, the reconstructed mass of $2g$ under various veto thresholds of the main barrel is shown. Although a tight cut of 1MeV is effective to reduce the background, we set a cut point at 5 MeV to keep the acceptance.

Finally in Fig. 4.25, the reconstructed mass spectrum after cuts is shown. The signal-to-noise ratio of the p^0 peak is improved by a factor of 2.5.

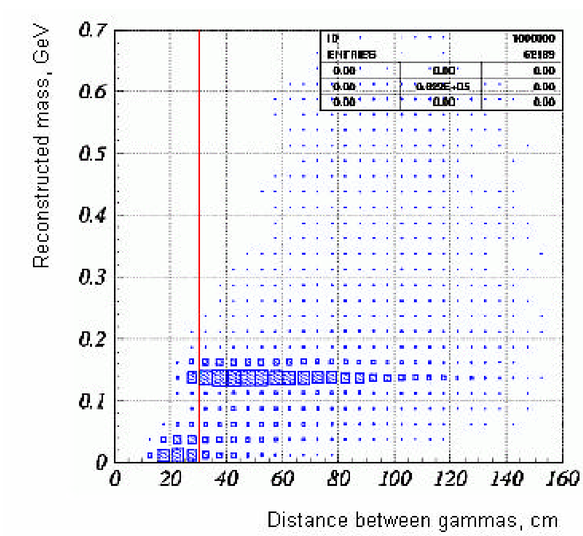

Fig. 4.22. Reconstructed mass of $2g$ vs. distance between gs.

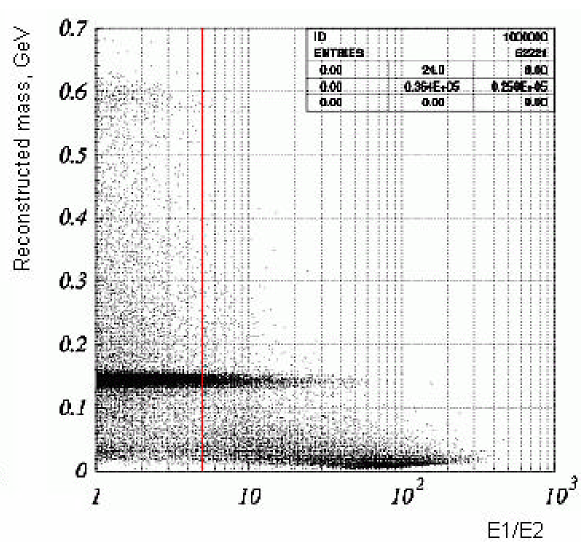

Fig. 4.23. Reconstructed mass of $2g$ vs. the energy ratio of gs.

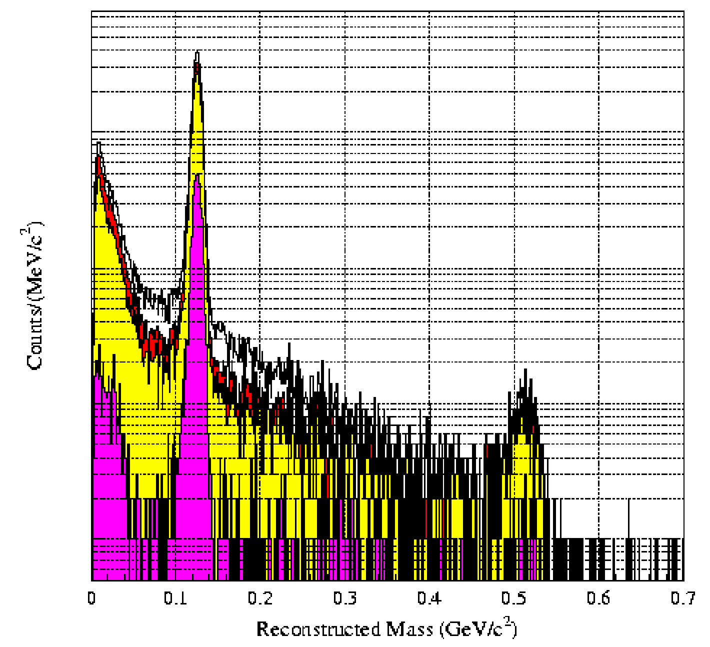

Fig. 4.24. Distribution of the reconstructed mass of 2*g* under various veto-cut conditions of the main barrel.

WHITE – raw distribution
RED – 10 MeV threshold
YELLOW – 5 MeV threshold
PINK – 1 MeV threshold

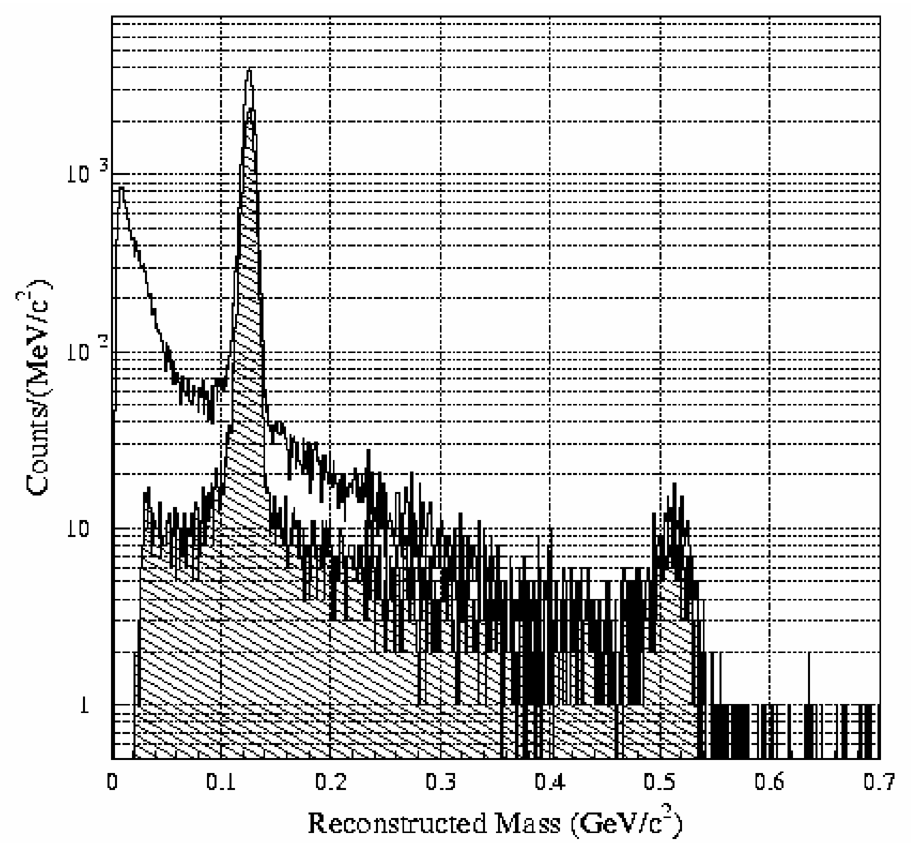

Fig.4.25 Distribution of the reconstructed mass of 2*g* before (blank histogram) and after cuts (filled histogram). The noise-to-signal ratio decreased from 2.2% to 0.9% in the p^0 mass region.

Then, an iteration process was started using the clean data. At the beginning, the gain constants obtained from cosmic muons were the initial values of an iteration. Then, for the n-th crystal we selected those events of which one g cluster had a local maximum in this crystal, and calculated the invariant mass of $g\,g$ as

$$M^n_{gg} = \sqrt{2 \cdot E_n E(1 - \cos q)},$$

where E_n is the energy of a g whose local maximum is in the n-th crystal, E is the energy of the second g and q is the angle between 2 gs.

After processing all data, the correction factor for the n-th crystal was calculated as the ratio M_p / M^n_{gg}, where M_p is the true p^0 mass. After the gain factors for all crystals were updated, the next iteration was started. The iteration process was repeated 5 times.

The distribution of the reconstructed mass after the iterations is shown in Fig 4.26. The mass of p^0 moved to its correct position and s was reduced. Table 4.1 gives the parameters of p^0 and h mesons before and after the iteration process. The resolution of the p^0 and h masses were improved by 28% and 45%, respectively.

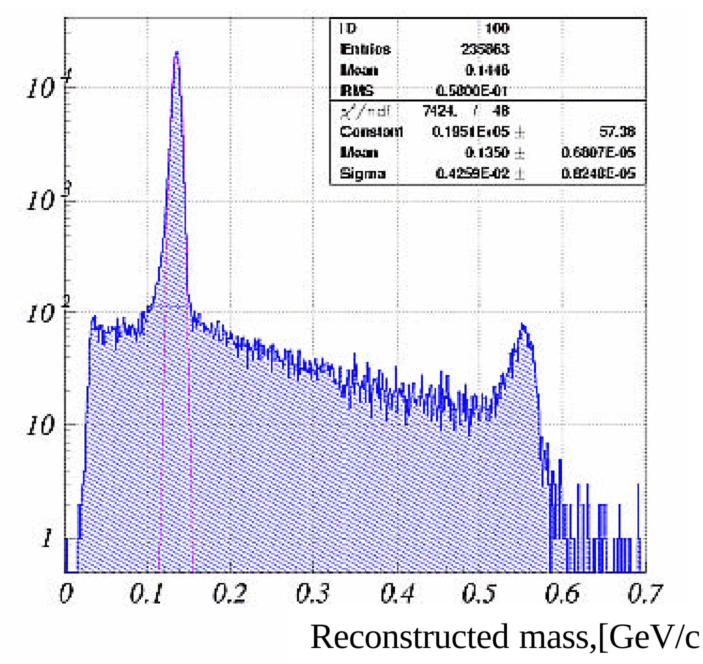

Fig. 4.26. Distribution of the reconstructed mass after the iteration process.

Table 4.1. Parameters of the π^0 and η -mesons before and after the iteration process.

	Before iteration	After iteration	PDG
π^0 mass [MeV/c^2]	126	135	135
η mass [MeV/c^2]	508	548	547.3
Mass resolution of π^0 [MeV/c^2]	4.81	4.27	
Mass resolution of η [MeV/c^2]	19.1	13.5	

Fig.4.27 shows the distribution of the ratio of the gain factors before and after the iteration process. The crystals located in the outside and inner side (KTeV crystals) regions of the CsI calorimeter were not corrected because of boundary effects in the γ energy and position reconstruction. For them, a more detailed study is required to estimate the shower leakage. This will be done in a future analysis. Now we applied a correction of 7% as a constant shift to the outer crystals, which is a mean value of the correction factor for the inner crystals.

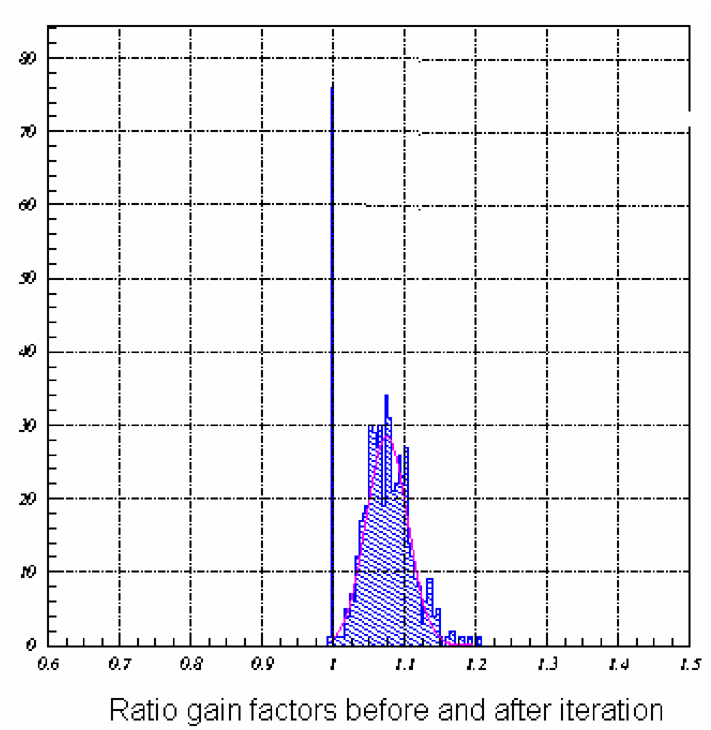

Fig. 4.27. Distribution of the ratio of the gain factors before and after iterations. The events with the ratio = 1 correspond to the edge (outside peripheral and inner KTeV) crystals, which were not corrected by the iteration process.

4.4 Energy calibration of the veto detectors

4.4.1 CC03 and Sandwich counters

CC03 is a beam counter built in the beam hole of the CsI calorimeter. The sandwich counters cover holes on the outer periphery of the calorimeter because the shape of the holes doesn't allow us to make such crystals. Since the direction of the scintillator layers of CC03 and Sandwich counters are parallel to the beam, it is difficult to calibrate them by the beam. A calibration was done by cosmic muons after these detectors were integrated into the frame of the CsI calorimeter.

For the calibration, the path length of the cosmic muon track through scintillator layers was calculated using detailed information about the position of each scintillator layer. Then, by normalizing by the path length, the mean charge deposited per 1 cm of scintillator was calculated. Fig. 4.28 shows the raw charge (a), the path length in the scintillator (b) and the normalized charge (c) distributions for one module of CC03. The path length has a peak near 3.5 cm, which corresponds to the muons perpendicularly passing through 7 scintillator layers of 0.5 cm thick.

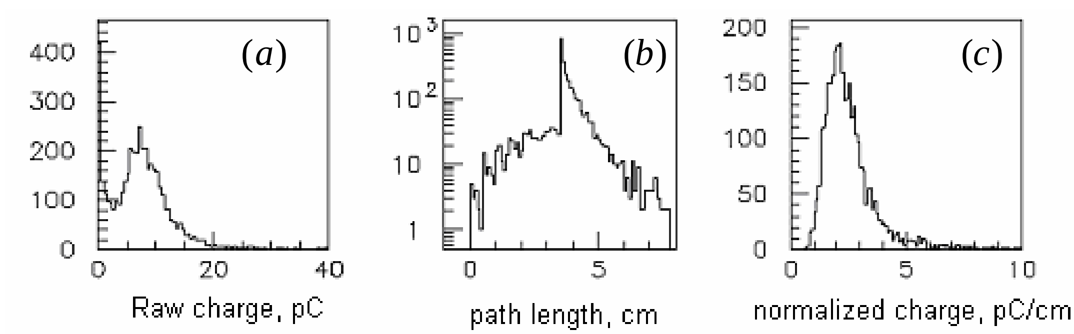

Fig. 4.28 Distribution of the raw charge (a), the reconstructed path length in scintillator (b) and the charge spectrum normalized to the path length (c) for channel #1 of CC03

Since the lead/scintillator sandwich counters are small and the number of scintillator layers is also as small as 2-3, the situation is somewhat more complicated due to poor statistics. However, even here there is a correlation between charge deposited and the calculated path length for all 3 types of sandwiches, which differ by size and the number of scintillator layers (Fig. 4.29).

The normalized spectra show a clear peak for all modules. The distribution was fitted by the Gaussian function. Assuming that the mean energy loss per centimeter in the scintillator is 1.99MeV, as same as MIP, the gain factor was calculated.

This method allows us to calibrate the Sandwich counters with 15% accuracy. Although the accuracy is poor, it is not necessary to be very accurate for them, because they do not participate in *g* reconstruction, due to a boundary problem of shower leakage from the calorimeter.

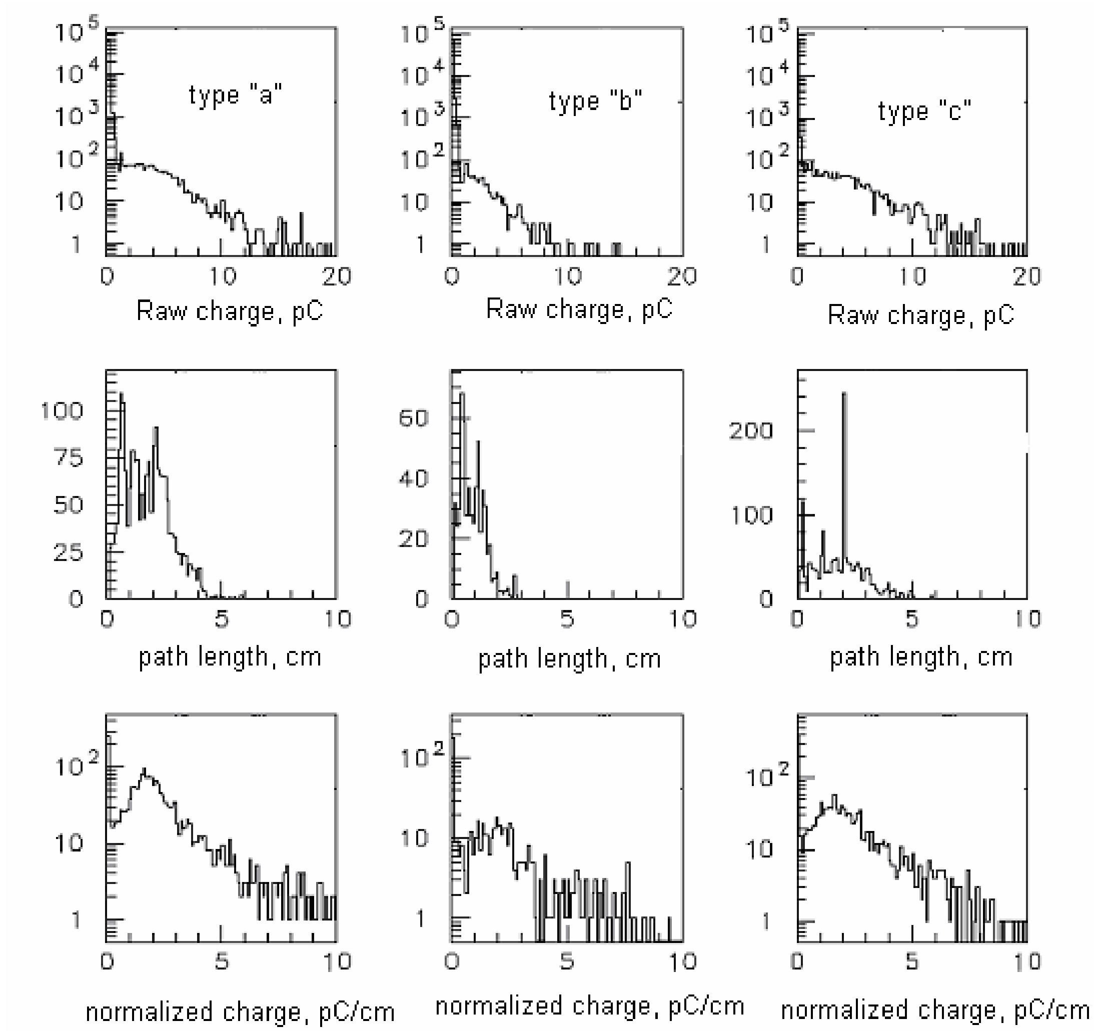

Fig. 4. 29 Distribution of the raw charge spectrum (upper figures), the calculated path length (middle) and the normalized charge spectrum (down) for each type of sandwic h counter. The big peaks in the path-length spectrum correspond to the crossing of muons parallel to the scintillator layers.

4.4.2 The collar counters CC02,CC04,CC05,CC06 and CC07

The collar counters (CC02, CC04, CC05) are sandwich (lead-scintillator) counters with scintillator layers perpendicular to the beam direction. CC06 and CC07 are lead-glass detectors. Therefore, a punch-through muon beam was used for the calibration.

The distance between CC02 and CC04 is about 4 meters, and they were used for triggering in order to clarify the muon track events during the analysis. Under these requirements, the track of the muon was considered to be parallel to the beam, which was perpendicular to the scintillator layers.

Counters CC06 and CC07 are larger than CC04 and CC05, and thus, in addition to the above events, we used muon events triggered by the CsI calorimeter. We required that only one CsI crystal ha d an energy deposit.

Fig. 4.30 shows the typical muon spectra for the collar counters. C lean MIP peaks are observed. The high voltage was adjusted and the gain factors were obtained, as listed in Table 4.2.

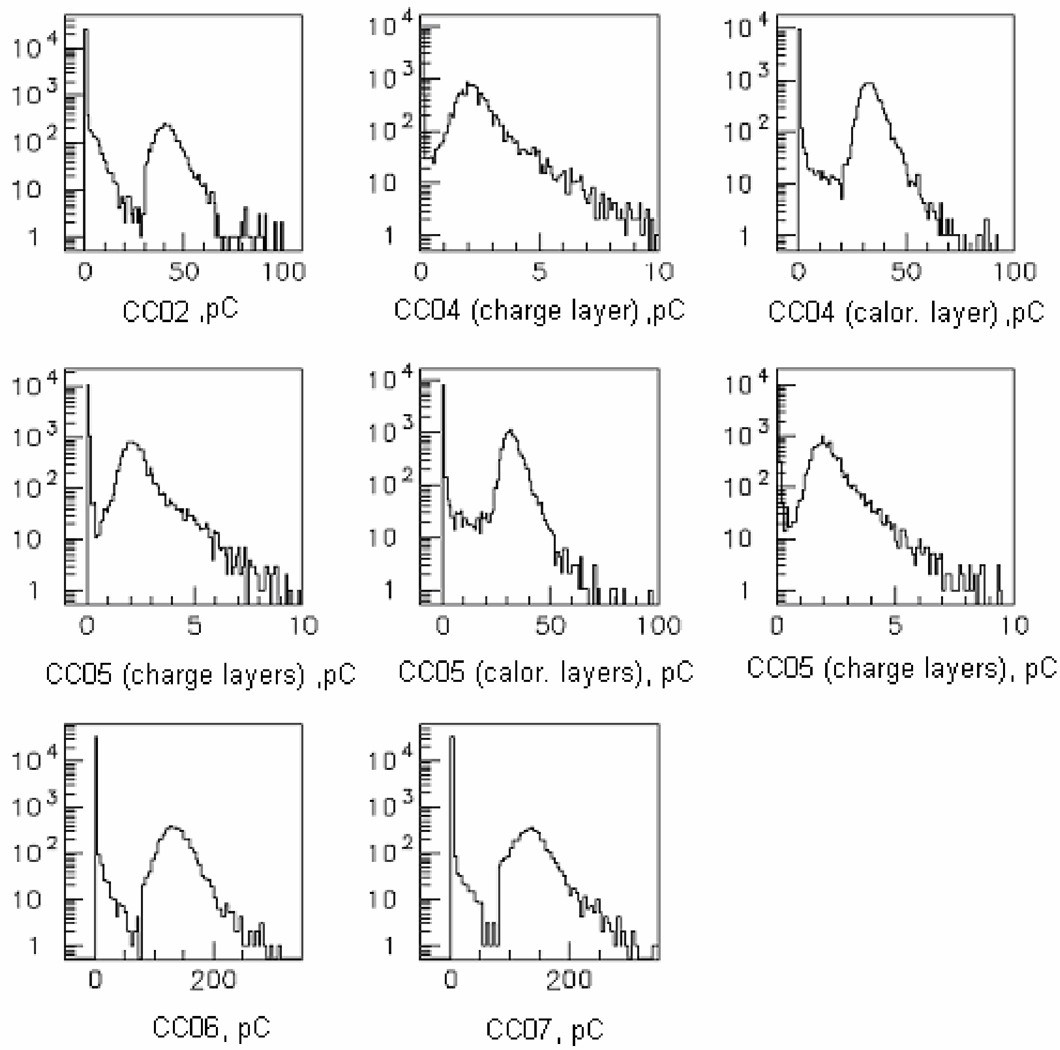

Fig. 4.30. Typical charge distribution of the collar counters for the muon beam.

Table 4.2 Basic parameters of the collar counters and gain factors.

counter	type	Number of scintillator layers	Energy deposit by MIP	Gain factor
CC02	Lead-scintillator	42	21 MeV	0.5 pC/MeV
CC04 charge veto	Scintillator	2	1 MeV	1.5 pC/MeV
CC04 calorimeter	Lead-scintillator	32	16 MeV	0.5 pC/MeV
CC05 front charge veto	Scintillator	2	1 MeV	1.5 pC/MeV
CC05 calorimeter	Lead-scintillator	30	15 MeV	0.5 pC/MeV
CC05 back charge veto	Scintillator	2	1 MeV	1.5 pC/MeV
CC06	Lead glass	15 cm	144 MeV	0.66 pC/MeV
CC07	Lead glass	15 cm	144 MeV	0.66 pC/MeV

4.4.3 Main charge veto

The main charge veto consists of 32 bent pieces of scintillator (outer part) and 4 pieces of scintillator around the beam (inner part). Therefore, the calibration methods are different. (Fig. 4.31).

Some part of the outer channels is perpendicular to the beam line. The muon beam was used for its calibration. The muon events were selected by requiring the energy deposit to be only in one CsI crystal. The selection of the position of the crystal in the radial direction along the charge veto piece allows us to see the attenuation of the signal (Fig. 4.32). At a distance of about 60 cm from the beam axis, there is a minimum; thus during the calibration we used the crystals located at 50-60cm distance from the beam axis for selecting the muon track parallel to the beam axis, which is perpendicular to the scintillator plate.

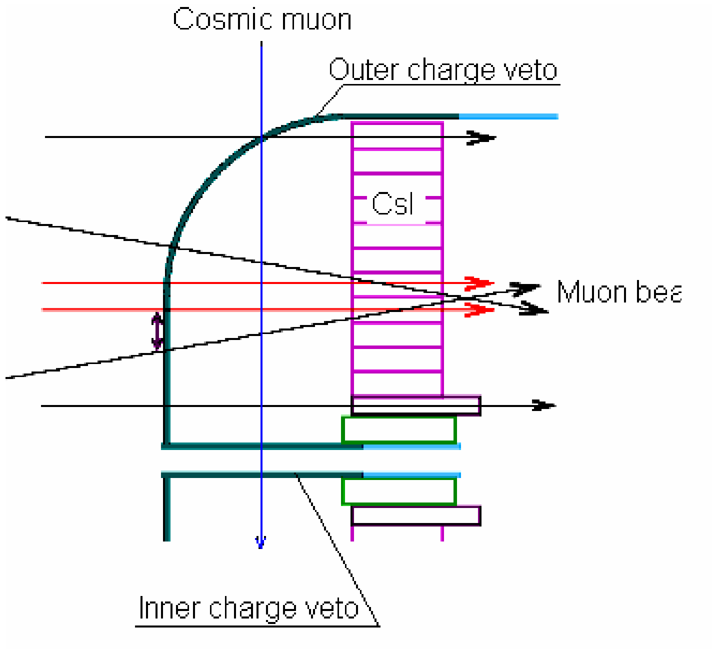

Fig. 4.31. Schematic view of the calibration process for the outer charge veto by muons (red lines) and for the inner - charge veto by cosmic (blue line) rays.

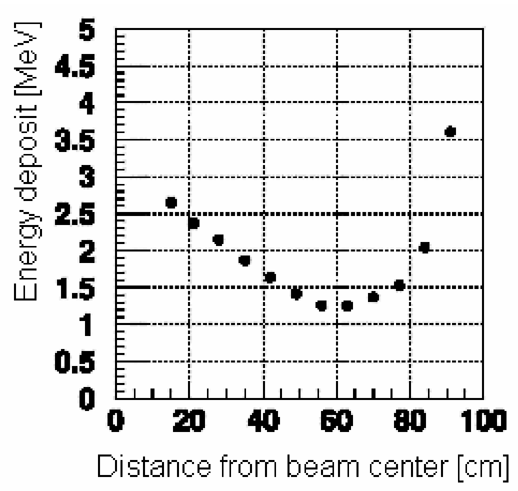

Fig. 4.32. Attenuation curve for the outer - charge veto.

Because the inner pieces are located parallel to the beam, we used cosmic muons for the calibration. The events were selected by a coincidence of the outer and inner charge veto. In Fig 4.33, the typical spectrums for the outer and inner channels are shown. In both cases, the MIP peak is clean and was used for the calibration.

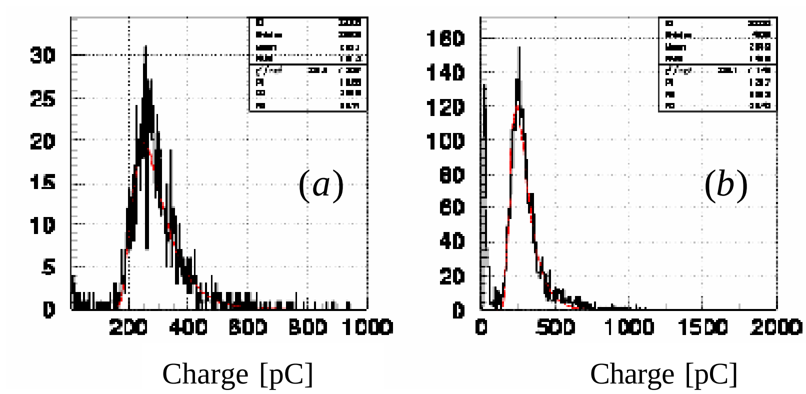

Fig. 4.33. Typical distributions of the output charge in the outer charge veto for punch-through muons (a) and in the inner charge veto for cosmic (b) muons.

4.4.4 Main barrel and barrel charge veto

For calibrating of the main barrel and barrel charge veto, cosmic muons were used. In the online stage, the coincidence of the opposite main barrel clusters was used as a trigger (Fig. 4.34). In the offline processing stage for cleaning events, we required the coincidence of opposite modules with no energy deposit in the neighborhood modules. Each MBR module has two PMT's, and thus the time difference can be used for hit position measurement. Also, the ratio of the output charges from both ends has a correlation with the hit position due to attenuation, as shown in Fig. 4.35. Here, the position zero corresponds to the center of the module.

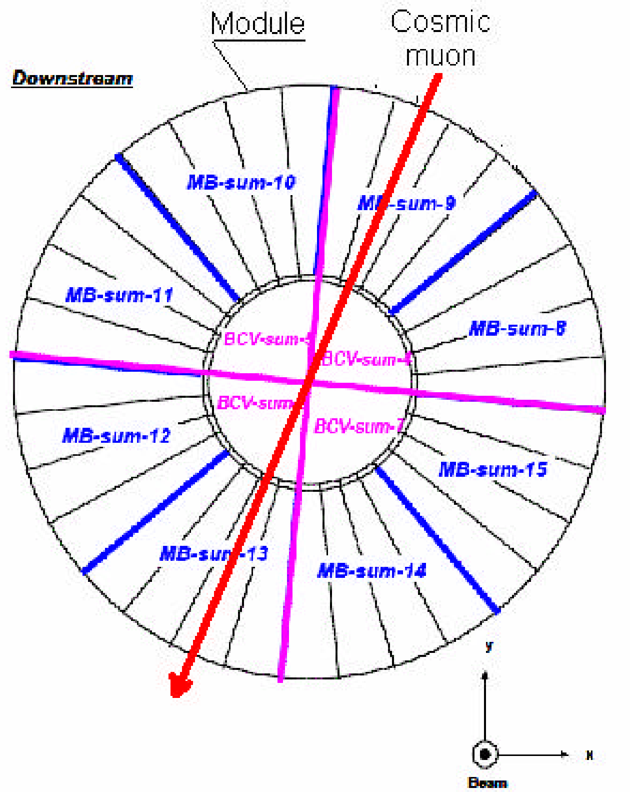

Fig. 4.34. Trigger scheme for calibrating the MBR by cosmic muons

For the calibration, we required the muon track to pass through the center of both modules using timing information.

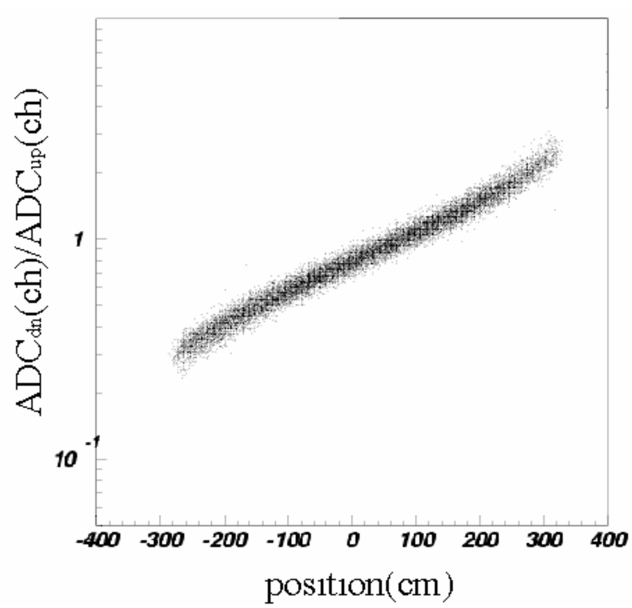

Fig. 4.35. Correlation of the ratio of output charges from both ends and the hit position for the MBR module. Zero corresponds to center of the module.

Fig. 4.36 shows the typical spectrum for the main barrel channel and the barrel charge veto channel. For both detectors, the cosmic peak can be clearly seen. The distributions of the gain factors for all channels are presented in Fig. 4.37. The accuracy of calibration is within 2 % for the main barrel and 5% for the barrel charge veto.

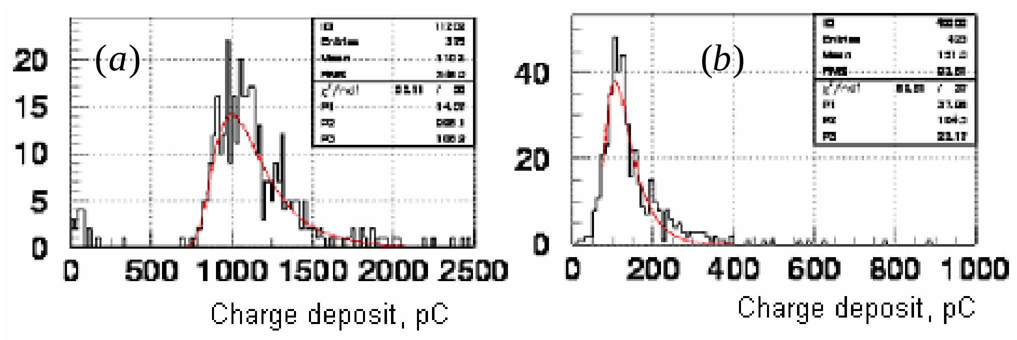

Fig. 4.36. Typical charge spectra of the cosmic muons for the main barrel (a) and for the barrel charge veto (b).

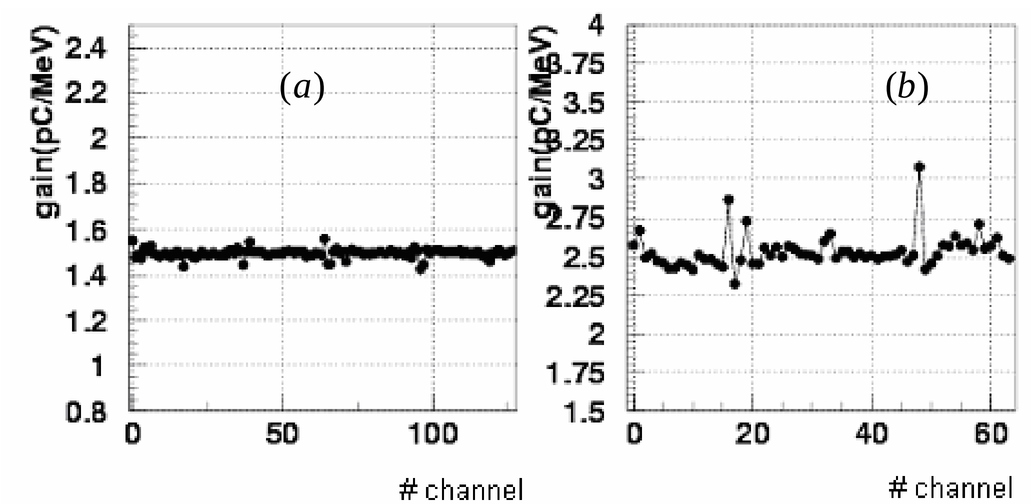

Fig. 4.37. Distributions of the gain factors for the main barrel (a) and for the barrel charge veto (b) detectors.

4.4.5 Beam anti (BA) and beam charge veto

The beam anti is a difficult detector from the view point of gain calibration. A neutral beam (neutrons and g's) hits it directly, and the gain drifts under beam loading. The effect can be measured by the LED gain monitor system (see Section 4.2).

For calibration we took the muon beam data triggered by the BA itself. The MIP peak for the beam hole charge veto, scintillator and quartz channel of BA are shown in Figs. 4.38 and

4.39. After calibration, in order to eliminate the gain drift effect, we applied a LED correction (see section 4.2).

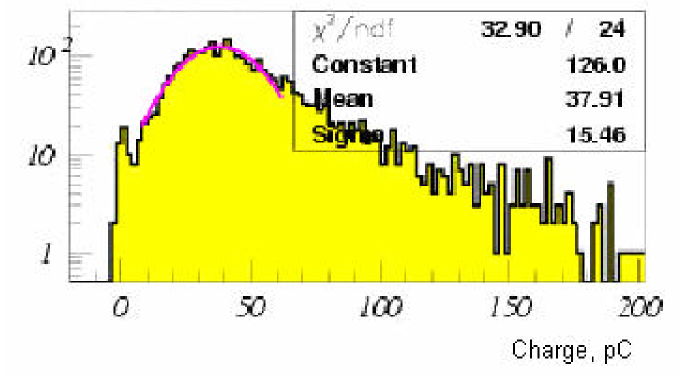

Fig. 4.38. MIP peak for the beam hole charge veto channel.

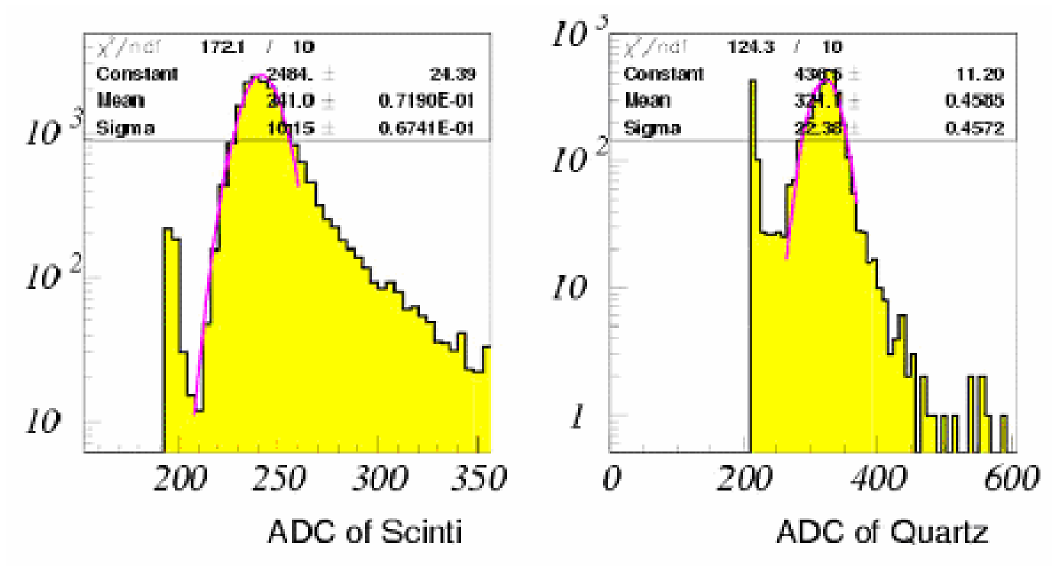

Fig. 4.39. Muon peak of the scintillator channel and that of the quartz channel of the beam anti.

4.5 Timing calibration of the CsI calorimeter

Concerning the CsI hit timing calibration [43], we have to take the following two usages of the timing into account:

- The CsI calorimeter is used for making a trigger signal.
- We need to measure the *g* hit timing accurately enough to reject accidental backgrounds.

Fig 4.40 shows a general scheme of the electronics concerning the time signal propagation. The signals from the PMT come to the Amp-Discriminator (Amp/Disc) modules, where 8 signals are bound (CsI hardware cluster) in a sum output and sent to a trigger logic through the discriminator with a threshold of 40 MeV. The trigger logic sends a gate signal to the ADC to start a charge reading from the PMT and to the TDC for starting the time counting. Each individual signal passes through a discriminator in the Amp/Disc card with a 1MeV threshold, and through a 90 m twisted-pair cable delay; it stops the time counting at TDC.

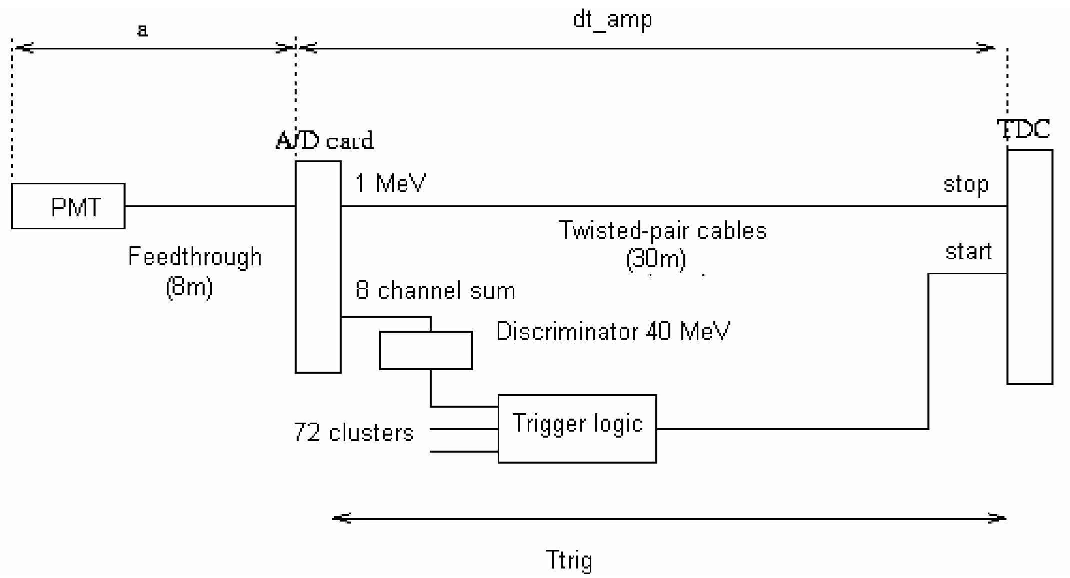

Fig. 4.40. Scheme of signal propagation from the PMT to the TDC.

Our main trigger is generated by the conditions that the number of CsI clusters is larger than or equal to two. Also, the trigger timing depends on the crystals in the cluster that get hits. If there are different delays in the region from the PMT to the Amp/Disc module, the trigger timing will be spread. Therefore, trimming of the cables before the Amp/Disc modules is needed to eliminate any differences in theses delays.

Another point concerns the signal that goes from the PMT to the TDC with a long delay cable. The differences in the cable length and differences in the delays in the Amp/Disc module, itself, make the distribution of the g hit timing wider. These delays should be measured and used as a correction factor in the data-processing stage.

The overall problem of measuring of the delays in the PMT-TDC line can be divided into 2 parts: from the PMT to the Amp/Disc module ("a" in Fig 4.40), and from the Amp/Disc module to the TDC ("td_amp" in Fig 4.40). The second part can be calibrated by a direct measurement by a pulser. This was also done at the beginning of the data taking. The delays from the PMT to the Amp/Disc module can not be measured directly. Therefore, a calibration method using cosmic muons passing through the CsI calorimeter was developed.

The cosmic muon track was reconstructed in the CsI calorimeter, and then information about the timing of the crystals in a track was collected. For such events, the TDC_i value for the i^{th} crystal and for the j^{th} event can be descried as

$$TDC^j{}_i = Ttrig^j + a_i + dt\_amp_i + TOF^j{}_i + TOLP^j{}_i \,, \qquad (4.1)$$

where $Ttrig^j$, trigger timing;

a_i, delay from PMT to Amp/Disc module;

dt_amp_i, delay from the Amp/Disc module to the TDC;

$TOF_i{}^j$, time-of-flight correction; and

$TOLP_i{}^j$, time-of-light-propagation in the crystal to the PMT.

Inside one event, the trigger timing is the same, but it varies event by event. Therefore, only the TDC difference of any two channels for each event has any meaning. The delays a_i and dt_amp_i are constant for each channel. The dt_amp_i delays were measured by a pulser. The a_i delays were calculated in the iteration process. A difference of a_i leads to a trigger timing variation. The goal was to estimate these delays and to decrease the difference by trimming the signal cables from the PMT.

After cosmic–ray track reconstruction in the CsI calorimeter, it is possible to calculate the delay coming from the time of flight of the cosmic muon between CsI crystals. The intersections of the track with the cells were calculated, and the TOF_i from the upper-most crystal in a track to that crystal could be estimated. The velocity of the cosmic muon was assumed to be 30cm/ns (speed of light). The $TOLP_i$ can also be estimated from the parameters of the track (see below).

Then, by applying the corrections to the TDC of an individual channel, the trigger timing can be estimated as

$$Ttrig^j = TDC^j{}_i - a_i - dt\_amp_i - TOF^j{}_i - TOLP_i^j \,. \qquad (4.2)$$

We can derive the trigger timing, $Ttrig^j$, from the information of each crystal in a track. For a given event, $Ttrig^j$ must be the same for all channels. A discrepancy comes from errors estimating the corrections and poorly calibrated a_i delays. Thus $Ttrig^j$ varies from crystal to crystal. Assuming that our corrections are perfect we moved all discrepancy to the correction of the a_i delays.

The mean value was used for an estimation of the true trigger timing,

$$Ttrig^{j^*} = \frac{1}{N}\sum_{1}^{N} Ttrig_i^j = \frac{1}{N}\sum_{1}^{N}(TDC_i - a_i - dt\_amp_i - TOF_i - TOLP_i), \quad (4.3)$$

where $Ttrig^{\,j}$ is the trigger timing calculated based on the i^{th} crystal timing.

Then, the correction to a_i delays can be calculated as the difference between the individual trigger timing and the mean values;

$$\Delta a_i = Ttrig_i^j - Ttrig^{j^*} . \quad (4.4)$$

After collecting many events, the new values of the delays, calculated as $a_i^* = a_i + \Delta a_i$, are used for the next step of the iteration.

- In the first step of the iteration, all a_i delays were set to 0, and the $TOLP_i$ correction was not applied. In that case, the long track events were selected. Long track means the cosmic muon passes through a full disc of the CsI calorimeter. Such events can be identified by requiring the first and last crystals in a track to be outer crystals. Here, the slope of the track in the Z-direction is unknown, but is limited by our requirements concerning the long tracks.

- In the second iteration step, only short tracks are selected. A short track means a cosmic muon that hits the front or back surface of the CsI disc, and also leaves it from the front or back surface. In this case, the first and the last crystals in a track are located inside the calorimeter, as shown in Fig. 4.41.

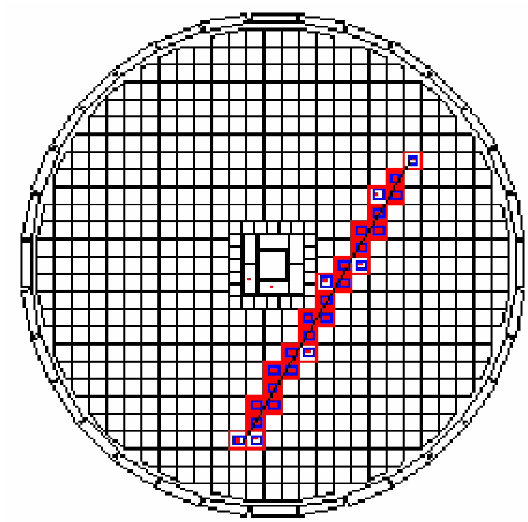

Fig.4.41 The example of the short cosmic ray track in the CsI calorimeter

For this short track, it is possible to estimate the slope of the cosmic track in the Z-direction, since the entrance and the exit points are known. The only one ambiguity is that there are 2 solutions: the muon is incident from the front surface or the back surface of the calorimeter. In order to solve this ambiguity, the time difference between the first and last crystals in a track was estimated. By taking into account the TOF between them, this difference reflects the difference in the light-propagation time in the crystals. Fig 4. 42 shows this distribution. Two peaks correspond to events in which cosmic muons are incident on the front surface (positive time difference) or the back surface (negative one). The peak positions are 3.9 ns and -3.4 ns, correspondingly. This is not consistent with the speed of light in the CsI crystal (16.7 cm/ns or 1.8 ns for 30 cm long crystals). The measured propagation speed of light

(8.2cm/ns) can be considered as an effective speed of light in the CsI crystal, which reflects the longer path length of light propagation, including reflections from the borders of the crystal.

This effective speed of light was used for a light propagation time correction ($TOLP_i$). Fig 4.42 (b) shows the same time difference between the first and the last crystals in a track after the TOLP correction.

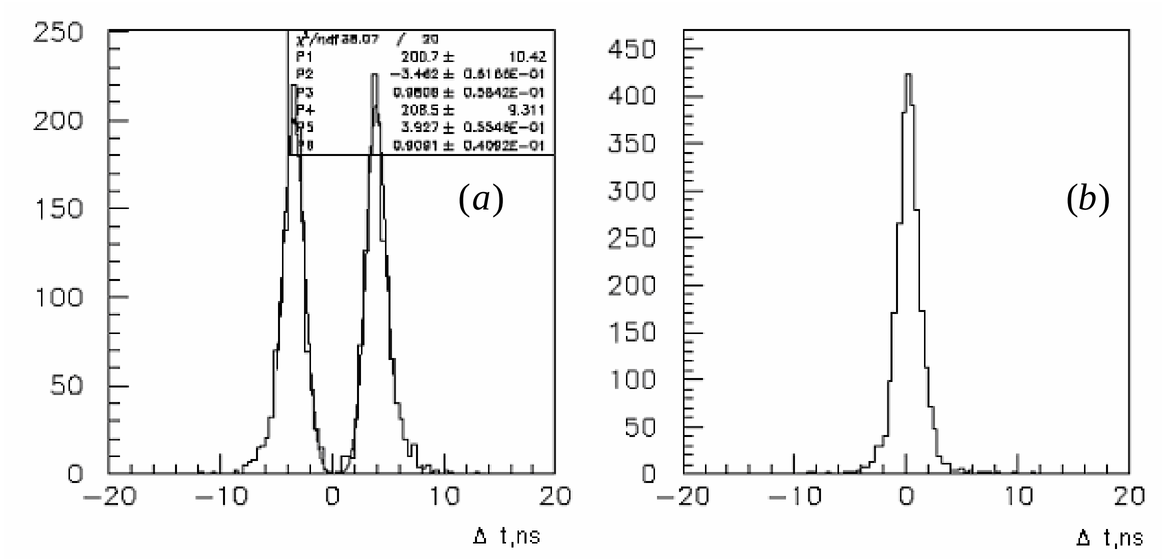

Fig.4.42. Distribution of the time difference between the first and last crystals in a track before (a) and after (b) the TOLP correction. The time-of-flight (TOF) was taken into account.

In the short-track case, we can clearly separate the slopes of the cosmic-ray tracks and reconstruct the 3 dimensional tracks. Then, the $TOLP_i$ correction can be calculated as $TOLP_i = dZ/c_{eff}$ (dZ, distance from intersection point to the PMT; c_{eff} = 8.2 cm/ns, effective speed of light in CsI) and applied for each crystal in a track (Fig. 4.43).

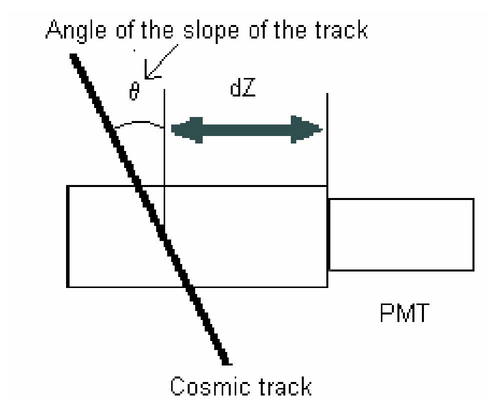

Fig. 4.43. Schematic view of the tracks sloped in the Z direction.

In this step we calculated the corrections (Da_i). Then, the a_i delays were updated and a new iteration step was started.

- In a previous step, we applied the $TOLP_i$ correction only to the inner crystals. The last iteration step has a goal to extend this correction to the outer crystals. For that, the long track events were selected, and, for estimating of the $Ttrig$, only the inner crystals participated. The strategy is to try to estimate the slope of the cosmic-ray track only by using timing information from the inner crystals.

Fig 4.44 shows the distribution of the calculated slope of the track in the Z-direction. The vertical tracks have a larger probability than the slanted ones, and the distribution has a peak at around zero. Two spikes around $\tan\theta = \pm 0.2$ correspond to events where the calculated slope is larger than the maximum allowed slope. In that case, the slope is assumed to be the maximum. There is a clear correlation between the TDC values of the crystals in a track after a time-of-flight correction; the TOLP correction is calculated based on the estimated slope (Fig. 4.45). In this way we can apply the TOLP correction for the outer crystals.

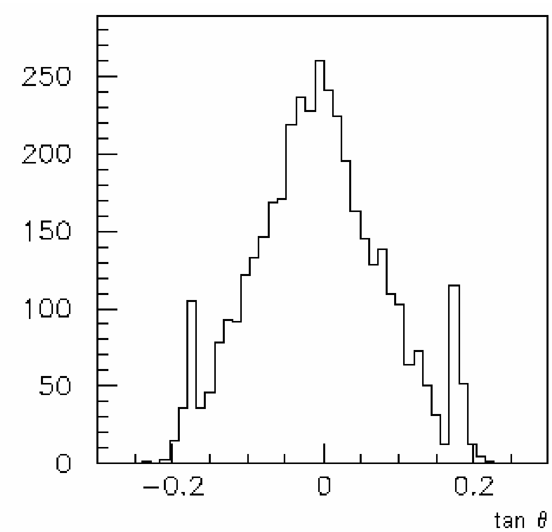

Fig. 4.44. Distribution of the tangent of the slope angle of the long track derived from information of only the inner crystals.

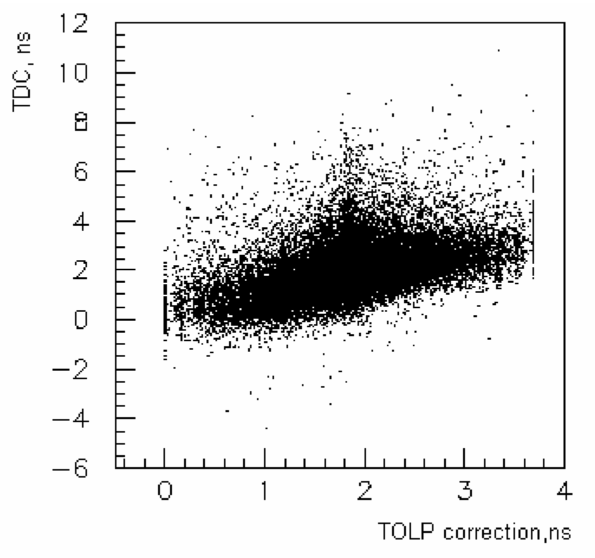

Fig. 4.45. Correlation between the hit timing of the crystals in a track and the TOLP correction.

Fig. 4.46 shows the result of each iteration step. This is the time difference between any two crystals in a track. At the beginning (black histogram) there is a wide distribution with a RMS of 4.8 ns. After the TOF correction (red histogram), the RMS is reduced by more than 2 times. The TOLP correction (blue one) also helps. Finally, after applying a time-walk correction (pink), the RMS becomes 0.8 ns, which reflect the time resolution of the system.

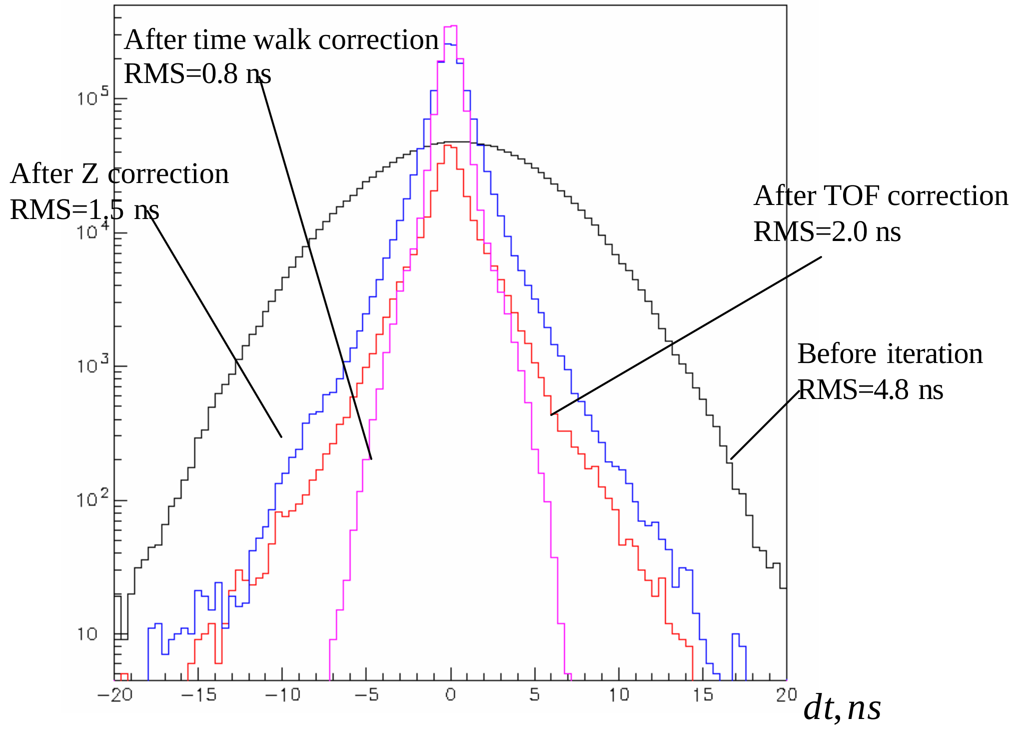

Fig. 4.46. Distribution of the time difference between any 2 crystals in a track before and after various corrections.

Finally, the calculated a_i delays were used for a timing measurement of the K_L^0 decays. Fig 4.47 shows the distribution of the g hit timing for reconstructed $K_L^0 \rightarrow 3p^0$ decays without the a_i correction (a) and with it (b). The s of distribution was improved from 3.1ns to 1.0ns.

The other point that requires a calibration of the delays is related to smearing of the trigger signal. Here, we made a calibration of the delays from the PMT to the Amp/Disc modules, a_i. Fig. 4.48 shows a clear correlation between a_i and the HV settings of the PMT. This means that the main source of the distortion in the time delay comes from the HV setting. The KTeV and corner crystals, which use different types of PMT's, are clearly separated.

In order to eliminate these differences, we made a trimming of the signal cables between the PMT's and the Amp/Disc modules. Fig. 4.49 shows the results of the. We could reach about a $\pm$ 1ns width.

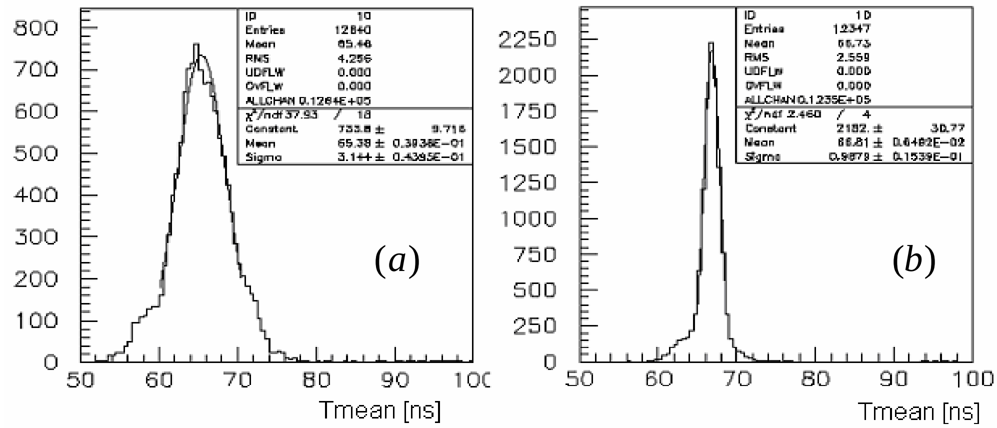

Fig. 4. 47. Distribution of the *g* timing for $K_L^0 \to 3p^0$ decays without the a_i correction (a) and with one (b).

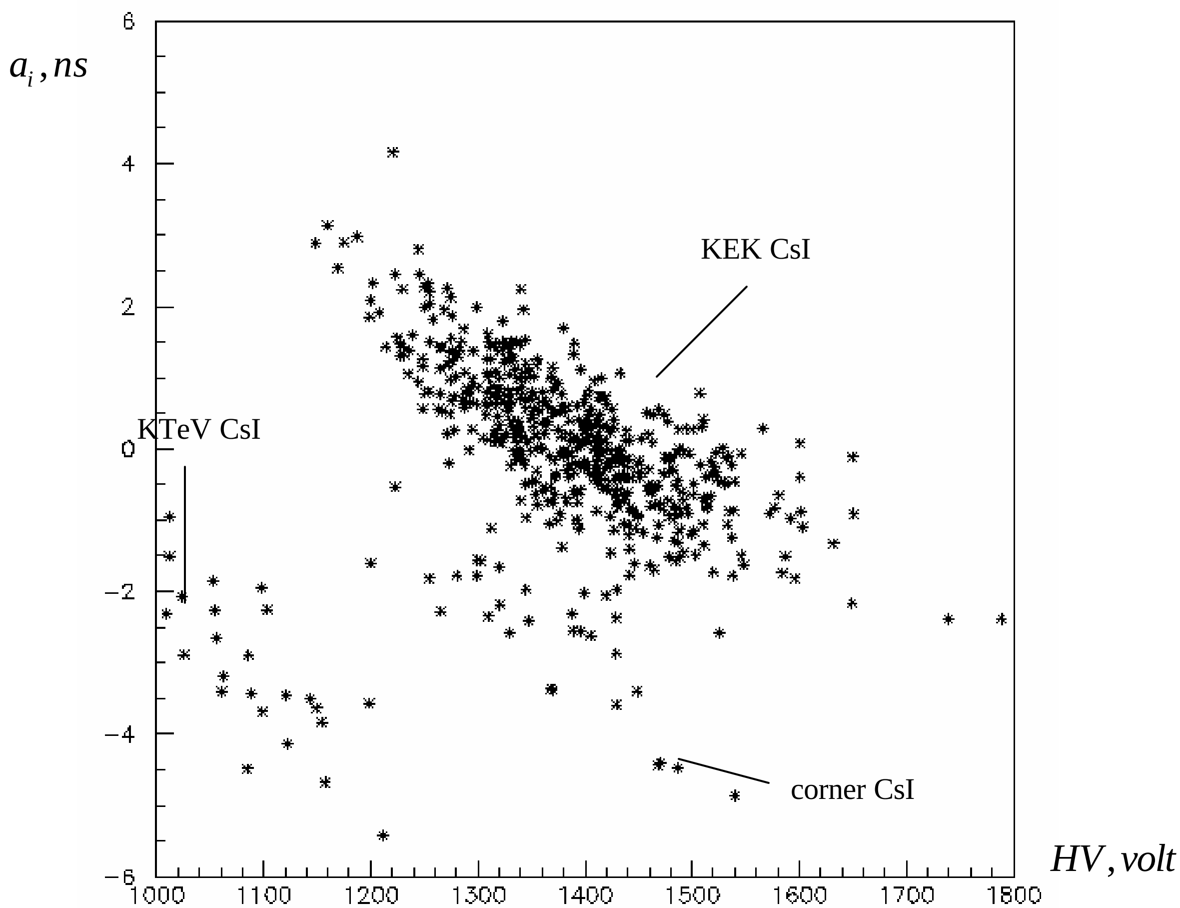

Fig.4. 48. Correlation between a_i and the HV setting of the PMT's.

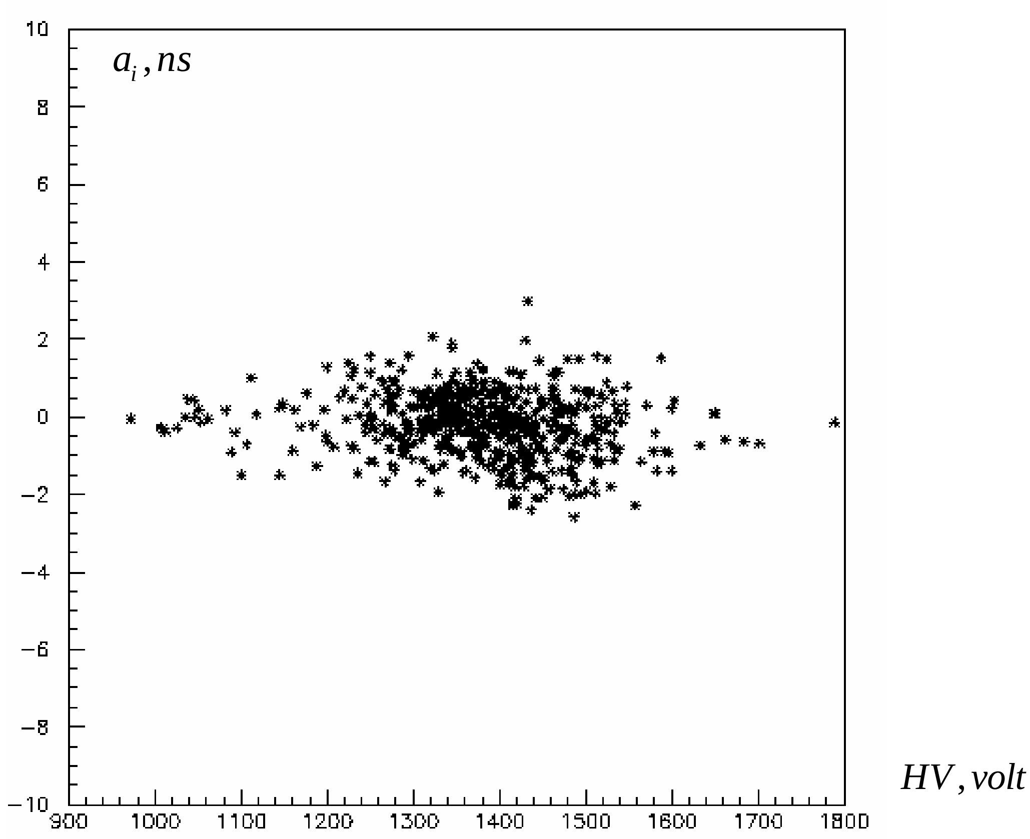

Fig. 4.49. Correlation between a_i and the HV setting of the PMT's after trimming.

Chapter 5

Analysis

5.1 Data skimming

During the run we collected about 6 Tb of physics data. Because this is very large, it was very hard to process these data directly. Also, the data files contained data for all triggers. In order to remove non-physics events, we did a skim of the data. Also, additional cuts for preliminary identification of events were applied to separate the data into streams characterized by the number of g clusters. Then, the $2g$, $4g$, $6g$ streams were used to reconstruct the $K_L^0 \to p^0 v\bar{v}$ and $K_L^0 \to gg$, $K_L^0 \to 2p^0$, $K_L^0 \to 3p^0$ decays, correspondingly. This data skimming saved processing time and reduced the data size of each stream.

During the run we simultaneously collected data with various triggers:

- Pedestal trigger (1Hz)
- Cosmic trigger (~60Hz, during off-spill)
- Xe/LED trigger (~1Hz)
- $N_{\text{cluster}} \geq 2$ – physics trigger (~200Hz)

- CC04 and CC05 coincidence – muon trigger (~10Hz)
- Accidental triggers (~30Hz)

In the first step of skimming, non-physics data were removed from the data files. The contamination was about 20%.

The routine then started to search for clusters of CsI hits. All crystals with an energy deposit of less than 1 MeV were considered to be empty crystals. Neighboring crystals with an energy deposit of more than 1MeV were united into a cluster. The clustering routine then sought the crystal with the biggest energy deposit (local maximum) among neighboring ones in each cluster. An event was rejected if there was a local maximum in the KTeV crystal. For such an event, it was not possible to distinguish a real *g* hit from shower leakage from CC03. Also, in the case of a real hit, some part of the shower could leak into CC03, which resulted in incorrect reconstruction of the *g* energy and hit position. The contamination of such events was about 40% of the total ones.

The remaining 40% of the data was divided into *n* γ streams based on the preliminary γ identification, where *n* is a number of γ clusters. A cluster with a local maximum energy deposit of more than 50 MeV was considered to be a γ candidate. In a further analysis, we will apply a higher cut for the γ energy. After counting the number of γ candidates, additional local maxima were required to have less than a 20MeV energy deposit. Fig. 5.1 shows the distribution of the reduction in the number of reconstructed $K_L^0 \to 3p^0$ events passing through the cut for additional local maximum energy. Below a 20 MeV threshold we started to loose a large amount of events. This cut means the preliminary veto by the CsI calorimeter. In a further analysis, the thresholds for additional cuts will be tighter.

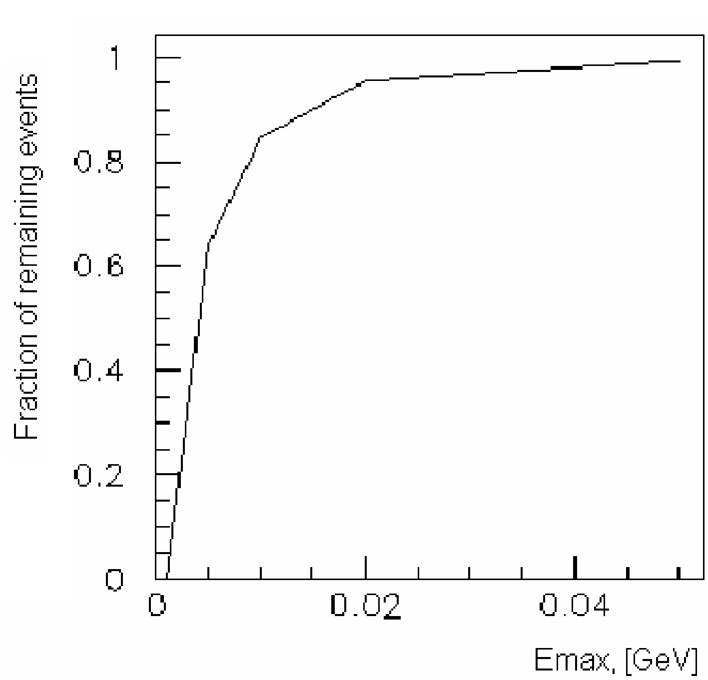

Fig.5.1 Fraction of reconstructed $K_L^0 \to 3p^0$ events remaining after cuts for the energy deposit of an additional local maximum. The data are taken from $K_L^0 \to 3p^0$ MC.

After this preliminary *g* identification, streams of the n*g* events were prepared. Table 5.1 is a summary of skimming results. The streams “gam1-6” correspond to 1-6 gamma events. There is a 0.02% contribution from "gam7+" where there are more than 6 γs. If the energy of one of the local maximums was between 20-50 MeV, such an event was counted into the "gam+bad" stream.

Table 5.1. Summary of the skimming results for the data.

All data	Non-physical triggers	Local max in KTeV
100%	19.5%	37.9%

gam1	gam2	gam3	gam4	gam5	gam6	gam7+	gam+bad
15.2%	9.3%	1.9%	1.9%	4.0%	3.9%	0.02%	5.0%

The acceptance loss of $K_L^0 \to 3\pi^0, 2\pi^0, \gamma\gamma$ decays by these requirements was estimated by a MC calculation. We reconstructed the events of $K_L^0 \to 3\pi^0, 2\pi^0, \gamma\gamma$ decays, and applied the typical kinematical cuts (section 5.3.5). Then, the requirements of the skimming process were applied: the local maximum of a γ cluster candidate has an energy deposit grater than 50 MeV, there is no additional local maximum with an energy over 20 MeV, and there is no local maximum in the KTeV crystals. It was found that the acceptance loss due to this skimming process was 0.5% for $K_L^0 \to \pi^0 \nu\bar{\nu}$, 0.5% for $K_L^0 \to 2\pi^0$ and 0.2% for $K_L^0 \to 3\pi^0$.

Thus, this skimming reduced the data size of the 2 γ stream by one order of magnitude with only a 0.5% acceptance loss for $K_L^0 \to \pi^0 \nu\bar{\nu}$.

5.2 Kinematical reconstruction

At the beginning of off-line data processing, the clustering routine scanned all crystals, and then the neighboring crystals with an energy deposition of more than 1 MeV were united in clusters. One or more local maximums could exist inside one cluster, and each local maximum with more than 50 MeV was treated as a γ candidate; their energies and hit positions were reconstructed.

5.2.1 Hit position of γ

For position reconstruction, we started from a center-of-gravity algorithm by considering a 3x3 matrix of crystals around the local maximum. However, this position does not linearly correspond to the real incident position. Moreover the difference between two values depends on the energy, position and angle of the incident γ. We therefore performed a MC study, and made a conversion table to convert the position obtained by the center-of-gravity algorithm to the real hit position.

In the MC, a single γ with a uniform energy distribution in the range of 0.1-3GeV was generated under various azimuth and polar angles. The cluster was then found, and the γ hit position was reconstructed. Assuming that we knew the incident angle, corrections were applied. Fig 5.2(a) shows the resolution at the stage of the center-of gravity algorithm and (b) that after the correction. The width of the distribution was reduced to 0.8 cm. This accuracy is very good compared with the size of the crystal (7x7 cm).

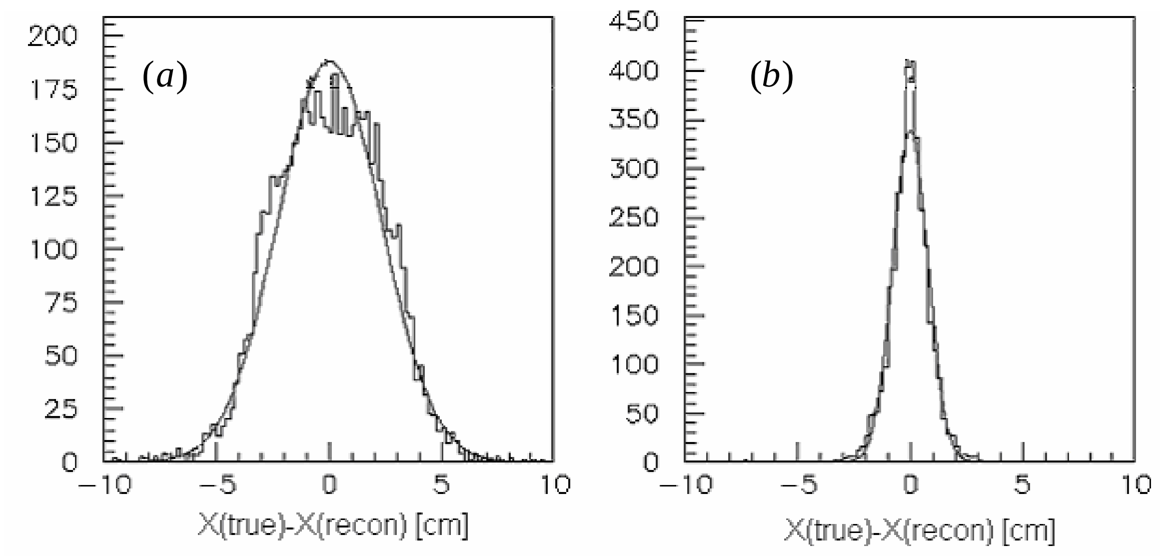

Fig. 5.2. Difference between the true hit position of γ and the reconstructed one. The center-of-gravity algorithm (a) and the center-of-gravity algorithm with correction (b) were used. The spectra were obtained from MC.

Here, in the MC, we know the incident angle of γ. In the real data, it can be estimated by reconstructing of the decay vertex based on the initial values of the positions obtained from the center-of-gravity algorithm. This method produces a good estimation of the angle, because it is not sensitive to the accuracy of the decay vertex reconstruction. From the other side, if the decay vertex is reconstructed incorrectly (for example in the case of the odd pairing) the correction will be incorrect, and it increases the error of hit position estimation. In a further analysis, we will try to reconstruct the angle directly from cluster information.

5.2.2 Energy of g

In order to reconstruct the kinematics, we need to estimate the energy of the γs. Summing up the energies of the 3x3 matrix of crystals is the simplest way, but it might underestimate the incident energy. Fig 5.3 (a) shows the difference between the true energy and the sum energy of the 3x3 matrix. A correction factor of 5%, not depending on the energy, was introduced. The corrected distribution (Fig.5.3.b) becomes balanced relative to zero with a width of 10 MeV. A more complicated correction may improve the resolution.

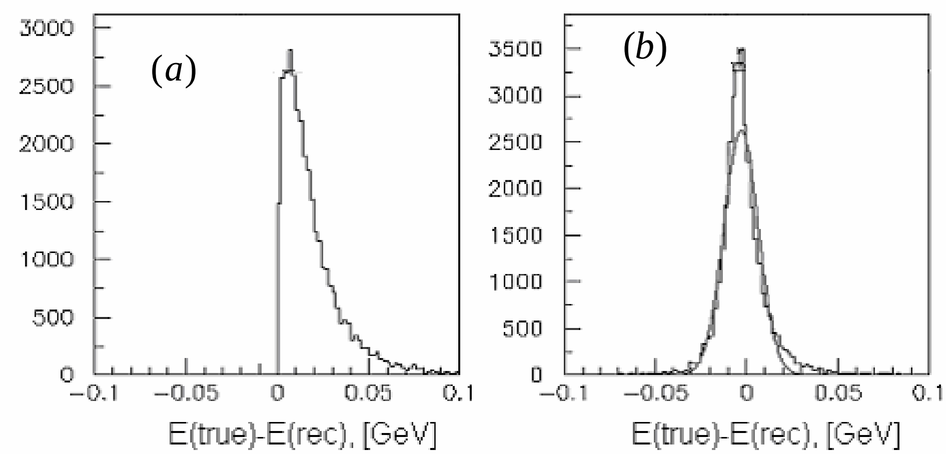

Fig. 5.3. Difference between the true and reconstructed energies of the γ. The sum energy of the 3x3 matrix of crystals was used (a). By increasing the reconstructed energy by 5%, the distribution becomes balanced relative to zero (b). The spectra were obtained from MC.

5.2.3 Decay vertex

- ***Single particle decay***

For reconstructing $p^0 \to gg$ or $K_L^0 \to gg$ decays, we first sought we seek the two γ cluster in the CsI calorimeter. Then, for each γ, the hit position obtained by the center-of-gravity algorithm and the energy as a sum of the 3x3 matrix were reconstructed. Then, the decay vertex was reconstructed as follows:

- The angle between vectors of two γ's is estimated from $\cos f = 1 - \frac{m^2}{2E_1E_2}$, where E_1, E_2 are the energies of the γ's and m is the mass of the particle, that decays.
- From the triangle (Fig. 5.4), we can write $R_{12}^2 = R_1^2 + R_2^2 - 2R_1R_2\cos f$, where $R_i = \sqrt{(\Delta Z)^2 + x_i^2 + y_i^2}$, (x_i, y_i) is the hit position of the i-th γ and f is the angle between the vectors of the γ's, which is estimated above, $R_{12} = \sqrt{(x_1 - x_2)^2 + (y_1 - y_2)^2}$.

These equations result in a second-order equation relative $(\Delta Z)^2$. We found that two solutions for $(\Delta Z)^2$ appeared only a few% cases, and thus rejected such events. Also, in $Z = Z_{CsI} \pm \sqrt{(\Delta Z)^2}$, we always chose the sign "-", which means that the decay occurred before the CsI calorimeter, where Z_{CsI} is the position of the CsI calorimeter, and Z is the decay point. Finally, we obtained only one solution for Z.

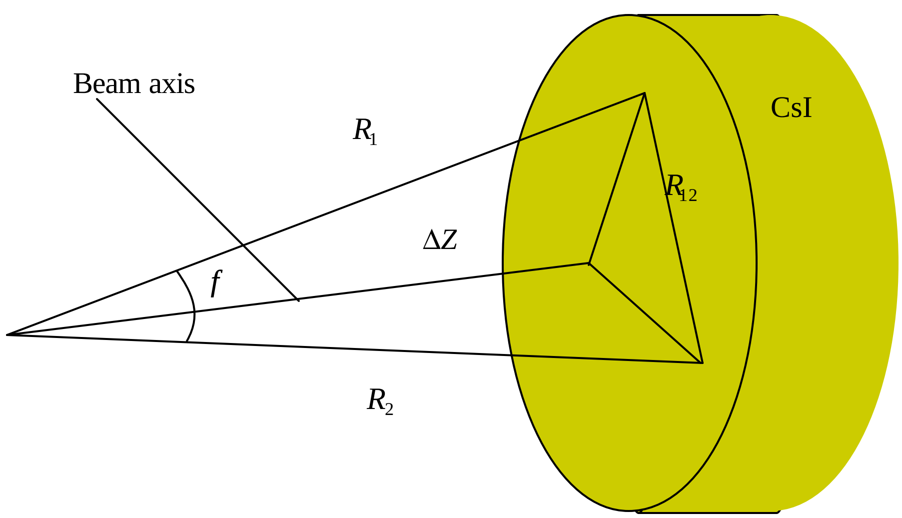

Fig. 5.4. Schematic view of the kinematics of the 2γ decay.

Then, knowing the decay vertex, the incident angles of the γ's to the CsI calorimeter were calculated, and corrections to the hit positions were applied. Also, the energies of the γ's were corrected. Then, based on the corrected hit positions and energies of the γ's, the decay vertex was calculated again.

- ***Tree decays***

Decays such as $K_L^0 \to 3p^0 \to 6g$ and $K_L^0 \to 2p^0 \to 4g$ occurred in two stages. We thus first reconstructed the decay vertexes of the secondary p^0's, and then estimated the common decay vertex.

After selecting the γ clusters, we grouped them into pairs and, assuming the parent particles of p^0, reconstructed the decay vertex of each pair, as described above. The decay vertexes must be close to each other, because the p^0's decayed immediately ($ct = 25.1nm$, where t is the time life). We also introduced the variable c^2, characterized by a spread of the vertexes;

$$c^2 = \sum_1^n \frac{(Z_i - \overline{Z})^2}{Err(Z_i)^2},$$

where Z_i is the vertex point of the i-th p^0, $\overline{Z} = \frac{1}{n}\sum Z_i$ is the mean value of all individual vertexes, and n is the number of secondary p^0's. The errors $Err(Z_i)$ were estimated based on the resolution of the hit positions and the energies of the reconstructed γ's. We assumed them to be $s(x) = 1.5cm$ and $s(E) = E\sqrt{2\%/\sqrt{E} \oplus 2\%}$, where E is given by GeV, and then propagated them through the equations for the Z_i calculation.

For $K_L^0 \to 3p^0$ and $K_L^0 \to 2p^0$, there are 15 and 3 combinations of γ pairs, respectively. We calculated the mean decay point, $\overline{Z}$, for each pairing, and selected the combination with the minimum c^2 as a true combination. Then, using the common decay point, $\overline{Z}$, we recalculated the kinematics of the γ's and p^0's. Also, the masses of K_L^0 and p^0 were treated as free parameters.

In the process of selecting the true pairing, we sometime make a mistake if the best and second c^2's were close to each other. In this case, it was not possible to distinguish true paring, but we could suppress these events by setting the cut to the second c^2.

In order to confirm the reconstruction procedure we carried out a MC simulation of the $K_L^0 \to 3p^0$ decay. Fig. 5.5 (a) shows the difference between the true and reconstructed decay points. There is a systematic shift of 5 cm, which comes from the not well-tuned reconstruction procedure of the hit position and energy of the γ's.

This procedure gave the decay vertex as being located on the beam axis. In the case of the $K_L^0 \to 3p^0$, $K_L^0 \to 2p^0$ and $K_L^0 \to gg$ decays, we could estimate the shift of the decay vertex in the XY plane perpendicular to the beam axis, because there were no escaped particles. The idea for the $K_L^0 \to 3p^0$ decay is shown in Fig. 56. The vector of the K_L^0 momentum should point at the center-of-gravity (COG) of 6 clusters in the CsI calorimeter. If we connect the target (origin point of K_L^0) and COG of 6 clusters by a line, we can estimate the shift of the decay vertex in the transverse plane, which results in a correct estimation of the transverse momentum of K_L^0, and also reduces the width of the distribution (Fig. 5.5 b).

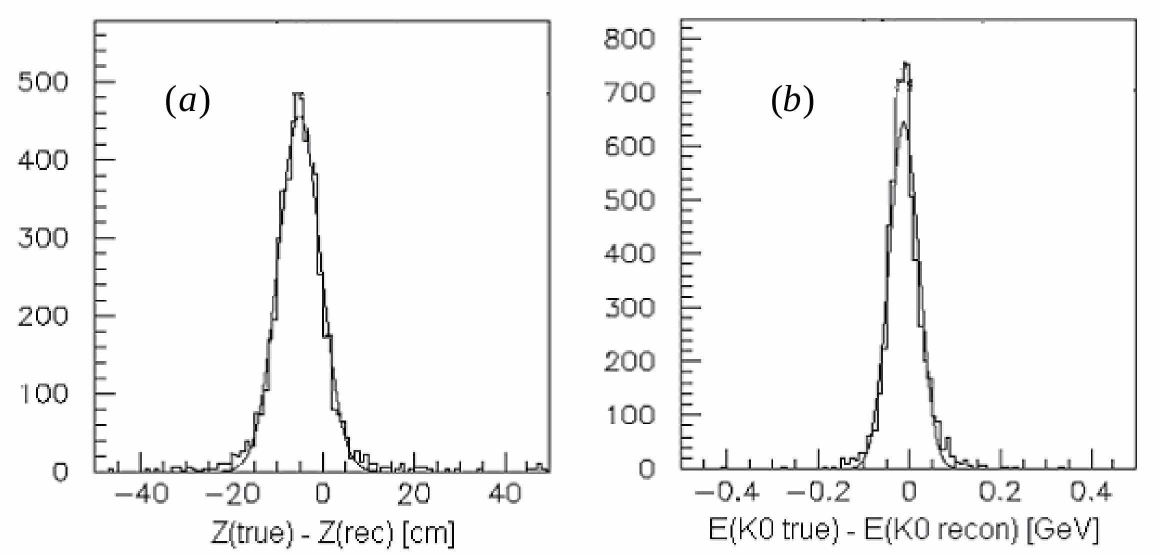

Fig.5.5. Difference between the true and reconstructed decay points (a) and the difference between the true and reconstructed energy of K_L^0 (b). The spectra were obtained from $K_L^0 \to 3p^0$ MC.

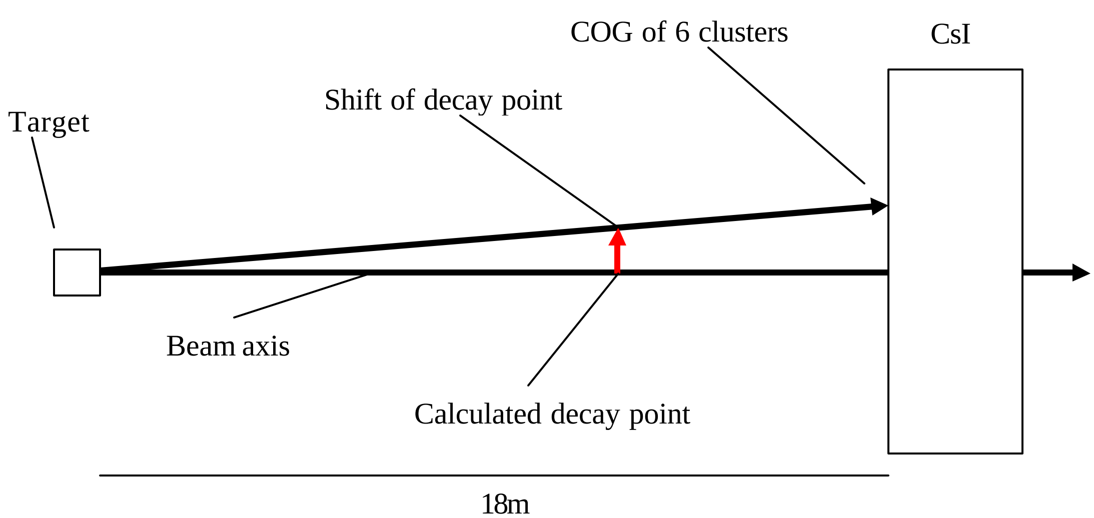

Fig. 5.6. Schematic view of the recalculation of the transverse position of the decay point.

5.2.4 Momentum correction

For a reliable MC simulation it is necessary to have a generator of K^0_L which will transport through the setup. The momentum spectrum of the origin particles (K^0_L) is important because it influences the energy scale of the secondary particles after decays that interact with the detector material and produce a signal.

In the beginning, the spectrum of the momentum distribution of K^0_L was obtained from a beam-line simulation. Based on this result, the $K_L^0 \to 3\pi^0$ decays were simulated. The K^0_L's were generated at the exit of the C6 collimator. One routine was used to reconstruct the 6γ events in data and MC. The reconstructed momentum spectra are shown in Fig. 5.7(a). The ratio of two distributions (Fig. 5.7.b) shows some discrepancy in the generation of the K^0_L in MC and the real momentum spectrum. The reconstructed decay vertex distributions in the data and MC (Fig.5.7 c) also do not match. The ratio of the spectra is not flat (Fig.5.7.d)

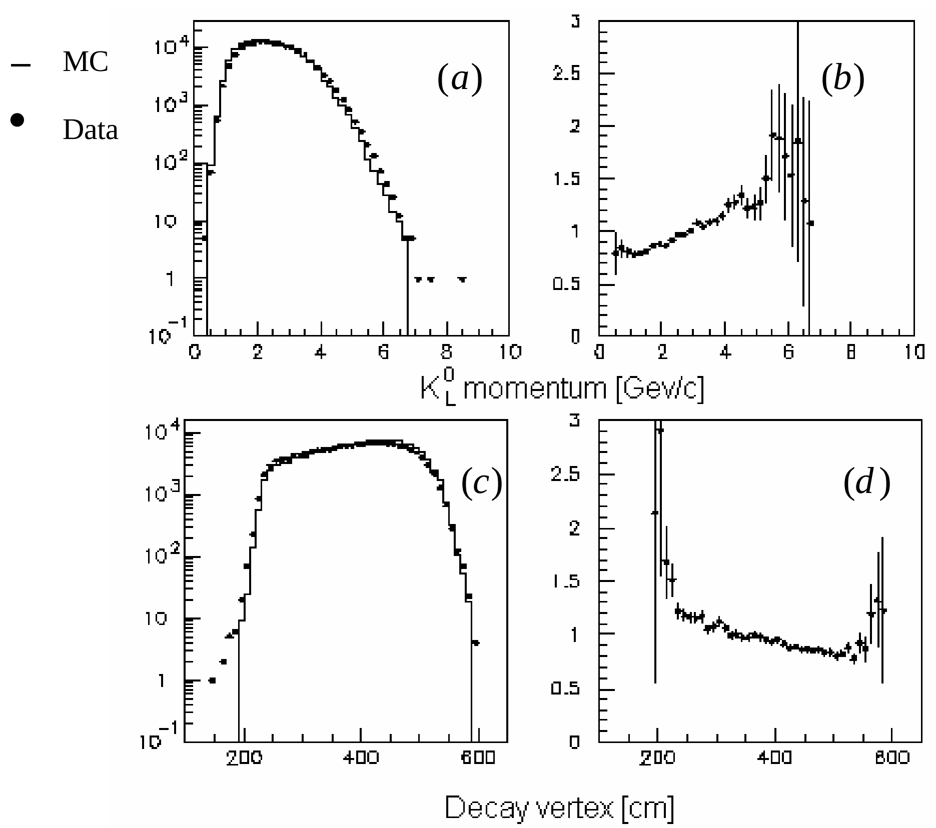

Fig.5.7.(a). Distribution of the reconstructed momentum of the K^0_L, (b) ratio of the momentum spectra obtained from data and from MC., (c) distribution of the reconstructed decay vertex, (d) ratio of the decay vertex spectra obtained from the data and from MC.

For MC we used the $K_L^0 \to 3\pi^0$ decay simulation; for the data we used 6γ events.

For correcting the momentum distribution used for K^0_L generation in MC, we fit the spectrum of the ratio of the data and MC by a line. We then re-weighted all of the histograms. The results are shown in Fig. 5.8. The slope in the distributions of the ratio between the data and MC for the momentum and decay vertex disappeared.

In further analysis of the $K_L^0 \to 3p^0, 2p^0, gg$ and $K_L^0 \to p^0 \nu\bar{\nu}$ decays, we re-weighted the histograms using the result of this fit.

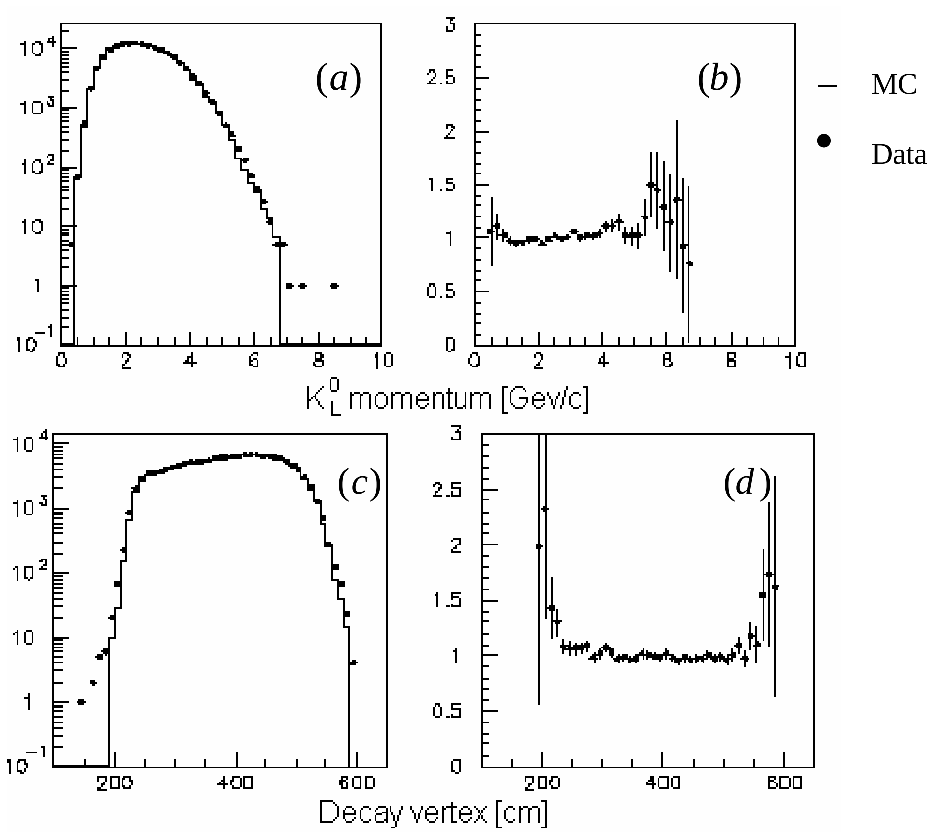

Fig.5.8 (a) Distribution of the reconstructed momentum of the K^0_L, (b) ratio of the momentum spectra obtained from the data and from MC., (c) distribution of the reconstructed decay vertex, (d) ratio of the decay vertex spectra obtained from the data and from MC. For MC we used the $K_L^0 \to 3p^0$ decay simulation; for the data, we used 6γ events.

5.3 *Reconstruction of the neutral decay modes*

5.3.1 Introduction

Since the physics data were collected by the trigger $N_{clust} \geq 2$, they also contained other neutral decay modes, such as $K_L^0 \to 3\pi^0, 2\pi^0, \gamma\gamma$. Those decays will be used not only to normalize the number of K_L^0's coming to the detector, but also to monitor various kinds of detector performances. Therefore, reconstructing those decays is very important for understanding the performance of our experimental setup.

They have relatively large branching ratios of 21% for $K_L^0 \to 3\pi^0$, 0.091% for $K_L^0 \to 2\pi^0$ and 0.03% for $K_L^0 \to \gamma\gamma$. Moreover, they have more definite kinematical constraints than $K_L^0 \to \pi^0 \nu\bar{\nu}$, because there are no missing particles in these decays, like the neutrinos in the $K_L^0 \to \pi^0 \nu\bar{\nu}$ decay. They can be clearly reconstructed and purely identified. First of all, the obtained clean and pure samples can be used to study various experimental parameters, such as the beam profile, and the K_L^0 spectrum and flux, etc. Clear line-shape distributions of $K_L^0 \to 3\pi^0$ and $K_L^0 \to 2\pi^0$ provide an overall check of our energy and timing calibrations. A check of relative yields among these three decays is one of the most critical checks of our detection system. In addition to the pure $K_L^0 \to 3\pi^0$, $K_L^0 \to 2\pi^0$ and $K_L^0 \to \gamma\gamma$ decay samples, from these analyses, we will obtain several pure background samples that can be used for background studies, as described in the last part of this section.

Finally, as described in the next section, by using the pure signal and background samples, we can make a systematic study of the vetoes, which is one of the most crucial studies in the present experiment.

There are two ways to clean-up the 6-, 4- and 2-γ data for extracting clean and pure $K_L^0 \to 3\pi^0$, $K_L^0 \to 2\pi^0$ and $K_L^0 \to \gamma\gamma$ samples. One method is to apply tighter vetoing. However, in this case we will lose a chance to check the performance of the various veto counters. It will also suffer from an unknown loss of accidental signals. Therefore, we took the other way. Data clean-up was performed only by kinematical constraints using the CsI calorimeter. Of course, since we already applied a loose veto in the on-line stage (at the trigger stage) in order to reduce the trigger rate; we have to start our analysis to apply the same online veto to the Monte Carlo simulation.

5.3.2 Online veto

In order to avoid event loss due to accidental vetoes during event reconstruction in the offline analysis, we didn't apply any veto for the data. However, for MC we applied the vetoes used for online data taking. This allowed us to compare the various spectra obtained from both of the data and MC.

During data taking, the signals from veto detectors were summed by Amp/Disc modules into cluster signals, and the veto thresholds were applied to them. The thresholds were determined by the edges of the energy distributions of the experimental data. For the MC simulation of the online veto, we summed up the individual channels in the same way as in the electronics.

As an example, the sum of all channels of CC03 was used for the online veto. In Fig 5.9, the distribution of the sum of the individual channels of the CC03 detector is shown (blank histogram). The yellow histogram shows the events where there was a cluster signal. The sharp edge shows the online threshold. Events over ~15MeV were rejected in the online trigger. The tail (blank histogram) exists due to events outside of the time window for the vetoing. By the same way, we can estimate the threshold level for each detector that participated in the online veto.

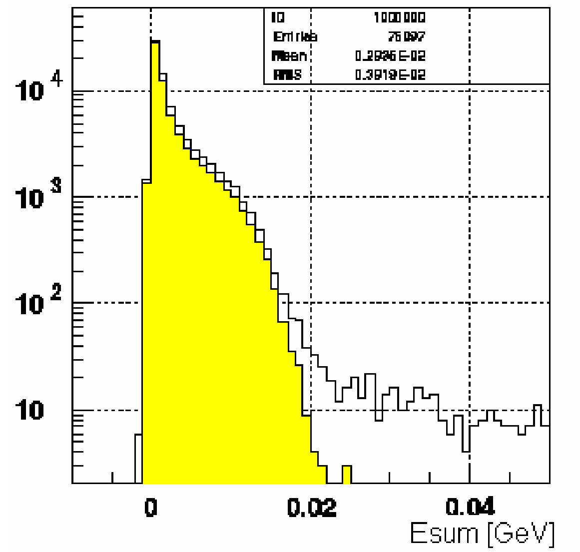

Fig 5.9 Distribution of the sum of the individual channels of CC03. The yellow histogram shows events where there was a cluster signal.

Table 5.2 gives a summary of the thresholds.

Table 5.2 Thresholds for veto detectors that participated in online vetoing.

Detector	Online threshold
Charge veto	1.2 MeV (for each cluster)
CC02	15.0 MeV (sum all)
CC03	15.0 MeV (sum all)
CC04	45.0 MeV (sum all)
CC05	25.0 MeV (sum all)
Main barrel	25.0 MeV (for sum of downstream-clusters)
Front barrel	30.0 MeV (for each cluster)

5.3.3 MC simulation

For a detailed study of the data and for decomposing of the effects that play a role, we made a Monte-Carlo simulation (MC) using GEANT 3.

From the beam-line simulation [41] we obtained the spectra of the K_L^0 at the exit of the C6 collimator (last collimator in the beam line), as shown in Fig. 5.10 (a). It was fitted by an analytic function and used to generate K^0_L at the entrance of the E391a setup. The origin point and the direction of the momentum vector were also generated based on the beam-line simulation. Then, the momentum spectrum of K^0_L was corrected by matching the measured data and MC spectra of the reconstructed $K_L^0 \to 3\pi^0$ decay. Only small corrections were necessary, which showed the reliability of the beam-line simulation.

To simulate the neutron-related background, the momentum distribution of the neutrons was also obtained from the beam-line simulation. The neutron was considered to belong to the beam halo if the hit point extrapolated to the CC05 plane was outside of the beam hole. Otherwise, it was considered to belong to the beam core. Fig.5.10(b) shows a scatter plot of the momentum of the neutron and its radial distance from the beam axis at the exit of the C6 collimator. The group of events with small R contains the beam core neutrons, which might have a large momentum. The momentum of the halo neutrons is much lower.

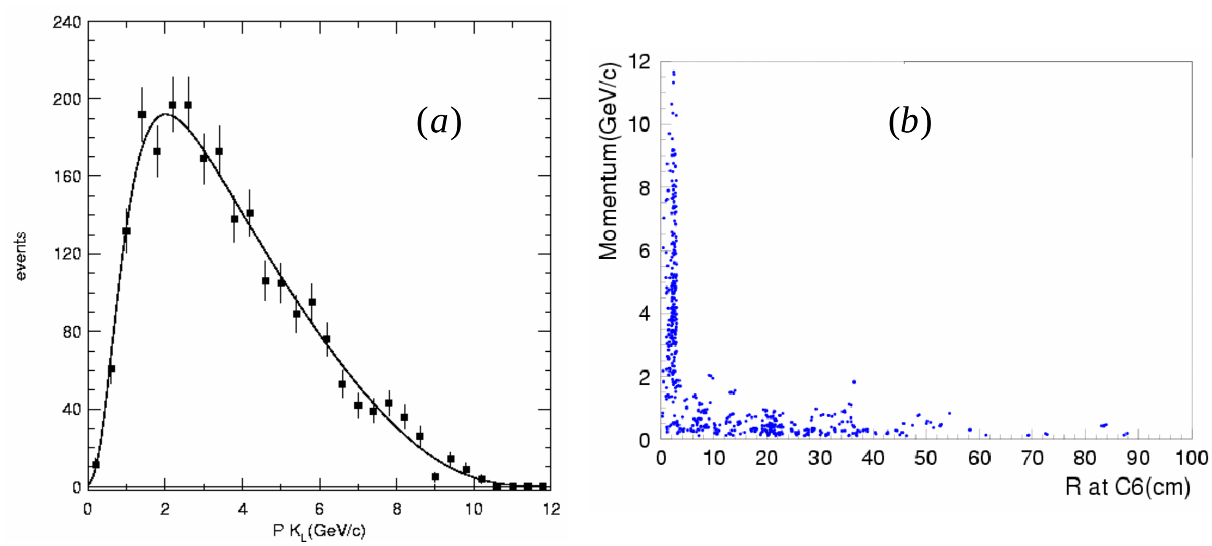

Fig. 5.10. (a) Distribution of the momentum of K_L^0. The dots are from a MC simulation; the curve is the result of fitting by an analytic function. (b) Scatter plot of the momentum of the neutrons and distance from the beam axis at the exit of the C6 collimator.

The results of the beam line simulation were used to simulate the beam coming to the E391a setup. Yields of 2326 K_L^0, 600 halo neutrons and 1.55x10^5 beam core neutrons per 10^{10} protons on the target (pot) were obtained from the beam-line simulation.

For a background study, we generated various decay modes, such as $K_L^0 \to 3\pi^0, 2\pi^0, \gamma\gamma, \pi^+\pi^-\pi^0$, and then tracked them through the E391a setup and simulated the interaction with the materials of the detectors.

The simulation of the detector reply was considered in terms of the energy deposit in the active material of the detector. Some detectors, like MBR, have a large size; also additional factors, such as signal attenuation, play a role for them. For MBR, they were measured in a cosmic-ray test, and were applied to derive the detector response in MC. We also took into account that the calibration of MBR was done at the center of the module (section 4.4.3), and thus the signal propagation and attenuation effects were considered in the MC simulation.

5.3.4 Reconstruction of $\pi^0 \to \gamma\gamma$ decays (candidates of $K_L^0 \to \pi^0 \nu\bar{\nu}$)

The 2γ skimmed data stream was used for the analysis of 2γ events. At first, the decay vertex was reconstructed assuming that 2γ were produced from π^0, and that it occurred on the beam axis; the X and Y coordinates of the decay point were set to 0.

Although no additional clusters in the CsI calorimeter with a local maximum energy greater than 20 MeV were required in the skimming process, it will be tightened later against a soft γ hit.

In order to eliminate any edge effects in the CsI calorimeter, we rejected events with a reconstructed hit position inside the KTeV crystals (around the beam hole) and in the outside region (R>80cm). The calorimeter, itself, has a 100 cm radius. This is associated with the inaccurate reconstruction of the hit position and energy of γ near the calorimeter border. Also, at the current stage, because we didn’t analyze overlapping showers, the distance between the reconstructed hit positions of two γ’s was required to be greater than 21 cm.

Also, online thresholds were applied to the veto detectors in MC.

5.3.4.1 *Contributions of the neutral* K_L^0 *decays*

To study the K_L^0 background contribution to the $K_L^0 \to p^0 \nu\bar{\nu}$ decays, we generated the MC events for $K_L^0 \to 3p^0, 2p^0, gg$ decays, and analyzed them as 2 γ events, assuming that the original particle was p^0. All MC events were skimmed, and online veto thresholds were applied.

The reconstructed decay vertex and energy of the γ's in the CsI calorimeter are shown in Fig. 5. 11. In the decay vertex distribution of the data, there is a bump near 300 cm corresponding to the CC02 position. Also, a large number of events exist near the calorimeter at around 550 cm. The MC can't reproduce both the distribution of the decay vertex and γ energy. Especially, the discrepancy between the data and the MC is large at the downstream position of the decay vertex and at the low γ energy region.

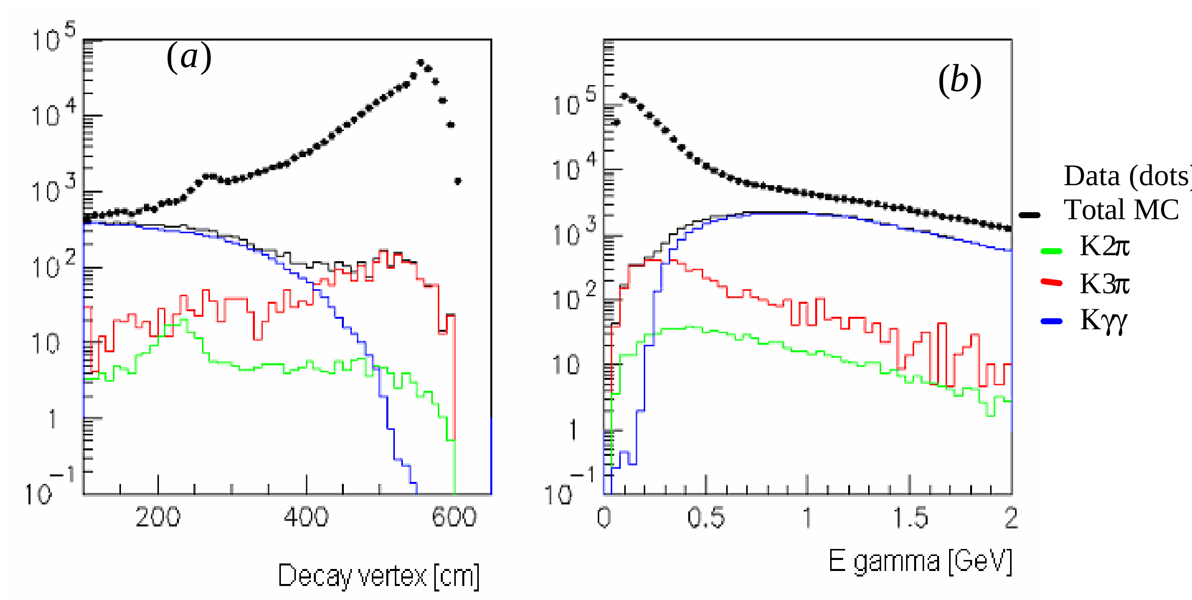

Fig. 5. 11. Distribution of the reconstructed decay vertex of 2g clusters in the CsI array, assuming the original particle is p^0. (a) Energy distribution of the γ's. (b) MC events from $K_L^0 \to 3p^0, 2p^0, gg$ decays processed as 2 γ events.

5.3.4.2 *Contribution of the* $K_L^0 \to p^+ p^- p^0$ *decays*

One of the background sources is $K_L^0 \to p^+ p^- p^0$ decay, where charged pions pass through the beam hole of CC03 and g 's from the p^0 decay hit the CsI calorimeter. The online energy threshold of the downstream detectors is not sufficient to reject the charged particles from $K_L^0 \to \pi^+\pi^-\pi^0$ events at the online stage.

We generated about 10^9 K^0_L at the exit of the C6 collimator to simulate the detector response to $K_L^0 \to \pi^+\pi^-\pi^0$ decays. Fig. 5.12 shows the decay vertex and γ energy distributions with $K_L^0 \to \pi^+\pi^-\pi^0$ contributions added.

The $K_L^0 \to \pi^+\pi^-\pi^0$ decays fill the middle part of the decay vertex spectrum and some part of the low energy γ spectrum, but there still exists a discrepancy. The bump near the CC02 region is not reproduced by the K^0 decays.

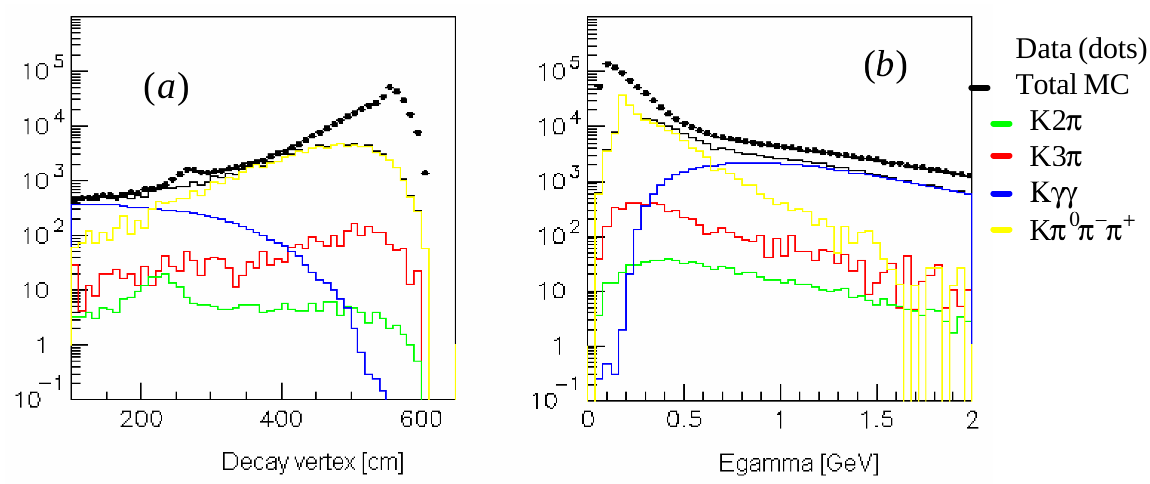

Fig. 5.12 Distribution of the reconstructed decay vertex of 2γ clusters in the CsI array assuming the original particle is π^0 (a) and energy distribution of the γ's (b). The $K_L^0 \to \pi^+\pi^-\pi^0$ MC is added.

5.3.4.3 *Halo neutrons*

One candidate to fill the discrepancy is halo neutrons. They can interact with the material in the detector and produce π^0's, which subsequently decay into 2 γ's, or hit the CsI calorimeter directly and produce false clusters through a hadronic shower.

These neutrons may appear due to scattering with collimators; at the exit they move away from the beam axis. Another source is neutrons that pass through the shield around the collimators. In order to estimate the contributions of the halo neutrons, a special MC calculation was made using the GEANT-FLUKA package.

For the background estimation, the halo neutrons were generated at the exit of the C6 collimator, and transported through the E391 detector. In Fig. 5.13 the halo neutron vertex distribution is added. The interaction of neutrons with CC02 reproduces the bump near Z=300 cm. However, the events near the calorimeter are not yet fully described.

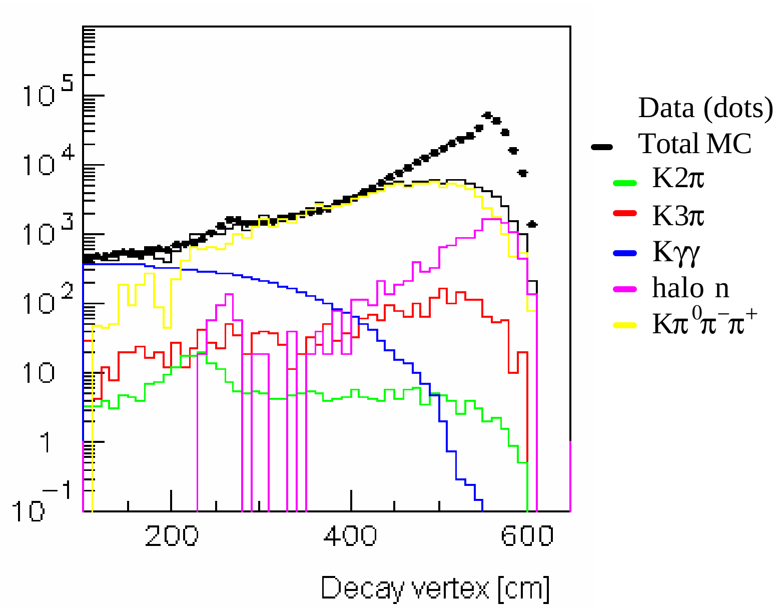

Fig. 5.13 Distribution of the decay vertex after adding the contribution from the halo neutrons in MC.

5.3.4.4 *Beam core neutrons*

The 2*g* events located near the CsI calorimeter have not been described by K_L^0 decays plus halo neutrons. One possible source is the interaction of the beam core neutrons with the material of the detector. A hint can be found in the distribution of the center-of-gravity of two clusters in the CsI calorimeter on the horizontal (X) and vertical(Y) axes for events at Z>500 cm. As shown in Fig. 5.14, the X distribution is symmetric, but the Y distribution is asymmetric, which suggests that the neutron hits to the upper part are more preferable.

A candidate for the interacting material is the membrane separating the low and high-vacuum regions. The membrane pipe passes through a beam hole made of the inner charge veto scintillators and CC03, and extends to the CC04 position, as shown in Fig.2.15 The membrane pipe doesn't have a strong supporting structure, and is kept by tension applied by wires from the downstream ends. If the wire tension becomes weak, the membrane pipe can be bent, and some part might touch the beam core in the region before the CsI calorimeter.

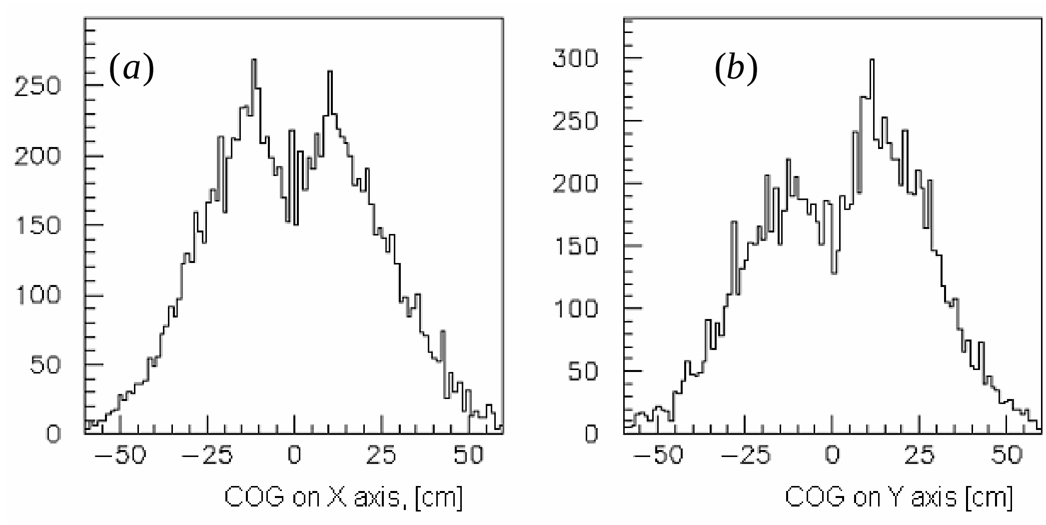

Fig. 5.14 Distribution of the center of gravity of 2 clusters at Z>500cm; (a) on the horizontal axis X, (b) on the vertical axis Y.

Assuming that a drooping membrane is a source of the unexplained events near the CsI calorimeter, we conducted a special MC simulation. However, it is hard to know the shape of the membrane and, correspondingly, the amount of interacting material. In the MC we assumed a piece of the membrane material that covered the full beam hole, and then normalized the number of events by matching the MC spectra to the experimental data. This factor reflects the amount of interacting material. Also, in order to study the effect of the membrane window at CC04, we assumed the membrane material at that position in the MC (Fig. 5.15). To increase the speed of the MC, we increased the density (from $1 g/cm^3$ to $10 g/cm^3$) and thickness of the membrane (from 0.2mm to 2mm). This effectively increased the number of neutrons by a factor of 100.

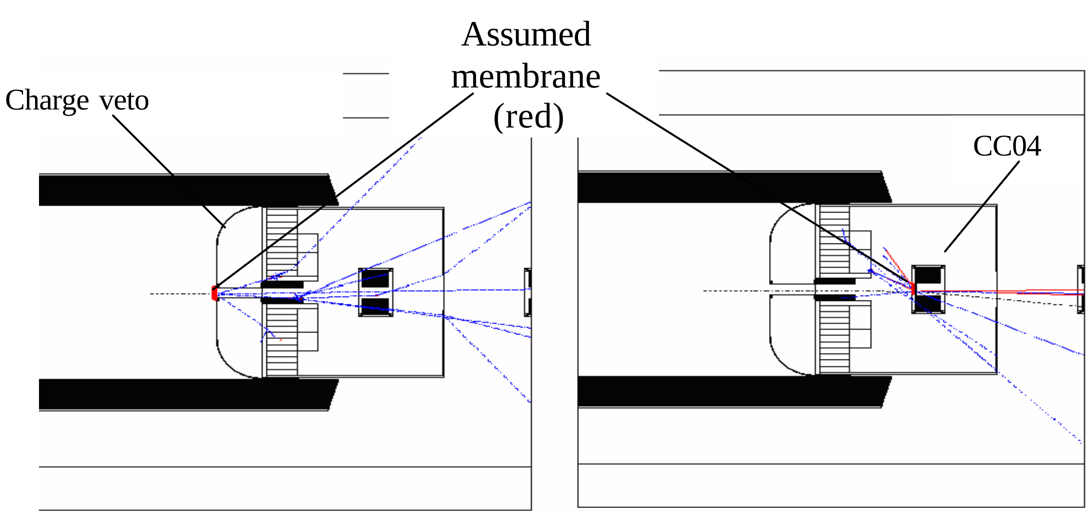

Fig. 5.15. Event display of the neutron interaction with the assumed membrane material places at the entrance and exit of the detector beam hole.

We generated 2×10^{10} core neutron events (~500 spills equivalent). Fig. 5.16 shows the decay vertex distribution after adding the simulation result of core neutrons with the membrane at the charge veto and CC04 positions shown in Fig. 5.15. The core neutron interaction produces the peak before the CsI calorimeter. The black histogram shows core neutron interactions with the membrane at CC04. It also contributes to the peak, because the decay vertex is always assumed to be before the CsI calorimeter. The peak position in the data and MC is the same. Since the dropping shape of the membrane is not well known, we multiplied the number of events by a factor of 3 to reproduce the height of the peak in the spectra (Fig 5.17).

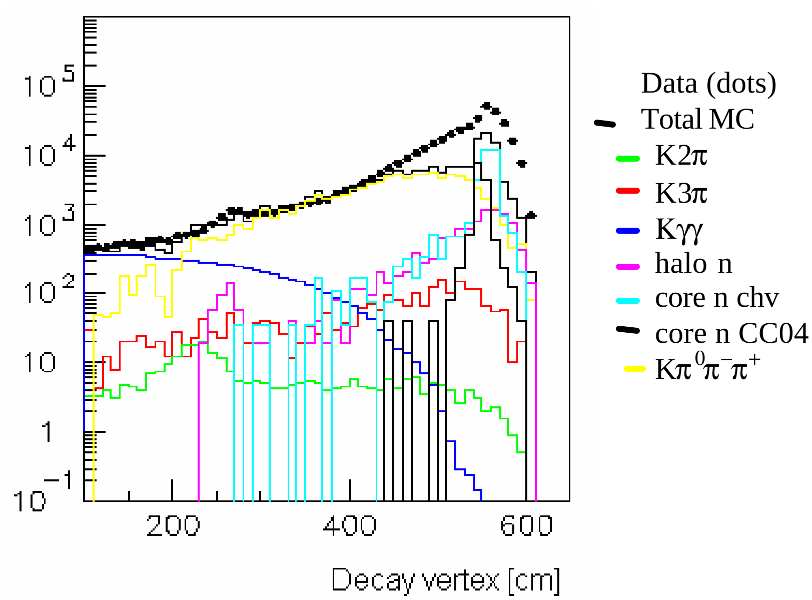

Fig. 5.16. Distribution of the decay vertex after adding the contribution from the core neutrons in the MC.

In order to confirm the droop of the membrane, we opened the vacuum vessel after a beam run and took a picture. The membrane beam pipe really fell down, and some part of the beam touched the membrane (Fig.5.18)

An additional source might be accidental events. In Fig.5.19, the distribution of the ratio of the local maximum energy (Emax) of the cluster over energy of the cluster (Eclust), defined by the 3x3 array of crystals, is shown. The spectrum of the total MC follows the shape of the data, but in the region near 1 there is an inconsistency between the data and MC. These events correspond to clusters where almost all of the energy of the cluster is located in the local maximum. Such clusters can be produced by accidental events or charged particles. The last assumption requires a detailed study of the inefficiency of the charged veto detector. This study will be done later.

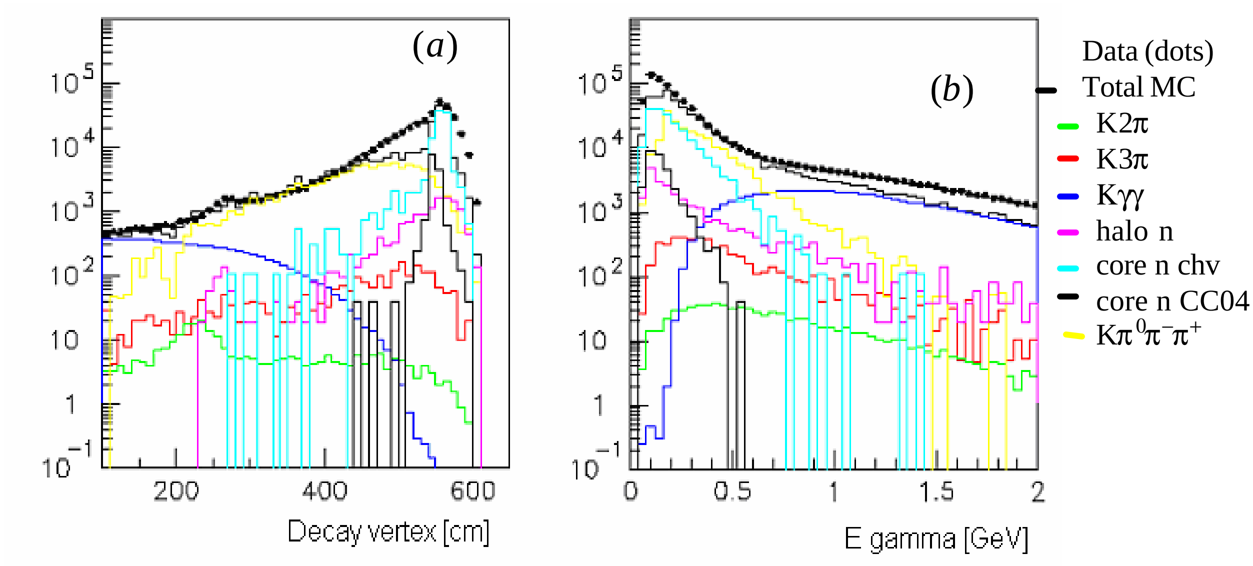

Fig.5.17. Comparison between the data and the MC results for 2-γ events. (a) The decay vertex distribution; (b) γ energy, after adding the result of the core neutron simulation. Still there remains a discrepancy between the data and the MC spectra in the region before the CsI calorimeter. The core neutrons explain the existence of the peak.

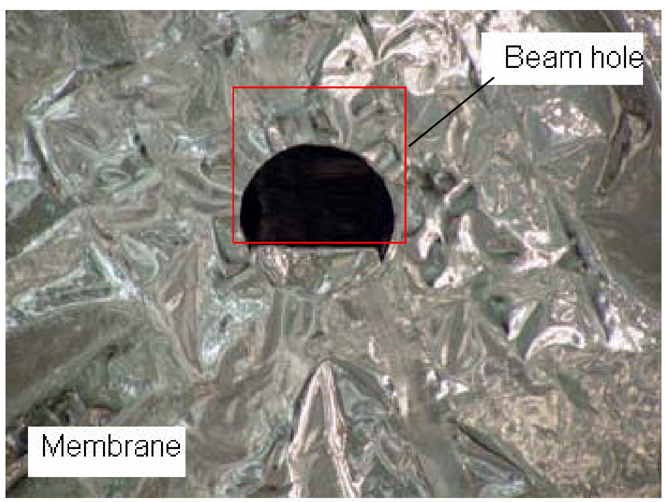

Fig. 5.18 Picture of the membrane at the entrance of the beam hole.

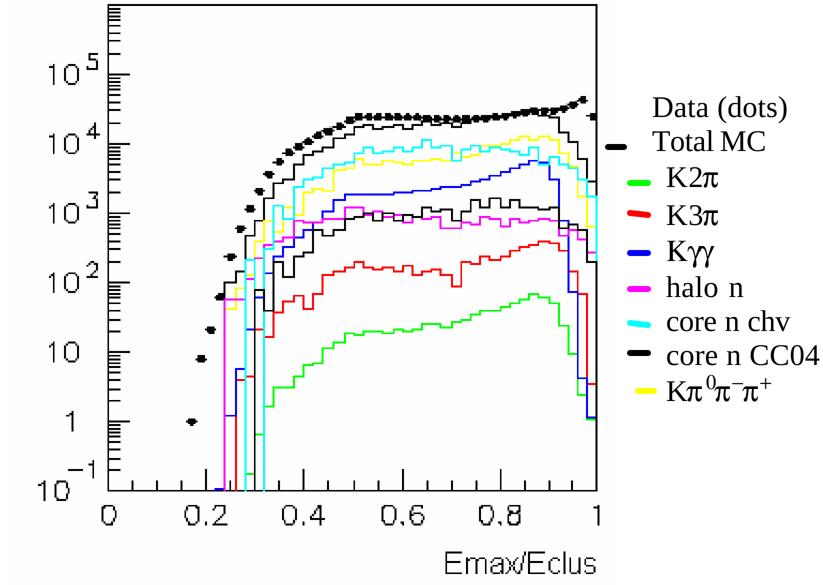

Fig. 5.19. Distribution of the ratio of the local maximum energy (Emax) of the cluster over the energy of the cluster (Eclust).

5.3.4.5 *Optimization of the kinematical cuts*

As was shown above in the reconstruction of 2-γ events assuming a π^0 mass, we found various backgrounds. Plots of the transverse momentum vs. decay vertex for various background sources obtained by the MC simulation are shown in Fig. 5.20. The online veto thresholds were applied.

- Neutral K^0 decays ($K_L^0 \rightarrow 3\pi^0, 2\pi^0, \gamma\gamma$), where 2γ hit the CsI calorimeter, additional particles escape to veto system, and some part of events are rejected by online veto. Also, there are events where 2 γ's are fused in one cluster.
- $K_L^0 \rightarrow \pi^+\pi^-\pi^0$ decays, of which 2γ's from π^0 hit the calorimeter and π^+ and π^- escape to the veto system. The online threshold for CC04 was set above the MIP peak, and CC06, CC07, Beam hole charge veto and BA were not included in the online veto, which kept these decays near the CsI calorimeter when charged pions passed through the beam hole of CC03. In the P_T vs. decay vertex plot, there is a clear correlation: the transverse momentum increases closer to the calorimeter.
- Core neutrons ('core n chv') interact with the membrane material at 550 cm and produce π^0's. There is a huge peak at the 550 cm position. However, a tail touches the signal box region.

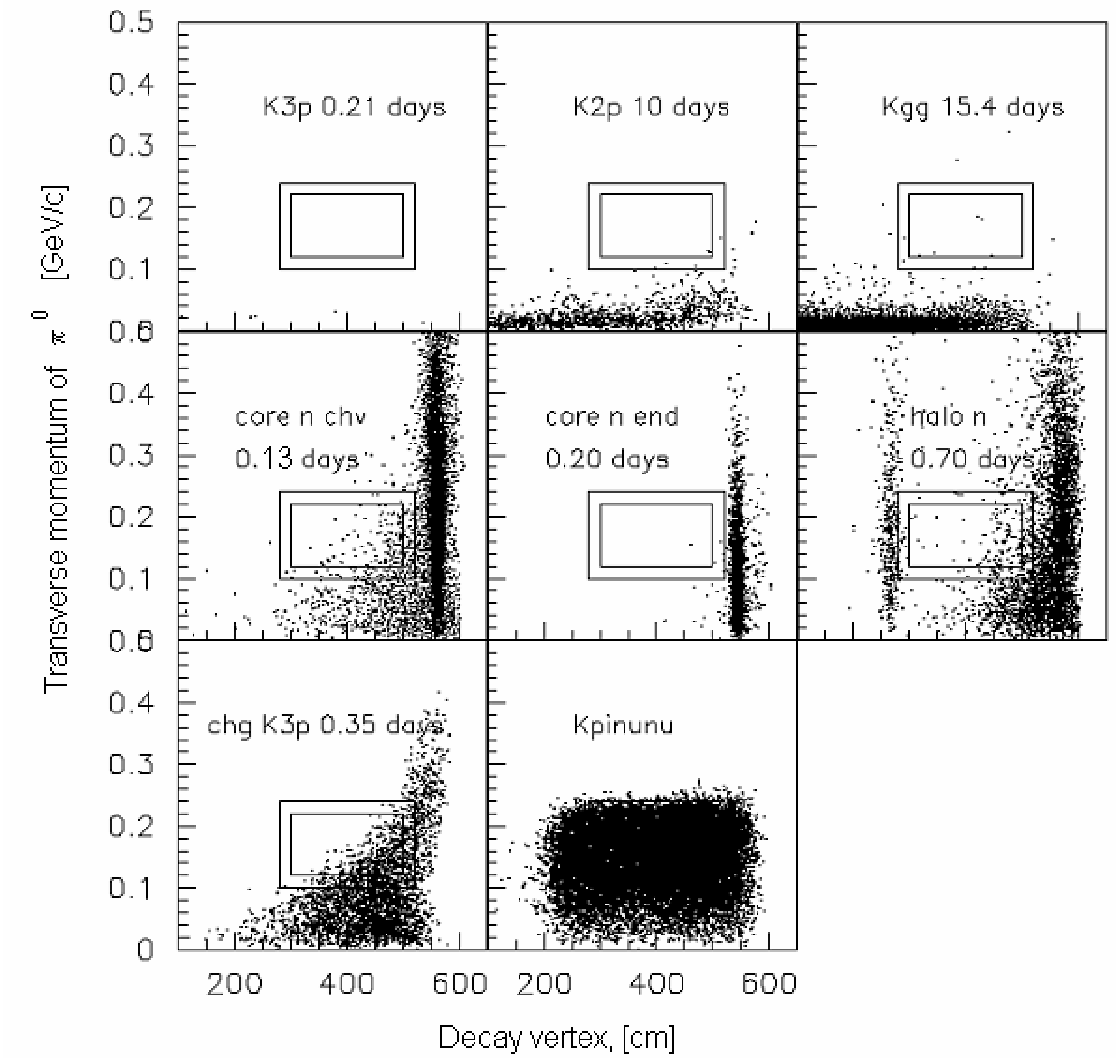

Fig. 5.20. Plots of the transverse momentum vs. reconstructed decay vertex for different background sources. The MC statistics are shown in terms of one day of data.

- Core neutrons (‘core n end’) interact with the end-cap of the membrane pipe and produce p^{0}’s, which go back to hit the calorimeter. In our current reconstruction procedure, we can’t recognize the direction of γ, and so the decay vertex is assumed to be in front of the calorimeter. The energy of such clusters is relatively small, and the events can be suppressed by requiring the γ energy to be larger than 200 MeV.
- Halo neutrons spread out around the beam line and interact with the detector material. As shown in Fig. 5.20, there are many events surrounding the signal box. CC02 and CHV are apparent sources of p^{0}’s produced by the halo neutrons. Moreover, a neutron that hits the CsI calorimeter can also produce a hadronic shower, and make two separated clusters. Such two clusters are

located relatively close to each other, and a distance cut is efficient against them.

To optimize the kinematical cuts, data samples are used. The 2γ events can be divided into 4 groups on a plot of P_T vs. decay vertex, as shown in Fig. 5.21.

There are two types of neutron-induced backgrounds. One is the case that the neutron hits the CsI calorimeter directly and produces a hadronic shower, which is observed as two clusters. Such clusters might be close to each other, and a cut on the distance between clusters is useful. Also, the shower shape of the hadronic cluster produced by the neutron is different from that of the electromagnetic shower. By selecting events in region "C", we can optimize the neutron/ γ separation parameters.

The other type is induced by neutron interactions with the detector materials which produce π^0's. In this case the clusters in the CsI calorimeter are γ clusters, and the reconstructed kinematics is similar to the $K_L^0 \to \pi^0 \nu\bar{\nu}$ decays. Such events can be rejected by vetoes because the neutron interaction might produce additional particles. Region "B" mostly contains such events.

The backgrounds from K_L^0 decays are contained mostly in region "D" under the signal box. In this sample there might be additional particles, and these can be used for veto studies after suppressing of the $K_L^0 \to \gamma\gamma$ contamination. The most probable process is a fusion of γ's from $K_L^0 \to 3\pi^0$ and $K_L^0 \to 2\pi^0$, which causes miss reconstruction of the vertex point. In such a case, the cluster shape and balance of the γ energies might be useful parameters.

To estimate of the acceptance loss during kinematical cut optimization we used the $K_L^0 \to \pi^0 \nu\bar{\nu}$ MC sample in region "A" (signal box).

- A(black): $K_L^0 \to \pi^0 \nu\bar{\nu}$ signal region.
- B(red): Background region induced by the halo neutrons.
- C(blue): Background region induced by the halo and core neutrons.
- D(green): Background region induced by the K^0_L decays.

Events in regions "B,C,D" were taken from the 2γ data sample. Sample "A" is a MC.

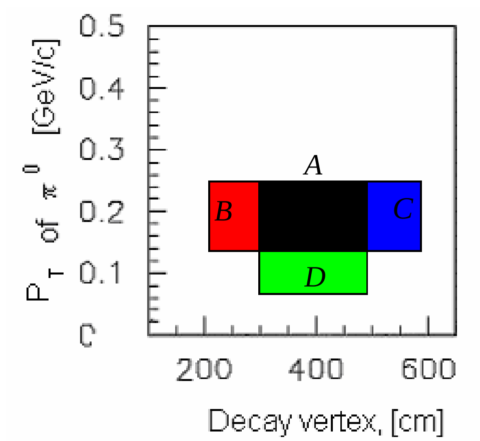

Fig. 5.21. Schematic view of four regions used to optimize of the kinematical parameters.

o *Cluster shape analysis*

The basic idea is the fact that there is a difference in the cluster shape between the γ and the neutron. For a γ cluster, the energy is mostly located in the crystal with the largest energy deposit (local maximum). In the case of the fusion of $2g$, or a hadronic shower produced by a neutron, the energy is more widely spread over the crystals in a cluster. We developed two variables for cluster shape analysis:

$$E_{\max}/E_{cluster} \text{ and } \frac{E_1 + E_2 + E_3}{E_{cluster}},$$

where $E_{cluster}$ is the total cluster energy, E_{max} is the energy of the local maximum and $E_1 > E_2 > E_3$ are the energies of the crystals in a cluster with biggest energy deposit.

The first variable is effective to discriminate fused clusters. Because the Moliere radius for CsI crystals is 3.8 cm, our 7x7 cm crystal captures about 80% of the energy of the shower if γ hits the center of the crystal. This value is smeared by the energy, position and incident angle of γ.

Fig 5.22 shows the distributions of $E_{\max}/E_{cluster}$ for a single γ cluster (a) and for fused clusters (b). In the case of single γ cluster, 85% of the energy of the cluster is concentrated in the local maximum crystal. In the case of a fused cluster, the energy is shared with neighboring crystals. The data was obtained from the $K3p^0$ MC, where for the fused g's we required the distance between hits to be less than 14 cm (2 crystals).

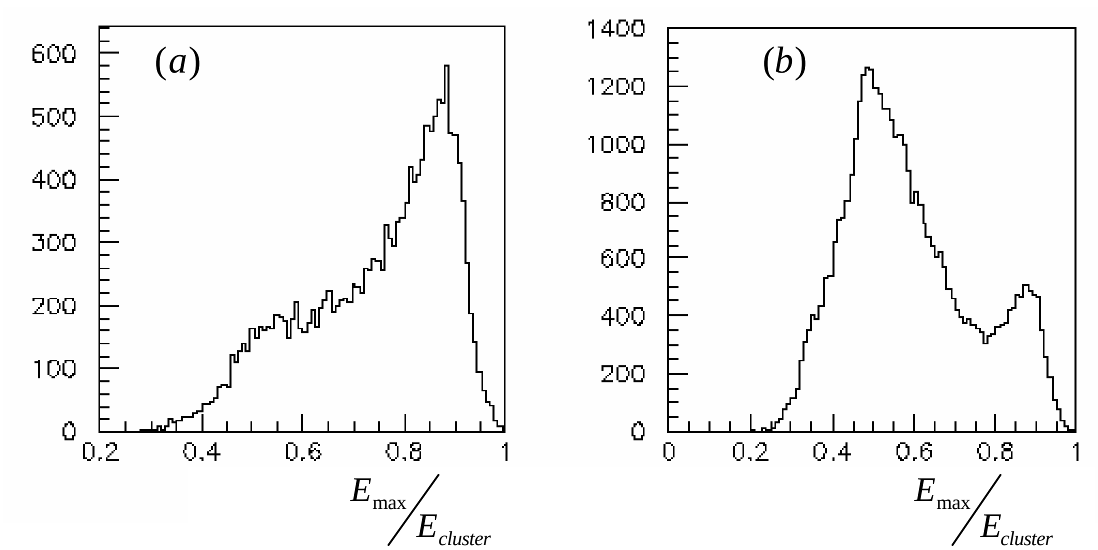

Fig. 5.22. Distribution of $E_{\max}/E_{cluster}$ for single γ clusters (a) and fused clusters (b).

Both variables, $E_{\max}/E_{cluster}$ and $\frac{E_1+E_2+E_3}{E_{cluster}}$, are also helpful for neutron/γ separation. They are related to the size of the cluster. The distributions of $\frac{E_1+E_2+E_3}{E_{cluster}}$ for γ clusters (a) and neutron clusters (a) are shown in Fig. 5.23.

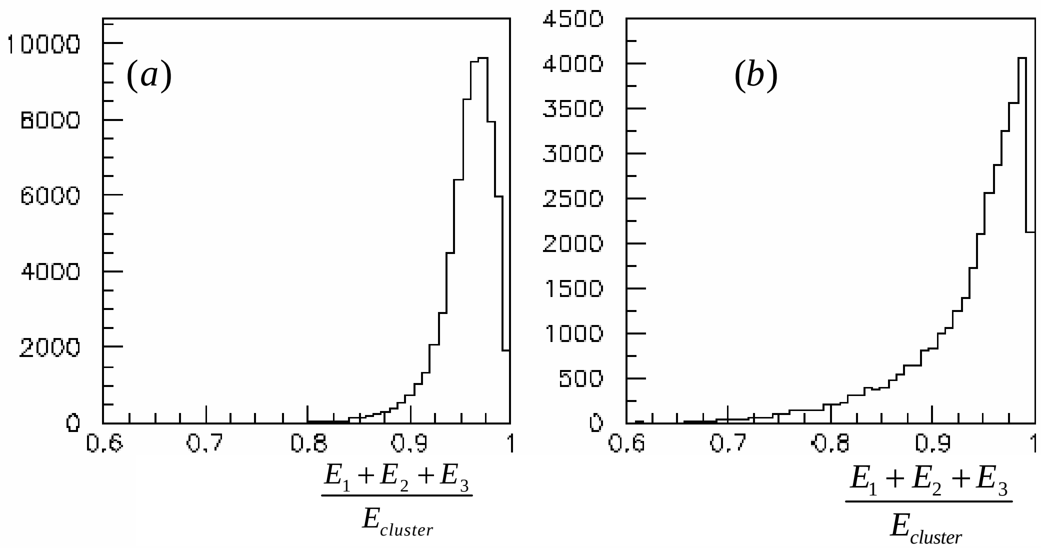

Fig. 5.23. Distribution of $\frac{E_1+E_2+E_3}{E_{cluster}}$ for γ clusters (a) and neutron cluster (b).

The shapes for γ and neutron clusters are different (Fig. 5.23). For the γ cluster distribution, the upper edge is sharp, but for neutron clusters it is shifted towards 1.0, and so the cut point at about 0.98 or 0.97 is very sensitive to the neutron γ separation

In Fig. 5.24 the distributions of both variables for the $K_L^0 \to p^0 \nu\bar{\nu}$ MC "A" sample (black histogram), "B" sample (red histogram), "C" sample (blue histogram) and "D" sample (green histogram) are shown.

The resemblance of the shape of the "B" sample with the $K_L^0 \to p^0 \nu\bar{\nu}$ MC sample indicates that the clusters of the "B" sample are really produced by γ's. The discrepancy seen in the $\frac{E_1+E_2+E_3}{E_{cluster}}$ distribution comes from a difference in the γ energies.

The "D" sample might also be γ, but it suffers from fusion. Two peaks of $E_{\max}/E_{cluster}$ at 0.5 (maximum for fused γ's) and at 0.85 (maximum for single γ) (Fig. 5.22) suggest the dominance of the fused clusters. The shape of $E_{\max}/E_{cluster}$ near 1.0 is similar to that of the "C" sample, which contains a neutron cluster. Thus means that there is some contribution of the neutron events in the "D" sample.

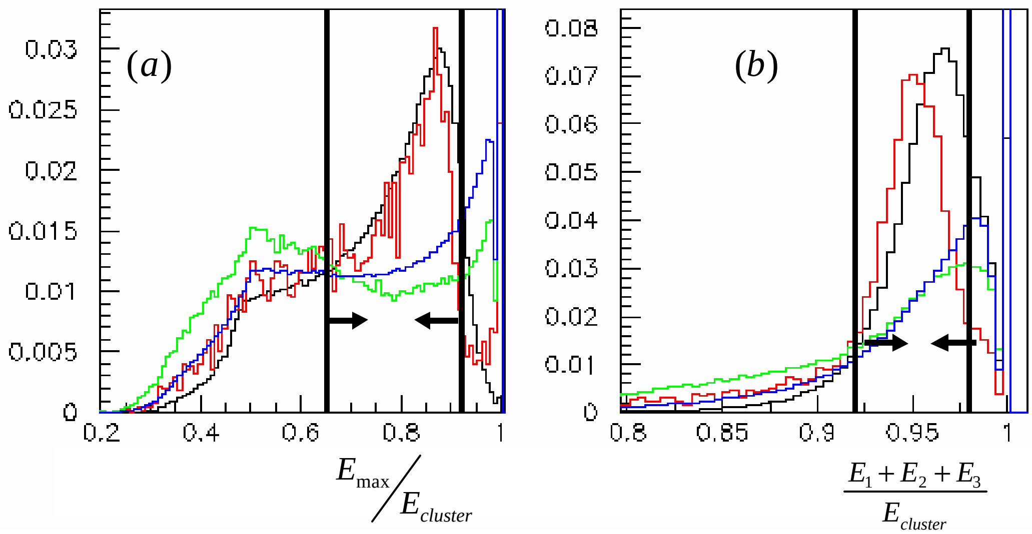

Fig. 5.24. Distribution of the cluster shape variables, $E_{max}/E_{cluster}$ (a) and $\frac{E_1+E_2+E_3}{E_{cluster}}$ (b), for "A" (black), "B" (red), "C" (blue), "D" samples (green).

The "C" sample has a cluster shape different from the $K_L^0 \to p^0 \nu\bar{\nu}$ MC sample. There is a sharp peak at the position $\frac{E_1+E_2+E_3}{E_{cluster}}=1$.

The cut points were chosen as

$$0.65 < E_{max}/E_{cluster} < 0.92 \quad \text{and} \quad 0.92 < \frac{E_1+E_2+E_3}{E_{cluster}} < 0.98.$$

- *Distance and energy balance of g's*

The cluster shape is valuable for rejection of the neutron and fused clusters, but not for the "B" samples, which are produced by neutron interactions with CC02. For this region, we have to introduce additional variables.

The distance between γ clusters on the CsI calorimeter is one of the variables as shown in Fig. 5.25(a). The blue histogram represents the "C" sample. The edge at 20 cm comes from rejection during reconstruction of the events with overlapped clusters. The distance between two clusters produced by neutrons is small, and the "C" sample can be efficiently suppressed by criteria > 50 cm. It is also effective against the "D" sample, because some neutron events exist in it. Also, one γ with high energy may produce two separated clusters in the calorimeter, which can be misidentified as two γ's.

The energy balance, $\left|\frac{E_1 - E_2}{E_1 + E_2}\right|$, of the γ's is another important variable, where E_1 and E_2 are the γ's energy. It is efficient for the "B" and "D" samples (Fig.5.25.b). Especially, in the "D" sample there are many fused clusters that have unbalanced γ energies. Since the $\left|\frac{E_1 - E_2}{E_1 + E_2}\right|$ distribution of $K_L^0 \to \pi^0 \nu\bar{\nu}$ MC is flat up to 0.5, we choose 0.5 as the cut point.

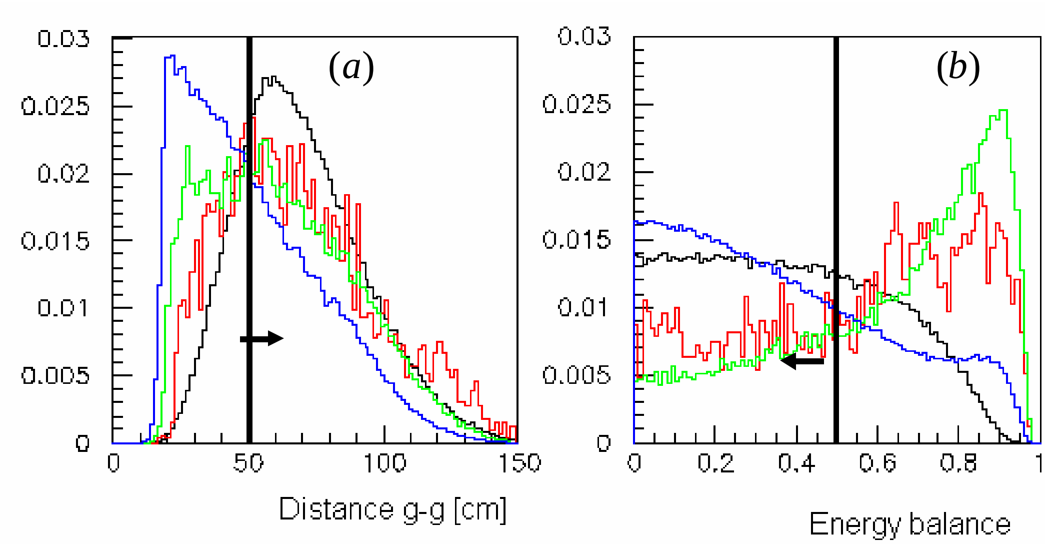

Fig. 5.25 Distribution of the distance between two clusters (a) and the energy balance, $\left|\frac{E_1 - E_2}{E_1 + E_2}\right|$, of two γ's (b) for the MC $K_L^0 \to \pi^0 \nu\bar{\nu}$ sample (black), "B" (red), "C" (blue), "D" samples (green).

5.3.5 Normalization channels

5.3.5.1 *6 γ events and reconstruction of $K_L^0 \to 3\pi^0$ decay*

$K_L^0 \to 3\pi^0$ decay was reconstructed using a skimmed 6 γ stream. There are 15 different combinations of a clusters into π^0's. The combination with the minimum χ^2 was chosen as the true pairing. The decay vertex was then calculated as the mean value of the π^0 vertexes, and was shifted in the transverse plane, as described above.

In order to eliminate edge effects in the CsI calorimeter, we rejected events with a reconstructed hit positions inside the KTeV crystals (around beam hole) and in the outside region

(R>80cm). Also, at the current stage, we didn't consider overlapping showers, and so the distance between the reconstructed hit positions of the γ's is required to be grater tha n 21 cm.

Fig.5.26 shows the distribution of the differences between individual γ timing and the mean value. The corrections of the time-of-flight from the reconstructed decay point to the hit point in CsI for each γ were also applied. The width of the distribution is 0.5 ns. Also for event selection we required the γ timing to be within 3σ of the peak.

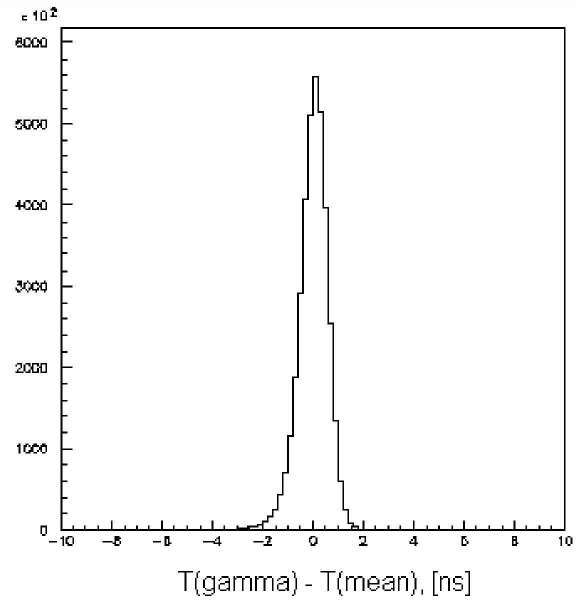

Fig. 5.26 Distribution of the difference between individual γ timings and mean values. σ is 0.5ns.

In a MC simulation we generated 0.21 days of equivalent statistics for the $K_L^0 \to 3\pi^0$ decays. In order to reduce the acceptance loss due to accidental events, we didn't apply any cuts for veto response to the data. For the MC we applied an online-type veto. Under these conditions, we started to check the consistency between the raw spectra of the data and MC.

In Fig. 5.27 we compare the raw spectra of the reconstructed invariant mass of 6γ (a), and the reconstructed decay vertex (b) between the data and MC are presented. As can be seen, MC reasonably reproduces the shape of the data. Other kinematical variables also have good agreement between the data and MC. In the reconstructed invariant mass spectrum there is a clean peak at the K^0 mass position of 498 GeV/c^2. However, it suffers from low and high mass tails.

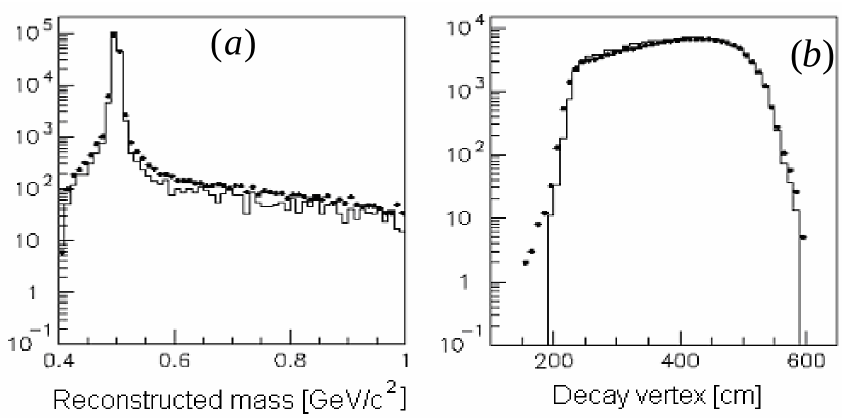

Fig. 5.27 Comparison of the data and MC of the raw spectra of the reconstructed invariant mass of the 6 γ's (a) and the decay vertex (b). The histogram is $K_L^0 \to 3\pi^0$ MC; the dots are data.

The main source of these tails is a miss-pairing of the γ's to p^{0}. During a paring of the γ's, we selected the combination with the minimum c^{2} and rejected the other combinations. Fig.5.28 shows the correlation between the reconstructed mass of 6γ and the ratio of the decay vertex with the best c^{2} to that with the second c^{2}. As can be seen, the low and high-mass tail events are grouped in a specific region.

Let's select the mass tail events and the mass region events as shown in Fig. 5.28. In Fig. 5.29 the distribution for these samples of the best c^{2} (a) and the second c^{2} (b) are shown. The mass region events are presented by solid lines and the tail events by dashed lines. As can be seen, most tail events have a small second c^{2} value. This means, for tail events we choose the combination with the best c^{2}, while the combination with the second c^{2} is true. This kind of events is already suppressed by 3 orders (Fig.5.27.a), but the miss-combination tail makes a contribution to the mass region events, and the reconstructed kinematics is incorrect. To suppress the miss-combination, we apply cuts for the best c^{2} to be less than 2 and the second c^{2} to be more than 20. This greatly suppresses tail events (Fig. 5.34).

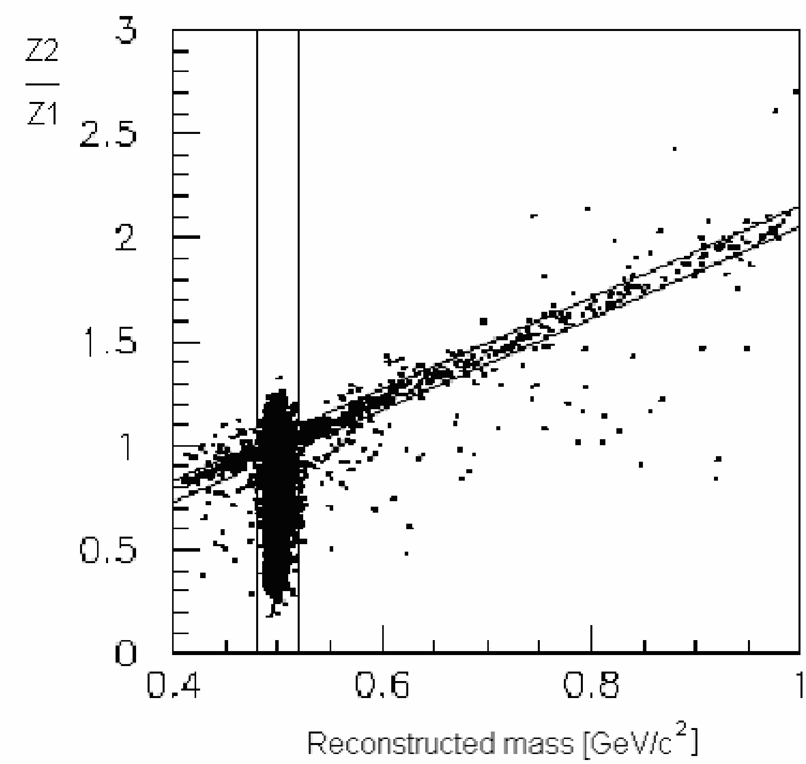

Fig. 5.28 Correlation between the reconstructed mass of 6γ and the ratio of the reconstructed decay vertexes with the best c^{2} (Z1) over with the second c^{2} (Z2) combination.

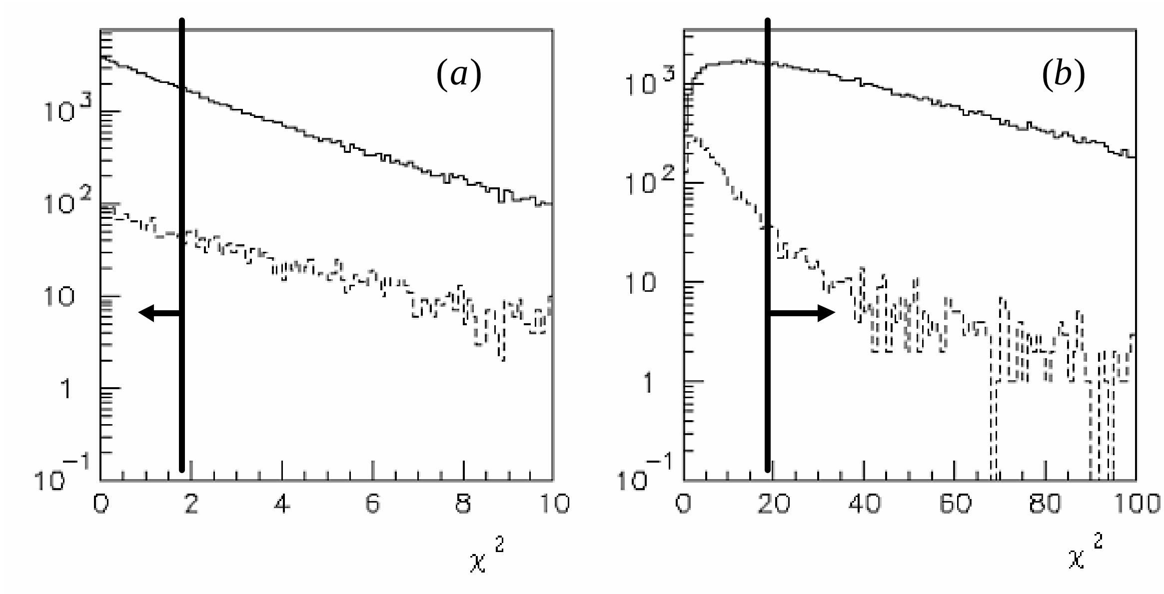

Fig. 5.29 Distribution of the best c^2 (a) and the second c^2 (b) for mass region events (solid line) and tail events (dashed lines).

We also corrected the shift of the decay vertex in the transverse plane by using a line connecting the target and the center-of-gravity of the 6 clusters in the CsI calorimeter plane (section 5.2.3). This reflects the size of the beam coming from the target (Fig. 5.30.b). It was required to be less than 4 cm. The transverse momentum was also limited to be less than 10MeV/c (Fig. 5.30.a). Finally, the decay region was selected from 300 cm to 500 cm.

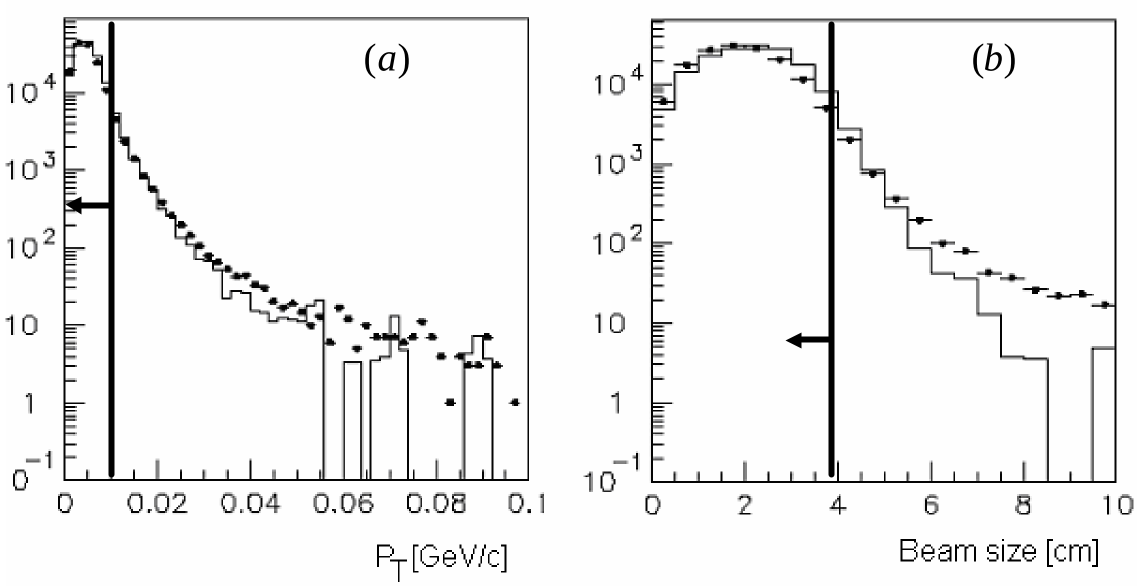

Fig. 5. 30 Distribution of the reconstructed P_T (a) and beam size (radial position of the decay vertex) of the 6 γ's (b).

At first, the cut points were chosen by eye which considering the shape of the distributions. We then made an optimization of the cut points. The events inside 3 *s* of the peak were considered to be good events, and all others as bad events. We applied all cuts to their nominal values, and then released one cut. The ratio of the number of events under two conditions (with and without applying given cut) gave us the efficiency of this cut. By changing the cut point, we tried to find the optimum point between losing good events and suppressing bad events.

In Fig. 5.31 the example of the cut optimization for the beam size is shown. By applying different cut thresholds we lose events inside the mass region (Fig. 5.31.a) and also suppress events outside of the mass region, bad events (Fig 5.31.b). The solid line is the data and the dashed ones is the MC. Both distributions were normalized by the number of events when all cuts except the given ones were applied. The discrepancy between the background rejections might come from accidental events in the CsI calorimeter.

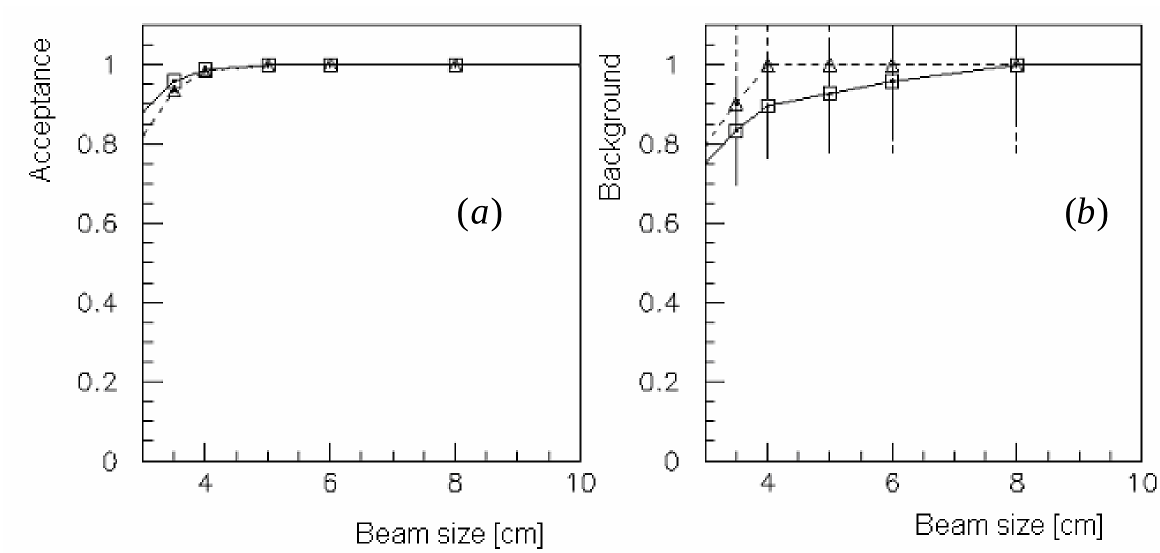

Fig. 5.31 Behaviors of the loss of good events (a) and the rejection of bad events (b) under different cut thresholds for the beam size. For a of the given cut, all other cuts were applied to their nominal values. The solid line is the data and the dashed one is the MC.

By taking the ratio of these curves, we can see an improvement of the signal-to-noise ratio under various cut thresholds (Fig 5.32). Finally, the cut point was chosen as 4cm. A tighter threshold results in losing events in the mass region. Also, other cuts were studied by the same method, and the cut thresholds were optimized to reduce the mass tail events and saving the mass region events.

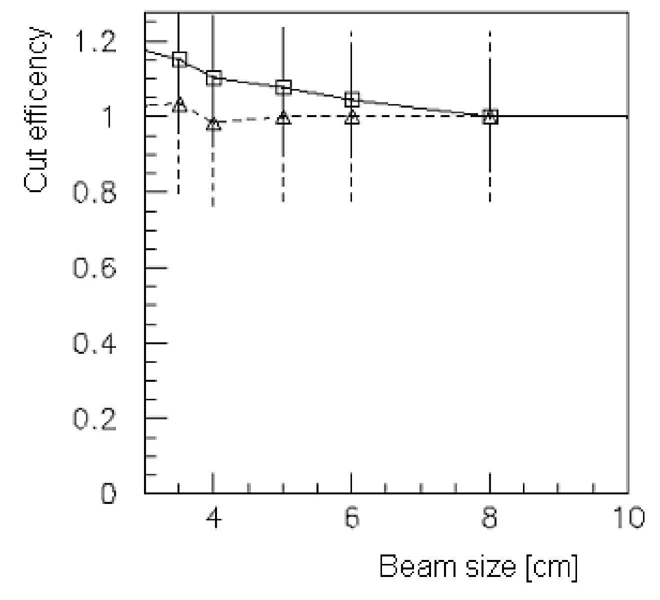

Fig. 5.32 Signal-to-noise ratio under various cut thresholds of the beam size. All other cuts were applied at their nominal values. The solid line is the data and the dashed one are the MC.

By these cuts we suppressed the tail events (Fig.5.34) by one order more. The ratio of the tail events (outside 3σ of mass peak) over the mass peak events (inside 3σ of mass peak) was improved from 11.6% to 0.7%. In total, the 29669 events remained inside 3σ of the peak after all cuts.

Fig. 5.33 summarizes the acceptance loss due to individual cuts. The solid line is the data and the dashed line is the MC. The acceptance loss due to the cuts is in agreement between the data and the MC, except for the best χ^2 cut. Currently, because we can't reproduce the resolution of our calorimeter in MC, there is this discrepancy. We will solve this problem later.

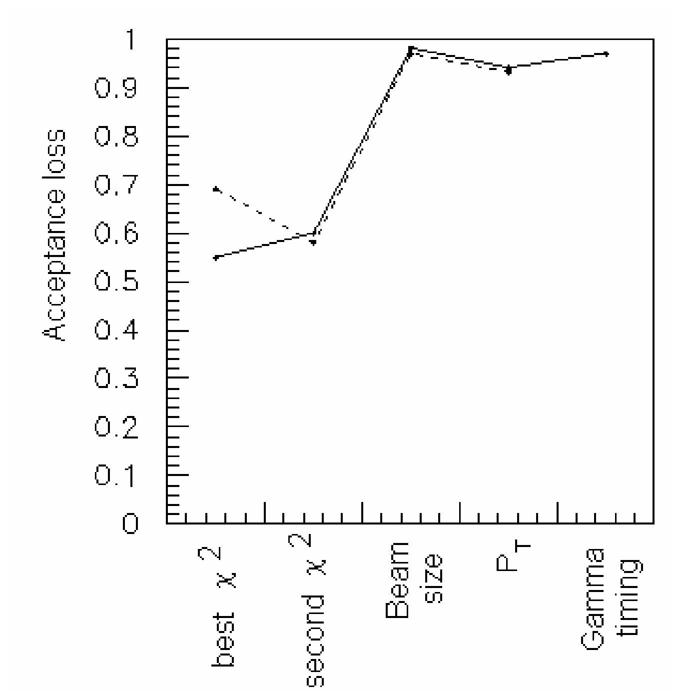

Fig 5.33 Behavior of the acceptance loss due to the various cuts for the data (solid line) and MC (dashed line)

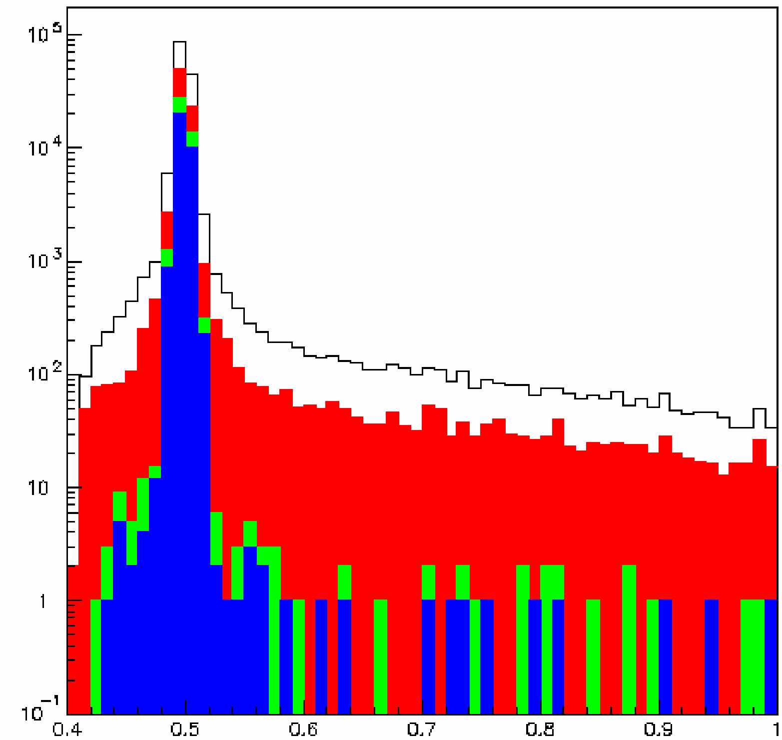

Fig. 5.34 Distribution of the reconstructed invariant mass of 6γ; raw spectrum (blank histogram), after the best (red histogram) and second c^2 cuts (green histogram), after remaining cuts (blue histogram).

The acceptance of the $K_L^0 \to 3p^0$ decay was calculated as the ratio of the number of events saved after all cuts over the number of the generated K^0 at the exit of the C6 collimator in the MC:

$$Acc = (1.9 \pm 0.02) \cdot 10^{-5}.$$

In order to eliminate the discrepancy in the acceptance loss due to the best c^2 cut between the data and the MC we corrected the acceptance by the ratio of the loss due to this cut in the MC(69.4%) and in the data (53.9%) as

$$Acc^* = 1.9 \cdot 10^{-5} \frac{53.9\%}{69.4\%} = (1.45 \pm 0.01) \cdot 10^{-5}.$$

Also, the acceptance loss due to a γ timing cut of 0.97 was included;

$$Acc^* = 1.45 \cdot 10^{-5} \bullet 0.97 = (1.41 \pm 0.01) \cdot 10^{-5}.$$

In one day of data collection we obtained 29669 events of the $K_L^0 \to 3p^0$ decay with an acceptance of $(1.41 \pm 0.01)\text{x}10^{-5}$.

5.3.5.2 *4 g events and reconstruction of $K_L^0 \to 2p^0$ decay*

The $K_L^0 \to 2p^0$ decay was reconstructed using the skimmed 4γ stream. There are only 3 different combinations of the clusters into p^0's. The combination with the minimum c^2 is chosen as the true pairing. The decay vertex was then calculated as the mean value of the p^0 vertexes, and was shifted in the transverse plane, as described above.

Also, the events with border hits were rejected, and the distance between the γ's was required to be greater then 21 cm. The difference in the γ timing was required to be less then $\pm 3s$ (s=0.53n) of the peak.

In the MC simulation we generated about 10 days of equivalent statistics of K^0_L at the exit C6 collimator, and decayed it in the $K_L^0 \to 2p^0$ decay mode. In order to study the background contribution, we used the $K_L^0 \to 3p^0$ MC considering it as 4γ events. Also, only online type vetoes were applied for MC, and nothing for the data (assuming the online veto during data taking)

Fig. 5.35 shows the reconstructed invariant mass (a) of 4γ and the reconstructed decay vertex (b). The green histogram is the $K_L^0 \to 2p^0$ MC, the red one is the $K_L^0 \to 3p^0$ MC and the black one is the total MC. The data are presented by dots. As can be seen, the MC reproduces the shape of the data distribution reasonably well. The main background is from $K_L^0 \to 3p^0$ decays. Such a large contribution is due to the high thresholds for veto detectors. In the invariant mass spectrum, there is a peak at a K^0 mass of 498 GeV/c^2. However, it suffers from a tail of $K_L^0 \to 3p^0$ events.

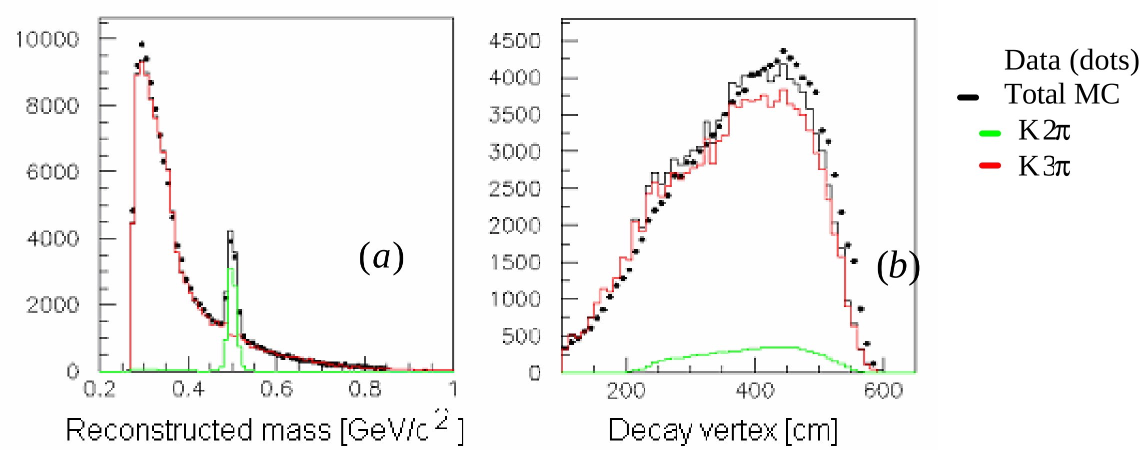

Fig. 5.35. Comparison of the data and the MC of the raw spectra of the reconstructed invariant mass of the 6γ (a) and the decay vertex (b). The histograms are the MC; dots are the data.

At first we checked the miss-pairing problem using the $K_L^0 \rightarrow 2\pi^0$ MC. We took the correlation between the ratio of the decay vertexes for the best χ^2 and the second χ^2 and the reconstructed invariant mass. It is shown in Fig.5.36. We observed the same group of events as in the case of the $K_L^0 \rightarrow 3\pi^0$ decays (Fig.5.28). We thus applied the cuts for both the best and the second χ^2's in the same way as in the $K_L^0 \rightarrow 3\pi^0$ decays. Also, the beam size was required to be less than 3 cm.

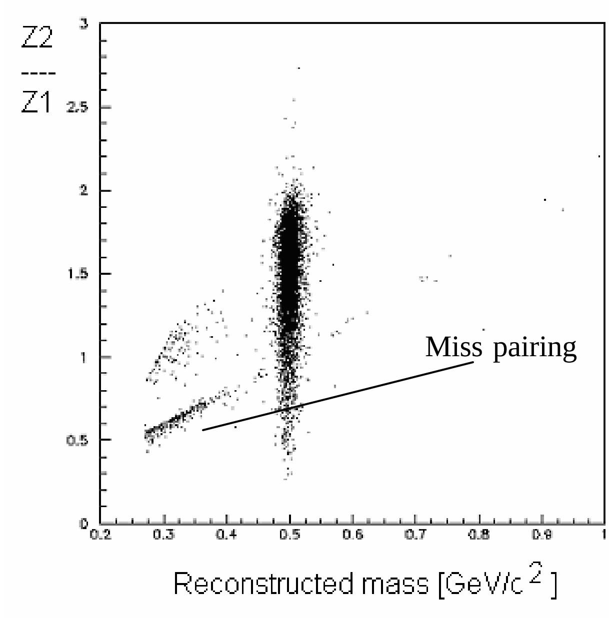

Fig. 5.36 Correlation between the ratio of the reconstructed vertex with the best χ^2 (Z1) over one with the second χ^2 (Z2), and the reconstructed invariant mass of 4γ clusters. This is a result of the $K_L^0 \rightarrow 2\pi^0$ MC.

Since the $K_L^0 \rightarrow 2\pi^0$ decay is a 2-body decay, the π^0's would fly away in one plane. In other words, the angle between the projections of the π^0 momentum vectors in a plane perpendicular to the beam axis must be 180 degrees. We required the angle to be greater than 179^o.

One more kinematical cut that is useful for background rejection from the $K_L^0 \rightarrow 3\pi^0$ decay is the angle between the momentum vectors of the π^0's. Mostly background events from the $K_L^0 \rightarrow 3\pi^0$ decay are located in a small angle region (Fig. 5.37). Unfortunately, the $K_L^0 \rightarrow 2\pi^0$ decays are also concentrated there, but require the angle to be greater than 15^o; we reject many more background events than we lose $K_L^0 \rightarrow 2\pi^0$ events, so the signal-noise ratio might be improved.

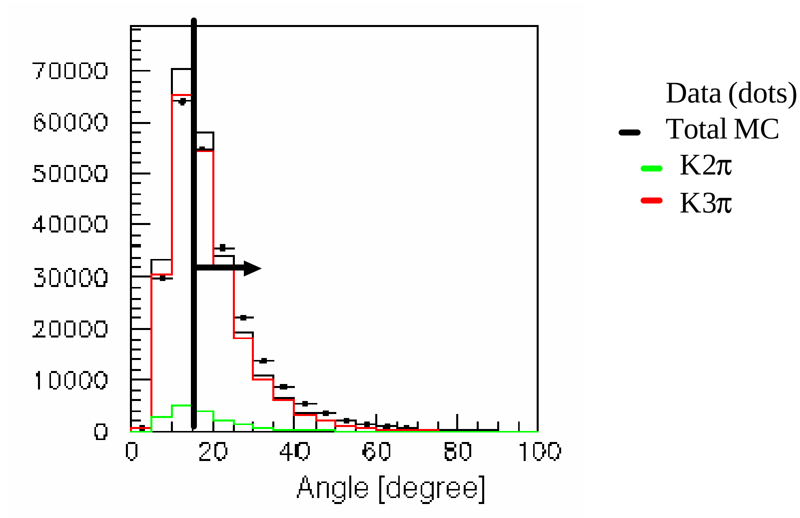

Fig 5.37. Distribution of the reconstructed angle between vectors of the p^{0} momentum vectors in 3D space.

We used the 3x3 matrix of CsI crystals for an energy calculation of each γ. If the found cluster comes from a single γ, the energy might be contained mostly in the local maximum of the cluster. If the cluster was made by fused γ's, the cluster is large and the energy is widely spread among the crystals in the cluster. Fig. 5.22(b) shows the distribution of the ratio of the energy of the local maximum over the energy of the cluster, $E_{\max}/E_{cluster}$, for fused events (distance between γ's less than 14 cm).

Fig 5.38 (b) shows the distribution of $E_{\max}/E_{cluster}$. The MC well reproduces the data, and we set the cut point as 0.5.

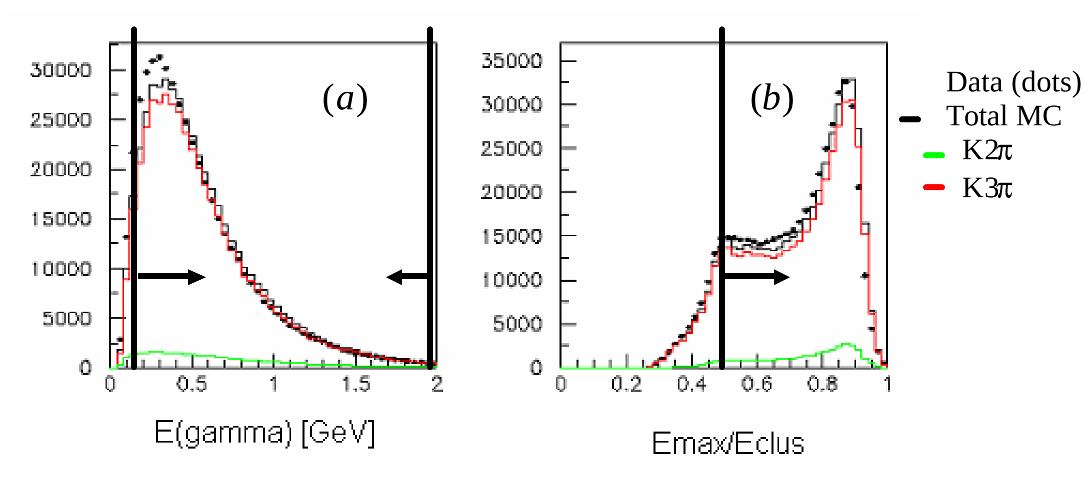

Fig. 5.38 Distribution of the energy of the γ's (a) and the ratio of the local maximum energy in the cluster to the total energy of the cluster (b).

We then required the transverse momentum of the reconstructed K^0 to be less 15 MeV/c; the decay region was selected from 300 cm to 500 cm. Also, the energy of the γ's should be greater than 150MeV and less than 2GeV (Fig 5.38.a).

After fixing the set of cuts, we optimized the cuts point by the same method as in the $K_L^0 \to 3\pi^0$ case. However, the definitions of good events and background events were different. The mass spectrum was fitted by Gaussian plus linear functions in the region near the mass peak. The number of background events in the 3σ mass region was estimated from a linear function, and was subtracted from the total number of events in the 3σ mass region. The remaining events were considered as good events. Optimization was done in terms of improving the signal-to-noise ratio.

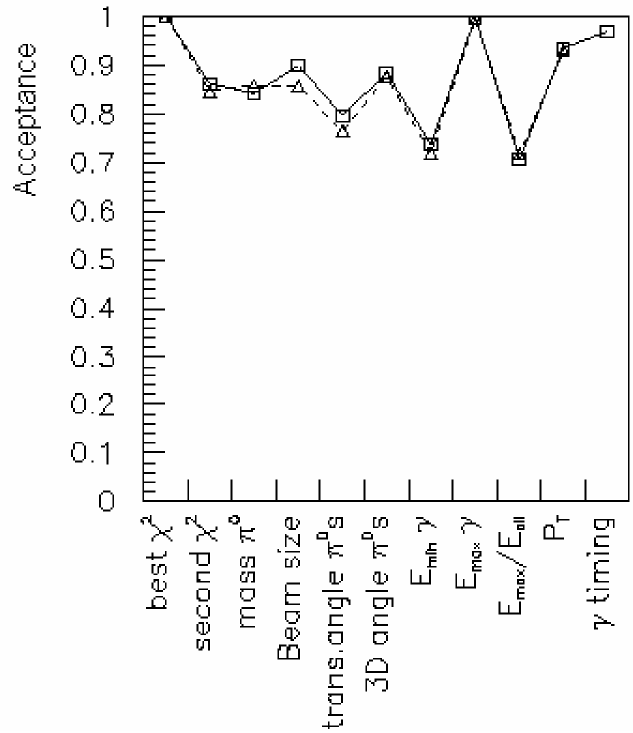

Fig 5.39 The behavior the acceptance loss of the various cuts for data (solid line) and MC (dashed line)

Fig. 5.39 shows the result of the cut optimization – the relative loss events under each cut – the ratio of the number of good events after applying all cuts, except given and after applying all cuts. The solid line is the data and the dashed line is the MC. As can be seen, there is a good agreement between them. The best χ^2 cut and the maximum γ energy at these values are not sensitive to the acceptance loss.

Finally, by these cuts we suppressed the contribution of the $K_L^0 \to 3\pi^0$ decays in the mass region of the $K_L^0 \to 2\pi^0$ decays. The ratio of the background events (estimated based on a linear function fitting) and the good mass peak events (inside 3σ of mass) were improved from 42.7% to 2.7%. In total, 991.4 $K_L^0 \to 2\pi^0$ events remained after all cuts. Fig. 5.40 shows the distribution of the reconstructed mass after all cuts (a).

The acceptance of the $K_L^0 \to 2\pi^0$ decay was calculated as the ratio of the number of events saved after all cuts over the number of generated K^0's at the exit of the C6 collimator:

$$Acc = (1.12 \pm 0.01) \cdot 10^{-4}.$$

The acceptance loss due to the γ timing cut was taken into account as 0.97. Finally, we had 991.4 $K_L^0 \to 2\pi^0$ decay events with an acceptance of $(1.09 \pm 0.01)\cdot 10^{-4}$ and only a 2.7% background contribution to the mass region.

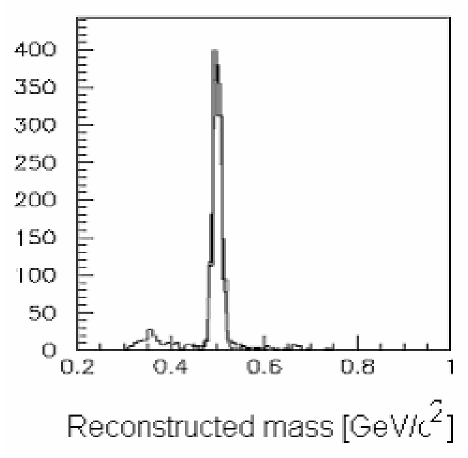

Fig. 5.40. Distribution of the reconstructed invariant mass of 4γ after all cuts.

5.3.5.3 *2-γ events and reconstruction of $K_L^0 \to \gamma\gamma$ decays*

The same data (2γ stream) can be reanalyzed by assuming that the parent of 2γ is K_L^0 instead of π^0. This assumption moves the reconstructed decay vertex closer to the CsI calorimeter. Since the $K_L^0 \to \gamma\gamma$ decay has no additional particle, the P_T of 2γ is balanced; we corrected the decay point in the transverse plane using the line connecting the center-of-gravity of two clusters in the CsI and the target position, as was done in the $K_L^0 \to 3\pi^0$ and $K_L^0 \to 2\pi^0$ reconstruction (see above).

In section 5.3.4, we identify the main background sources for the 2γ sample: neutral K_L^0 decay, $K_L^0 \to \pi^+\pi^-\pi^0$ mode, halo neutrons and some contribution of the core neutrons due to interactions with the material of the membrane.

As in the case of 4γ and 6γ analyses, we rejected events with border hits (inside and outside the calorimeter) and required at least 21 cm of distance between the γ hit positions.

Fig 5.41 shows the distribution of the reconstructed decay vertex. The peak near the CsI calorimeter is described by the core neutrons with some contribution from the halo neutrons and the $K_L^0 \to \pi^+\pi^-\pi^0$ mode. The $K_L^0 \to 3\pi^0, 2\pi^0$ neutral decays have tails in the signal region, but $K_L^0 \to \gamma\gamma$ decays dominate in the decay region.

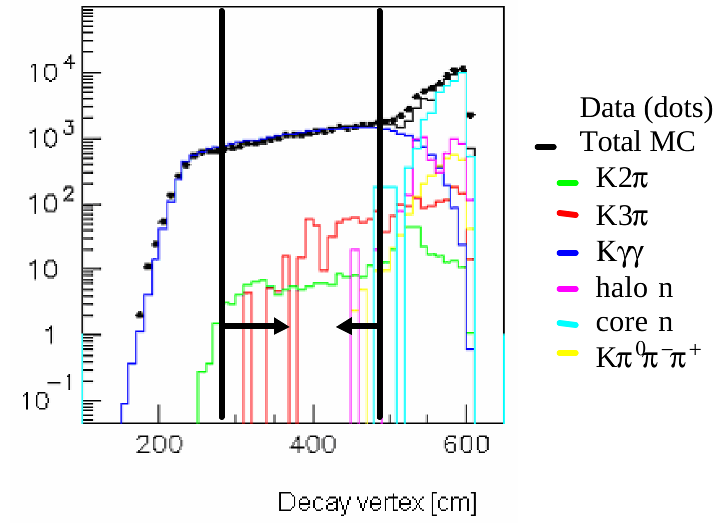

Fig. 5.41. Reconstructed decay vertex distribution.

In order to purify $K_L^0 \to gg$ decays, we applied cuts for the beam size and P_T as 4 cm and 15 MeV/c, respectively. Most of the events outside of the beam size and large P_T came from neutrons (Fig. 5.42). Halo neutrons and $K_L^0 \to p^+ p^- p^0$ events distribute flat in both the beam size and P_T. The distributions of neutral decays was also extend to a large beam size and P_T.

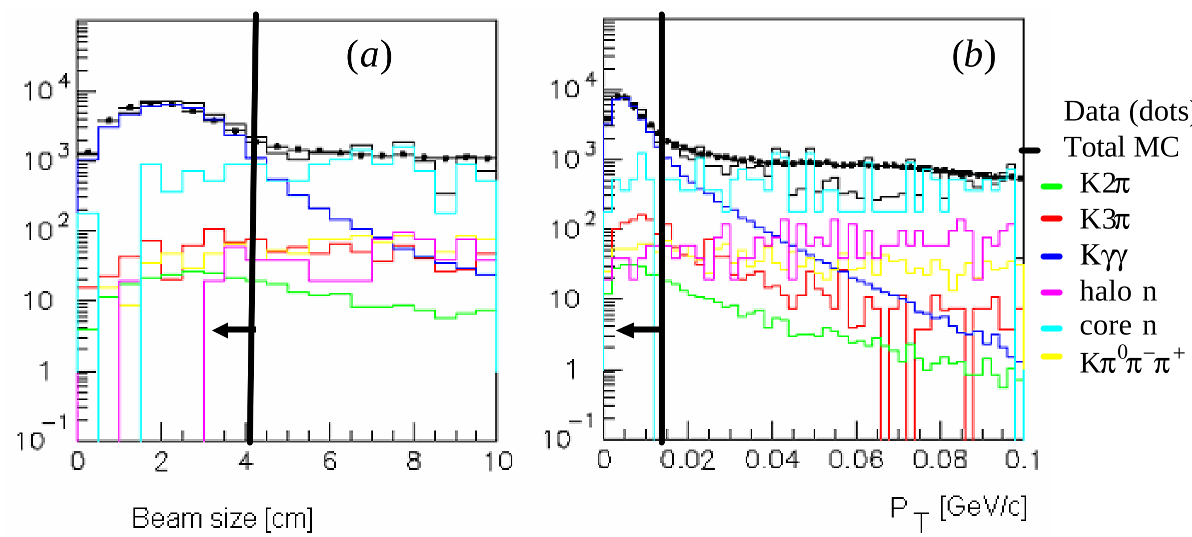

Fig.5.42 Distribution of the beam size (a) and P_T (b) of the reconstructed K^0_L. The total MC is shown by the black histogram.

Core neutron events are mostly located near the CsI calorimeter, but still have a tail touching the signal region. In order to reduce this tail, we applied the $E_{max}/E_{cluster}$ and $\frac{E_1+E_2+E_3}{E_{cluster}}$ cuts, which are sensitive to the neutron/ γ separation, as described in section 5.4.3. The distributions of $E_{\max}/E_{cluster}$ and $\frac{E_1+E_2+E_3}{E_{cluster}}$ (Fig. 5.43) are similar to the case of p^0, but the set of events is different because some events can't be reconstructed assuming the K_L^0 mass. The optimal region for $E_{\max}/E_{cluster}$ was found to be 0.55-0.95 and that of for $\frac{E_1+E_2+E_3}{E_{cluster}}$ was 0.9-0.975.

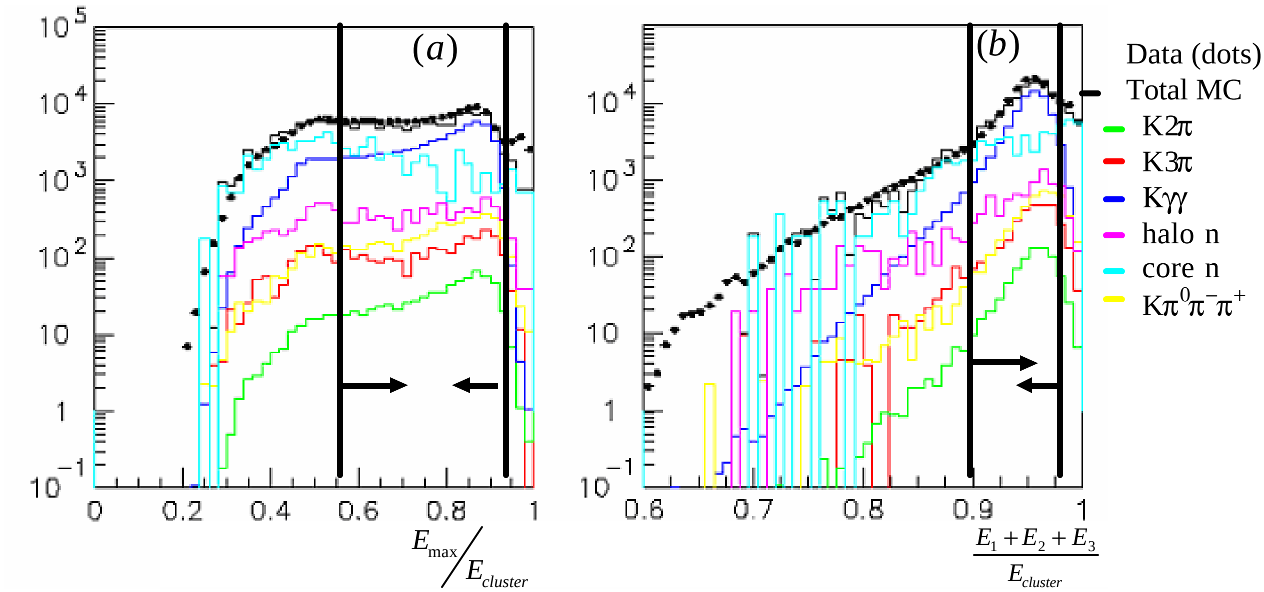

Fig. 5.43 Distribution of the ratio of the local maximum energy of a cluster over the total energy (a) and the sum of three crystals with the biggest energy deposit in the cluster over the energy of the cluster (b). The neutrons and γ clusters have different shapes of these distributions.

The decay vertex region was set as 300-500 cm.

Because the MC well reproduces the data, we used the ratio of the $K_L^0 \to gg$ MC and backgrounds MC samples for optimizing the cuts. The acceptance losses for $K_L^0 \to gg$ due to individual cuts are shown in Fig 5.45. Also, from MC we obtained the remaining backgrounds to be 0.7% (Fig.5.44).

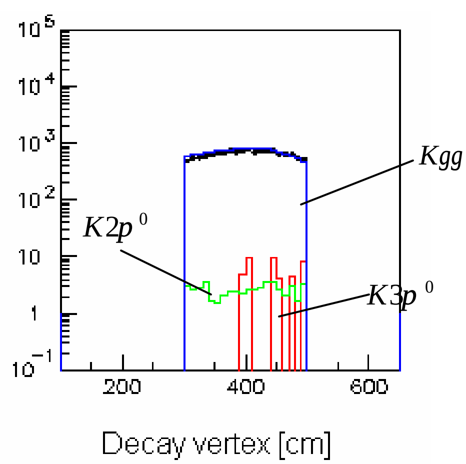

Fig 5.44 Decay vertex distribution after applying all cuts. The dots are data.

Finally, after applying all cuts, we obtained 13037 events. Among them, 0.7% are background and 12951 events are signals. The acceptance was estimated from MC as

$$Acc = (2.157 \pm 0.005) \cdot 10^{-3},$$

where 4% of acceptance loss due to timing cut (3 s) was taken into account.

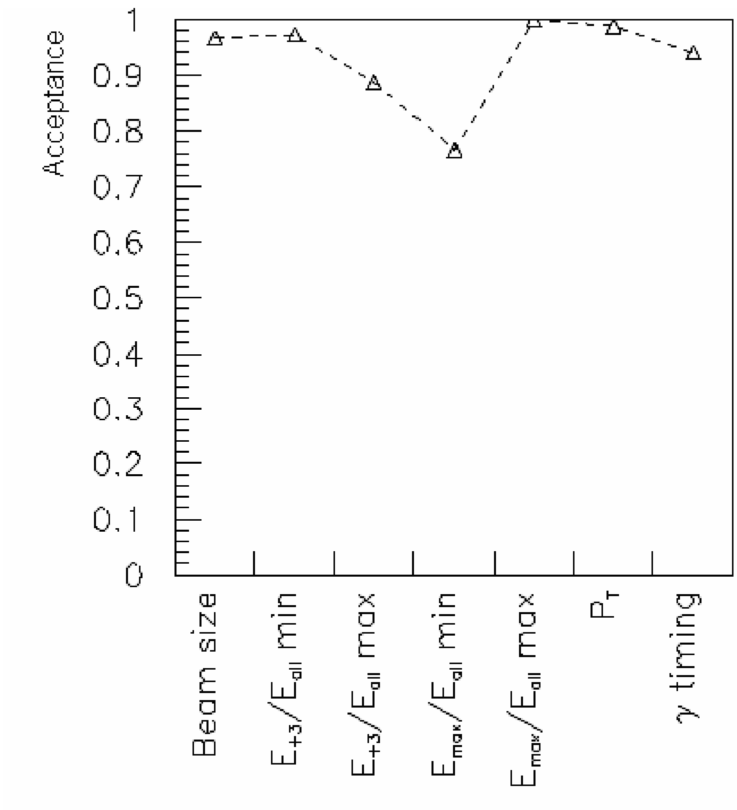

Fig.5.45 Distribution of the acceptance loss due to the individual cuts. All cuts, except for the given one, were fixed at their values, and the given cut was varied.

5.3.5.4 *Comparison of the branching ratios among three neutral decay modes*

The neutral decay modes will be used to estimate of the number of K^{0}'s and for a BR estimation of the $K_L^0 \rightarrow p^{0} \nu\bar{\nu}$ decay. It is important to check the consistency of all reconstructed modes. This will show the reliability of our reconstruction procedures.

In Table 5.3 we summarize the yields of the neutral decays $K_L^0 \rightarrow 3p^{0}, 2p^{0}, gg$ in one day. The branching ratios, BR(PDG), are values given by the Particle Data Group [42].

Table 5.3 Summary of the reconstructed neutral K^0_L decays.

	$K_L^0 \to 3\pi^0$	$K_L^0 \to 2\pi^0$	$K_L^0 \to \gamma\gamma$
BR(PDG)	21.13%	$9.27\text{x}10^{-4}$	$5.86\text{x}10^{-4}$
Number of reconstructed events (background are subtracted)	29669	991.4	12951
Acceptance	$1.41\text{x}10^{-5}$	$1.09\text{x}10^{-4}$	$2.157\text{x}10^{-3}$
Backgrounds contribution		2.7%	0.7%
Number of K^0_L (N^*)	$0.99\text{x}10^{10}$	$0.98\text{x}10^{10}$	$1.02\text{x}10^{10}$

The number of events, N^*, which are normalized by the acceptance and the branching ratio, reflects the number of K^0's coming to the setup. This number should not depend on the decay mode.

$$\frac{N^*(K3\pi^0)}{N^*(K2\pi^0)} = \frac{BR(K2\pi^0)}{BR(K3\pi^0)} \frac{N(K3\pi^0)}{N(K2\pi^0)} \frac{Acc(K2\pi^0)}{Acc(K3\pi^0)} = 1.02 \pm 0.04$$

$$\frac{N^*(K2\pi^0)}{N^*(K\gamma\gamma)} = 0.96 \pm 0.04$$

$$\frac{N^*(K3\pi^0)}{N^*(K\gamma\gamma)} = 0.97 \pm 0.02$$

It is found that the yields of all three decay modes agree with each other within 4%, which is within the statistical errors.

5.4 Study of the veto counters

One of the background sources to the $K_L^0 \to \pi^0 \nu\bar{\nu}$ decay is other K^0 decays, where 2γ hit the CsI calorimeter, and other particles hit the veto counters. Since the additional particles take away the transverse momentum, it results in fake events of $K_L^0 \to \pi^0 \nu\bar{\nu}$ if they are undetected. Such events can not be killed by kinematical cuts, and must be suppressed by the veto counters. In the E391 setup, the veto and the CsI calorimeter cover almost full 4π geometry. The calorimeter also plays the role of vetoes against additional clusters. They are suppressed by a skimming process, but it is still necessary to take care of soft γ's, which escaped the above process. We thus made a study and optimization of the veto counters and the calorimeter used as a veto.

5.4.1 Pure signal and background samples ($K_L^0 \to 3\pi^0, 2\pi^0, \gamma\gamma$)

To estimate the acceptance loss due to veto cuts, it is useful to prepare clean data samples of the decay process without any additional particles. The data sample must be purified without touching the veto by applying only the kinematical cuts. If the purity of the sample is high enough, the reduction of events due to the veto is equal to the acceptance loss. Also, by applying all veto cuts we can estimate the total acceptance loss due to the veto.

On the other hand, an event sample having additional particles is always a pure background sample, which may be used to estimate background rejection by the veto.

In a veto study, the timing information is also crucial. It can be used to separate between direct hits of real additional particles and shower leakage effects appearing in a veto detector. It greatly helps to avoid the acceptance loss.

We thus have prepared pure samples of the $K_L^0 \to 3\pi^0$, $K_L^0 \to 2\pi^0$ and $K_L^0 \to \gamma\gamma$ decays. They were purified only by kinematical cuts. No tighter veto than the online veto was applied. The background contaminations for $K_L^0 \to 3\pi^0$, $K_L^0 \to 2\pi^0$ (2.7%) and $K_L^0 \to \gamma\gamma$ (0.7%) samples were negligibly small, and the numbers of events in these samples were about 30k, 1k and 13k, respectively.

To study the background structure in the veto detectors, we must prepare pure samples of events having additional particles. One of the pure background samples is a cluster of events below the K_L^0 mass peak in the 4γ invariant mass distribution, which is shown in Fig. 5.35(a). The mass distribution is well reproduced by $K_L^0 \to 3\pi^0$ MC, where only 4 clusters are identified in the CsI calorimeter out of 6γ from $K_L^0 \to 3\pi^0$. The other background sample, which we can prepare, is events in the $K_L^0 \to \gamma\gamma$ sample with a decay vertex greater than 500 cm (Fig.5.41), and with P_T greater than 15MeV/c (Fig. 5.42.a). In this region the backgrounds from K_L^0 decays and neutrons are concentrated and the contamination of the $K_L^0 \to \gamma\gamma$ decay is suppressed.

The differences in the energy and timing distributions of the veto counters between pure signal and background samples can be used for background structure identification. The time windows for the vetoing might be selected only for those events that must be rejected without touching the shower leakage region. In this way we can reject background events without losing the acceptance for signal events. Also, because we concentrated the rejection only in the direct hit timing region, the acceptance loss is mostly due to accidental events. This means that all 3 pure signal samples must show the same acceptance loss.

For veto optimization we used a "D" sample of 2γ events (Fig. 5.21). As shown in Fig. 5.20, the events from $K_L^0 \to 3\pi^0$, $K_L^0 \to 2\pi^0$ and $K_L^0 \to \pi^+\pi^-\pi^0$ decays are mostly located in the "D" region. After removing $K_L^0 \to \gamma\gamma$ decays that have no additional particles, by selecting a large acoplanarity angle, events in the "D" region can be defined as a background sample. Kinematical cuts, which are described in previous section, are also applied in order to reduce the neutron events.

We can thus prepare three signal samples to estimate of the acceptance loss and the background sample (region "D") to study background rejection. By taking the ratio of events reduction for these signal and background samples as a function of the veto threshold, we can obtain the Figure-of-Merit of a given cut.

For a veto study it is very important to check the correlation between the energy deposit and the hit timing of the veto detectors for both the signal and background samples. Setting the time window for the veto is another important step in the veto study in order to keep the acceptance for the signal.

5.4.2 Veto study of each detector

The procedure for the study of the veto detector is as follows:

- Study the correlation between the energy deposit and the hit timing for the signal and background samples and set the time window for the veto.
- Apply the various cuts for the energy deposit and calculate the acceptance loss using signal samples.
- The background rejection is estimated form the event loss of the "D" sample.
- Define the Figure-of-Merit and select the optimum point for the energy threshold.

5.4.2.1 Main barrel (MBR)

The main barrel is the main detector for a veto. It has the biggest aperture, and is most important for background rejection. The main barrel covers the decay region before the CsI calorimeter, and also some part of the CsI calorimeter, in order to prevent the particles that hit the edge of the calorimeter to escape.

Fig. 5.46 shows the correlation between the mean and the difference of the timings of the downstream and upstream PMT's for the inner modules. In those plots the large values of T(down)-T(up) and Tmean mean the upstream hit and the later timing, respectively. Figures (a,b,c) are plots for pure signal samples of $K_L^0 \to 3p^{0}, 2p^{0}, gg$. The shower leakage (backsplash) effect is seen at the same position for all samples. Figures (d,e) are plots of the background $K_L^0 \to 2p^{0}$ and $K_L^0 \to gg$ samples. The left bump near the shower leakage events is a direct hit of additional particles into MBR. The shower leakage is delayed from the direct hit.

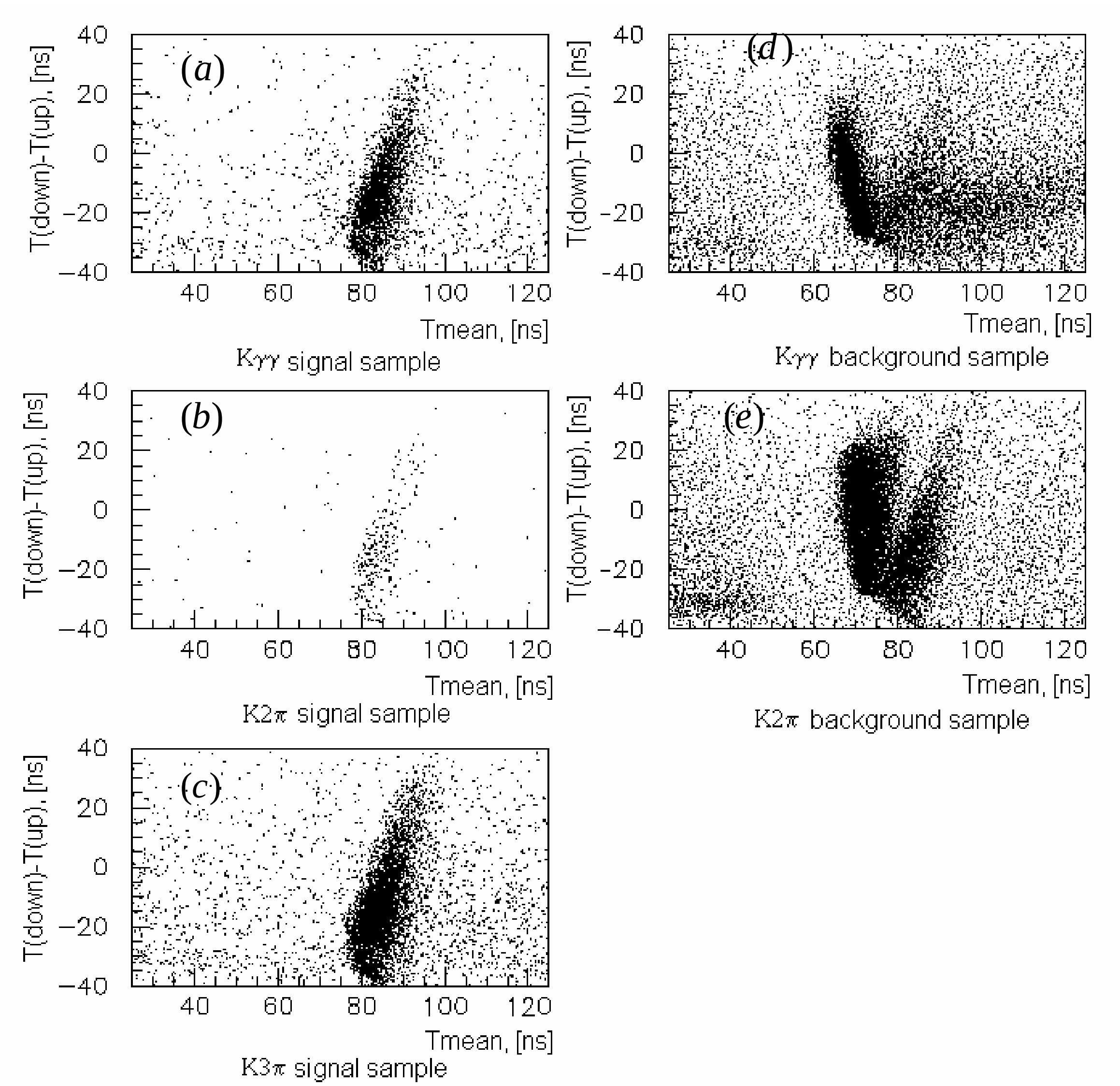

Fig. 5.46 Plots of the time difference, T(down)-T(up), vs. the mean timing Tmean=(T(down)+T(up)/2 of both PMT of inner modules for signal samples (a,b,c) and background samples (d,e).

There is an additional group of events in the 2γ background sample that does not exist in the 4γ background and other samples. These events are delayed more than the shower leakage and concentrated at the downstream part of the MBR. Fig. 5.47 shows the same correlation plots for the MC sample of $K_L^0 \to 2p^0$ (a) and halo neutrons (b) considered as 2γ events. In Fig.5.47(a) the direct hit and shower leakage events are located in the limited region. The event timing does not extend over the shower leakage. On the other hand (Fig.5.47.b), where neutrons produce two clusters in the CsI calorimeter, there is a group of events that is delayed over a shower leakage similar to the data sample, as shown in Fig. 5.46.

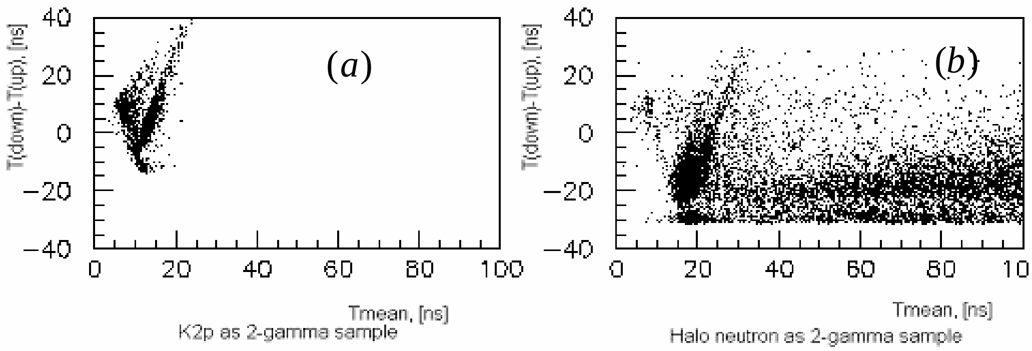

Fig. 5.47 Plot of the time difference between the downstream and upstream PMT's vs. their mean value for $K_L^0 \to 2p^0$ MC (a) and the halo neutron MC (b), considered as 2γ events.

We set the time window as shown in Fig. 5.48. From the signal sample, the region of the shower leakage was defined as shown in Fig. 5.48(a) and was then excluded from the veto (b). A veto was applied to "region 1" and also to "region 2", which was limited by ± 20ns relative to the mean line of the neutron group events.

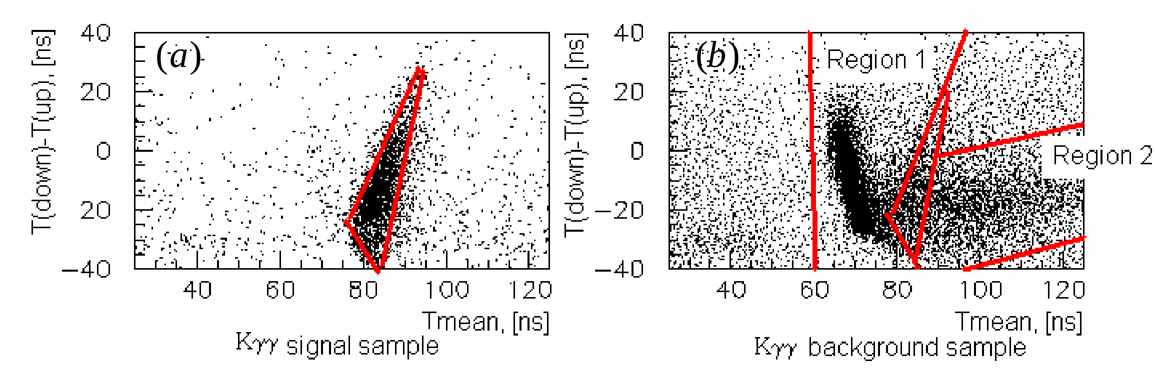

Fig. 5.48 Plot of the time difference between the downstream and upstream PMT's vs. their mean value for the $K_L^0 \to gg$ signal (a) and the background (b) samples.

Up to now, we considered the case that there are TDC signals for both PMT's. However, sometimes a soft γ generates a TDC signal only on one side. Fig. 5.49 shows plots of energy vs.

timing for the upstream and downstream inner modules in the case that there is no TDC signal on the other side.

For the upstream PMT's (Fig.5.49 a,c) we can see a clear separation of the shower leakage and direct hit events, but it is impossible for the downstream PMT's (Fig.5.49 b,d). Both effects are mixed. The delayed background exists due to neutrons. We thus applied a time and energy window for vetoing events having a single TDC, as shown in Fig.5.49 (b,d). The position of the lowest energy line was changed during optimization.

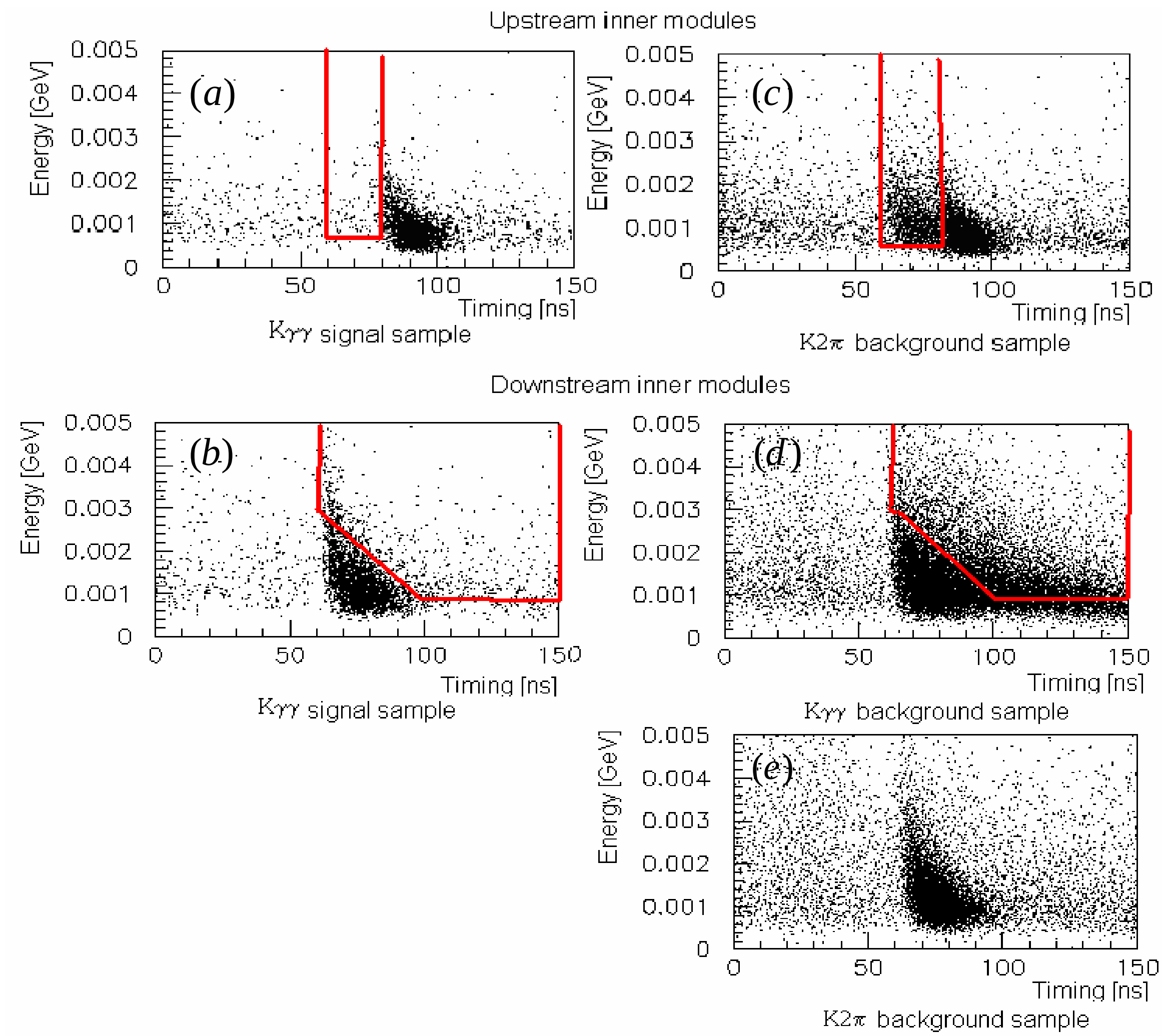

Fig. 5.49 Energy vs. Timing scatter plots for the upstream inner modules (a,c) and the downstream inner modules (b,d,e), where there is no TDC signal on the opposite side. The plots are shown for $K_L^0 \rightarrow gg$ signal samples (a,b) and $K_L^0 \rightarrow 2p^0$ background samples (c,d,e).

We then applied various energy thresholds to the signals of the MBR inner module and checked for a decreasing tendency of the number of events for signal samples (acceptance loss) and that of for the background sample (background rejection). These are shown in Fig. 5.50. The number of events without applying an energy threshold is used for normalization. The acceptance and background start decreasing with lowing the threshold to around 5 MeV. However, because the ratio of the two values has a maximum at around 3MeV, it was chosen as a cut point. The acceptance loss at 3MeV is about 5% and the rejection factor is about 10%.

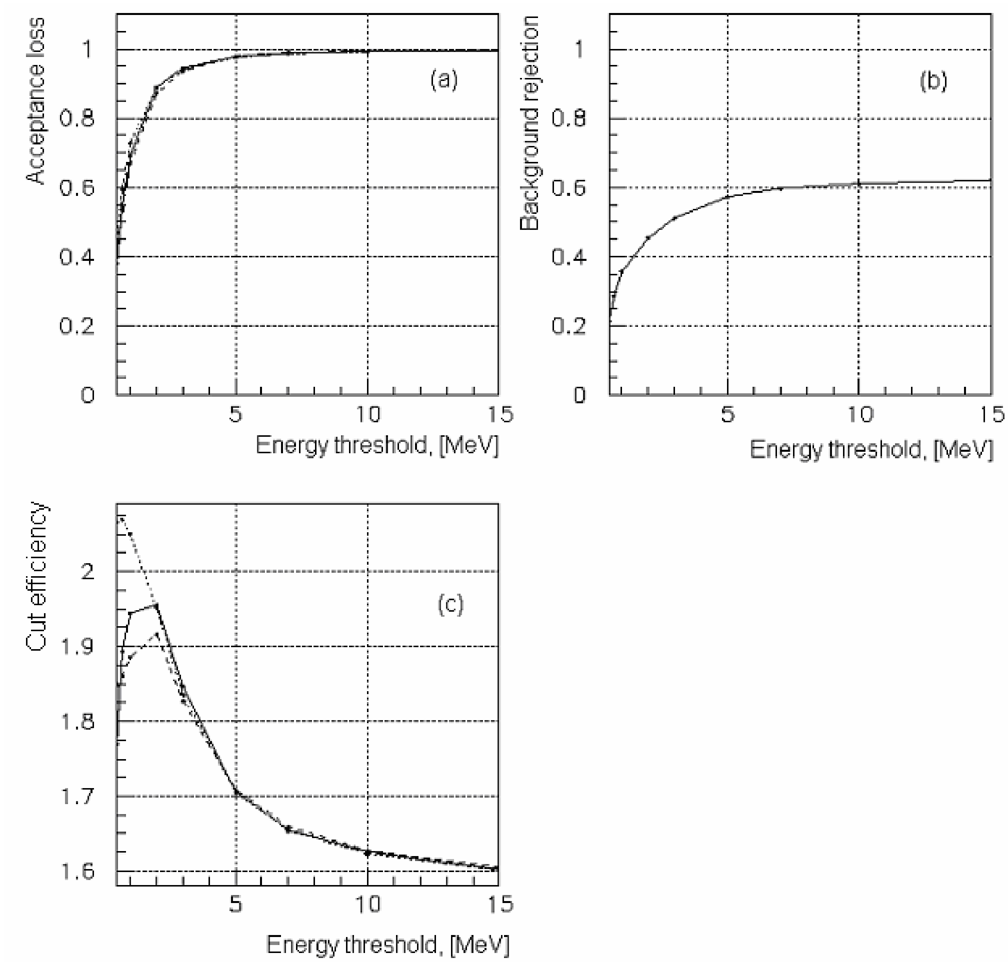

Fig. 5.50 Distribution of the acceptance loss (a), derived from the $K_L^0 \to 3p^0, 2p^0, gg$ signal samples, background rejection (b), estimated from background samples, and cut efficiency (c) obtained from the ratio of these curves. Data are shown for the inner main barrel modules. The solid line is for the $K_L^0 \to 3p^0$ sample, the dashed line is for the $K_L^0 \to 2p^0$ sample and the dotted line is the for $K_L^0 \to gg$ sample.

The energy threshold to each module was applied as follows:

- If there are both TDC signals (upstream and downstream) then select the maximum energy deposit among the upstream and downstream PMT's
- If there is only one TDC signal, then select the energy of this PMT.
- If there are no both TDC signals on both PMT's then select the maximum energy deposition among two PMT's

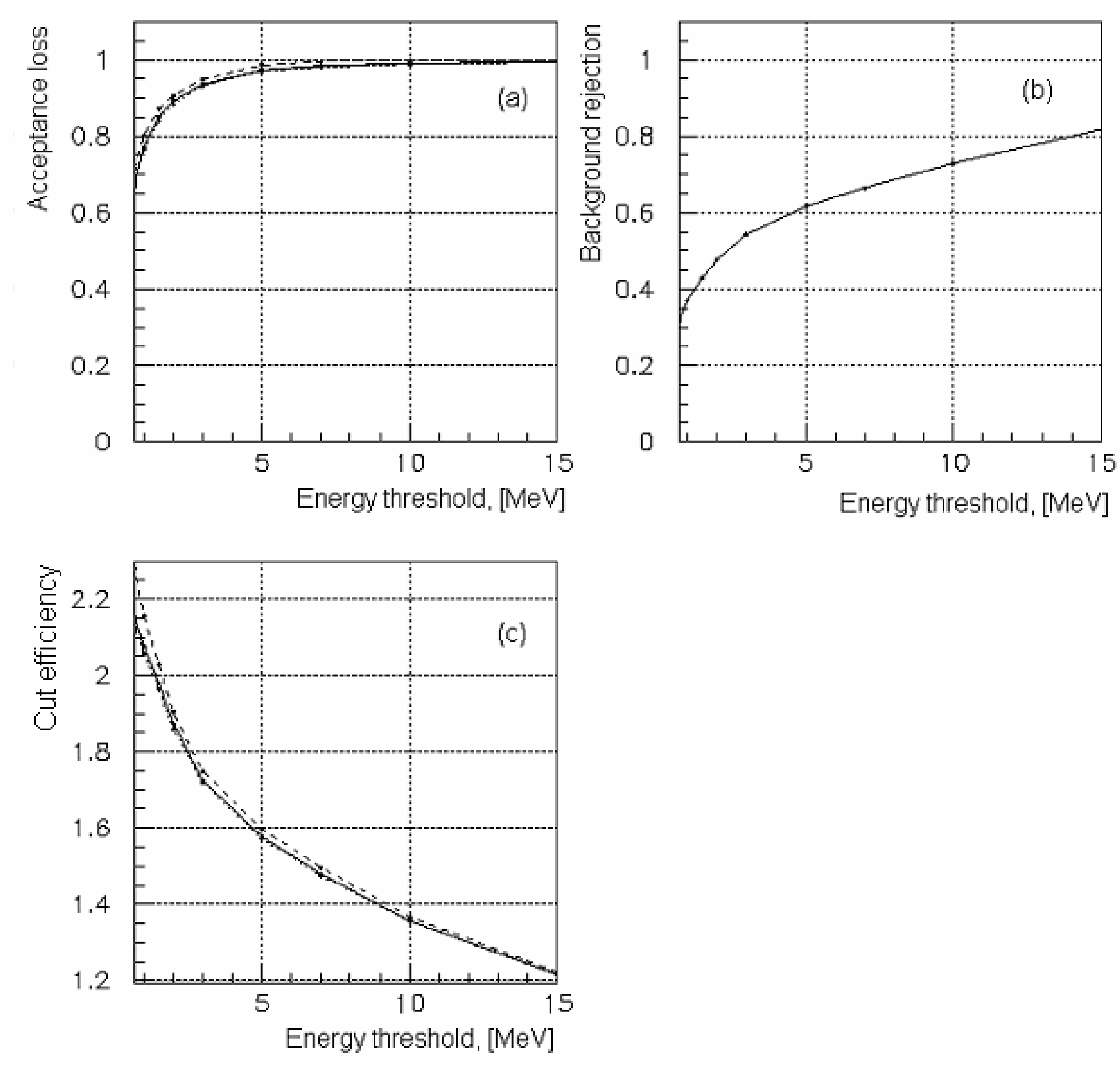

Fig. 5.51 Distribution of the acceptance loss (a), derived from $K_L^0 \to 3\pi^0, 2\pi^0, \gamma\gamma$ signal samples, background rejection (b), estimated from background samples, and S/N ratio (c) obtained from the ratio of these curves. Data are shown for the outer main barrel modules. The solid line is for the $K_L^0 \to 3\pi^0$ sample, the dashed line is for the $K_L^0 \to 2\pi^0$ sample and the dotted line is for the $K_L^0 \to \gamma\gamma$ sample

Since the outer main barrel modules suffer from a shower leakage effect much less, we can set a tighter cut for them. The same type time window was set as the inner modules. The results of the optimization are shown in Fig. 5.51 The cut efficiency (c) doesn't have a maximum point. Thus we set a 1 MeV threshold for the cut points. The acceptance loss is about 20%.

5.4.2.2 CC03

The CC03 counter is installed in the beam hole of the CsI calorimeter. Energy vs. timing plots for the $K_L^0 \to gg$ signal and background samples are shown in Fig. 5.52. In the signal sample there is a small number of events. This is because we made a tight requirement for the KTeV CsI crystals surrounding the CC03 counter at the skimming procedure. In the background sample real direct hits in CC03 remain. We set a time window of $\pm 7.4\text{ns}$, which is 3 s of the timing resolution of CC03 with respect to the CsI signals. We optimized the energy thresholds using the signal and background samples (Fig.5.53). Since there is a maximum for the cut efficiency at about 2-3 MeV, as shown in Fig. 5.53 (b), a cut point of 3 MeV was chosen. The acceptance loss is about 5%.

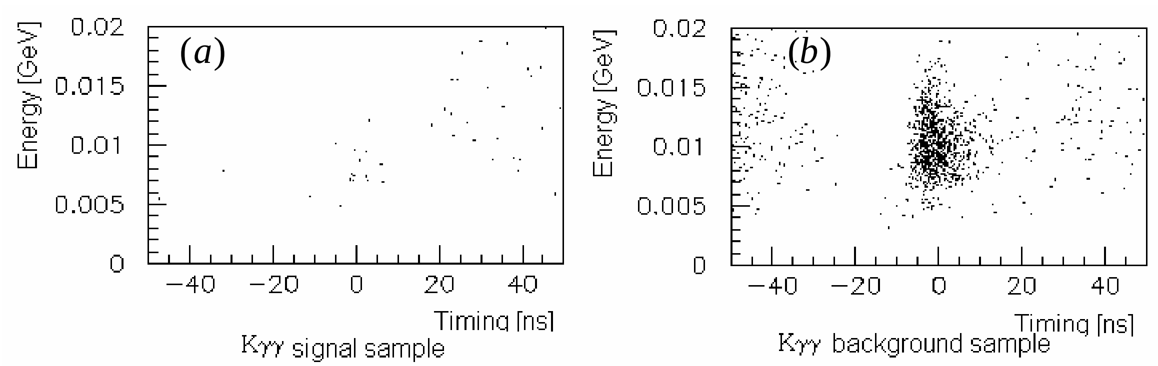

Fig. 5.52 Energy vs. Timing plot for the CC03 counter for the $K_L^0 \to gg$ signal (a) and the background (b) samples.

5.4.2.3 CC02

The CC02 counter is located at the exit of the front barrel at the end of the first decay volume. We used the $K_L^0 \to 3p^0$ signal and $K_L^0 \to gg$ background samples for optimization. The time window was defined from the energy vs. timing plot (Fig. 5.54) as of $3s$ ($\pm$5.2ns) of the timing distribution. Because the cut efficiency (Fig.5.55.b) has no maximum, we selected a cut point of 1MeV. The acceptance loss (Fig.5.55.a) is 5%, which is relatively small.

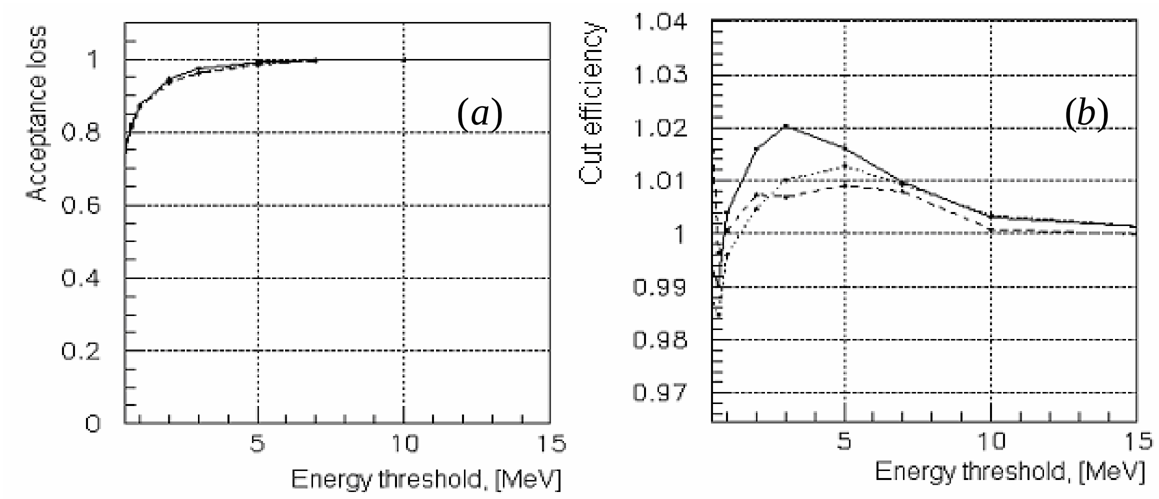

Fig. 5.53 Acceptance loss (a) and cut efficiency (b) for the CC03 detector.

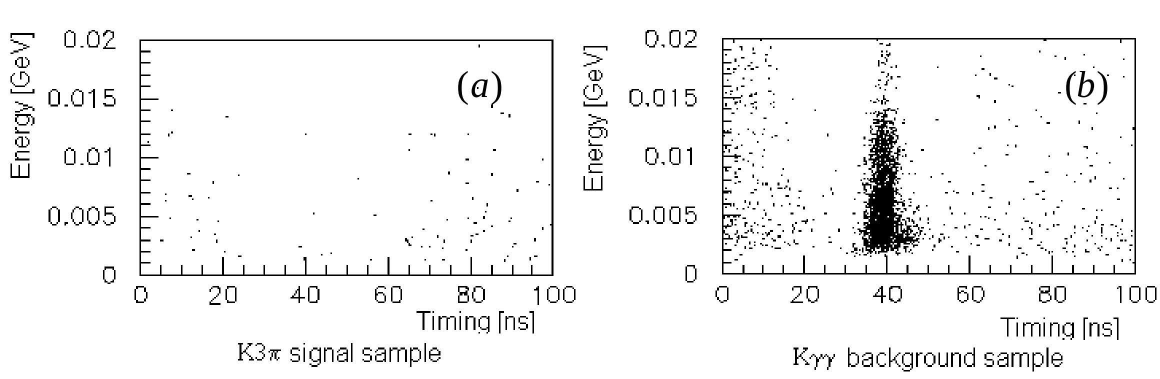

Fig. 5.54 Energy vs. Timing plot for the CC02 counter for the $K_L^0 \to 3p^0$ signal (a) and the $K_L^0 \to gg$ background (b) samples

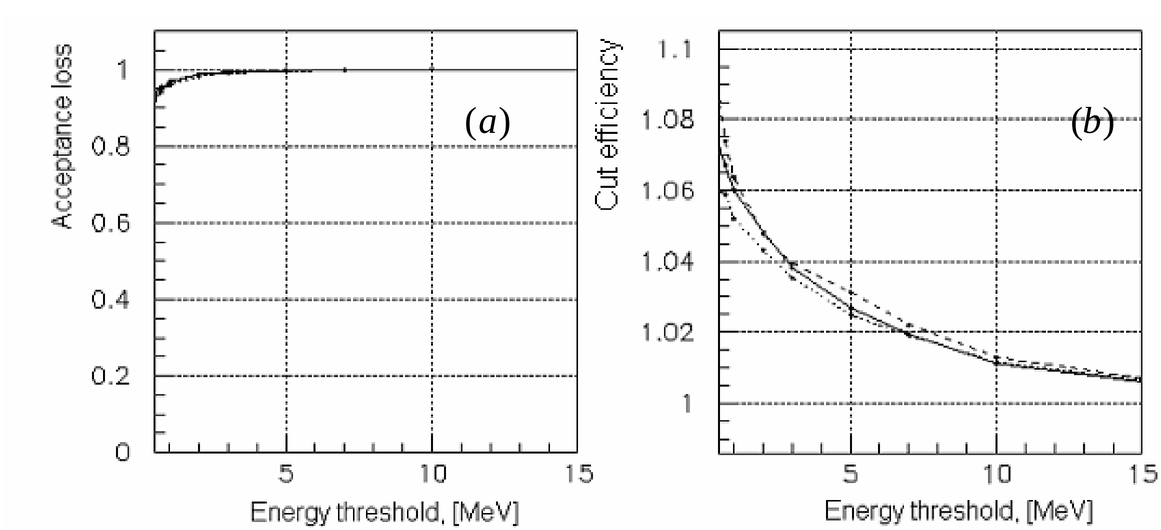

Fig. 5.55 Acceptance loss (a) and cut efficiency (b) for the CC02 detector.

5.4.2.4 Front barrel

The front barrel forms a first decay region, and also covers the upstream part of the main decay volume. Because the distance between the CsI calorimeter and the front barrel is about 3m, the shower leakage (backsplash) effect is small and delayed from direct hit events. As shown in Fig. 5.56, the clean $K_L^0 \to 3p^0$ sample suffers mostly by accidental events. The shower leakage makes a small bump near 110 ns (a). In the background sample (b), a separation between the direct hits and shower leakages is observed. The time windows were set at $\pm 3s$ (s=4.6ns for the inner modules and s=5.9ns for the outer modules). The energy threshold was applied to the sum of the inner and outer modules, and optimized as shown in Fig. 5.57. A cut point of 2 MeV was selected and the acceptance loss is 10 %.

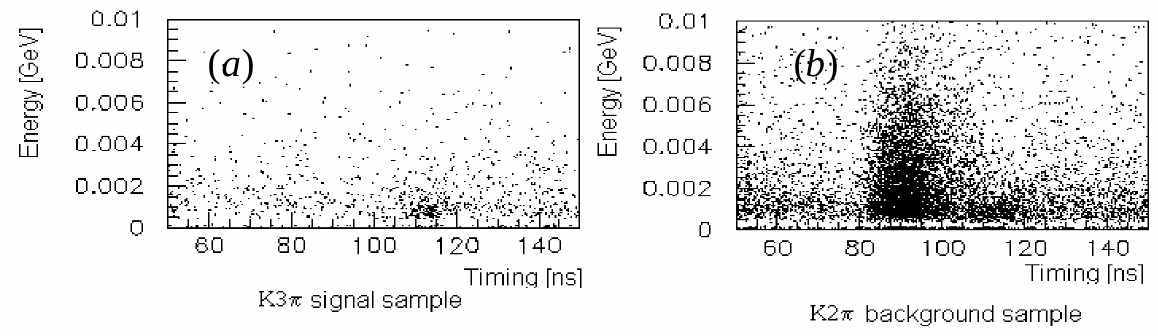

Fig. 5.56 Energy vs. Timing plot for the $K_L^0 \to 3p^0$ signal (a) and the $K_L^0 \to 2p^0$ background (b) samples for the inner front barrel modules.

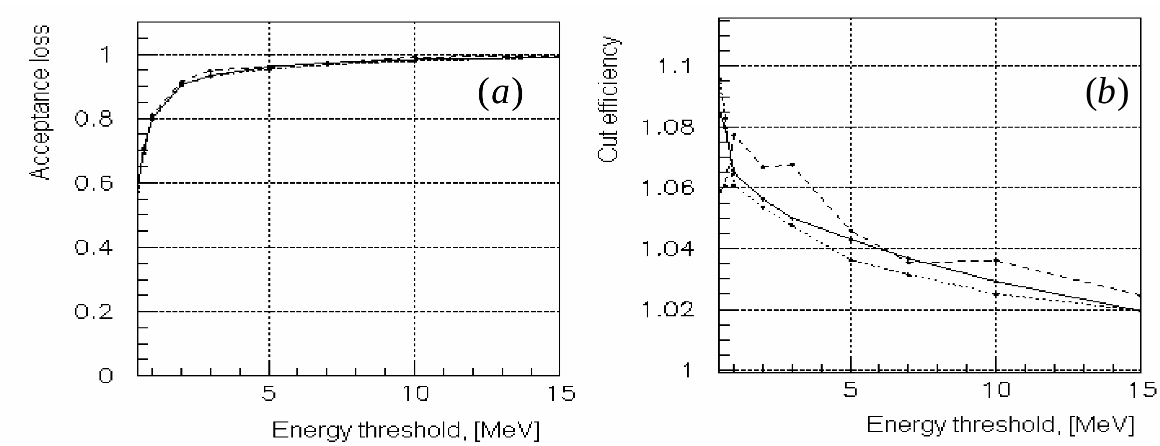

Fig. 5.57 Acceptance loss (a) and cut efficiency (b) for the front barrel. The energies of the inner and outer modules were summed up.

5.4.2.5 CC04,CC05,CC06,CC07.

The CC04, CC05 and CC06 counters are not sensitive in terms of the rejection power and the acceptance loss. The cut efficiency is a level of a few percent. We applied a loose veto of 20 MeV for these detectors inside time windows of $3s$. The CC07 suffered due to accidental events (Fig 5.58), which might also have come from backsplash from BA. The cut efficiency reaches higher than 8% at a threshold of 10 MeV with an acceptance loss of 10% (Fig. 5.59).

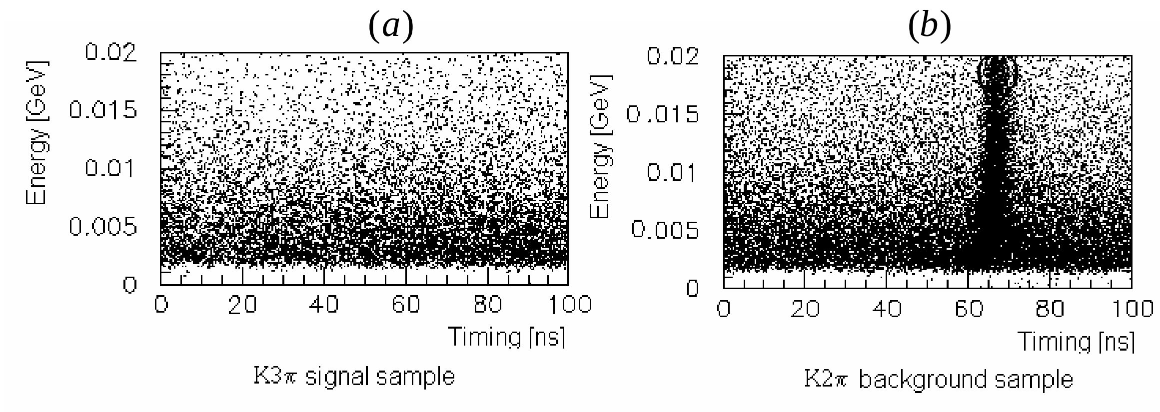

Fig.5.58 Energy vs. Timing plot for the $K_L^0 \rightarrow 3p^0$ signal (a) and the $K_L^0 \rightarrow gg$ background (b) samples for the CC07 counter.

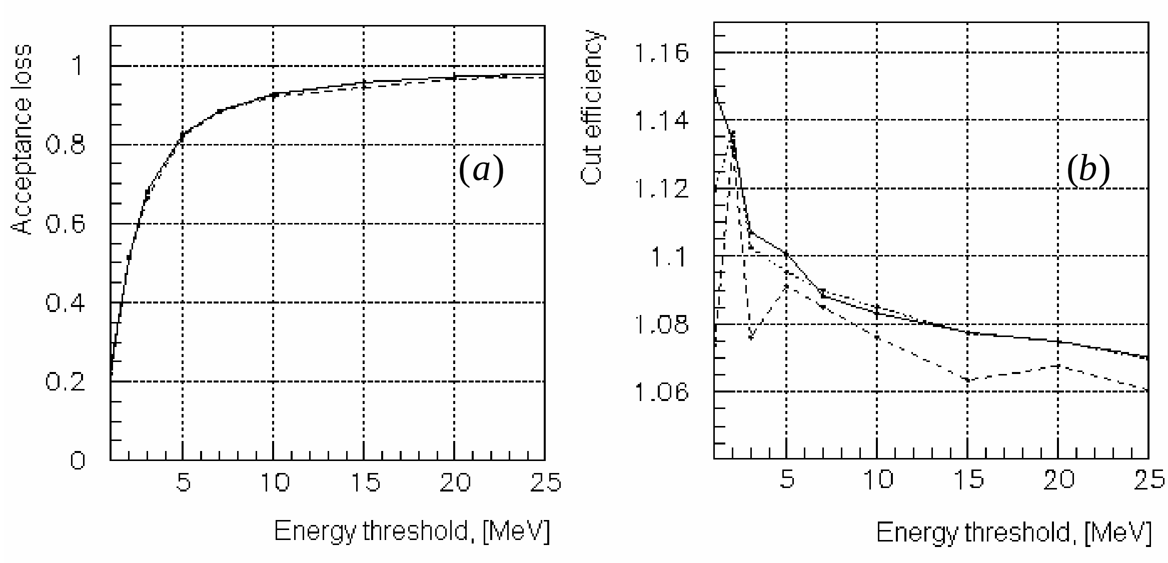

Fig. 5.59 Acceptance loss (a) and cut efficiency (b) for the CC07 counter.

5.4.2.6 Charge layers of the CC04 and CC05, Beam hole counter and Main Charge Veto(CHV)

$K_L^0 \to \pi^+\pi^-\pi^0$ decays make a big contribution to the 2γ background. It mostly comes from the case that γ's from a π^0 hit the CsI calorimeter and charged π's pass through the beam hole of the calorimeter and hit the downstream detectors. In order to suppress such events, we installed charge layers in front of CC04, CC05 and BA.

Fig. 5.60 shows a plot of the energy vs. timing for the beam hole counter, which is placed in front of BA. This detector has a multi-hit TDC and we can see huge accidental hits and peak for on-time events (Fig. 5.60.b), which corresponds to the charged particle track. The time window was set as 3σ (σ=4.5ns). Fig. 5.61 shows the acceptance loss (a) and the cut efficiency (b) for the beam hole counter. At a threshold of 0.1 MeV, the improvement of the cut efficiency goes to saturation. The acceptance loss is 15%.

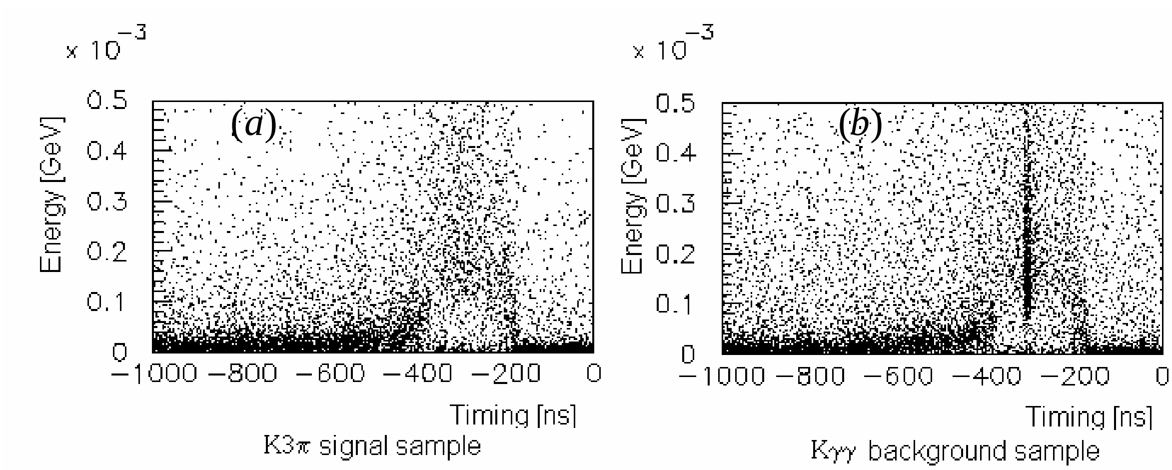

Fig. 5.60 Energy vs. Timing plot for the $K_L^0 \to 3\pi^0$ signal (a) and the $K_L^0 \to \gamma\gamma$ background (b) samples for the beam hole counter.

For the charge layers of CC04 and CC05 we applied an energy threshold of 0.5 MeV without a timing window. We also required the energy deposit for all downstream collar counters (CC04,5,6,7) to be less than the MIP energy deposit for each detector, regardless of the timing information.

For the CHV the cut efficiency was as small as 1-2%. Therefore, we applied a 1 MeV (just below MIP) threshold without a time window.

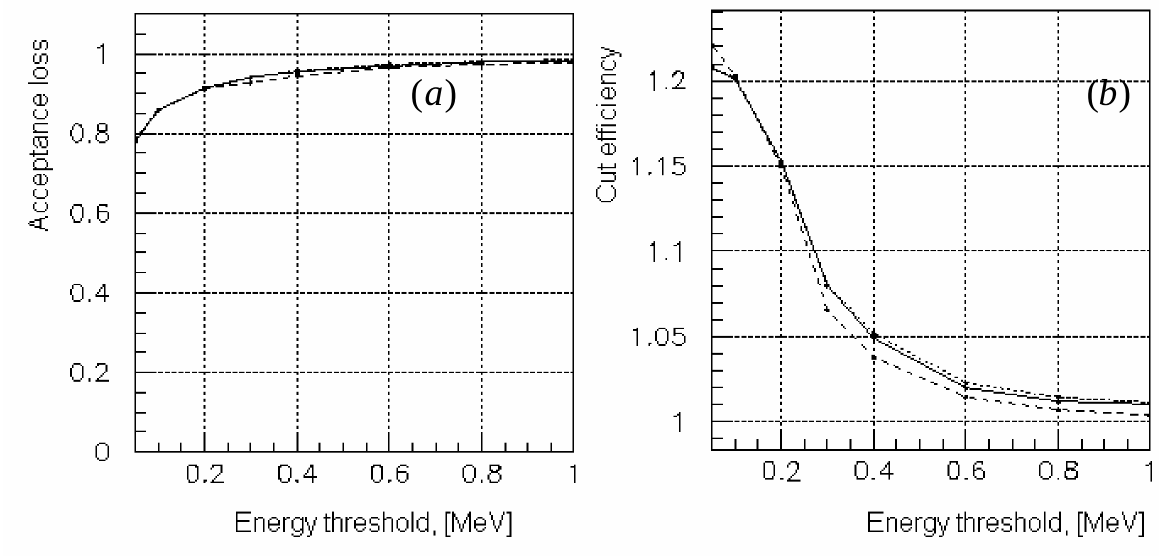

Fig. 5.61 Acceptance loss (a) and cut efficiency (b) for the beam hole counter.

5.4.2.7 Beam anti detector (BA)

A neutral beam directly hit BA. The beam neutrons, K_L^0's and decay particles from K_L^0's are mixed. It is especially necessary to separate the neutron and γ signal. The γ signal, which contains the K_L^0 decay product, should be used for the veto. At this moment we have prepared a simple shower profile cut as follows:

- TDC value must be within $\pm 4s$
- Number of fired scintillator layers ≥ 3
- Total energy deposit in the scintillator layers (on-time) > 10 MeV
- Energy emitted in a quartz > 0.5 MIP-equivalent for quartz
- Energy deposit in the 6^{th} scintillator module < 90 % and in 5^{th} and 6^{th} modules <95 % of the total energy.

If all conditions are satisfied, the event is discarded. Otherwise it is considered to be a neutron event. The acceptance loss is estimated to be at about 17% with a cut efficiency of 15%.

5.4.2.8 *Summary*

Finally, we applied the veto thresholds with timing cuts as follow:

Detector	Energy threshold	Timing peak position	s of the timing peak	Width of the time window
CC02	1 MeV	39.8 ns	1.7 ns	$\pm 3s$
CC03	3 MeV	-1.3 ns	2.5 ns	$\pm 3s$
CC04 (chrg)	0.5 MeV			Not used
CC04 (cal)	20 MeV w/ timing + 30 MeV w/o timing	56.5 ns	1.8 ns	$\pm 3s$
CC05 (chrg)	0.5 MeV			Not used
CC05 (cal)	20 MeV w/ timing + 30 MeV w/o timing	60.9 ns	1.9 ns	± 3
CC06	20 MeV w/ timing + 100 MeV w/o timing	64.7 ns	2.4 ns	$\pm 3s$
CC07	10 MeV w/ timing + 100 MeV w/o timing	67.0 ns	2.8 ns	$\pm 3s$
FBR (inner)	2 MeV*	90.8 ns	4.6 ns	$\pm 3s$
FBR (outer)		101.3 ns	5.9 ns	$\pm 3s$
CHV	1 MeV			Not used
BH CHV	0.1 MeV	305.1 ns	4.5 ns	$\pm 3s$
MBR (inner)	3 MeV**			
MBR (outer)	1 MeV**			
BA	***			

* An energy threshold for the front barrel is applied to the sum of the inner module and corresponding outer module.

** See above (MBR optimization)

*** See above (Beam anti)

Finally, by applying all vetoes, we estimated the veto acceptance using 3 clean signal samples as follows:

$K_L^0 \to 3\pi^0$: (37.4$\pm$ 0.8)%,

$K_L^0 \to 2\pi^0$: (38.5$\pm$ 3.8)%,

$K_L^0 \to \gamma\gamma$: (37.9$\pm$ 0.7)%.

They are consistent with each other. Also in total the weighted mean value is (37.7$\pm$ 0.5%). A relatively big error in the $K_L^0 \to 2\pi^0$ estimation comes from the low statistics of the clean sample and a relatively big background contribution (2.7%) into a clean sample.

Because we concentrated the rejection only in the direct hit timing region, the acceptance loss was mostly due to accidental events. Therefore, all three signal samples show the same acceptance loss.

5.5 Study on the $K_L^0 \to \pi^0 \nu\bar{\nu}$ decays

5.5.1 Candidates for $K_L^0 \to \pi^0 \nu\bar{\nu}$ decays

Fig. 5.62 shows a scatter plot of the P_T vs. decay vertex of a 2γ sample from one day of data. This is raw data before any cuts just after the skimming process. There is a large number of events in the region before the CsI calorimeter (500-600 cm). They can be explained by the interaction of the beam with the membrane, as mentioned. Also, a concentration of events can be seen near the CC02 (200-300 cm) region. A large number of events exist at a small P_T near the CsI calorimeter (400-550 cm). They have small γ energy

At first we applied kinematical cuts (Fig 5.63): neutron/γ cluster separation, fusion cluster cut, distance between γ hits, and balance of the γ energies and energy of the each γ greater than 200MeV. As can be seen, these cuts are effective against events in the decay vertex region of 500-600 cm. Also, the region under the signal box becomes cleaner. They mostly come from K^0 decays, and should be reduced by vetoes. A very clean structure appears at the CC02 position. In addition, a cluster of events can be clearly seen with a decay vertex of less than 300 cm and a small P_T, which come from $K_L^0 \to \gamma\gamma$ decays. By applying a tight cut on CC02 we can reduce π^0 production on it. Events before the CsI calorimeter with a small P_T were suppressed by the cut $E_\gamma \geq 200 MeV$.

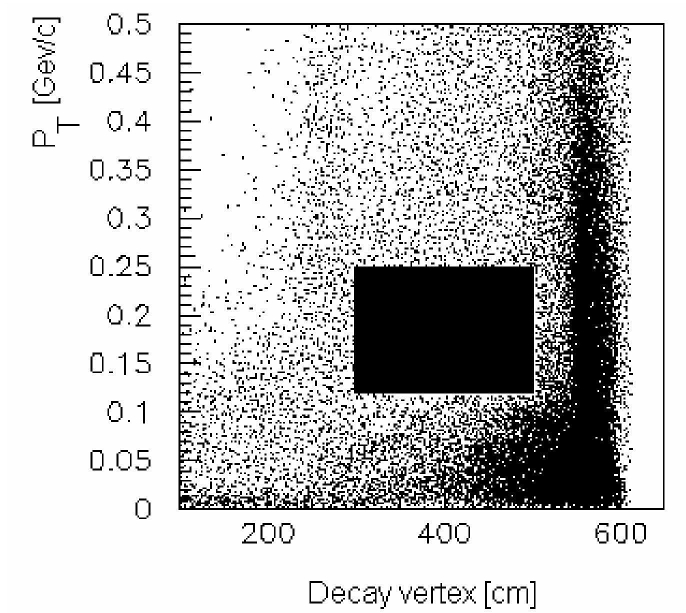

Fig. 5.62 Scatter plot of 2γ events before any cuts.

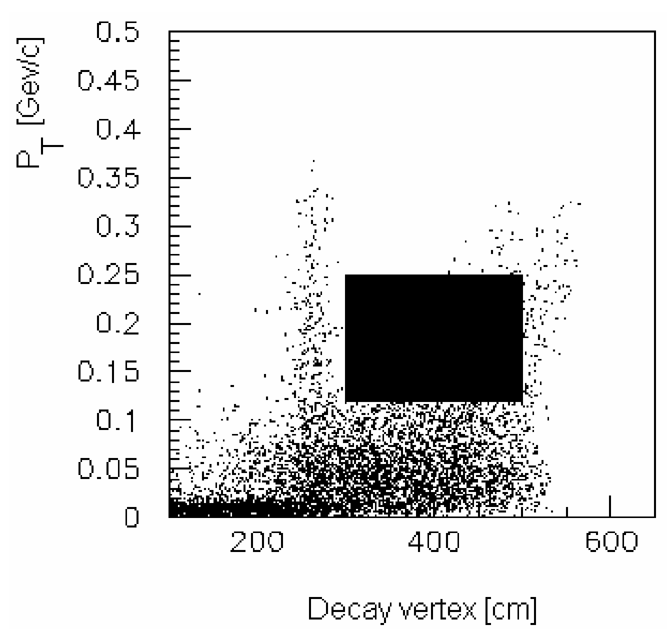

Fig. 5.63 Scatter plot of 2γ events after applying kinematical cuts.

We next applied the veto, and obtained a scatter plot, as shown in Fig 5.64. The events under the signal box were suppressed, and only one event exists in the region just under the signal box with P_T<0.10-0.12 GeV/c. The cluster of $K_L^0 \rightarrow gg$ events remains, but it can be rejected by requiring the acoplanarity angle to be larger than 20^0. The events at 500-600 cm on the right side of the signal box have almost disappeared. The events at CC02 are also suppressed, but still exist and a few events are located near the signal box.

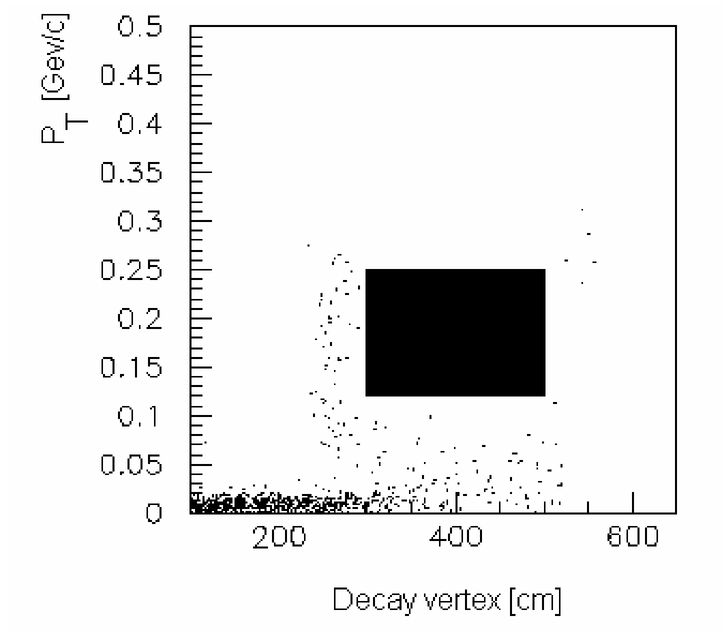

Fig. 5.64 Scatter plot of 2γ events after applying kinematical cuts and vetoes.

5.5.2 Box opening and acceptance estimation

After applying all cuts, we simply estimated the background contribution into the signal box. It is less than 1. We then opened the signal box (Fig 5.65). There is no event inside the signal box.

As described above, MC well reproduces the data in all kinematical variables. We checked the yields of $K_L^0 \rightarrow 3p^0, 2p^0, gg$ decays without touching the veto, which means only the online type veto was applied, and found good consistency in their relative yields.

So, an estimation of the acceptance was made in the following steps:

- $K_L^0 \rightarrow p^0 \nu\bar{\nu}$ MC (5x10^6 K_L^0's at the exit of the C6 collimator) was used for estimating the number of events that survived after the skimming and reconstruction procedures. Also, from MC, we estimated the acceptance loss due to kinematical cuts. The acceptance equals to (3.20 ± 0.08) x10^{-4}.
- Then, using the pure signal samples of $K_L^0 \rightarrow 3p^0, 2p^0, gg$ decays we estimated the acceptance loss due to a veto separately for each sample. All three estimations showed a good agreement between them. The acceptance loss doesn't depend on the number of γ's and the kinematics of the decay. There is no reason that the acceptance loss due to the veto is different for the $K_L^0 \rightarrow p^0 \nu\bar{\nu}$ decay. Thus the veto acceptance as the weighted mean value equals to (37.7 ± 0.5)%.

- Finally, we obtained the total acceptance as:

  Acc=$(3.20\pm 0.08)\,\mathrm{x}10^{-4} * (0.377 \pm 0.005) = (1.21 \pm 0.03)\,\mathrm{x}10^{-4}$.

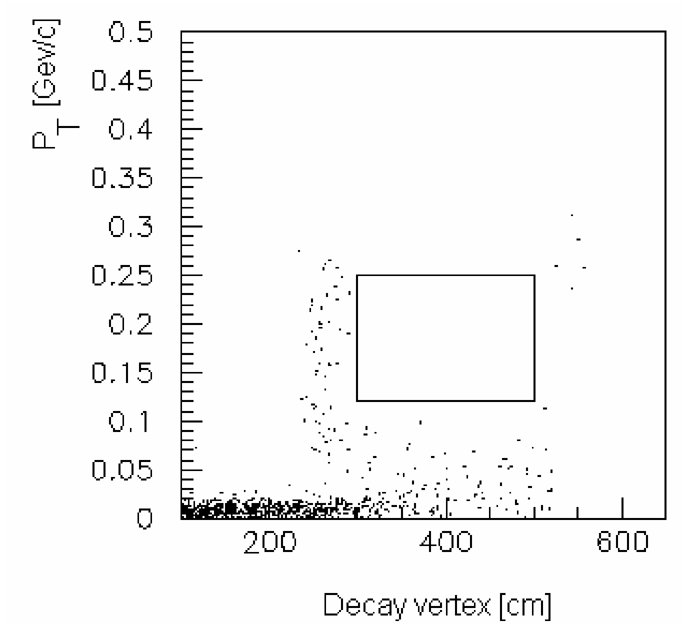

Fig. 5.65 Scatter plot of 2-γ events after all cuts. Inside the signal box there are no events.

Table 5.4 shows the result. The values were obtained when each cut was applied subsequently. The acceptance was defined as the number of events surviving after each cut divided by the number of K_L^0 generated at the exit of C6 collimator.

The $K_L^0 \to 3\pi^0$ process was used to normalize the number of incident K^0. Since there is no event in the signal box, we estimated the single event sensitivity (SES) for the $K_L^0 \to \pi^0 \nu\bar{\nu}$ decay using one-day data sample as

$$SES\left(K_L^0 \to \pi^0 \nu\bar{\nu}\right) = BR\left(K_L^0 \to 3\pi^0\right) \frac{N(K_L^0 \to \pi^0 \nu\bar{\nu})}{N(K_L^0 \to 3\pi^0)} \frac{Acc(K_L^0 \to 3\pi^0)}{Acc(K_L^0 \to \pi^0 \nu\bar{\nu})}$$

$$= 0.2113 \frac{1}{29669} \frac{1.41 \cdot 10^{-5}}{1.21 \cdot 10^{-4}} = (8.3 \pm 0.2) \cdot 10^{-7}$$

As mentioned in discussion section 5.7, we expect about 0.03 background events in the signal region. This is negligibly small, and the upper limit of the branching ratio at the 90% confidence level, $1.91\mathrm{x}10^{-6}$, was obtained by multiplying the value of SES by a factor of 2.3

Table 5.4. Acceptance of $K_L^0 \to \pi^0 \nu\bar{\nu}$ if we apply the kinematical cuts subsequently one by one.

Cuts	Acceptance
Decay + geometry + skimming	5.49×10^{-3}
E γ>200MeV	3.55×10^{-3}
Distance γ–γ >50 cm	2.77×10^{-3}
$0.92 < \dfrac{E_1 + E_2 + E_3}{E_{cluster}} < 0.98$	1.71×10^{-3}
$0.6 < E_{\max} / E_{cluster} < 0.92$	9.46×10^{-4}
Energy balance < 0.5	7.56×10^{-4}
signal box: 300 < Z < 500 cm + 0.12< P_T < 0.25 GeV/c	3.20×10^{-4}
Veto	1.21×10^{-4}

5.6 Results

Finally, we opened the signal box and no events were found inside. The acceptance was estimated from a MC simulation for $K_L^0 \to \pi^0 \nu\bar{\nu}$ decay. The MC simulation was critically checked for the $K_L^0 \to 3\pi^0, 2\pi^0, \gamma\gamma$ decays, as described before. The acceptance for the $K_L^0 \to \pi^0 \nu\bar{\nu}$ decay was estimated to be 1.21×10^{-4}, including a 37.7% veto acceptance.

The K^0_L yields showed good agreement among three monitor samples of $K_L^0 \to 3\pi^0, 2\pi^0, \gamma\gamma$ decays, when we used the branching ratios given by PDG. We estimated the flux of K^0_L using the $K_L^0 \to 3\pi^0$ decays to be 0.99×10^{10} K^0_L for one day of data. Then, the single-event sensitivity was calculated to be 8.3×10^{-7}. The upper limit for the branching ratio of $K_L^0 \to \pi^0 \nu\bar{\nu}$ decay is 1.91×10^{-6} at the 90% confidence level.

5.7 Discussion

As shown in Fig. 5.65, many events remain around the signal box. We tried to estimate the background inside the signal box using these surrounding events.

1) The events on the left side of the signal box ("B region") come from π^0's produced by neutron interactions with CC02. After applying kinematical cuts, a clean structure was observed, as shown in Fig.5.63. In order to estimate a tail extending to the signal box from these events, we used the distribution in the decay vertex for a "B" sample, which is a sample before applying the veto cuts, as shown in Fig. 5.66(a). It was fitted by a Gaussian function. Then, using the width of the Gaussian function we fitted again the sample after applying all veto cuts (Fig. 5.66.b). The number of events estimated by the Gaussian tail to the signal box is 0.03.

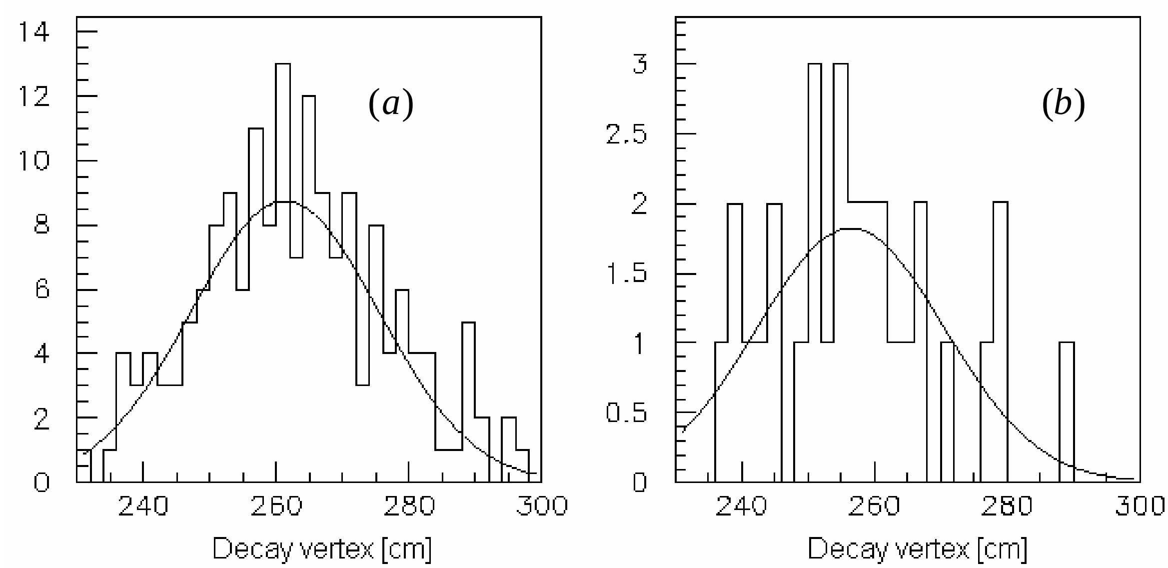

Fig. 5.66 Distribution of the decay vertex for the "B" sample before (a) and after (b) applying veto cuts fitted by Gaussian. The kinematical cuts were applied to both of them.

2) Events from the interactions of halo and beam-core neutrons with material are mostly concentrated on the right side of the signal box ("C" region). They are almost suppressed by the kinematical and veto cuts, and only one event remains in the "C" region. Since the statistics is very poor, it is impossible to estimate the background in the signal box from this source. But it might be negligibly small.

3) The events from neutral K^0_L decays are located in the region under the signal box ("A" region) and the $K2\pi^0$ decay is the most dangerous among various decays. From a MC

sample of 10 day-statistics, no event was found in the signal box after applying all kinematical and veto cuts. So the background might be less than 0.1 event for one-day statistics.

The finite value of 0.03 events is only expected from item 1), which comes from π^0's produced by halo neutrons at the CC02 position. It contains a margin to increase the statistics by a factor of 33, which is comparable with our factor of 60 (full data/one-day data). The improvement of the resolution might shrink the distribution of the decay vertex near CC02, and also a decrease of the energy threshold of CC02 will improve the rejection of these events.

Other backgrounds are hard to estimate due to the low statistics of the data and MC, although their contribution might be small. A detailed study will be done in future analysis using larger samples of one week and 1/3 data sets.

Since the single-event sensitivity for a one-day sample is 8.3×10^{-7}, we will reach the level of 1.8×10^{-8} in full statistics, if we simply extrapolate. It is poorer than the expected sensitivity of 3×10^{-10} by a factor of 60. One of the reasons is a small acceptance. Since the present acceptance value of 1.21×10^{-4} includes the decay probability, we extracted the acceptance normalized for the decays in our fiducial region (300-500cm). It is 0.6% and is smaller than the expected acceptance of 8% by a factor of 13.

There are several points giving a remarkable acceptance loss, and can possibly be improved. At first, in the reconstruction procedure, we rejected events if the hit point of γ was outside of the 80 cm radius. It is related with poor reconstruction of the energy and hit position of a γ near the border due to shower leakage from the CsI calorimeter which has a radius of about 100cm. By increasing the reconstruction area up to 90 cm, we can improve the acceptance. More careful treatment of the γ hits near and in KTeV crystals is also expected to increase the acceptance of $K_L^0 \to \pi^0 \nu\bar{\nu}$.

Another point for a recovery of the acceptance exists in the cluster shape cuts. The variables $E_{\max}/E_{cluster}$ and $\frac{E_1+E_2+E_3}{E_{cluster}}$ were introduced to reject the neutron interaction and cluster fusing in the CsI calorimeter. They are based on a simple estimation of the shower size, which seems to be too simple. A detailed analysis of the difference in the shower shape for neutrons and γ's might be effective for neutron/γ cluster separation, which allows us to save the acceptance. Identification of the fused clusters can be also done based on the shower shape analysis

As described in the section of background identification, we faced to the unexpected background from the beam neutron interaction with a membrane. It produced a large peak in the decay vertex distribution near the CsI calorimeter. At present, we had to introduce a tight cut for the distance between g hits. This also resulted in reducing the downstream end of the fiducial volume (signal box) from 550cm (proposal) to 500cm. In this thesis we didn't make the optimization of the position of the signal box, which is potentially one of the sources to increase the acceptance.

It is necessary to mention the veto study. To estimate the acceptance loss due to the veto we used pure signal samples of the $K_L^0 \rightarrow 3p^0, 2p^0, gg$ decays. They show a good consistency between all samples. The acceptance loss doesn't depend on the number of g's and the kinematics of the decay. This means that the acceptance loss does not come from backsplash, but from accidental effects. In the present analysis we introduced rather sophisticated time windows for the veto to understand it using the pure samples.

MBR is one of the most important veto detectors, which makes the biggest contribution to the acceptance loss. We found that MBR is sensitive to a neutron passing through the modules, and a careful treatment of the time windows for the veto allows us to suppress the neutron events. A more detailed study of veto might help to increase the acceptance.

Another reason of the poor sensitivity is a shorter beam time. Some part of the beam time was lost due to problems related to the accelerator. Also, we spent some time for the beam tuning and detector calibration. In total, we collected about 60 days of data instead of the expected 100 days. After all, a factor of 3 remains as a decrease from the proposed value. It might come from many sources, such as a difference of the K_L spectrum from calculation, the dead time and the target efficiency to produce K_L.

In summary, we still have a possibility to recover the acceptance for the $K_L^0 \rightarrow p^0 \nu\bar{\nu}$ decay to reach the 10^{-9} - 10^{-10} level of the single-event sensitivity. In any case it is important to reach our goal of $3x10^{-10}$, because in the recent study of Buras [36] it is pointed out the branching ratio of $K_L^0 \rightarrow p^0 \nu\bar{\nu}$ might increase up to $3x10^{10}$.

Chapter 6

Conclusion

The E391 experiment was successfully run for data taking from February 15 to June 1, 2004. All systems worked stably and no dead channels appeared during all period. The full collected statistics of physics data is equivalent to 60 days of continuous data taken.

The E391 experiment is a pilot experiment, and it is important to check new techniques used for searching for $K_L^0 \to p^0 v\bar{v}$ decay. We confirmed most of them through an analysis of the one-day data sample. The pencil beam clearly separates the $K_L^0 \to gg$ decays from other decay modes using P_T. The separation of the vacuum volumes into two regions by a thin membrane allowed us to evacuate the air efficiently. The vacuum level could reach 10^{-4} Pa after 1 day of evacuation. We could apply a very low veto threshold of a few MeV to the veto detectors.

In the present first step of analysis using one day of data, we could develop various software tools and confirm the good quality of data.

- We could establish in-situ calibration of detectors. All detectors were calibrated using punch-though or cosmic muons. For the CsI calorimeter we refined the calibration by using g's from p^{0} decays produced on a target. Also, all detectors showed good stability.

- We developed GEANT-3 MC simulation and reconstruction codes. The reconstruction code was applied to both data and MC. MC well reproduces the experimental spectra of various kinematical variables. We developed one of the analysis methods using pure signal samples of the $K3p^{0}$ (~30k events), $K2p^{0}$ (~1k events) and Kgg (~13k events) decays. The purification process relayed a negligibly small contamination of for $K3p^{0}$, 2.7% for $K2p^{0}$ and 0.7% for Kgg. We prepared background samples of the $K2p^{0}$ and Kgg decays. The pure signal samples showed a good agreement between the data and the MC. The relative branching ratios obtained from three pure samples are in a good agreement with those given by PDG.
- Background sources were explored by comparing the data with the MC at the level of online for 2-g events. They are the decays of $K3p^{0}$, $K2p^{0}$, Kgg, and $K \rightarrow p^{0}p^{+}p^{-}$, halo neutron interaction with CC02 and CHV. However, we found additional background sources: two clusters due to a hadronic shower in the CsI calorimeter produced by a single neutron and interactions of the beam core neutrons with the membrane. We then developed several kinematical and cluster shape cuts to suppress the background due to the neutron interaction.
- The acceptance loss due to the veto was surely estimated from pure signal samples. Since we found a severe effect of backsplash, we developed a time window for the veto signal.

Finally, we obtained the upper limit for the branching ratio of $K_L^0 \rightarrow p^0 \nu\bar{\nu}$ decay to be 1.91×10^{-6} (90% CL).

In summary, the present analysis using a one-day sample was very valuable to check several techniques newly developed for the $K_L^0 \rightarrow p^0 \nu\bar{\nu}$ measurement. It was also very important to understand the data quality and to find unexpected phenomena. Not only the methods developed in the present analysis are being applied for the analysis of a larger sample, but also the results are reflected to several upgrades of the detector system for the second run, which was just started in the middle of January 2005.

References

1. H. Christenson *et al*. Phys. Rev. Lett. **13,** 138 (1964)
2. K.Abe *et.al*. Phys. Rev. Lett **87,** 091802 (2001).
3. T. Inagaki *et al.*, “Measurement of the $K_L^0 \to p^0 \nu\bar{\nu}$ decay”, KEK Internal 96-13 (1996)
4. A.J. Buras, hep-ph/9905437 (1999)
5. M. Koboyahsi and T. Msakawa, Prog. Theor. Phys. **49,** 652 (1973)
6. L. Wolfenstein. Phys. Rev. Let. **51,** 1945 (1983)
7. Phys. Lett. **B592**, 130 (2004)
8. I.S. Towner and J.C Hardy, nucl-th/9809087 (1998)
9. Yu.A.Mostovoi *et al*. Phys. Atomic Nucl. **64** (2001)
10. Phys. Lett. **B592**, 131 (2004)
11. V. Cirigliano *et al.* Eur. Phys. J. **C23**,121 (2002)
12. P.Abreu *et al.* Phys. Lett. **B439**,209 (1998)
13. The LEP Collaborations *et al*. hep-exp/0112021 (2002)
14. Phys. Lett. **B592**, 134 (2004)
15. Phys. Lett. **B592**, 133 (2004)
16. hep-ph/0304132 (2003)
17. Phys. Lett. **B592**, 131 (2004)
18. Phys. Lett. **B592**, 793 (2004)
19. T.Affolder. Phys. Rev. Lett. **86,** 3233 (2001)
20. Phys. Lett. **B592**, 140 (2004)
21. Phys Rev.Lett.**89**,211802 (2002)
22. R. Belusevic “Neutral kaon”, KEK preprint 97-264 (1998)
23. T Inami and C.S. Lim, Prog, Theor, Phys. **65**, 297 (1981)
24. W Marciano and Z Parsa, Phys.Rev.**D53,** R1 (1996)
25. G Buchalla *et al*., Rev Mod. Phys **68,** 1125 (1989)
26. G. Buchalla, hep-ph/9612307 (1996).

27. S. Plaszczynski and M.H Schune, hep-ph/9911280 (1999).
28. L. Silvestrini *et al*., hep-ph/0009248 (2000).
29. A. Buras *et al.*, hep-ph/0007313 (2000).
30. M. Brhlik, hep-ph/990948 (1999).
31. M.S. Canowitz, hep-ph/9905478 (1999).
32. T. Hattori *et al.*, hep-ph/9908447 (1999).
33. Z. Xiao *et al.*, hep-ph/9903348 (1999).
34. Z. Xiao *et al.*, hep-ph/9903347 (1999).
35. Y. Kiyo *et al.*, hep-ph/9900948 (1998).
36. A.Buras hep-ph/0312259 (2004)
37. K.Abe *et al*. hep-ex/0308040 (2003)
38. B.Aubert *et al*. hep-ex/0308012 (2003)
39. A.Alavi-Harati *et al*. Phys.Rev. **D61,** 072006 (2000)
40. J.Adams *et al*. hep-ex/9806007 (1998)
41. KEK Preprint 2004-85 H (Will be published in NIM)
42. Particle Data Group, Phys.Lett. **B592**, (2004)
43. KEK Preprint 2004-86 H (Will be published in NIM)